UNIVERSITAT POLITÈCNICA DE VALÈNCIA
DEPARTAMENTO DE MÁQUINAS Y MOTORES TÉRMICOS

OPTICAL INVESTIGATIONS ON DIESEL SPRAY DYNAMICS AND IN-FLAME SOOT FORMATION

DOCTORAL THESIS
Presented by:
Tiemin Xuan
Directed by:
Dr. José María García Oliver

Valencia, December, 2017

DOCTORAL THESIS

OPTICAL INVESTIGATIONS ON DIESEL SPRAY DYNAMICS AND IN-FLAME SOOT FORMATION

Presented by:	Tiemin Xuan
Directed by:	Dr. José María García Oliver

Examining Board:

President:	Dr. Benajes Calvo, Jesus Vicente
Secretary:	Dr. Juliá Bolivar, José Enrique
Examiners:	Dr. Le Moyne, Luis

Reviewing Board:

Dr. Martos Ramos, Francisco Javier
Dr. Tornatore, Cinzia
Dr. Le Moyne, Luis

Valencia, December, 2017

Resumen.

En las últimas décadas ha avanzado mucho la comprensión científica sobre el proceso de combustión de los chorros diesel de inyección directa gracias al desarrollo de todo tipo de técnicas e instalaciones ópticas. Además, se han desarrollado y mejorado una gran cantidad de modelos de Dinámica de Fluidos Computacional (CFD), los cuales se usan para el desarrollo de motores altamente eficientes y con bajas emisiones. Sin embargo, debido a la complejidad de los procesos físicos y químicos involucrados en este proceso de combustión, así como a las limitaciones significativas de los experimentos, aún hay muchas cuestiones sin responder: ¿Cómo afecta la combustión a la dinámica del chorro? ¿Cómo cuantificar de forma efectiva la cantidad de hollín y la temperatura del mismo en la llama? ¿Cómo afecta el flujo del aire y las inyecciones partidas al desarrollo del chorro y a la formación de hollín en condiciones no quiescente? Para ayudar a resolver las preguntas planteadas, el objetivo de este trabajo se pone en investigar al dinámica del chorro y la formación de hollín de los chorros Diesel de inyección directa en condiciones quiescentes y no quiescentes por medio de diferentes técnicas ópticas.

El trabajo se ha dividido en dos bloques principales. El primero está centrado en el estudio de las modificaciones inducidas por la combustión en la dinámica del chorro, así como la caracterización de la formación de hollín en la llama, todo ello en condiciones quiescentes. Dichas condiciones son proporcionadas por una maqueta de flujo continuo a alta presión y temperatura. La expansión radial y axial del chorro reactivo se ha investigado usando n-dodecano, n-heptano y una mezcla binaria de combustibles primarios de referencia (80% n-heptano y 20% iso-octano en masa), basándose en una base de datos existente medida mediante visualización de schlieren. Se ha estudiado tanto el papel de las condiciones de operación como las propiedades del combustible. A continuación se ha desarrollado por primera vez una técnica combinada de extinción-radiación, aplicada a la medida de hollín en llamas diesel. Gracias a esta técnica, tanto la fracción volumétrica de hollín como la temperatura se obtuvieron simultáneamente considerando los efectos de la autoabsorción en la radiación. Todo este trabajo se ha desarrollado dentro del marco de actividades de la Engine Combustion Network (ECN).

El segundo bloque corresponde a la caracterización de la dinámica del chorro y de la formación de hollín en condiciones no quiescentes, que ocurren en la cámara de combustión de un motor monocilíndrico de dos tiempos con accesos ópticos. En esta parte, se ha llevado a cabo en primer lugar la visualización del chorro para una inyección única en condiciones no-reactivas y reactivas. Se han aplicado la visualización simultánea de schlieren y de la quimioluminiscencia del radical OH* para obtener la penetración del chorro y la longitud de despegue de la llama, mientras que la visualización de la extinción de ombroscopía difusa (DBI) se ha aplicado para cuantificar la formaciónde hollín. Los resultados se han comparado con los de la base de datos de la Engine Combustion Network antes mencionados, para estudiar los efectos del movimiento del aire inducido por el movimiento del pistón sobre el desarrollo del chorro y del hollín. Finalmente, se han usado diferentes estrategias de inyección partida para estudiar cómo la primera inyección afecta a los procesos de

mezcla y a formación de hollín de la segunda, al cambiar el tiempo de separación entre ambos eventos de inyección o la cantidad inyectada en el primer pulso.

Resum.

En les últimes dècades ha avançat molt la comprensió científica sobre el procés de combustió dels dolls dièsel d'injecció directa gràcies al desenvolupament de tot tipus de tècniques i instal·lacions òptiques. A més, s'han desenvolupat i millorat una gran quantitat de models de Dinàmica de Fluids Computacional (CFD), els quals s'usen per al desenvolupament de motors altament eficients i amb baixes emissions. No obstant açò, a causa de la complexitat dels processos físics i químics involucrats en aquest procés de combustió, així com de les limitacions significatives dels experiments, encara hi ha moltes qüestions sense respondre: Com afecta la combustió a la dinàmica del doll? Com quantificar de forma efectiva la quantitat de sutge i la temperatura del mateix en la flama? Com afecta el flux de l'aire i les injeccions partides al desenvolupament del doll i a la formació de sutge en condicions no quiescents? Per a ajudar a resoldre les preguntes plantejades, l'objectiu d'aquest treball es posa a investigar al dinàmica del doll i la formació de sutge dels dolls Dièsel d'injecció directa en condicions quiescents i no quiescents per mitjançant diferents tècniques òptiques.

El treball s'ha dividit en dos blocs principals. El primer està centrat en l'estudi de les modificacions induïdes per la combustió en la dinàmica del doll, així com la caracterització de la formació de sutge en la flama, tot açò en condicions quiescents. Aquestes condicions són proporcionades per una maqueta de flux continu a alta pressió i temperatura. L'expansió radial i axial del doll reactiu s'ha investigat usant n-dodecà, n-heptà i una mescla binària de combustibles primaris de referència (80% n-heptà i 20% iso-octà en massa), basant-se en una base de dades existent mesura mitjançant visualització de schlieren. S'ha estudiat tant el paper de les condicions d'operació com les propietats del combustible. A continuació s'ha desenvolupat per primera vegada una tècnica combinada d'extinció-radiació, aplicada a la mesura de sutge en flames dièsel. Gràcies a aquesta tècnica, tant la fracció volumètrica de sutge com la temperatura es van obtenir simultàniament considerant els efectes de l'autoabsorció en la radiació. Tot aquest treball s'ha desenvolupat dins del marc d'activitats de la Engine Combustion Network (ECN).

El segon bloc correspon a la caracterització de la dinàmica del doll i de la formació de sutge en condicions no quiescents, que ocorren en la cambra de combustió d'un motor monocilíndric de dos temps amb accessos òptics. En aquesta part, s'ha dut a terme en primer lloc la visualització del doll per a una injecció única en condicions no-reactives i reactives. S'han aplicat la visualització simultània de schlieren i de la quimioluminescència del radical OH* per a obtenir la penetració del doll i la longitud d'enlairament de la flama, mentre que la visualització de l'extinció d'ombroscopia difusa (DBI) s'ha aplicat per a quantificar la formaciónde sutge. Els resultats s'han comparat amb els de la base de dades de la Engine Combustion Network abans esmentats, per a estudiar els efectes del moviment de l'aire induït pel moviment del pistó sobre el desenvolupament del doll i del sutge. Finalment, s'han usat diferents estratègies d'injecció partida per a estudiar com la primera injecció afecta als processos de mescla i a formació de sutge de la segona, en canviar el temps de separació entre tots dos esdeveniments d'injecció o la quantitat injectada en el primer pols.

Abstract.

In recent decades, the scientific understanding of the combustion process of direct injection diesel spray has progressed a lot, thanks to the development of all kinds of optical facilities and techniques. In addition, a large amount of efficient and accurate Computational Fluid Dynamics (CFD) models, which are used for the design of highly efficient, low emission engines has been developed and improved. However, because of the complexity of the physical and chemical process involved in this combustion process, as well as significant experimental limitations and uncertainties, there are still a lot of remaining questions: How do combustion affect spray dynamics? How can in-flame soot amount and soot temperature be quantified effectively? How does the airflow and split-injection affect spray development and soot formation under non-quiescent conditions? To help solve these raised questions, the objective of this work is set to investigate the spray dynamics and soot formation process of direct injection diesel sprays under both quiescent and non-quiescent conditions by means of different optical techniques.

The work has been divided into two main blocks. The first one is focused on the study of combustion-induced modifications in spray dynamics, as well as the characterization of in-flame soot formation under quiescent conditions. The quiescent conditions are provided by a kind of high-temperature high-pressure constant flow vessel. The radial and axial reacting spray expansion were investigated using n-dodecane, n-heptane and one binary blend of Primary Reference Fuels (80% n-heptane and 20% iso-octane in mass) based on a existing database from Schlieren imaging technique. Both operating conditions and fuel properties on this combustion-induced expansion were studied. Next, a combined extinction-radiation technique was first developed and applied in diesel spray soot measurement. Thanks to this technique, both the in-flame soot volume fraction and temperature were obtained simultaneously by considering the self-absorption effect on radiation. All this work has been carried out within the framework of activities of the engine combustion network (ECN).

The second block corresponds to the characterization of spray dynamics and soot formation under non-quiescent conditions, which occur within the combustion chamber of a single-cylinder two-stroke optical engine. In this part, the spray visualization for single-injection under both non-reacting and reacting operating conditions was conducted first. Schlieren and $OH*$ chemiluminescence were simultaneously applied to obtain the spray tip penetration and flame lift-off length, while the Diffuse Back Illumination (DBI) extinction imaging was applied to quantify the instantaneous soot formation. Results were compared with Engine Combustion Network database mentioned above to study the airflow effects induced by piston movement on spray and soot development. Finally, different split-injection strategies were used to study how the first injection affects the mixing and soot formation processes of the second one, by changing the dwell time between both injection events or the first injection quantity.

To my family

Acknowledgements

More than four years have passed since my first day in Valencia. Looking back, this long journey is full of difficulties and challenges. I still can feel the painful moments during the early days when I went through loneliness, helplessness, language barrier and culture shock. I am glad I did not give up and reach the end. Besides the knowledge of engines and skills on how to do science, I also get a deep knowing about myself and make some good friends. These four years deserve to be treasured during my whole life. Of course, I could not finish this work without those people who give me guidance, help, and company during this long journey. I would like to take this opportunity to express my thanks to some of them.

First, I would like to acknowledge Prof. Francisco Payri and Prof. José María Desantes to give me this opportunity of working in this worldwide recognized research center. I also need to thank Dr. Bart Somers for accepting me to do the internship for three months at the Eindhoven University of Technology.

Especially, I would like to express my gratitude to my director Dr. José María García-Oliver for his invaluable guidance, huge patience and confidence on me over the last four years. As my director, I would say he is more like an older brother. I still remember his disappointed face, when I told him I gave up learning Spanish because he always believes it will be helpful for my future career. He keeps being very helpful and supportive in every aspect of my work and life. Besides scientific knowledge, the more important thing I learned from him is the scientific spirit. I feel so lucky to be his student.

In addition, I also would like to thank Prof. José Vicente Pastor for his guidance and suggestions on the optical techniques and research papers. I would like to include also Dr. Antonio García who also gave me some suggestions on my research works.

I also need to thank Dr. Carlos Micó Reche and Dr. Walter Martín Vera-Tudela Fajardo. When I was a freshman, they taught me a lot about these optical techniques and image processing step by step with huge patience. I am really grateful for their selfless support. I also need to thank all my colleagues in the group of Optical techniques, like Mattia Pinotti, Leonardo Pachano, who give me a lot of help and we spent a great time. Besides, I also need to thank the colleagues in the in the injection team, like Alberto Viera, Dr. Gabriela Bracho, who help me a lot one injection rate measurement and modeling. Especially, I need thank Prof. Raul Payri for giving me the opportunities to do the measurements in IAPAT and did not complain my stupid mistakes. I would like also thank my friend Daniel Estepa who helped a lot as a translator on all kinds of applications forms. I cannot forget to acknowledge the administration staffs and technicians (Amparo, Elena, Daniel, José Enrique, Omar...) for their kind support on my paper works and experiments. I also need to thank all my Chinese friends whom I met in Valencia, they help me passing a happy life.

Most of all, I thank my wife Wenjun Zhang for her unwavering support and encourage me every step of the way. Thanks to my parents and family for their continuous support through my entire life.

This work was partially funded by the Government of Spain through COMEFF Project (TRA2014-59483-R). In addition, the authors acknowledge that some equipment used in this work has been partially supported by FEDER project funds (FEDER-ICTS-2012-06), framed in the operational program of unique scientific and technical infrastructure of the Ministry of Science and Innovation of Spain. The authors want also to express their gratitude to CONVERGENT SCIENCE Inc for their kind support for this research.

Table of Contents

Index of Figures

Index of Tables

Nomenclature

Latin

A/F	Air/Fuel ratio
$(A/F)_{st}$	Stoichiometric Air/Fuel ratio
C_a	Nozzle area coefficient
KL	Optical thickness with K, extinction coefficient and L, path length
C_d	Nozzle discharge coefficient
C_M	Nozzle momentum coefficient
C_v	Nozzle velocity coefficient
f_v	Soot volume fraction
d	Nozzle orifice diameter
S	Spray penetration
Z_{st}	Stoichiometric mixture fraction
U	injection velocity
m	Mass
$\dot{m}$	Mass flow rate
$\dot{M}$	Momentum flux
t	Time
T	Temperature
P	pressure
v	volume
c_v	Specific heat atconstant volume
I_0	Incident intensity
I_t	Transmitted intensity
I_b	Blackbody radiation intensity
I_f	flame radiation intensity

k_e	extinction coefficient
f	focus length
R	Spray radius
$2C$	2-color pyrometry

Greek

ε	Emissivity
Δ	Increment / Variation
λ	Wavelength
σ	Standard deviation
θ	Spray angle
ρ	Density
ϕ	Equivalence ratio

Subscripts

g	Relative to ambient gas
f	Relative to fuel
inj	Relative to ambient gas
max	Maximum
min	Minimum
sat	Saturation
st	Stoichiometric
$soot$	Relative to soot
t	Relative to transmission
b	blackbody
DBI	Relative to Diffused background-illumination technique
LEM	Relative to laser extinction method
$2C$	Relative to two-color method
r	Relative to radiation

Initials and acronyms

ICE	Internal combustion engine
CFD	Computational Fluid Dynamics
ECN	Engine Combustion Network
TDC	Top Dead Center
DBI	Diffused background-illumination

ID	Ignition delay
CPF	Constant Pressure Flow facility
UHC	Unburned hydrocarbons
CAD	Crank angle degree
EGR	Exhaust gas recirculation
EOI	End of injection
EOC	End of combustion
FWHM	Full width at half maximum
EVC	Exhaust valve closing angle
EVO	Exhaust valve opening angle
IVC	Intake valve closing angle
IVO	Intake valve opening angle
LOL	Flame lift-off length
AHRR	Apparent heat release rate
SOC	Start of combustion
SOI	Start of injection
ASOI	After the start of injection
RDG	Rayleigh-Debye-Gans theory
ASOE	After start of energizing
CER	Combined extinction-radiation
PID	Proportional-integral-derivative
CN	Cetane Number
LIF	laser-induced fluorescence
UV-VIS LAS	Ultraviolet and visible light absorption and scattering
UV-LA	Ultraviolet light absorption
PAH	Polycyclic aromatic hydrocarbons
LEM	Laser Extinction Method
CCD	Charge-coupled device
SE	standard error
CVP	Constant Volume Preburn

Chapter 1

Introduction

Contents

1.1 Background and motivations

Diesel engine is the most efficient, mass-produced internal combustion engine (ICE) ever built for transportation purposes and is widely used all over the world. Increasingly stringent environmental and fuel economy requirements have pushed researchers to pursue high-fuel-efficiency and low-emission engines [1]. To meet future emission legislation and energy crisis, an improvement of the understanding for the fundamental physical and chemical processes that take place during the combustion process in Diesel engine is needed.

Conventional engine design approaches that rely on prototype development are too time-consuming and expensive. The development of predictive and efficient Computational Fluid Dynamics (CFD) models provide a significant step forward in the ability to rapidly design highly efficient, low emission engines [2]. However, significant limitations and uncertainties exist in our knowledge of these fundamental processes and their coupling. Therefore, detailed experimental databases are needed to build and validate CFD models.

Thanks to the development of all kinds of test rigs and optical techniques, nowadays, it is possible to visualize the whole combustion process and quantify each transient chemical component and all kinds of spray parameters, as shown in Figure 1.1.

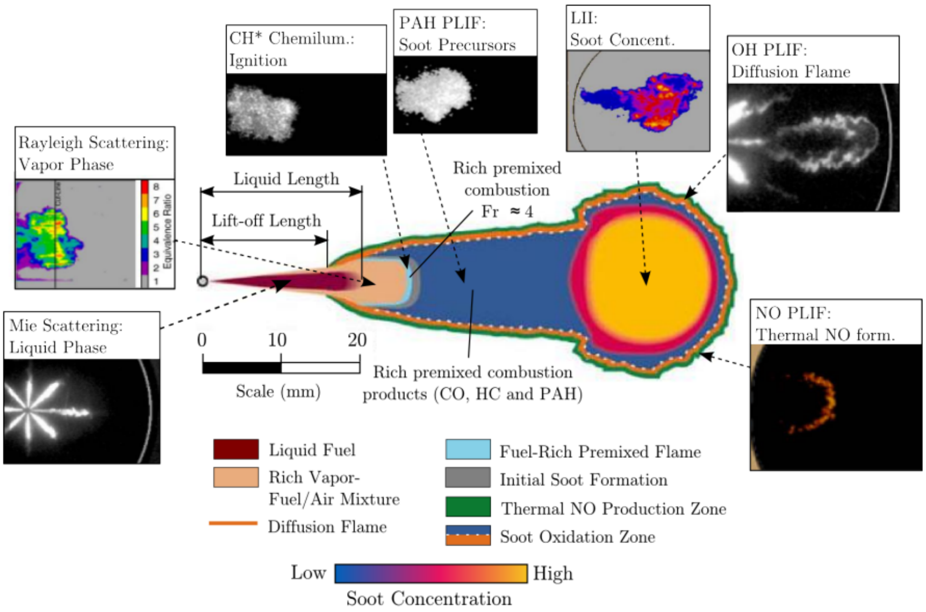

Figure 1.1. *Schematic of direct-injection diesel spray and corresponding diagnostics [3, 4].*

However, the changes of the thermal-dynamic conditions, the spray wall-impingement and the air-flow effects caused by the piston movement and chamber geometry make the combustion process in Diesel engine much more complicated, which will bring quite a challenge to CFD simulation for a whole combustion cycle. Therefore, as an intermediate step, fuel spray processes are investigated in specific test chamber under highly controlled boundary conditions: injections are performed in a nearly quiescent environment, where the characteristics of the charge are known and the interaction with the wall controlled or avoided. This purpose-designed high-pressure high-temperature facilities also have the fundamental advantage of being endowed with large accesses that simplify the implementation of the diagnostics [5]. Currently, two mainly different types of experimental setups exist to perform this type of research: Constant Volume Preburn (CVP) vessel and Constant Pressure Flow (CPF) vessel, as shown in Figure 1.2.

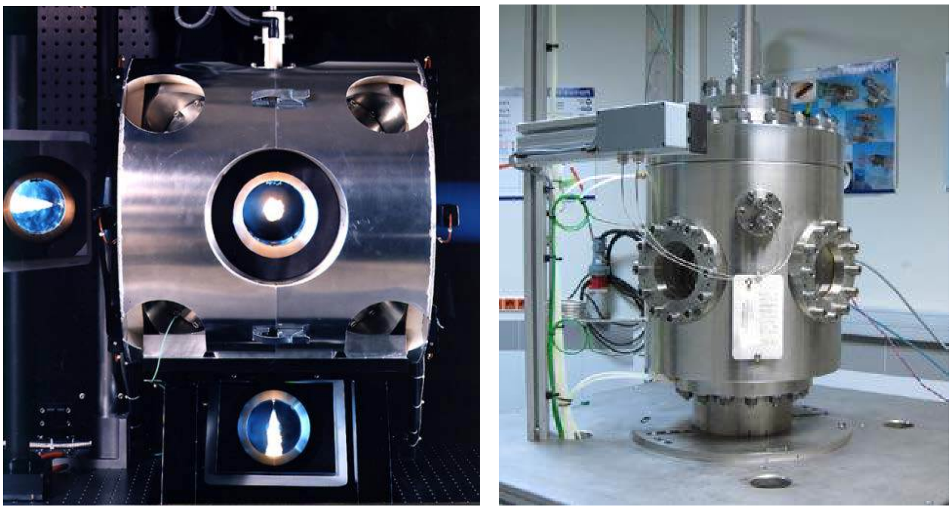

(a) CVP from Sandia national lab (b) CPF from CMT-Motores Térmicos

Figure 1.2. *High-pressure high-temperature facilities [6].*

Based on above considerations, two optical facilities were applied in this thesis: a high-temperature high-pressure constant pressure flow vessel and a two stroke single-cylinder optical engine. These works conducted in the CPF are framed within the activities of the engine combustion network (ECN): the ECN is a worldwide group of research institutes that started a international collaboration to provide high quality data and consistent results to modelers. The work of the group lays on several coordinated efforts in the Diesel research field: the complete definition of a standard operating condition, the use of nominal identical injectors and the organic cross check of the data obtained by different facilities and through different techniques [6].

Fuel-air mixing plays a significant role in combustion and emission process in diesel engine. The complexity of the phenomena characterizing this process has posed a significant challenge to the research community boosting the investigations in this field. Both experimental and computational tools have been significantly developed along the last decades and important goals have been achieved [3, 7, 8]. Most of the studies investigating the air entrainment and mixing process of the spray are performed under non-reacting and quiescent conditions [9–11]: the inert free spray without considering combustion and airflow effects enables an easier approach to determine the mixing field which makes it possible to develop more accurate mixing models based on simple momentum conservation and a reduced number of parameter [10, 12, 13]. However, few works in the literature address the effects that combustion and airflow in cylinder have on the shape and mixing of the spray.

Particulate matter (PM) emissions formed in the combustion of diesel engine not only have negative impacts on human health and environment, but also make exhaust after treatment system necessary. Therefore, reducing PM emission to meet the strict regulations is a significant challenge for engine researchers. As the major contributor to PM emissions, the understanding on soot formation and oxidation processes during combustion is quite important. However, because of the high complexity of several superimposed physical phenomena and chemical kinetic mechanisms, the knowledge of in-flame soot formation process is still limited and it is still a big challenge for CFD simulation to get a good quantification on soot amount. On the other hand, more powerful diagnostics tools are required that measure the properties of soot in various environments more precisely.

Multiple injection strategies have been studied and widely applied in conventional diesel engines in past decades because of a lot of benefits which they can bring on emissions and fuel economy. Many researchers investigated the physical and combustion characteristics of these multiple injection strategies starting with split-injection [14–18]. However, many questions remain unanswered regarding the spray dynamics and soot formation by means of different split-injection strategies (different dwell time, different first injection duration, for example).

1.2 Objectives

The main goal of this thesis is to improve the understanding of spray dynamics and soot formation during combustion process for direct injection Diesel sprays. The analysis for single-injection under quiescent conditions is studied first in the CPF. After that, based on the understanding of spray characteristics under quiescent conditions, the single-injection and split-injection sprays are further studied under non-quiescent conditions in the two-stroke optical engine. In order to reach the above defined goals, the following objectives have been defined:

- Study the effects of combustion on spray dynamics.
- Develop optical techniques for soot diagnosis.

- Improve understanding of the basic process of soot production in direct injection diesel flame.
- Study spray characteristics under non-quiescent conditions.
- Study the spray dynamics and instantaneous soot formation of different split-injection strategies.

1.3 Outline

This thesis is organized in six chapters including the present introduction (*Chapter 1*) providing an overview of the whole document.

As mentioned earlier, this work focuses on the fundamental study of the combustion process. *Chapter 2* gives a detailed description of the combustion process of the direct injection diesel spray inside the combustion chamber and a introduction of recent investigations on split-injection to provide a background knowledge of the studies in this thesis.

Chapter 3 illustrates the experimental methodology as well as the theoretical tool applied in this thesis. It includes the two kinds of experimental facilities, the principles and processing methods of all optical techniques and the fundamental of a developed 1D spray model.

The analysis of combustion-induced effects on spray dynamics and analysis on soot formation under quiescent conditions are presented in *Chapter 4*. It includes two main subsections. A methodology to quantify radial and axial expansion and corresponding parametric variation analysis as well as fuel effects are provided first based on existing database. Furthermore, the soot formation during quasi-steady flame was measured and analyzed in CPF by means of a combined extinction-radiation technique.

In *Chapter 5*, the spray dynamics and soot formation under non-quiescent conditions are studied under similar operating conditions with CPF tests but in the two-stroke Diesel engine, where a strong airflow exists because of the piston movement. Based on the understanding on spray characteristics for single-injection spray, the characteristics of direct injection Diesel spray with different strategies of split-injection are further studied. The effects of different dwell time and first injection quantities on the fuel-air mixing and combustion process of second injection are analyzed.

The last chapter summarizes some important conclusions found in this thesis. Moreover, some suggestions for future works are also presented.

Bibliography

[1] Pei Yuanjiang. *Transported PDF Modelling of Spray Combustion at Practical Diesel Engine Conditions.* Doctoral Thesis, University of New South Wales, 2013.

[2] Meijer Maarten. *Direct Injection Fuel Spray Combustion Studied by Optical Diagnostics "A spray A".* Doctoral Thesis, Eindhoven University of Technology, 2014.

[3] Dec John E. "A conceptual model of DI diesel combustion based on laser-sheet imaging". *Sae*, n^o 412, pp. 970873, 1997.

[4] Reche Carlos Mico. *Development of measurement and visualization techniques for characterization of mixing and combustion processes with surrogate fuel.* Doctoral Thesis, Universitat Politecnica de Valencia, 2015.

[5] Bardi Michele. *Partial Needle Lift and Injection Rate Shape Effect on the Formation and Combustion of the Diesel Spray.* Doctoral Thesis, Universitat Politecnica de Valencia, 2014.

[6] Bardi Michele, Payri Raul, Malbec Louis-Marie, Bruneaux Gilles, Pickett Lyle M, Manin Julien, Bazyn Tim and Genzale Caroline L. "Engine Combustion Network: Comparison of Spray Development, Vaporization, and Combustion in Different Combustion Vessels". *Atomization and Sprays*, Vol. 22 n^o 10, pp. 807–842, 2012.

[7] Musculus Mark P B, Miles Paul C. and Pickett Lyle M. *Conceptual models for partially premixed low-temperature diesel combustion*, volume 39. Elsevier Ltd, 2013.

[8] Bhattacharjee Subhasish and Haworth Daniel C. "Simulations of transient n-heptane and n-dodecane spray flames under engine-relevant conditions using a transported PDF method". *Combustion and Flame*, Vol. 160 n^o 10, pp. 2083–2102, 2013.

[9] Naber Jeffrey D and Siebers Dennis L. "Effects of Gas Density and Vaporization on Penetration and Dispersion of Diesel Sprays". *SAE Paper 960034*, Vol. 105 n^o 412, pp. 82—-111, 1996.

[10] Musculus Mark P. B. "Entrainment waves in decelerating transient turbulent jets". *Journal of Fluid Mechanics*, Vol. 638 n^o 1, pp. 117, 2009.

[11] Sasaki, Satoru Akagawa Hisashi and Tsujimura Kinji. "A Study on Surrounding Air Flow Induced by Diesel Sprays". *SAE Technical Paper*, n^o 724, 1998.

[12] Reitz Rolf D. and Bracco F. B. "On the Dependence of Spray Angle and Other Spray Parameters on Nozzle Design and Operating Conditions". In *SAE Technical Paper.* SAE International, 02 1979.

[13] Hiroyasu Hiro and Arai Masataka. "Structures of Fuel Sprays in Diesel Engines". In *SAE Technical Paper.* SAE International, 02 1990.

[14] Bruneaux Gilles and Maligne David. "Study of the Mixing and Combustion Processes of Consecutive Short Double Diesel Injections". *SAE International Journal of Engines*, Vol. 2 n^o 1, pp. 1151, 2009.

[15] Pickett Lyle M, Kook Sanghoon and Williams Timothy C. "Transient Liquid Penetration of Early-Injection Diesel Sprays". *SAE Int. J. Engines*, Vol. 2 n^o 1, pp. 785–804, 2009.

[16] Skeen Scott, Manin Julien and Pickett Lyle M. "Visualization of Ignition Processes in High-Pressure Sprays with Multiple Injections of n-Dodecane". *SAE Int. J. Engines*, Vol. 8 n^o 2, pp. 696–715, 2015.

[17] Moiz Ahmed Abdul, Ameen Muhsin M., Lee Seong Young and Som Sibendu. "Study of soot production for double injections of n-dodecane in CI engine-like conditions". *Combustion and Flame*, Vol. 173, pp. 123–131, 2016.

[18] Moiz Ahmed Abdul, Cung Khanh D. and Lee Seong-Young. "Simultaneous Schlieren-PLIF Studies for Ignition and Soot Luminosity Visualization With Close-Coupled High-Pressure Double Injections of n-Dodecane". *Journal of Energy Resources Technology*, Vol. 139 n^o 1, pp. 012207, 2017.

Chapter 2

Combustion process in a direct injection diesel spray

Contents

2.1 Introduction

The objective of this chapter is to provide some basis for understanding the work presented in this thesis. Thus, a detailed description of the combustion process of the direct injection diesel spray inside the combustion chamber is provided. The essential phases of Diesel combustion process can be summarized as follows. Fuel is injected at a high velocity by means of the injection system into the combustion chamber where a high density and high temperature environment is formed. The liquid phase atomizes to small drops because of the cavitation, turbulence and aerodynamic. With the hot gas entrainment and heat transfer, fuel drops vaporize and this vapor phase continues to penetrate. Thanks to the high temperature and pressure, auto-ignition occurs within a proper fuel-air mixture. After that, spray starts the expansion and continues moving downstream. This event takes place in a millisecond order of magnitude but involves extremely complex interaction between numerous physical and chemical processes, for which further understanding is still needed nowadays [1–3].

First, a basic description of the diesel combustion phases will be presented to give a general overview. Then, the spray behavior during the whole injection event under quiescent conditions will be described in detail. It consists of the atomization, fuel-air mixing, evaporation process before ignition and the flame development, soot formation during combustion. These studies can provide a baseline for understanding the additional effects on fuel jet development caused by strong gas flows. At last, some recent studies on mixing and combustion process of split-injection spray will be reviewed. The detailed study of this topic will be presented in later chapter.

2.2 Overview of conventional diesel combustion process

A classical description of the conventional diesel combustion process is presented here by means of the analysis of the apparent heat release rate (AHRR) of a single cylinder two-stroke engine, as shown in Figure 2.1. Meanwhile, a corresponding time sequence of the high-speed schlieren images of reacting spray is also presented in Figure 2.2 to provide a clear macroscopical view of the spray behavior during different stages. The test rig and the schlieren optical technique will be described in detail in next chapter. The AHRR is derived from cylinder pressure trace according to the first law of thermodynamics [1]. As commonly identified in the literature [4], the whole combustion process from start of injection(SOI) to the end of combustion (EOC) can be divided into three stages by the vertical dashed line in Figure 2.1 and they are elaborated in detail as following:

- **Ignition delay:** This period was defined as the interval between the start of injection (SOI) and the start of combustion (SOC) when the spontaneous high temperature ignition takes place and an apparent heat release becomes detectable. At the beginning of this stage, the injected

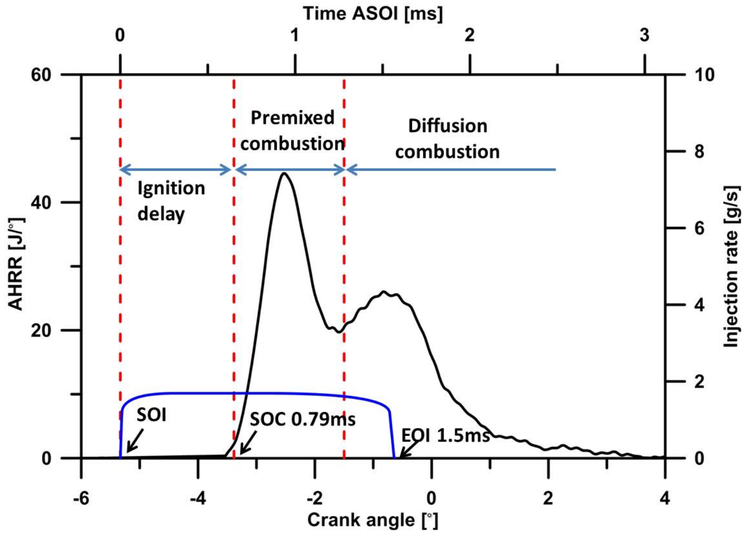

Figure 2.1. *Apparent heat release rate(black line) and injection rate(blue line) of a single cylinder two-stroke diesel engine equipped with a single-hole injector. Injection duration is 1.5 ms.* ($T_g = 870K$, $\rho_g = 22.8kg/m^3$, $O_2 = 21\%$).

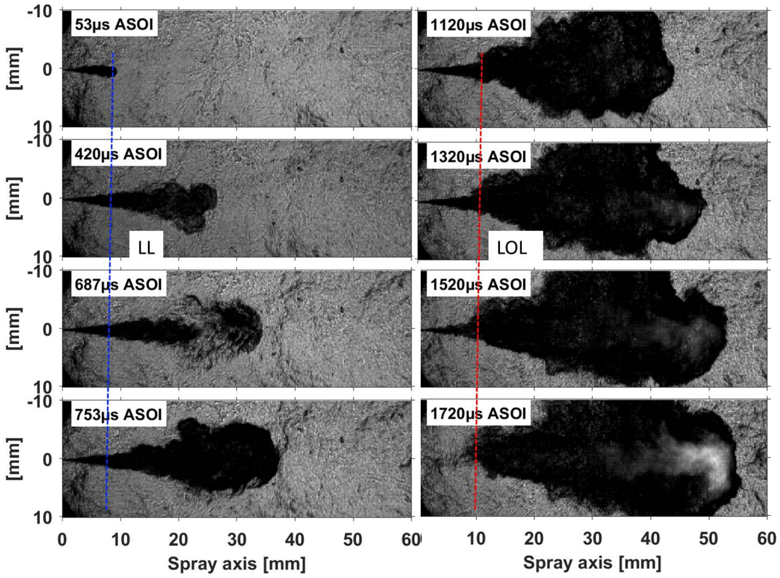

Figure 2.2. *Time sequence of schlieren images with an operating condition mentioned in Figure 2.1. Vertical dashed blue line and red line represent liquid length and flame lift-off length respectively.*

fuel undergoes a succession of physical processes. First, the liquid fuel is broken up into small droplets and the spray expands into a roughly conical jet as the volume of in-cylinder gases entrained into the jet increases with downstream distance from the injector [5]. Entrainment correlations [6, 7] predict that increasing entrainment downstream causes the equivalence ratio to vary along the jet axis approximately inversely with the distance to the orifice. The thermal energy provided by the entrained in-cylinder gas heats up and vaporizes the liquid fuel. At some location downstream of the injector, termed the "liquid length", all of the fuel enters the vapor phase [6, 8]. The liquid length is presented with vertical dashed blue line in Figure 2.2, which was quantified with a diffused background-illumination extinction imaging (DBI) technique. This optical technique will be described in detail in next chapter. Thus, all the spray part at the downstream of LL is the vapor phase at 420 μs after start of injection (ASOI). As the momentum carries the fuel-air mixture downstream, it continues to entrain more of the hot in-cylinder gases which results in a sequence of chemical reactions related with low temperature auto-ignition [9–11]. The spray tip from Schlieren images becomes transparent because of the similar local temperature with that of ambient gases, which is caused by this cool-flame heat release [12–14], as shown in Figure 2.2 at 687 μs ASOI.

- **Premixed Combustion:** A short time after the initial chemical reactions of the first-stage ignition, it evolves into a high-temperature combustion stage and results in a rapid increase on heat release rate. This phase starts from a apparent detectable AHRR and ends with a relative minimum after the first peak, as shown in Figure 2.1. This high-temperature combustion leads a fast expansion on spray shape, as observed in Figure 2.2 at 753 μs ASOI. During this stage some final species (CO_2 and H_2O) are formed. Meanwhile, as the temperature rises, polycyclic aromatic hydrocarbon(PAH) soot-precursor species quickly form in the hot ($\sim 1600-2000K$), fuel-rich combustion products of the premixed burn. Soot formation follows, filling the entire downstream jet cross section [5, 15]. Further details of the physical and chemical phenomena associated to this phase are approached in Section 2.3.3.

- **Diffusion Combustion:** Once the fuel and air which premixed during the ignition delay have been consumed, a diffusion flame forms on the periphery of the fuel-rich, high-temperature downstream region of the jet, where the heat release rate is controlled by the rate at which mixture becomes available for burning [1, 5]. The upstream edge of the diffusion flame does not extend fully to the injector nozzle, but rather it remains some distance downstream, termed the “lift-off length” (LOL) [16, 17] as presented with the vertical dashed red line in Figure 2.2. If the injection is long enough, the flame tip is also able to stabilize at some distance. After the initial transient of the jet penetration and ignition processes,but before the end of injection (EOI), the diesel jet enters a “quasi-steady” period - when the characteristic description of the combusting jet does not change. With increased entrainment of ambient gas with low axial momentum, vapor-fuel mixtures near the injector transitioned from fuel-rich to fuel-lean immediately after the end of injection (EOI) and the entrainment wave decelerates the flow and causes it to stagnate near the injector, which could contribute to incomplete combustion, unburned hydrocarbon (UHC) or combustion recession [18–22]. The most influential parameters for combustion recession are the ambient thermodynamic conditions, injector parameters, and the EOI transient [23]. Apparently, it is not able to be observed from this case, as shown in Figure 2.2 at 1720 μs ASOI.

2.3 Diesel spray under quiescent conditions

This section will provides a detailed extended description for each of the above mentioned phases of fuel air mixing and combustion processes under quiescent-type diesel engine conditions. The results presented in this section can also provide a baseline for assessing the additional effects on fuel jet development caused by strong in-cylinder flows.

2.3.1 Atomization

Atomization of Diesel spray is the process by means of which liquid spray is transformed into a cloud of droplets from a continuous media when the liquid fuel penetrates within the combustion chamber. The increase of exchange of surface between air and fuel plays an significant role on the consequent spray vaporization and combustion processes. The atomization process is typically initiated as a result of high-pressure liquid fuel discharged from injector nozzle carrying with its important physical features like liquid-phase turbulent flows and cavitation effects from the generation of gas-phase bubbles that can potentially implode as they travel internally downstream of the flow and are ejected into the chamber. The disintegration or breakup occurs when the disruptive forces exceed surface tension forces. External forces, such as aerodynamic forces, surface shear forces, centrifugal forces and electrostatic forces, acting on the liquid surface may distort the bulk liquid and promote the disruption. External forces may lead to oscillations and perturbations of the interfaces. These oscillations may be amplified and result in the breakup of the liquid into small droplets. This initial breakup process is often referred to as the primary breakup. A population of larger droplets produced in the primary atomization may be unstable if they exceed a critical droplet size and thus may undergo further disruption into smaller droplets. This process is usually termed as the secondary breakup [24]. A schematic of this process in shown in Figure 2.3. Based on the optical depth and experimental approach that can be used for its study, the regions of the spray are also classified as dense and dilute region, as shown in Figure 2.4.

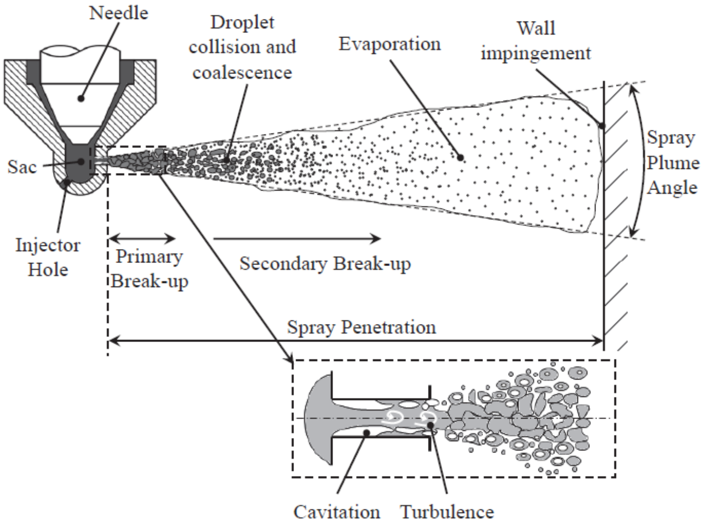

Figure 2.3. *Schematic of atomization of Diesel spray [24].*

Dense spray region

At the exit of injector, intact liquid structures (e.g. ligaments, or a so-called "liquid core", see Figure 2.4) extrude into the gas phase, but for highly atomizing sprays, evidence indicates that they break up very quickly (or immediately in some cases) via turbulence, cavitation, rapid development of surface wave structures, other forms of shear, or a combination of these mechanisms. The liquid core produces "primary droplets" as it disintegrates via primary breakup mechanics, and this defines the "dense spray" or "near field" region. Primary breakup thus serves as the initial source of droplets having a specific size distribution, location, and momentum vectors that control the development of the spray [25].

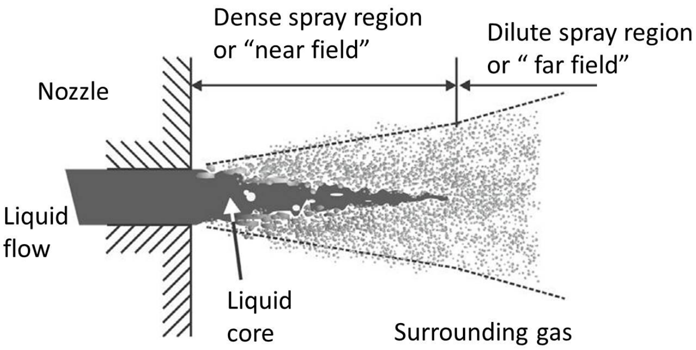

Figure 2.4. *Dense spray region [25].*

A plenty of optical techniques have been developed and applied to investigate this region. It has been reported [26, 27] that the gas-phase velocity field can be reconstructed by "Molecular Tagging Velocimetry" in relatively dense sprays. The primary breakup and the structure of the jet can be observed by "Ballistic imaging" [28, 29], "X-ray imaging" [30, 31] and "Diffused background illumination" [32–34]. These emerging optical techniques look as promising candidates for studying dense sprays since they suffer less from multiple scattering and beam attenuation. Applications of these techniques in real dense sprays are still limited and further improvements are needed [35]. On the other hand, the primary breakup model has been developed and applied a lot in Computational Fluid Dynamics (CFD) simulations. Earlier investigation of single fluid pressure atomization, divided the breakup regimes of a circular liquid jet into three areas depending on the liquid Reynolds number and the Ohnesorge number [36]. Considering the strong influence of cavitation on spray atomization, more and more researchers brought the cavitation into the primary breakup model [37, 38].

Dilute spray region

In this region, the aerodynamic forces arising due to the relative inter-phase velocities cause instabilities resulting in a further disintegration of droplets and ligaments into even smaller fragments. This process is so-called secondary breakup as mentioned above [39]. Weber [40] proposed a breakup criterion based on the Weber number, which is widely accepted. Based on the breakup mechanism, which depends on the Weber number and the deformation (breakup) time, secondary breakup can be classified into bag breakup, stripping breakup and catastrophic breakup as shown in Figure 2.5. Bag breakup occurs when the Weber number is approximately between 11 and 80. Then, due to the aerodynamic forces, the droplets form a relatively flat disk, which develops into a thin membrane. These membranes finally burst and form numerous small droplets. When the Weber number is approximately between 80 and 350, stripping breakup occurs. Now the flat disks develop inwards and the formed membranes collapse at the edges to form smaller droplets. In the case of Weber numbers above 850, catastrophic breakup occurs. Extremely high shear rates at the gas-liquid interfaces result in droplet elongation and finally into a fragmentation due to Rayleigh instabilities [41].

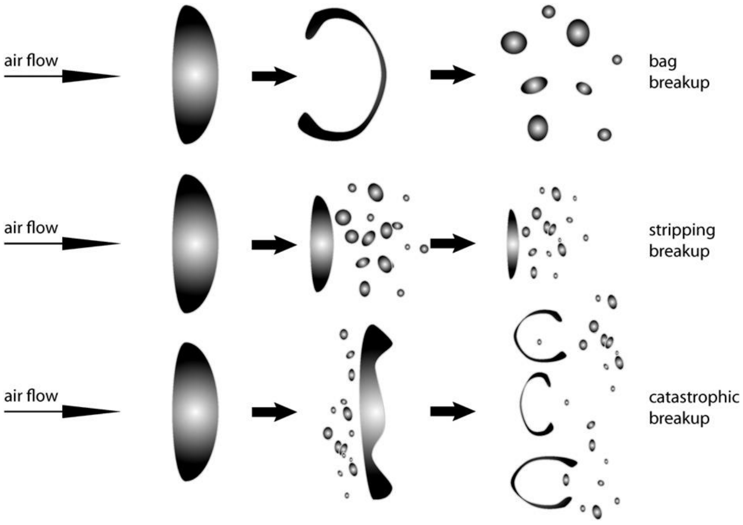

Figure 2.5. *Sketch of the various types of secondary breakup [39].*

2.3.2 Fuel-air mixing and evaporation

While the spray keeps on entraining much hotter gas, heat is being transferred from the ambient gas to the tiny drops of fuel; therefore, their relative velocities decrease as the droplets transfer their momentum to the air and the temperature of the liquid rises. The temperature increase causes the vapor pressure of the droplets surface to increase, so they start evaporating and the local mixture approaches the adiabatic saturation conditions [42].

When liquid phase penetrates to a point where the total fuel evaporation rate in the spray equals the fuel injection rate, the tip of the liquid region stops penetrating and begins fluctuating about a mean axial location [43]. After the fuel is fully vaporized, momentum carries the fuel ambient mixture downstream of the liquid length where it continues to entrain more of the hot in-cylinder gases. Some important macroscopical and microscopic parameters of the spray during this process, which are usually studied by researchers, are listed as follows.

Liquid length

Liquid-phase fuel penetration and vaporization are important factors in the DI diesel engine combustion processes. Penetration of the fuel is needed to promote fuel-air mixing as mentioned in the previous section, however, over-penetration of the liquid-phase fuel can lead to higher emissions if the liquid fuel impinges and collects on piston bowl walls [42]. As mentioned above, the liquid length (LL) is defined as the maximum location where the liquid penetration stabilizes. Based on Mie theory of light scattering by spherical particles [44, 45], two common optical techniques, Mie-scattering (MIE) and Diffused background-illumination (DBI), are usually applied for measureing liquid length [43, 46–52]. The uncertainties of these two techniques have been studied in reference [53]. They found the MIE is sensitive to the orientation of the illumination source, different liquid lengths could be obtained because of the changing reference intensity. On the other hand, DBI may be preferred to light-scatter diagnostics because the reference light intensity acts as a calibration source. However, beam-steering due to refractive index gradients can create extinction due to non-liquid sources. The most quantitative diagnostic for light extinction is a small laser with divergence accommodation using an integrating sphere. A schematic of the temporal evolution of liquid length which was measured by DBI and corresponding spray penetration can be seen in Figure 2.6.

The effects of a wide range of parameters on the liquid length have been studied by previous researchers. Siebers found the liquid length decreases with higher ambient temperature and density, however, the sensitivity of liquid length to both parameters decreases as they increase [43]. Variations in the thermodynamic properties of a fuel can cause order-of-magnitude or larger changes in liquid length at a given operating condition [54]. Additionally, one interesting founding from Siebers is that the liquid length increases linearly with orifice diameter, however, fuel injection pressure appears not to play any significant role on the liquid length establishment, as shown in Figure 2.7.

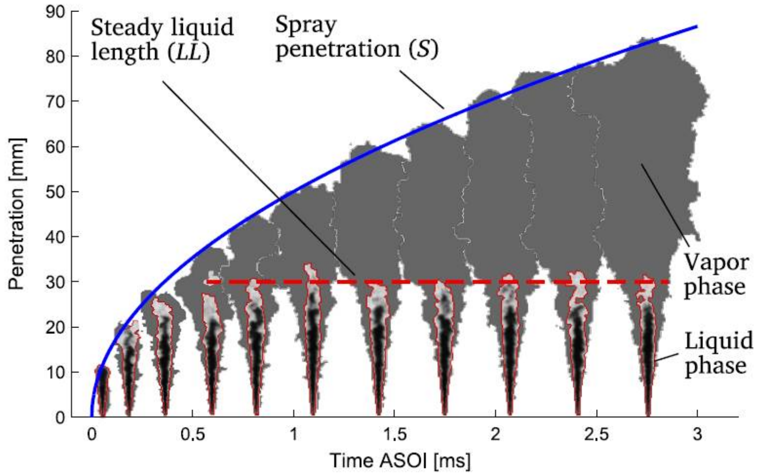

Figure 2.6. *Schematic of the liquid length and spray penetration under non-reacting condition [55].*

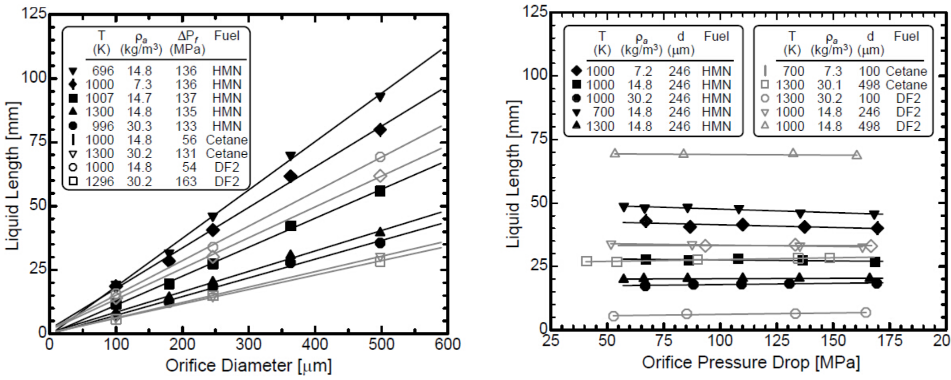

(a) Effects of orifice diameter (b) Effects of injection pressure

Figure 2.7. *Effects of orifice diameter and injection pressure on Liquid length [43].*

Based on the jet theory, the relationships for the injected fuel mass flow rate $\dot{m}_f$ and the total entrained gas mass flow rate $\dot{m}_a$ up to any axial location in a spray that result are:

$$\dot{m}_f \propto \rho_f \cdot d^2 \cdot U_f \tag{2.1}$$

$$\dot{m}_a \propto \sqrt{\rho_a \cdot \rho_f} \cdot d \cdot x \cdot U_f \cdot \tan(\theta/2) \tag{2.2}$$

The terms in the equations are the ambient gas density ρ_a, the fuel density ρ_f, the orifice diameter d, the injected fuel velocity U_f, the axial distance from the orifice x and the spreading angle of the spray θ. Based on above two equations, it can be found that an increase in injection velocity (i.e., injection pressure) will result in equal increases in the mass flow rates of the fuel and the entrained ambient gas at any axial location. As a result, fuel injection pressure should have no effect on the length of spray needed to entrain enough high-temperature ambient gas to vaporize the fuel. This observation led Siebers [8] to conclude that the evaporation process in conventional conditions of a Diesel engine is mostly controlled by turbulent mixing. Under such assumption, the liquid length can be reliably predicted using an entrainment correlation to find the downstream location where the fuel-ambient ratio is such that the thermal energy added to the jet by the entrained gas is just sufficient to fully-vaporize the fuel [8, 56]. The success of these predictions implies that for high-pressure diesel injection, vaporization is limited by mixing (entrainment), not by droplet atomization and vaporization processes [5]. Such “mixing-controlled” hypothesis which ultimately assimilates the Diesel spray to a gaseous jet was later implemented in the 1D models of García, Pastor, Musculus [19, 56–58]. For reference,the relationship obtained by dimensional analysis and implicit to the 1D by Pastor et al. [56] is presented:

$$LL = \frac{K_{ll} \cdot d_{eq}}{Y_{f,evap} \cdot \tan(\theta/2)} \tag{2.3}$$

where K_{ll} is a constant depending on ambient conditions, d_{eq} is the equivalent exit diameter of the nozzle, $Y_{f,evap}$ is the evaporation fraction for the given mixture, θ is the spray angle.

Spray penetration & Spray angle

The spray penetration of a fuel jet and its commensurate entrainment of air are needed to promote efficient air utilization in a DI diesel engine, which is important for optimizing engine performance. It is defined as the distance between the nozzle exit and the spray tip, as shown with the blue curve in Figure 2.6. It can be found from Figure 2.6 that the spray penetration is equal with liquid penetration at the beginning of injection before it reaches the stabilized liquid length. After that, the spray penetration becomes equal with the vapor penetration before the start of ignition. On the other hand, a common measure of spray dispersion is the cone angle of the outer boundary of a spray, referred to in this paper as the spray angle. The spray spreading angle is a fundamental parameter driving the entrainment of air in the spray and determining the fuel evaporation and combustion process. As the most common technique, high-speed schlieren imaging is widely applied by researchers to quantify the spray penetration [6, 53, 59–62]. The detailed information about this technique will be described in later chapter. One example of averaged schlieren images is shown in Figure 2.8 to illustrate the spray penetration and spray angle.

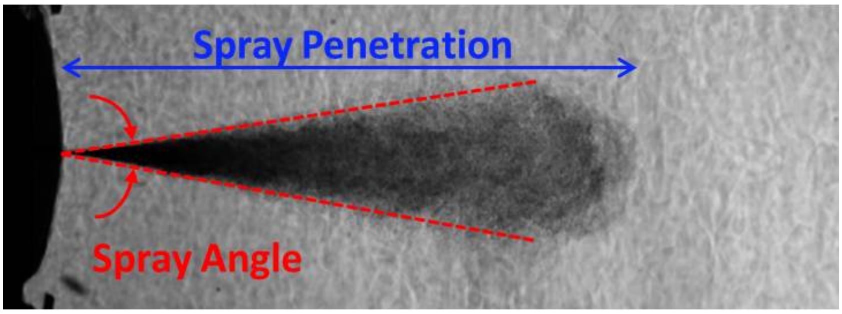

Figure 2.8. *Definition of Spray penetration and Spray angle with an averaged schlieren image.*

Many correlations based on experimental data and turbulent gas jet theory have been proposed for spray penetration. Hiroyasu and his coworkers [63] found that the initial spray penetration increases linearly with time and following jet breakup, increase as $\sqrt{t}$. Injection pressure has a more significant effect on the initial motion before breakup; ambient gas density has its major impact on the motion after breakup. Another formula developed by Dent [64] based on a gas jet mixing model shows a consistency with Hiroyasu on the relationship between penetration with ambient density which have a density dependence of $\rho_a^{-0.25}$. The conditions they examined included ambient gas densities up to 30 kg/m^3 and injection pressures up to 80 MPa. Based on a experimental database under a much wider range of non-vaporizing conditions, a scaling law for the penetration of a non-vaporizing (i.e., isothermal) fuel jet was developed by Naber and Siebers [6]. They also investigated the effects of vaporization on spray penetration. It was found the difference between vaporized and non-vaporized sprays reaches 20% at low density conditions. The authors hypothesize that this reduction is the result of a local increase of mixture density as it cools while evaporating fuel. In [58, 65], the authors propose an analytical solution based on momentum conservation along the spray axis and validate it with experimental measurements. Six kinds of fuels with different densities and boiling points were tested with schlieren by Kook and Pickett [46]. They concluded that no correlation between the fuel-air mixing and fuel volatility is found as evidenced by the similar vapor penetration and spray angle. Apart from the constant applied to the relationship and other minor details, all the equations presented also in more recent works [6, 66, 67] are in the form

$$S \propto \rho_a^{-0.25} \cdot \dot{M}^{0.25} \cdot \tan^{-0.25}(\theta/2) \cdot t^{0.5} \tag{2.4}$$

where S is the spray penetration, $\dot{M}$ is the spray momentum.

The spreading angle θ is usually defined as the angle included by the lines fitting the two sides of the spray (Figure 2.8). Nonetheless, the definition of the spreading angle that is given is not always consistent: Naber and Siebers [6], for example, used the portion of the jet that is between the injector and one-half the jet penetration distance. The area of the vapor boundary in this upstream region is fit to a triangle having the same area. The angle of this triangle is defined as the instantaneous spreading angle. Pastor et al. [68] based their definition on the fitting of two lines on the spray boundary until 60% of the spray penetration. Different correlations to predict the behavior of the spreading angle can be found in the literature [63, 69–72]. In general, the investigations carried out on the spreading angle, found an agreement on the main effects that determine the parameter: fuel/ambient density ratio, injector geometry and cavitation have been extensively proven to have an impact on the spreading angle. However, the quantification of these effect is still an open issue due, first of all, to the complexity of the phenomenon itself, that is the result of the combination of turbulence and aerodynamic instabilities; moreover, this specific measurement is particularly sensitive to many aspects of the experiments: the experimental technique employed, the details of the optical arrangement and the methodology employed for the image processing [53, 73] affect the sensitivity of the experimental system and, therefore, the spray boundaries detected. Furthermore, Pickett [53] found the spray angle changes near the injector, starting with a small angle that transitions to a larger angle farther downstream, based on 1D spray model and a wide of experimental database [53].

Fuel mixture fraction

Mixing between fuel and oxidizer is paramount for the quality of combustion. In an internal combustion engine, the mixture distribution affects the flame temperature, pollutant formation, unburned fuel emissions and combustion efficiency. Quantitative measurement of fueloxidizer mixing is necessary to better understand the different combustion strategies and their effects on pollutant formation [74]. The dense liquid portion of the spray near the nozzle is inaccessible to most quantitative optical diagnostics. Downstream of the dense liquid region, laser based diagnostics for fuel-oxidizer mixing that have been attempted in evaporating diesel sprays include Raman scattering [75, 76], laser-induced fluorescence/exciplex fluorescence (LIF/LIEF) [77, 78], Mie scattering [60, 79], Rayleigh scattering [74, 80]. Each technique has its own advantages and disadvantages. Elastic scattering techniques like Mie and Rayleigh suffer due to interference from scatterers other than the probed species, and Raman scattering is limited by low signal strength and poor spatial resolution (usually 1-D instead of 2-D). In the case of LIF/LIEF techniques, elastic scattering interferences are not as serious, but the fluorescence yield is generally a function of temperature, pressure, and ambient gas composition, making quantitative measurement of transient mixing processes at engine conditions difficult. Exciplex fluorescence has not proven quantitative for liquid concentration, limiting any attempt at quantification to the fully vaporized jet region, rather than the liquid spray region. In comparison with above techniques,the ultraviolet and visible light absorption and scattering technique(UV-VIS LAS) allows measuring the fuel concentration in both liquid and vapor region simultaneously [81].

2.3.3 Auto-ignition

As described in previous sections, the liquid-fuel spray mixes with the ambient gases, which provide the thermal energy to vaporize the fuel. The vaporization of the fuel reduces the sensible thermal energy of the ambient gases, which decreases the cylinder pressure from what it would have been without vaporization. The vaporization is therefore manifest as a decrease in the AHRR during the ignition delay period. Ignition reactions proceed in the hot mixture of vaporized fuel and ambient gas. As they become more exothermic, the chemical rate of heat release eventually exceeds the vaporization energy rate. This point, when the AHRR becomes positive, is a commonly used marker for the end of the ignition delay and the start of combustion [5]. Thus, the auto-ignition process consists of sequences of physical and chemical processes of substantial complexity within a quite short time. Thanks to the development of all kinds of optical techniques, researchers have identified the existence of a low intensity reaction stage before the main phase of the combustion [10, 11, 14, 82–85]. The heat release in this phase of the combustion is very low and, in many cases, it cannot even be appreciated. On the other hand, thanks to optically accessible test rigs, the imaging of the ignition enables to observe a distributed chemiluminescence light emissions occurring during this phase: these very weak light emissions can be observed only using intensified cameras and are distributed over the spray region. The evolution of their intensity and position has been the subject of many studies since it helps understanding the subsequent development of the combustion.

Based on a sequences of measurements under steady-state conditions by using a constant-volume combustion chamber, Higgins et al. [82] divided the basic sequences of auto-ignition into three stages: fuel vaporization and air-fuel mixing (physical induction stage), low-temperature (first-stage ignition) heat release and high-temperature (second-stage ignition) heat release. They are detailed as follows:

- **Physical induction stage:** it includes the time up to the start of the simultaneous rise in pressure and chemiluminescence. During this time, the main driver is the physics involved in the spray formation described in Section 2.3.1 and Section 2.3.4: atomization, air entrainment and fuel evaporation. Fuel vaporization causes a decrease in the temperature in the spray region; as the penetration and hot air entrainment continue, the fuel-air mixture temperature increases, overcoming the previous effect. In the regions where temperature reaches a certain value, the first stage of ignition begins: this represents the end of the physical induction period. However, it only means that the first stage ignition chemistry has become detectable and the demarcation between the physical induction period and the first stage of ignition depends somewhat on the sensitivity/resolution of the diagnostics used.

- **First-stage ignition period:** it extends from the time of first detectable rise in pressure and chemiluminescence until rapid heat release begins, marking the start of the second stage ignition chemistry. Early in the first stage, chain-branching reactions consume fuel, producing radicals and releasing small quantities of energy that increase pressure. Several research groups have used high-speed schlieren imaging to visualize low-temperature ignition processes in diesel sprays [12–14, 61, 86]. In those experiments, the low-temperature ignition event was observed as a local “softening” of refractive index gradients near the spray head. This phenomenon was attributed to the consumption of fuel vapor resulting in the production of intermediate species and heat release that increased the local temperature to a value closer to that of the ambient gases. Consequently, the local refractive index value approached that of the surrounding gases rendering the schlieren effect less pronounced [14], as shown in Figure 2.9 at 240 μs ASOI. The schlieren images in Figure 2.9 indicates that for the investigated operating conditions low temperature chemistry initiates at the radial periphery of the jet slightly behind the penetrating jet head. As Higgins et al. [82] suggested, the first-stage ignition chemistry grows broadly in the region of the spray comprised between the liquid length and the spray penetration, which is in agreement with Dec and Espey's observations [11]. Because of the relatively uniform distribution of chemiluminescence in this zone, it is likely that the first-stage chemistry develops uniformly throughout the region. Formaldehyde is easily detected by optical diagnostics [9, 14, 83, 87] and provides much insight into the spatial and temporal development of first-stage ignition. Kosaka et al. [83, 87] provide deeper insight into the species involved, by imaging the whole formaldehyde population (not only under excited state) thanks to laser induced fluorescence technique (LIF). This accurate 2D-analysis yet confirms the presence of formaldehyde during autoignition as was suggesting the spectra analysis performed by Dec and Espey [11]. Skeen et al. [14] compared high-speed Schlieren with single-shot formaldehyde planar laser induced fluorescence (PLIF) for detecting auto-ignition. They found Schlieren imaging proved to be less capable than PLIF at detecting the earliest appearance of low-temperature ignition as the first "softening" of the Schlieren effect was observed between 30 μs and 50 μs after the earliest appearance of formaldehyde PLIF (as shown in Figure 2.9).

- **Second-stage ignition period/Premixed burn period:** The beginning of significant heat release that leads into the sudden premixed-burn pressure-rise marks the start of the second stage of ignition. This stage begins when, as a result of air entrainment and heat release from first-stage ignition, the temperature increases to a level where hydrogen peroxide (H_2O_2) dissociation reactions dominate the chemistry ($\approx$900 K), producing significant heat release. This process is the trigger for the premixed-burn [82]. In the meantime, combustion propagates to the regions of vaporized mixture accumulated during ignition delay and which had not had the capacity to trigger ignition themselves. With the local temperature increase in their neighborhood, they now turn to reach the limit of flammability and significant heat release follows [2]. This significant heat release could lead to a much higher refractive index gradients and lower density within the spray. As a result, the spray head

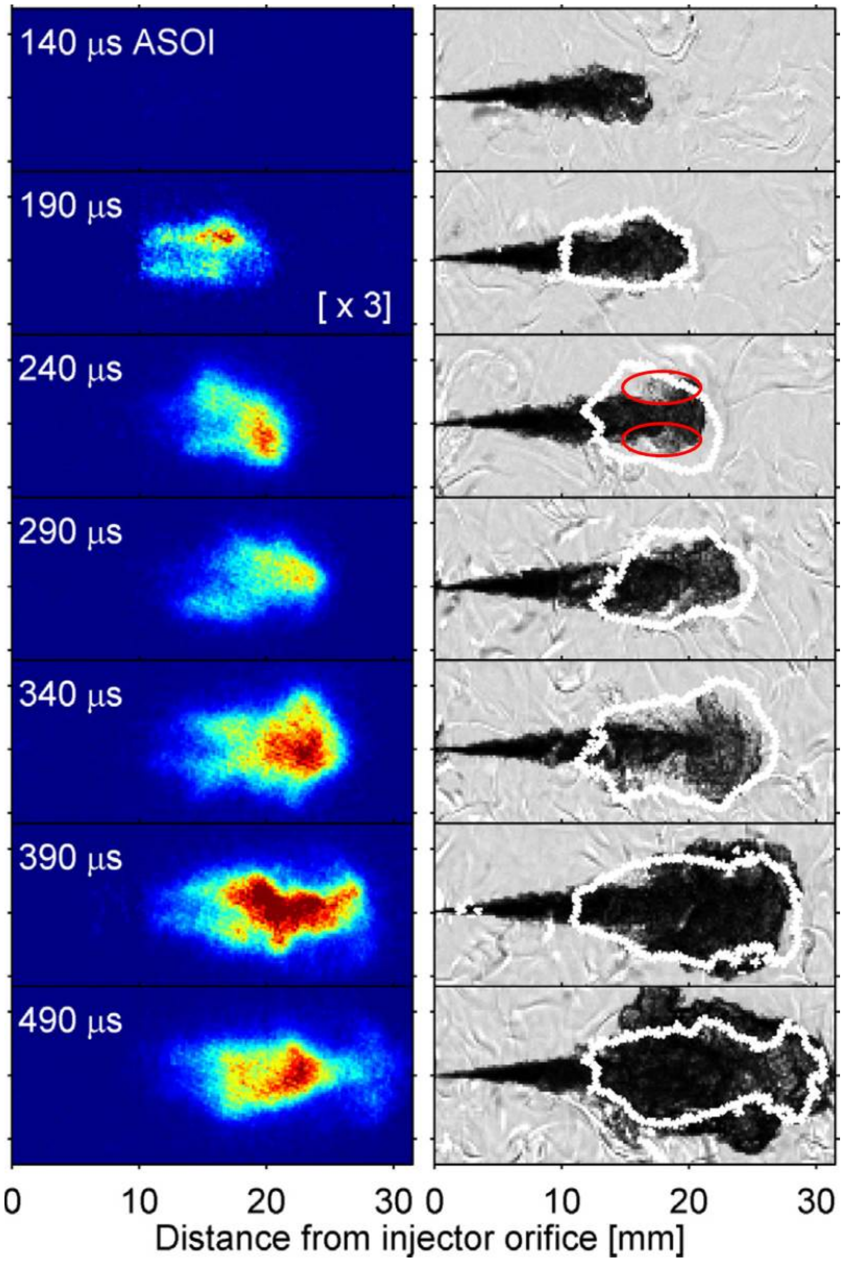

Figure 2.9. *Time sequence of formaldehyde PLIF (left panels) and schlieren images (right panels) for Spray A [14].*

region of schlieren imagines becomes dark again and starts expanding, as shown in Figure 2.9 at 390 μs ASOI. In addition, it can also be observed from Figure 2.9 that, after 390 μs ASOI, the formaldehyde closer to the injector persists here as well as at the later timings shown. The persistence of formaldehyde on the injector side of the lift-off location is consistent with the results of [9, 88] and suggests that the low-temperature auto-ignition chemistry plays a role in determining the quasi-steady flame location.

As mentioned above, the interval from start of injection to high-temperature combustion is typically referenced as the ignition delay for diesel combustion, which consists of the physical induction stage and first-stage ignition period. The ignition delay of the Diesel spray is critical for the global performances of the Diesel engine for different reasons: the peak in the heat release associated to the premixed-phase of the combustion is one of the main sources of noise of the engine; the high temperatures reached during this phase are responsible for NO_x production; the location where the ignition takes place strongly affects the subsequent evolution of the combustion [55].

The physical factors that affect the development of the fuel spray and the air charge state will influence the ignition delay. These quantities depend on the design of the fuel-injection system, the combustion chamber and the operating conditions [1]. On the other hand, both the physical and chemical properties of the fuel also have significant effects on ignition delay, especially the chemical characteristics. A lot of investigations have been carried out to study the effects of these parameters on ignition delay [89–92]. One of the most representatives has been presented by Pickett et al. [91] performing experimental measurements in an optical accessible combustion vessel. Pickett et al. proposed a law basing on Arrhenius type equation,

$$\tau_{ig} = A \cdot exp(E/RT_a) \cdot \rho_a^n \cdot Z_{st}^m \tag{2.5}$$

where τ_{ig} is the ignition delay, E is the global activation energy of the reactions, R is the universal gas constant, and Z_{st} is the stoichiometric mixture fraction (depending on the fuel composition and on the oxygen content of the gas in the combustion chamber).

2.3.4 Mixing-controlled combustion

Once the chemical reaction has gone through all the stages previously defined, the combustion process achieves a state which is known as mixing-controlled combustion or diffusion combustion phase. It extends until all the fuel injected is consumed. The diffusion combustion is considered as the process in which fuel and oxygen are not previously mixed and, therefore, mixing and combustion take place simultaneously. During this phase, the flame front establishes and progresses until reaching its natural maximum length, while being maintained by the convective and diffusive contribution of fuel and oxygen. During injection, the dominating process is convection thanks to the momentum introduced by the spray [2, 81]. When injection finishes, the diffusion process becomes more relevant and dominates the remaining reaction. Heywood [1] considers the stage after the end of injection as a final independent phase, known as late combustion phase.

Conceptual models

Several conceptual models can be found in literature [5, 9, 15, 93, 94], that seek to provide a clear and neat explanation of the structure of a reactive DI diesel jet. Currently, the most widespread and accepted vision is probably the conceptual model proposed by Dec [15] and later extended by Flynn et al. [93]. A schematic of the mixing-controlled combustion at a typical time during the first part from the conceptual model is shown in Figure 2.10.

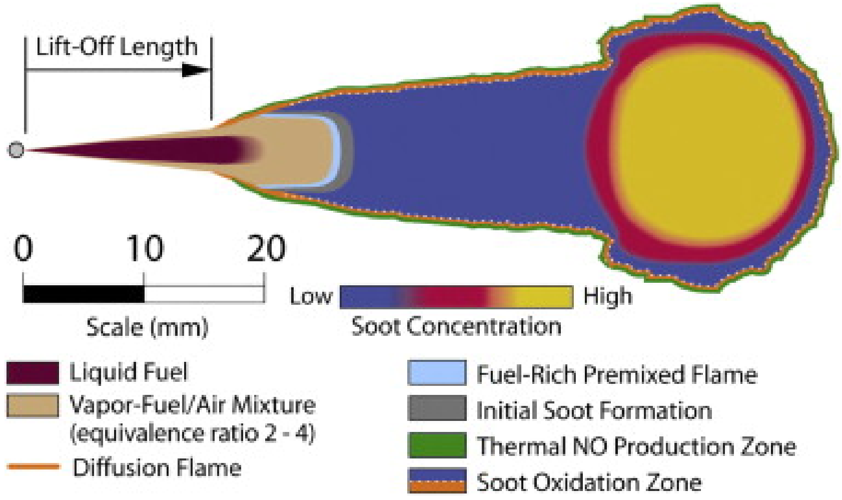

Figure 2.10. *A schematic showing the conceptual model of DI diesel combustion derived from laser-sheet imaging for a typical time during the first part of the mixing-controlled combustion [15].*

The region, located between nozzle exit and the onset of heat release, is similar to the spray observed under non-reacting conditions. A phenomenon of a lifted flame is observed because of the high local speeds, low temperature, high equivalence ratio [95]. The distance from the injector tip to the the most upstream location of the diffusion flame is referred to as the lift-off length (LOL). The mixture is rich and all the oxygen entrained along the LOL reacts in this first premixed phase of the combustion. However, since the mixture is very rich, the products formed in these reactions will constitute the fuel for the diffusive region. These products have the typical composition of a rich combustion: no oxygen, carbon monoxide, and partially burnt hydrocarbons that constitute the basis for the following soot formation. Downstream the lift-off length, the flame gets the typical structure of a diffusion flame, consisting of an internal volume occupied by intermediate combustion products and surrounded by a surface of reaction which impedes the oxygen to flow in. These substances, including unburned hydrocarbons possibly mixed with soot, complete their oxidation into carbon dioxide and water when finding the adequate amount of oxygen on the flame surface. Previous experiments conducted by Dec and Coy [96] showed that the thickness of such reactive surface was inferior to 120 μm while LIF measurements revealed it was the location of nitrogen oxides formation, consistent with conditions of high temperature ($\approx$2700 K when T_g = 950 K) and oxygen excess necessary for the appearance of this species [97].

Lift-off length

Once the ignition process has finished, the flame of a diesel spray under quiescent conditions tends to stabilize at a quasi-steady distance from the injector tip during the mixing-controlled phase until the end of injection. Although there may be some fluctuations due to turbulence, the flame LOL will present a quasi-steady mean value [17, 98, 99]. It separates the reacting spray into two parts, inert part(upstream the LOL) and reacting part(downstream the LOL). The air entrained prior to this position mixes with the fuel and after the LOL the premixed charge reacts immediately. OH^* is produced and when returning to its ground state produces chemiluminiscent radiation, which can help identify this characteristic location [16, 98].

There is growing evidence to suggest that flame LOL plays a significant role in DI diesel combustion and emission processes, making LOL of significant practical importance to diesel engines. Flame LOL is believed to affect diesel combustion and emission processes by allowing fuel and air to premix prior to reaching the initial combustion zone in a diesel spray [17]. The study of the LOL in Diesel spray allowed to understand one of the key steps of the soot formation in the Diesel combustion. In fact, the LOL determines the equivalence ratio in the premixed region and, therefore, the composition of the intermediate products within the diffusive region. Siebers and Higgins in [100] demonstrated that, the equivalence ratio at the LOL is included between $1.8 - 2.2$.

Works have been done by researchers to study the effects of different operating conditions, nozzle geometry and fuel properties on LOL [17, 86, 99, 101–103]. In Siebers and Higgins's work, they proposed an empirical power-law equation, which assesses the influence of each test condition in a analytical expression,

$$LOL = C \cdot d^{0.34} \cdot U \cdot \rho_a^{-0.85} \cdot T_a^{3.74} \cdot Z_{st}^{-1} \tag{2.6}$$

where d is the nozzle exit diameter, U is the injection velocity, Z_{st} is the stoichiometric mixture fraction, C is the proportionality constant, T_a and ρ_a are the ambient temperature and density, respectively.

In addition, Pickett et, al. [91] and Payri et, al. [104] also studied the relationship between ignition delay and LOL for different fuels with a wide range of cetane number. They found that fuels with shorter ignition delays (higher cetane numbers) generally produce shorter lift-off lengths. Pickett also concluded that the LOL is more relative with the cool-flame position and lift-off stabilization is not by flame propagation into upstream reactants. What's more, thanks to the development of optical diagnostic tools, the instantaneous LOL and flame evolution are able to be obtained by high-speed OH^* chemiluminescence [105], as shown in Figure 2.11. This high-speed approach allows a time-dependent analysis.

Soot formation

Soot emission from the engine reflects poor combustion and loss of engine efficiency. This issue initialised studies aiming in the reduction of soot generation and improvement of soot oxidation. Although the soot formation process has not been fully understood, it has been acknowledged that the process has negative impact on both the environment and human health. The epidemiology and toxicology of particulate matter present in ambient is a very active area of research [106].

The soot formation mechanisms were studied by Tree and Sensson [107] and the development of solid soot particles from liquid or vapor phase hydrocarbons mainly involves the following processes: pyrolysis, nucleation, coalescence, surface growth, agglomeration and oxidation. A schematic of

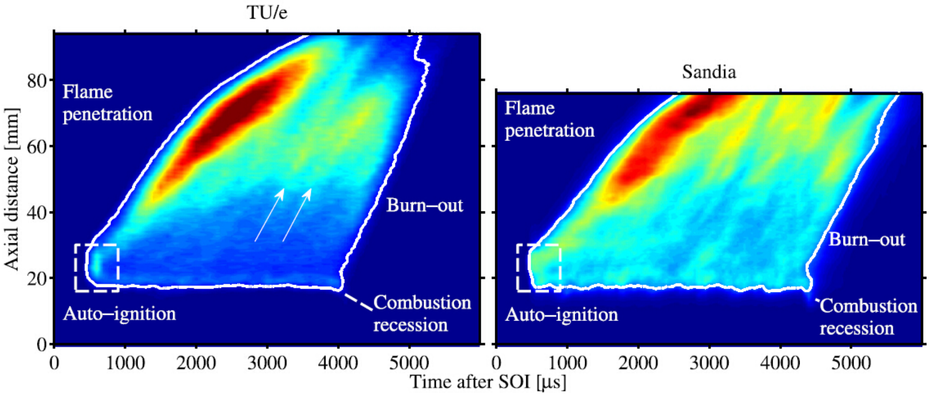

Figure 2.11. *Radially integrated OH* intensity obtained by TU/e and Sandia as a function of axial distance and time, with a contour defined by the intensity at the location of the steady LOL [105].*

the first five processes is presented in Figure 2.12. The authors specify that nucleation is the formation of particles from gas-phase reactants where two C_3H_3 radicals are likely to form the first ring. After growing and turning into PAH until reaching the size of nuclei (1.5-2 nm), particles dehydrogenate yielding a graphite-like structure of carbon atoms. This process occurs in radical-rich regions while requiring temperatures between 1300 and 1600 K. Yet, the majority of the soot mass is added during the time-consuming subsequent stage called "surface growth". Spherical primary particles (15-20 nm) of soot proceed from the coalescence of nuclei colliding, thereby decreasing the number of particles but holding the combined mass of soot particles constant. This phase corroborates that residence time has a large influence on the total soot mass or soot volume fraction. Relevance of residence time in soot formation processes was confirmed by Pickett et al. when they observed the lack of a unique equivalence ratio temperature region for soot precursor formation. Accordingly, this implies that the soot formation process rather depends upon the equivalence ratio, temperature path followed during jet mixing, and the residence time along the path [108, 109].

Thanks to the LIF techniques, the OH radicals, soot precursors (PAH) and soot can be visualized during the diesel spray combustion process. Besides Dec's conceptual model as mentioned above, similar conceptual models of soot formation process were summarized by Kosaka et al. [87] and Bruneaux [9] respectively based on these LIF measurements, as shown in Figure 2.13. At the onset of diffusion combustion, soot precursors (PAH) are formed immediately,

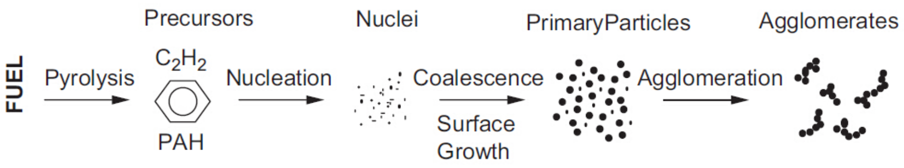

Figure 2.12. *Schematics of soot formation process [107].*

in the centre of the jet, owing to mixing of fuel-rich pockets with the hot diffusion flame products and possibly to production by the fuel-rich reaction zone. Kosaka et al. also commend that even some young soot particles are also converted by these precursors at the periphery of spray flame. During the quasi-steady diffusion combustion period,the soot precursors and young soot particles keep forming in the central fuel-rich region surrounded by the OH region. Broad regions of OH are observed at the upstream edges of the jet, which is consistent with the location of the mixing zone of the jet where lean regions are present. Soot particles are convected to the upstream side of head vortices and re-entrained into the lean side of flame, where the concentration of OH is high, and are oxidized rapidly.

In recent years, in order to have a better understanding of the soot processes in diesel combustion, optical diagnostics have been extensively applied. One of the characteristics of diesel combustion is its high luminosity caused by the thermal radiation of soot particles at high temperature. Based upon radiation measurement, Two-color method (2C) has been developed and used to quantify the temporal and 2D spatial evolution of the soot distribution and corresponding temperature [110–114], although there is a high uncertainty for the KL factor of the soot with this method [114, 115]. Laser-induced incandescence (LII) is another 2D soot distribution diagnostic technique based on soot thermal radiation. Soot particles are heated to a temperature well above the surrounding gas temperature due to the absorption of laser energy. The heated soot particles subsequently emit blackbody radiation corresponding to the elevated soot particle temperature. LII is able to qualitatively visualize the soot spatial distribution [81, 116–118]. However, the drawback of LII associated to hardware limitations of conventional measurement systems is that usually only one image per injection can be recorded, and accordingly information about the temporal evolution of soot during a single injection event is difficult to resolve, unless highly sophisticated laser sources and imaging systems are used [119]. Besides these techniques

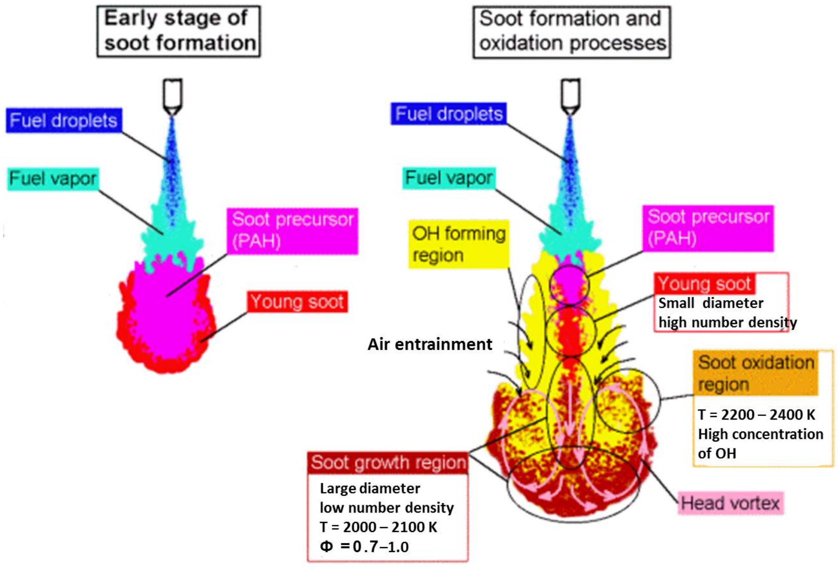

(a) Conceptual model from Kosaka et al.

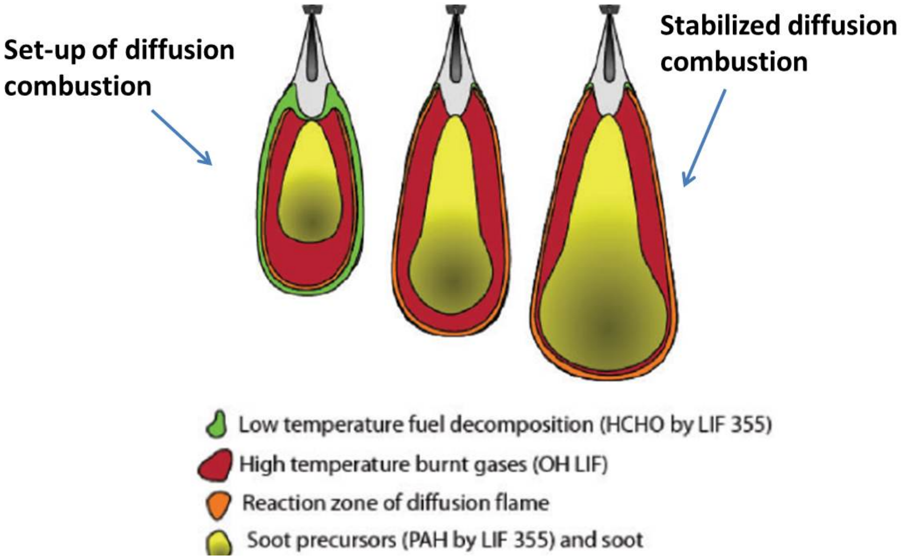

(b) Conceptual model from Bruneaux

Figure 2.13. *Conceptual model of soot formation, and oxidation processes in a diesel spray flame [9, 87].*

based on the thermal radiation of soot, another group of techniques are derived from the attenuation of light which is caused by absorption and scattering from the soot particles. Very often a point continuous laser is used in the so-called Laser-Extinction Method (LEM) [120–122]. After passing through the soot cloud, the laser beam is collected by an integrating sphere with a photodiode to measure the transmitted signal intensity. It is a simple and accurate way to measure soot process with a good time evolution. But it cannot get detailed information of the soot spatial distribution. However, with the availability of improved high speed cameras and light sources, a high-speed imaging extinction technique has been recently developed [123–125]. Compared with LEM, the light source is supplied by a bundle of diffused rays which cover the whole spray area and the collection section is replaced by a high speed camera. Thanks to the wider illumination background, and especially to the fact that its diffuse nature allows reducing light steering effects [123–125], both good spatial and time resolution can be achieved.

By means of these optical techniques, a lot of studies have been carried out to investigate the effects of different parameters (operating conditions, orifice diameter, injection strategies, fuel properties) on soot formation of diesel spray. Pickett and Siebers [120] studied the effects of ambient temperature, density and injection pressure on soot formation using LEM in a high-pressure high-temperature constant volume chamber under a wide range of Diesel-like conditions. Their results show that the peak soot level in a fuel jet increases with increasing ambient gas temperature, gas density and decreasing injection pressure. They also observed that soot closely correlates with the cross-sectional average equivalence ratio at the lift-off length, with soot levels decreasing as the equivalence ratio decreases. The effects of oxygen concentration on soot formation were studied by [108, 126]. Idicheria and Pickett mentioned the soot net production rate is determined by a competition between soot formation rates and its residence time (or oxidation rates). Soot formation rate is reduced with lower oxygen concentration because of the lower combustion temperature. However, at the same time, the soot residence time within flame becomes longer because the wider flame width and longer flame penetration under lower oxygen condition require more time for soot to be oxidized by mixing more ambient gas. Researchers [127–132] also studied fuel effects on soot formation. A higher C/H ratio, sulfur content and aromatic content could results in a higher soot production, while oxygen content can benefit to a lower soot production.

Reacting spray shape

Most of the studies investigating the air entrainment and mixing process of the Diesel spray are performed under non-reacting conditions [6, 63]: the inert spray enables an easier approach to determine the mixing field, since the number of species to be accounted for is lower and there are no light emissions coming from the combustion that normally interfere with the optical technique applied. Moreover, the study of the non-reacting spray reduces the unknowns of the problem, which makes it possible to develop more accurate mixing models to quantify the spray penetration based on simple momentum conservation and a reduced number of parameters [19, 58].

However, it is well know that the spray shape and air entrainment significantly changes as a consequence of the combustion process presenting a faster tip penetration and a radial expansion [133, 134]. These effects are certainly related to an alteration of the air-entrainment and the mixing process within the spray. The relationship between the combustion process and the shape of the spray can be a key factor to understand in details the mixing field under reacting conditions. Although effects of heat release on flow field and entrainment are a major topic in gas diffusion flames, few studies can be found in the literature that analyse in detail these phenomena: Pickett et al. presented a quantitative description of the reacting tip penetration [12] which, however, does not show a faster penetration than the non-reacting jet; Desantes et al. [133] performed a more detailed study quantifying the acceleration of the reacting spray tip in terms of the ratio of the tip penetration under reacting and inert conditions (Sr/Si). Based on this ratio, they divided the temporal evolution of the reacting Diesel spray into five stages as follows:

- **I Non-reacting phase**, previous to autoignition, where the mixing processes take place.
- **II Autoignition expansion phase**, where the spray volume suddenly increases (in axial and especially in radial direction) because of the onset of combustion.
- **III Stabilization phase**, where the reacting flow evolution does not progress faster than the inert case. If momentum is conserved,density drop due to combustion should result in a faster penetration of the spray. However, this is compensated by the strong initial increase in radial width. As a result, the reactive flow does not penetrate faster than the inert one.
- **IV Acceleration phase**, where the reacting tip penetration progresses sensitively faster than the inert one, and eventually detaches from that

of a non-reacting spray. During this period, the penetration ratio (Sr/Si) increases steadily with time.

- **V Quasi-steady flame phase**, where the tip penetration ratio reaches a steady value.

Combustion recession

Unburned hydrocarbon (UHC) emissions under low-temperature combustion (LTC) operating conditions have recently been linked to the end-of-injection transient in diesel injectors and the impact of this transient on the combustion of near-nozzle mixtures. After the end of injection, the position of the lifted flame can remain far downstream, leaving a large region of unburned or partially burned fuel-air mixture upstream [18, 135]. Under high-temperature conventional diesel combustion operating conditions, however, there is evidence to suggest that the lifted flame does propagate back towards the injector after the end of injection [13], as shown in Figure 2.14. Understanding and controlling combustion recession could offer a meaningful way to control engine emissions.

The effects of ambient conditions and end-of-injection transients on combustion have been investigated by Genzale et al. [21–23, 136]. They observed that the likelihood of combustion recession decreases with lower ambient temperature and oxygen concentration. As injection pressure is increased, the time required for combustion recession back to the injector slightly increases. At ambient conditions that do not favor combustion recession, increasing the end-of-injection transient duration promotes combustion recession. At high temperatures and/or oxygen concentrations, and also with longer end-of-injection transients, soot recession was observed, suggesting a trade-off in the emissions impact of combustion recession. Combustion recession under relatively lean conditions can help to reduce unburned hydrocarbons, but if mixtures are too rich, combustion recession can promote increased soot emissions. To link end-of-injection transients to ambient thermodynamic conditions and injector parameters, a scaling methodology for the likelihood of combustion recession in diesel sprays was also developed by Genzale et al [23].

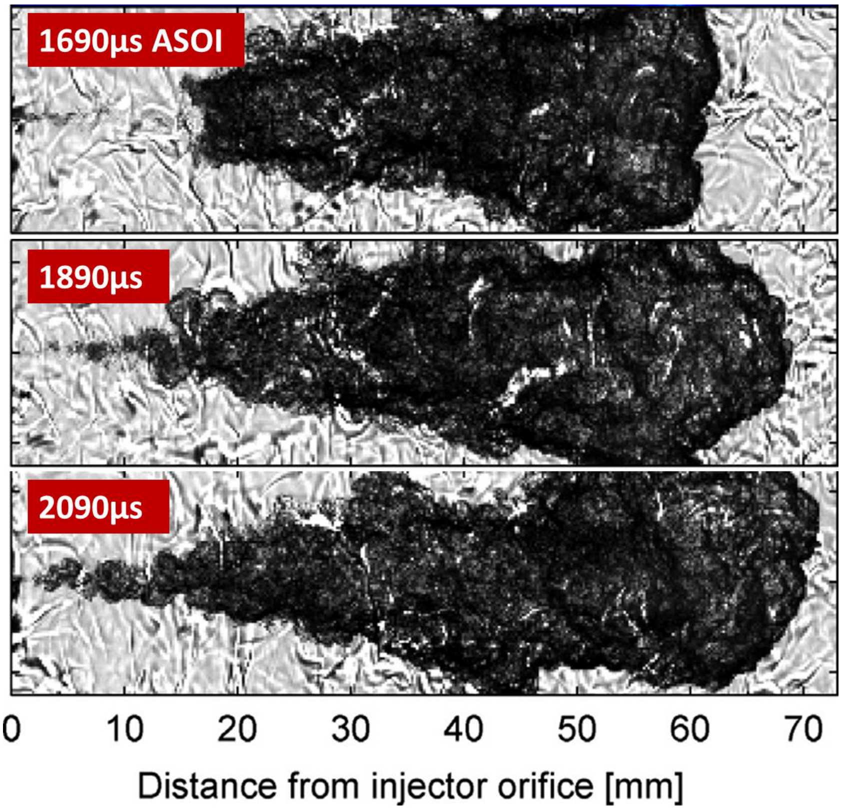

Figure 2.14. *Schlieren images of combustion recession [13].*

2.4 Split-injections

Multiple injection strategies have been studied and widely applied in conventional diesel engines in past decades because of a lot of benefits which they can bring on emissions and fuel economy. Nowadays, the injection timing and fuel quantity distribution are able to be controlled flexibly thanks to the high pressure common rail systems. Usually, the pilot injections are used to soften the combustion of main injection, which could reduce the cylinder temperature and the rise rate of cylinder pressure. As a consequence, the reductions in thermal NOx emission and engine noise could be achieved [137–139]. On the other hand, the post injections after main injection are usually applied to reduce unburned hydrocarbon (UHC) and soot formation. With increased entrainment of ambient gas with low axial momentum, vapor-fuel mixtures near the injector transitioned from fuel-rich to fuel-lean immediately after the end of injection (EOI) and the entrainment wave decelerates the flow and causes it to stagnate near the injector, which could contribute to incomplete combustion and UHC [18–20]. Post injection could push the residual lean mixture near the nozzle downstream and reach second-stage combustion with higher equivalence ratio and higher temperature environment. In addition, it has been proved that the engine-out soot can be reduced by post injection with a proper dwell time and quantity [140–142]. However the detailed mechanism is still needed to be further studied.

As mentioned above, there are many studies in the literature related to engine applications, but no so many fundamental studies are available. Because of the complexity of the interaction mechanism among these multiple injections (more than two injections), many researchers investigated the physical phenomena of these multiple injection strategies starting with split-injection (double injections). The characteristics of non-reacting split-injection were studied experimentally by [13, 143, 144]. Both Bruneaux [143] and Skeen [13] show that the vapor phase of second injection enters a "slipstream" which makes it penetrates faster than that of the first one and this phenomenon was also well reproduced by CFD model [145, 146]. Thanks to the velocity measurement, Bruneaux also found the interaction between two injections is stronger with a shorter dwell time, leading to an increase of the mixing rate at the head of second spray. In addition, the liquid-phase penetration of second injection was also found longer than the first one when the duration were kept same constant and both injections ended before the liquid-phase can reach the steady-state liquid length [144]. As for reacting sprays, the ignition processes of split-injection under different ambient temperature were studied elaborately by Skeen in a pre-burn combustion vessel with the fuel of n-Dodecane [13]. In general, the ignition delay (ID) of section injection is reduced by a factor of two or more relative to that of the first injection, which is caused by the entrainment of high combustion products and radical species remaining from first injection. The effects of dwell time between double injections on ignition delay were also studied in [147, 148]. However, detailed analysis is still needed to be presented. The transient flame lift-off length (LOL) development of split-injection was measured by Noud [149] by means of the high-speed OH^* chemiluminescence. It is interesting to see the LOL slowly progress further downstream after ignition of the second injection until the combustion recession takes place after EOI. Moiz et, al. investigated the effect of changing dwell time on transient soot formation by means of CFD simulation [150]. In their work, the decrease in soot production with longer dwell time was explained by a higher air-entrainment. The experimental validation and more possible factors which could contribute to soot formation need to be further studied.

2.5 Summary and conclusions

As presented throughout this chapter, lots of optical investigations on combustion process of direct injection diesel spray have been done in recent decades. Thanks to that, the numerous physical and chemical processes within such a short time becomes more and more clear. However, there are still some remaining questions on spray dynamics and soot formation process because of the limitation of optical techniques and complexity of combustion process. Remaining questions include:

- Non-reacting spray dynamics are becoming much clear. A cone angle can represent spray radial expansion, while the tip penetration can be calculated according to momentum conservation. But the knowledge on how to quantify the effects of combustion on spray radial expansion and penetration velocity is still limited.

- A lot of optical techniques on soot diagnostics have been developed by previous researchers. However, big uncertainties still exist on soot amount and temperature quantification. Are there some ways to improve the accuracy of these techniques?

- In-cylinder flow may have some meaningful impact on the spray evolution. How to improve the understanding of the effects of in-cylinder flow on spray and combustion process?

- Some investigations have been done on the study of split-injection diesel spray. How does the first injection affect fuel-air mixing and combustion process of the second injection by changing the dwell time or first injection duration?

The answers of these questions are desired outcomes of this research.

Bibliography

[1] Heywood J. B. *Internal combustion engine fundamentals.* McGraw-Hill Publishing, 1988.

[2] Nerva Jean-Guillaume. *An assessment of fuel physical and chemical properties in the combustion of a Diesel spray.* Doctoral Thesis, Universitat Politecnica de Valencia, 2013.

[3] Fajardo Walter Martin Vera-Tudela. *An experimental study of the effects of fuel properties on diesel spray processes using blends of single-component fuels.* Doctoral Thesis, Universitat Politecnica de Valencia, 2015.

[4] Kamimoto Takeyuki and Kobayashi Haruki. "Combustion processes in diesel engines". *Progress in Energy and Combustion Science*, Vol. 17 n^{o} 2, pp. 163–189, jan 1991.

[5] Musculus Mark P B, Miles Paul C. and Pickett Lyle M. *Conceptual models for partially premixed low-temperature diesel combustion*, volume 39. Elsevier Ltd, 2013.

[6] Naber Jeffrey D and Siebers Dennis L. "Effects of Gas Density and Vaporization on Penetration and Dispersion of Diesel Sprays". *SAE Paper 960034*, Vol. 105 n^{o} 412, pp. 82—-111, 1996.

[7] Ricou F. P. and Spalding D. B. "Measurements of entrainment by axisymmetrical turbulent jets". *Journal of Fluid Mechanics*, Vol. 11, pp. 21, 1961.

[8] Siebers Dennis L. "Scaling liquid-phase fuel penetration in diesel sprays based on mixing-limited vaporization". *SAE Paper 1999-01-0528*, Vol. 199-01-052 n^{o} 724, pp. 01–0528, 1999.

[9] Bruneaux G. "Combustion structure of free and wall-impinging diesel jets by simultaneous laser-induced fluorescence of formaldehyde, poly-aromatic hydrocarbons, and hydroxides". *International Journal of Engine Research*, Vol. 9 n^{o} 3, pp. 249–265, 2008.

[10] Dec John E. and Espey Christoph. "Ignition and early soot formation in a DI diesel engine using multiple 2-D imaging diagnostics". *SAE Transactions*, Vol. 104 n^{o} 3, pp. 853–875, 1995.

[11] Dec John E and Espey Christoph. "Chemiluminescence Imaging of Autoignition in a DI Diesel Engine". *SAE Technical Paper 982685*, n^{o} 724, 1998.

[12] Pickett Lyle M, Kook Sanghoon and Williams Timothy C. "Visualization of Diesel Spray Penetration, Cool-Flame, Ignition, High-Temperature Combustion, and Soot Formation Using High-Speed Imaging". *SAE Int. J. Engines*, Vol. 2 n^{o} 1, pp. 439–459, 2009.

[13] Skeen Scott, Manin Julien and Pickett Lyle M. "Visualization of Ignition Processes in High-Pressure Sprays with Multiple Injections of n-Dodecane". *SAE Int. J. Engines*, Vol. 8 n^{o} 2, pp. 696–715, 2015.

[14] Skeen Scott A., Manin Julien and Pickett Lyle M. "Simultaneous formaldehyde PLIF and high-speed schlieren imaging for ignition visualization in high-pressure spray flames". *Proceedings of the Combustion Institute*, Vol. 35 n^{o} 3, pp. 3167–3174, 2015.

[15] Dec John E. "A conceptual model of DI diesel combustion based on laser-sheet imaging". *Sae*, n^{o} 412, pp. 970873, 1997.

[16] Higgins Brian and Siebers Dennis. "Measurement of the Flame Lift-Off Location on Dl Diesel Sprays Using OH Chemiluminescence". *Sae 2001-01-0918*, n^{o} 724, 2001.

[17] Siebers D.L. and Higgins Brian. "Flame lift-off on direct-injection diesel sprays under quiescent conditions". *Sae Transactions*, Vol. 110 n^{o} 3, pp. 400–421, 2001.

[18] Musculus Mark P. B., Lachaux Thierry, Pickett Lyle M. and Idicheria Cherian A. “End-of-Injection Over-Mixing and Unburned Hydrocarbon Emissions in Low-Temperature- Combustion Diesel Engines”. *Sae*, Vol. 2007-01-09 n^o 724, pp. 776–0790, 2007.

[19] Musculus Mark P. B. “Entrainment waves in decelerating transient turbulent jets”. *Journal of Fluid Mechanics*, Vol. 638 n^o 1, pp. 117, 2009.

[20] Kook Sanghoon, Pickett Lyle M and Musculus Mark P B. “Influence of Diesel Injection Parameters on End-of-Injection Liquid Length Recession”. *SAE Int. J. Engines*, Vol. 2 n^o 1, pp. 1194–1210, 2009.

[21] Knox Benjamin W, Genzale Caroline L, Pickett Lyle M, Garcia-Oliver Jose M and Vera-Tudela Walter. “Combustion Recession after End of Injection in Diesel Sprays”. *SAE Int. J. Engines*, Vol. 8 n^o 2, pp. 679–695, 2015.

[22] Knox Benjamin and Genzale Caroline. “Effects of End-of-Injection Transients on Combustion Recession in Diesel Sprays”. *SAE International Journal of Engines*, Vol. 9 n^o 2, pp. 2016–01–0745, 2016.

[23] Knox Benjamin W. and Genzale Caroline L. “Scaling combustion recession after end of injection in diesel sprays”. *Combustion and Flame*, Vol. 177, pp. 24–36, 2017.

[24] Bravo Luis and Kweon Chol-bum. “A Review on Liquid Spray Models for Diesel Engine Computational Analysis”. *Army Research Laboratory*, n^o May, 2014.

[25] Linne Mark. “Imaging in the optically dense regions of a spray: A review of developing techniques”. *Progress in Energy and Combustion Science*, Vol. 39 n^o 5, pp. 403–440, 2013.

[26] Krüger S and Grünefeld G. “Droplet velocity and acceleration measurements in dense sprays by laser flow tagging”. *Applied Physics B*, Vol. 615, pp. 611–615, 2000.

[27] Krüger S and Grünefeld G. “Gas-phase velocity field measurements in dense sprays by laser-based flow tagging”. *Applied Physics B: Lasers and Optics*, Vol. 70 n^o 3, pp. 463–466, 2000.

[28] Sedarsky David, Berrocal Edouard and Linne Mark. “Numerical Analysis of Ballistic Imaging for Revealing Liquid Breakup in Dense Sprays”. *Atomization and Sprays*, Vol. 20 n^o 5, pp. 407–413, 2010.

[29] Linne Mark A., Paciaroni Megan, Berrocal Edouard and Sedarsky David. “Ballistic imaging of liquid breakup processes in dense sprays”. *Proceedings of the Combustion Institute*, Vol. 32 II n^o 2, pp. 2147–2161, 2009.

[30] Liu Zunping, Im Kyoung-Su, Xie Xing-bin, Wang Yujie, Zhang Xusheng, Moon Seoksu, Gao Jian, Fezzaa Kamel, Lai Ming-Chia, Harkay Kathy, Sajaev Vadim, Emery Louis and Wang Jin. “Ultra-Fast Phase-Contrast X-ray Imaging of Near-Nozzle Velocity Field of High-Speed Diesel Fuel Sprays”. *Ilass*, n^o May, 2010.

[31] Osta A R, Lee J and Sallam K A. “Investigating the Effect of the Injector Length/Diameter ratio on the Primary Breakup of Liquid Jets using X-ray Diagnostics”. *Iclass*, n^o July, 2009.

[32] Payri Raul, Bracho Gabriela, Marti-Aldaravi Pedro and Viera Alberto. “Near field visualization of diesel spray for different nozzle inclination angles in non-vaporizing conditions”. *Atomization and Sprays*, Vol. 27 n^o 3, pp. 251–267, 2017.

[33] Dahms Rainer N., Manin Julien, Pickett Lyle M. and Oefelein Joseph C. “Understanding high-pressure gas-liquid interface phenomena in Diesel engines”. *Proceedings of the Combustion Institute*, Vol. 34 n^o 1, pp. 1667–1675, 2013.

[34] Manin J., Bardi M., Pickett L. M., Dahms R. N. and Oefelein J. C. "Microscopic investigation of the atomization and mixing processes of diesel sprays injected into high pressure and temperature environments". *Fuel*, Vol. 134, pp. 531–543, 2014.

[35] Coghe A. and Cossali G. E. "Quantitative optical techniques for dense sprays investigation: A survey". *Optics and Lasers in Engineering*, Vol. 50 n^o 1, pp. 46–56, 2012.

[36] Reitz R. D. *Atomization and other breakup regimes of a liquid jet.* Doctoral Thesis, Princeton Univ., NJ., 1978.

[37] Baumgarten C, Stegemann J and Merker G. "A new model for cavitation induced primary break-up of diesel sprays". *Zaragoza*, Vol. 9 n^o 11, 2002.

[38] Som S. and Aggarwal S. K. "Effects of primary breakup modeling on spray and combustion characteristics of compression ignition engines". *Combustion and Flame*, Vol. 157 n^o 6, pp. 1179–1193, 2010.

[39] Jenny Patrick, Roekaerts Dirk and Beishuizen Nijso. "Modeling of turbulent dilute spray combustion". *Progress in Energy and Combustion Science*, Vol. 38 n^o 6, pp. 846–887, 2012.

[40] Weber Constantin. "Zum Zerfall eines Flüssigkeitsstrahles". *ZAMM - Journal of Applied Mathematics and Mechanics / Zeitschrift für Angewandte Mathematik und Mechanik*, Vol. 11 n^o 2, pp. 136–154, 1931.

[41] Zeoli N. and Gu S. "Numerical modelling of droplet break-up for gas atomisation". *Computational Materials Science*, Vol. 38 n^o 2, pp. 282–292, 2006.

[42] Dinos Arcoumanis Take Kamimoto et al. *Flow and Combustion in Reciprocating Engines.* Springer Berlin Heidelberg, 2009.

[43] Siebers Dennis L. "Liquid-Phase Fuel Penetration in Diesel Sprays". In *SAE Technical Paper.* SAE International, 02 1998.

[44] van de Hulst H. C. *Light Scattering by Small Particles.* 1957.

[45] Bohren C. F. and Huffman D. R. *Absorption and scattering of light by small particles.* 1983.

[46] Kook Sanghoon and Pickett Lyle M. "Liquid length and vapor penetration of conventional, Fischer-Tropsch, coal-derived, and surrogate fuel sprays at high-temperature and high-pressure ambient conditions". *Fuel*, Vol. 93, pp. 539–548, 2012.

[47] Pastor J. V., García-Oliver J. M., Nerva J. G. and Giménez B. "Fuel effect on the liquid-phase penetration of an evaporating spray under transient diesel-like conditions". *Fuel*, Vol. 90 n^o 11, pp. 3369–3381, 2011.

[48] Pastor José V, Garcia-oliver José M, Bermudez Vicente and Micó Carlos. "Spray Characterization for Pure Fuel and Binary Blends under Non-Reacting Conditions". *SAE Technical Paper*, 2014.

[49] Payri Raul, Gimeno Jaime, Bardi Michele and Plazas Alejandro H. "Study liquid length penetration results obtained with a direct acting piezo electric injector". *Applied Energy*, Vol. 106, pp. 152–162, 2013.

[50] Bardi Michele, Payri Raul, Malbec Louis-Marie, Bruneaux Gilles, Pickett Lyle M, Manin Julien, Bazyn Tim and Genzale Caroline L. "Engine Combustion Network: Comparison of Spray Development, Vaporization, and Combustion in Different Combustion Vessels". *Atomization and Sprays*, Vol. 22 n^o 10, pp. 807–842, 2012.

[51] Jung Yongjin, Manin Julien, Skeen Scott and Pickett Lyle M. "Measurement of Liquid and Vapor Penetration of Diesel Sprays with a Variation in Spreading Angle". *SAE Technical Paper 2015-01-0946*, 2015.

[52] Bardi Michele, Bruneaux Gilles and Malbec Louis-marie. "Study of ECN Injectors ' Behavior Repeatability with Focus on Aging Effect and Soot Fluctuations". *SAE Technical Paper*, Vol. 01 n^o 0845, 2016.

[53] Pickett Lyle M, Manin Julien, Genzale Caroline L, Siebers Dennis L, Musculus Mark P B and Idicheria Cherian A. "Relationship Between Diesel Fuel Spray Vapor Penetration/Dispersion and Local Fuel Mixture Fraction". *SAE Int. J. Engines*, Vol. 4 n^o 1, pp. 764–799, 2011.

[54] Higgins Brian S, Mueller Charles J and Siebers Dennis L. "Measurements of Fuel Effects on Liquid-Phase Penetration in DI Sprays". *SAE transactions*, Vol. 108 n^o 724, pp. 630–643, 1999.

[55] Bardi Michele. *Partial Needle Lift and Injection Rate Shape Effect on the Formation and Combustion of the Diesel Spray.* Doctoral Thesis, Universitat Politecnica de Valencia, 2014.

[56] Desantes J M, Lopez J J, Garcia J M and Pastor J M. "Evaporative diesel spray modeling". *Atomization and Sprays*, Vol. 17 n^o 3, pp. 193–231, 2007.

[57] García J. M. *Aportaciones al estudio del proceso de combustión turbulenta de chorros en motores Diesel de inyección directa.* Doctoral Thesis, 2004.

[58] Pastor José V., Javier López J., García José M. and Pastor José M. "A 1D model for the description of mixing-controlled inert diesel sprays". *Fuel*, Vol. 87 n^o 13-14, pp. 2871–2885, 2008.

[59] Briceno F J, Garcia-Oliver J M, Pastor J V and Payri R. "Analysis of Transient Liquid and Vapor Phase Penetration for Diesel Sprays Under Variable Injection Conditions". *Atomization and Sprays*, Vol. 21 n^o 6, pp. 503–520, 2011.

[60] Bruneaux G. "Liquid and Vapor Spray Structure in High Pressure common rail Diesel Injection". *Atomization and Sprays*, Vol. 11, pp. 533–556, 2001.

[61] Pastor Jose Vicente, Payri Raul, Garcia-Oliver Jose Maria and Nerva Jean-guillaume. "Schlieren Measurements of the ECN-Spray A Penetration under Inert and Reacting Conditions". *SAE Technical Paper 2012-01-0456*, 2012.

[62] Payri F., Payri R., Bardi M. and Carreres M. "Engine combustion network: Influence of the gas properties on the spray penetration and spreading angle". *Experimental Thermal and Fluid Science*, Vol. 53, pp. 236–243, 2014.

[63] Hiroyasu Hiro and Arai Masataka. "Structures of Fuel Sprays in Diesel Engines". In *SAE Technical Paper.* SAE International, 02 1990.

[64] Dent J. C. "A Basis for the Comparison of Various Experimental Methods for Studying Spray Penetration". In *SAE Technical Paper.* SAE International, 02 1971.

[65] Desantes J. M., Payri R., Salvador F. J. and Gil A. "Development and validation of a theoretical model for diesel spray penetration". *Fuel*, Vol. 85 n^o 7-8, pp. 910–917, 2006.

[66] Wan Yuepeng and Peters Norbert. "Scaling of spray penetration with evaporation". *Atomization and Sprays*, Vol. 9 n^o 2, pp. 111–132, 1999.

[67] Payri F., BermÃºdez V., Payri R. and Salvador F.J. "The influence of cavitation on the internal flow and the spray characteristics in diesel injection nozzles". *Fuel*, Vol. 83, pp. 419 – 431, 2004.

[68] Pastor Jose Vicente, Arrègle Jean and Palomares A. "Diesel spray images segmentation using a likelihood ratio test". *Applied Optics*, Vol. 40 n^o 17, pp. 2876–2885, 2001.

[69] Ranz William E. "Some experiments on orifice sprays". *The Canadian Journal of Chemical Engineering*, Vol. 36 n^o 4, pp. 175–181, 1958.

[70] Reitz Rolf D. and Bracco F. B. "On the Dependence of Spray Angle and Other Spray Parameters on Nozzle Design and Operating Conditions". In *SAE Technical Paper.* SAE International, 02 1979.

[71] Desantes Jose M., Pastor J. V., Payri Raul and Pastor Jose M. "Experimental characterization of internal nozzle flow and diesel spray behavior. Part II: evaporative conditions". *Atomization and Sprays*, Vol. 15 n^o 5, pp. 517–544, 2005.

[72] Delacourt E., Desmet B. and Besson B. "Characterisation of very high pressure diesel sprays using digital imaging techniques". *Fuel*, Vol. 84 n^o 7-8, pp. 859–867, 2005.

[73] MacIan V., Payri R., Garcia A. and Bardi M. "Experimental evaluation of the best approach for diesel spray images segmentation". *Experimental Techniques*, Vol. 36 n^o 6, pp. 26–34, 2012.

[74] Idicheria Cherian A and Pickett Lyle M. "Quantitative Mixing Measurements in a Vaporizing Diesel Spray by Rayleigh Imaging". *SAE Technical Paper*, Vol. 2007 n^o 724, pp. 776–790, 2007.

[75] Egermann, J. Göttler A. and Leipertz A. "Application of Spontaneous Raman Scattering for Studying the Diesel Mixture Formation Process Under Near-Wall Conditions". *SAE Technical Paper*, 2001.

[76] Hoffmann T, Hottenbach P, Koss H, Pauls C and Grünefeld G. "Investigation of Mixture Formation in Diesel Sprays under Quiescent Conditions using Raman , Mie and LIF Diagnostics". *SAE Technical Paper*, Vol. 2008 n^o 724, pp. 776–790, 2008.

[77] Bruneaux Gilles. "Mixing Process in High Pressure Diesel Jets by Normalized Laser Induced Exciplex Fluorescence Part I: Free Jet". *SAE Technical Paper*, 05 2005.

[78] Payri F, Pastor J V, Pastor J M and Julian J E. "Diesel Spray Analysis by Means of Planar Laser-Induced Exciplex Fluorescence". *International Journal of Engine Research*, Vol. 7 n^o 1, pp. 77–89, 2006.

[79] Kosaka Hidenori and Kamimoto Takeyuki. "Quantitative Measurement of Fuel Vapor Concentration in an Unsteady Evaporating Spray via a 2-D Mie-Scattering Imaging Technique". *SAE Technical Paper*, 10 1993.

[80] Espey Christoph, Dec John E., Litzinger Thomas A. and Santavicca Domenic A. "Planar laser rayleigh scattering for quantitative vapor-fuel imaging in a diesel jet". *Combustion and Flame*, Vol. 109 n^o 1, pp. 65 – 86, 1997.

[81] Reche Carlos Mico. *Development of measurement and visualization techniques for characterization of mixing and combustion processes with surrogate fuel.* Doctoral Thesis, Universitat Politecnica de Valencia, 2015.

[82] Higgins Brian, Siebers Dennis L and Aradi Allen. "Diesel-Spray Ignition and Premixed-Burn Behavior". *SAE Technical Paper 2000-01-0940*, n^o 724, 2000.

[83] Kosaka Hidenori, Drewes Volker H, Catalfamo Luca, Aradi Allen a, Iida Norimasa and Kamimoto Takeyuki. "Two-Dimensional Imaging of Formaldehyde Formed During the Ignition Process of a Diesel Fuel Spray". *SAE Technical Paper*, n^o 724, 2000.

[84] Jansons Marcis, Brar Amandeep, Estefanous Fadi, Florea Radu, Taraza Dinu, Henein Naeim and Bryzik Walter. "Experimental Investigation of Single and Two-Stage Ignition in a Diesel Engine". *SAE Technical Paper 2008-01-1071*, Vol. 2008 n^o 724, pp. 776–790, 2008.

[85] Lillo Peter M, Pickett Lyle M, Persson Helena, Andersson Oivind and Kook Sanghoon. "Diesel Spray Ignition Detection and Spatial/Temporal Correction". *SAE Paper 2012-01-1239*, pp. 1–21, 2012.

[86] Benajes Jesús, Payri Raúl, Bardi Michele and Martí-Aldaraví Pedro. "Experimental characterization of diesel ignition and lift-off length using a single-hole ECN injector". *Applied Thermal Engineering*, Vol. 58 n^o 1-2, pp. 554–563, 2013.

[87] Kosaka H, Aizawa T and Kamimoto T. "Two-dimensional imaging of ignition and soot formation processes in a diesel flame". *International Journal of Engine Research*, Vol. 6 n^o 1, pp. 21–42, 2005.

[88] Idicheria Cherian A. and Pickett Lyle M. "Formaldehyde Visualization Near Lift-off Location in a Diesel Jet". *SAE International*, 2006.

[89] Aggarwal S.K. "A review of spray ignition phenomena: Present status and future research". *Progress in Energy and Combustion Science*, Vol. 24 n^o 6, pp. 565–600, 1998.

[90] Dec John E. "Advanced compression-ignition engines - Understanding the in-cylinder processes". *Proceedings of the Combustion Institute*, Vol. 32 II n^o 2, pp. 2727–2742, 2009.

[91] Pickett Lyle M, Siebers Dennis L and Idicheria Cherian A. "Relationship Between Ignition Processes and the Lift-Off Length of Diesel Fuel Jets". *SAE Technical Paper*, n^o 724, pp. –, 2005.

[92] Malbec Louis-Marie Malbec, Eagle W. Ethan, Musculus Mark P. B. and Schihl Peter. "Influence of Injection Duration and Ambient Temperature on the Ignition Delay in a 2.34L Optical Diesel Engine". *SAE Int. J. Engines*, Vol. 9 n^o 1, 2016.

[93] Flynn Patrick F., Durrett Russell P., Hunter Gary L., zur Loye Axel O., Akinyemi O. C., Dec John E. and Westbrook Charles K. "Diesel Combustion: An Integrated View Combining Laser Diagnostics, Chemical Kinetics, And Empirical Validation". *SAE Technical Paper*, n^o 1999-01-0509, 1999.

[94] Jing Wei, Roberts William L. and Fang Tiegang. "Spray combustion of Jet-A and diesel fuels in a constant volume combustion chamber". *Energy Conversion and Management*, Vol. 89 n^o x, pp. 525–540, 2015.

[95] Venugopal Rishikesh and Abraham John. "A Review of Fundamental Studies Relevant to Flame Lift-off in Diesel Jets". *SAE Transactions*, n^o 724, pp. 776–0790, 2009.

[96] Dec John E and Coy Edward B. "OH Radical Imaging in a DI Diesel Engine and the Structure of the Early Diffusion Flame". *SAE Technical Paper*, n^o 412, 1996.

[97] Dec John E. and Canaan Robert E. "PLIF imaging of NO formation in a DI diesel engine". *Proceedings of the 1998 SAE International Congress & Exposition*, n^o 724, pp. 79–105, 1998.

[98] Peters Norbert. *Turbulent Combustion.* Cambridge Monographs on Mechanics. Cambridge University Press, 2000.

[99] Siebers Dennis, Higgins Brian and Pickett Lyle. " Flame Lift-Off on Direct-Injection Diesel Fuel Jets : Oxygen Concentration Effects In-Cylinder Diesel Particulates and NOx Control". *SAE paper*, n^o 724, 2002.

[100] Siebers Dennis L. and Higgins Brian S. “Effects of Injector Conditions on the Flame Lift-Off Length of DI Diesel Sprays”. In *Thermalfluidynamic Processes in Diesel Engines*, pp. 253–277, 9 2000.

[101] Musculus Mark P B. “Effects of the in-cylinder environment on diffusion flame lift-off in a DI diesel engine”. *SAE transactions*, n^o 724, 2003.

[102] Payri Raúl, Viera Juan Pablo, Pei Yuanjiang and Som Sibendu. “Experimental and numerical study of lift-off length and ignition delay of a two-component diesel surrogate”. *Fuel*, Vol. 158, pp. 957–967, 2015.

[103] Payri Raul, Viera Juan P., Gopalakrishnan Venkatesh and Szymkowicz Patrick G. “The effect of nozzle geometry over ignition delay and flame lift-off of reacting direct-injection sprays for three different fuels”. *Fuel*, Vol. 199, pp. 76 – 90, 2017.

[104] Payri Francisco, Pastor Jose V, Nerva Jean-Guillaume and Garcia-Oliver Jose M. “Lift-Off Length and KL Extinction Measurements of Biodiesel and Fischer-Tropsch Fuels under Quasi-Steady Diesel Engine Conditions”. *SAE International Journal of Engines*, Vol. 4 n^o 2, pp. 2278–2297, 2011.

[105] Maes Noud, Meijer Maarten, Dam Nico, Somers Bart, Baya Toda Hubert, Bruneaux Gilles, Skeen Scott A., Pickett Lyle M. and Manin Julien. “Characterization of Spray A flame structure for parametric variations in ECN constant-volume vessels using chemiluminescence and laser-induced fluorescence”. *Combustion and Flame*, Vol. 174, pp. 138–151, 2016.

[106] Menkiel Barbara. *Investigation of soot process in an optical diesel engine.* Doctoral Thesis, Brunel University, January 2012.

[107] Tree Dale R. and Svensson Kenth I. “Soot processes in compression ignition engines”. *Progress in Energy and Combustion Science*, Vol. 33 n^o 3, pp. 272–309, 2007.

[108] Idicheria Cherian A. and Pickett Lyle M. “Soot Formation in Diesel Combustion under High-EGR Conditions”. *SAE Technical Paper*, n^o 724, pp. 2005–01–3834, 2005.

[109] Pickett Lyle M., Caton J A, Musculus Mark P. B. and Lutz Andrew E. “Evaluation of the equivalence ratio-temperature region of diesel soot precursor formation using a two-stage Lagrangian model”. *International Journal of Engine Research*, Vol. 7 n^o 5, pp. 349–370, 2006.

[110] Hua Zhao N. Ladommatos. *Engine combustion instrumentation and diagnostics.* Warrrendale PA: Society of Automotive Engineers, 2001.

[111] Zhao Hua and Ladommatos N. “Optical Diagnostics for soot and temperature measurement in diesel engines”. *Progress in energy and combustion science*, Vol. 24, pp. 221–255, 1998.

[112] Payri F, Pastor J V, García J M and Pastor J M. “Contribution to the application of two-colour imaging to diesel combustion”. *Measurement Science and Technology*, Vol. 18 n^o 8, pp. 2579–2598, 2007.

[113] Musculus Mark P B, Singh Satbir and Reitz Rolf D. “Gradient effects on two-color soot optical pyrometry in a heavy-duty DI diesel engine”. *Combustion and Flame*, Vol. 153 n^o 1-2, pp. 216–227, 2008.

[114] Zhang Ji, Jing Wei, Roberts William L. and Fang Tiegang. “Soot temperature and KL factor for biodiesel and diesel spray combustion in a constant volume combustion chamber”. *Applied Energy*, Vol. 107, pp. 52–65, 2013.

[115] Skeen Scott, Manin Julien, Pickett Lyle, Dalen Kristine and Ivarsson Anders. "Quantitative Spatially Resolved Measurements of Total Radiation in High-Pressure Spray Flames". *SAE Technical Paper*, 2014.

[116] Wiltafsky Georg, Stolz Wolgang, Kohler Jurgen, Espey Christoph and 961200 S a E Technical Paper. "The Quantification of Laser-Induced Incandescence (LII) for Planar Time resolved Measurements of the Soot Volume Fraction in a Combusting Diesel Jet". *International Spring Fuels & Lubricants Meeting*, n^o Lii, 1996.

[117] Viskup Richard, Stanger Thomas, del Re Luigi, Reinisch Tristan and Bergmann Alexander. "Development of In-Situ, Full Stream, Laser Induced Incandescence Technique for Measurement of Transient Soot Emissions". *SAE International*, pág. 7, 2013.

[118] Pastor José V., García-Oliver José M., García Antonio, Micó Carlos and Möller Sebastian. "Application of optical diagnostics to the quantification of soot in n-alkane flames under diesel conditions". *Combustion and Flame*, Vol. 164, pp. 212–223, 2016.

[119] Sjöholm Johan. *High Repetition Rate Laser Diagnostics for Combustion Applications*. Doctoral Thesis, Lund University, 2012.

[120] Pickett Lyle M. and Siebers Dennis L. "Non-sooting, low flame temperature mixing controlled DI diesel combustion". *SAE transactions*, n^o 724, 2004.

[121] Musculus Mark P B and Pickett Lyle M. "Diagnostic considerations for optical laser-extinction measurements of soot in high-pressure transient combustion environments". *Combustion and Flame*, Vol. 141 n^o 4, pp. 371–391, 2005.

[122] Zheng Liang, Ma Xiao, Wang Zhi and Wang Jianxin. "An optical study on liquid-phase penetration, flame lift-off location and soot volume fraction distribution of gasoline-diesel blends in a constant volume vessel". *Fuel*, Vol. 139, pp. 365–373, 2015.

[123] Skeen Scott a, Manin Julien, Dalen Kristine and Pickett Lyle M. "Extinction-based Imaging of Soot Processes over a Range of Diesel Operating Conditions". *Internal combustion and gas turbine engines*, pp. 1–13, 2013.

[124] Manin Julien, Pickett Lyle M. and Skeen Scott A. "Two-Color Diffused Back-Illumination Imaging as a Diagnostic for Time-Resolved Soot Measurements in Reacting Sprays". *SAE International Journal of Engines*, Vol. 6 n^o 4, pp. 2013–01–2548, 2013.

[125] Westlye Fredrik R., Penney Keith, Ivarsson Anders, Pickett Lyle M., Manin Julien and Skeen Scott A. "Diffuse back-illumination setup for high temporally resolved extinction imaging". *Applied Optics*, Vol. 56 n^o 17, pp. 5028, 2017.

[126] Cenker E., Bruneaux G., Pickett L.M. and Schulz C. "Study of soot formation and oxidation in the engine combustion network (ECN), Spray A: Effects of ambient temperature and oxygen concentration". *SAE Int. J. Engines*, Vol. 6, pp. 352–365, 2013.

[127] Miyamoto Noboru, Ogawa Hideyuki Shibuya Masahiko Arai Keiji and Olivier Esmilaire. "Influence of the Molecular Structure of Hydrocarbon Fuels on Diesel Exhaust Emissions". *SAE Technical Paper*, n^o 412, 1994.

[128] Ullman, T., Spreen, K., and Mason R. "Effects of Cetane Number on Emissions From a Prototype 1998 Heavy-Duty Diesel Engine". *SAE Technical Paper 950251*, n^o 412, 1995.

[129] Pickett Lyle M and Siebers Dennis L. "Fuel Effects on Soot Processes of Fuel Jets at DI Diesel Conditions". *SAE Technical Paper*, n^o 724, pp. –, 2003.

[130] Svensson K I, Richards M J, Mackrory A J and Tree D R. “Fuel composition and molecular structure effects on soot formation in direct-injection flames under diesel engine conditions”. *SAE Transactions*, Vol. 114 n^o 3, pp. 594–604, 2005.

[131] Sanghoon Kook and Pickett Lyle M. “Effect of fuel volatility and ignition quality on combustion and soot formation at fixed premixing conditions”. *SAE Int. J. Engines*, Vol. 2 n^o 2, pp. 11–23, 2009.

[132] Kook Sanghoon and Pickett Lyle M. “Soot Volume Fraction and Morphology of Conventional, Fischer-Tropsch, Coal-Derived, and Surrogate Fuel at Diesel Conditions”. *SAE Int. J. Fuels Lubr.*, Vol. 5 n^o 2, pp. 647–664, 2012.

[133] Desantes José M., Pastor José V., García-Oliver José M. and Briceño Francisco J. “An experimental analysis on the evolution of the transient tip penetration in reacting Diesel sprays”. *Combustion and Flame*, Vol. 161 n^o 8, pp. 2137–2150, 2014.

[134] Gong Cheng, Jangi Mehdi, Lucchini Tommaso, D’Errico Gianluca and Bai Xue-Song. “Large Eddy Simulation of Air Entrainment and Mixing in Reacting and Non-Reacting Diesel Sprays”. *Flow, Turbulence and Combustion*, Vol. 93 n^o 3, pp. 385–404, 2014.

[135] Lachaux Thierry and Musculus Mark P B. “In-cylinder unburned hydrocarbon visualization during low-temperature compression-ignition engine combustion using formaldehyde PLIF”. *Proceedings of the Combustion Institute*, Vol. 31 II, pp. 2921–2929, 2007.

[136] Jarrahbashi Dorrin, Kim Sayop, Knox Benjamin W and Genzale Caroline L. “Computational analysis of end-of-injection transients and combustion recession”. *International Journal of Engine Research*, pág. 146808741770128, 2017.

[137] Bower Glenn R and Foster David E. “The Effect of Split Injection on Fuel Distribution in an Engine-Fed Combustion Chamber”. *Papers\SAE Papers\Diesel 1990-2002*, n^o 412, 1993.

[138] Tow T. C., Pierpont D. A. and Reitz Rolf D. “Reducing Particulate and NOx Emissions by Using Multiple Injections in a Heavy Duty D.I. Diesel Engine”. In *SAE Technical Paper*. SAE International, 03 1994.

[139] Han Z, Uludogan a, G. Hampson and Reitz R. “Mechanism of Soot and NOx Emission Reduction Using Multiple-injection in a Diesel Engine”. *SAE Technical Paper series*, Vol. 960633 n^o 412, 1996.

[140] O’Connor Jacqueline and Musculus Mark P. B. “Post Injections for Soot Reduction in Diesel Engines: A Review of Current Understanding”. *SAE Int. J. Engines*, Vol. 6 n^o 1, pp. 400–421, 2013.

[141] O’Connor Jacqueline and Musculus Mark. “Optical Investigation of the Reduction of Unburned Hydrocarbons Using Close-Coupled Post Injections at LTC Conditions in a Heavy-Duty Diesel Engine”. *SAE Int. J. Engines*, Vol. 6 n^o 1, pp. 379–399, 2013.

[142] O’Connor Jacqueline, Musculus Mark P B and Pickett Lyle M. “Effect of post injections on mixture preparation and unburned hydrocarbon emissions in a heavy-duty diesel engine”. *Combustion and Flame*, Vol. 170, pp. 111–123, 2016.

[143] Bruneaux Gilles and Maligne David. “Study of the Mixing and Combustion Processes of Consecutive Short Double Diesel Injections”. *SAE International Journal of Engines*, Vol. 2 n^o 1, pp. 1151, 2009.

[144] Pickett Lyle M, Kook Sanghoon and Williams Timothy C. “Transient Liquid Penetration of Early-Injection Diesel Sprays”. *SAE Int. J. Engines*, Vol. 2 n^o 1, pp. 785–804, 2009.

[145] Bolla Michele, Chishty Muhammad Aqib, Hawkes Evatt R and Kook Sanghoon. "Modeling combustion under engine combustion network Spray A conditions with multiple injections using the transported probability density function method". *International Journal of Engine Research*, Vol. 18 n^o 1-2, pp. 6–14, 2017.

[146] Blomberg Christopher Kim, Zeugin Lucas, Pandurangi Sushant S., Bolla Michele, Boulouchos Konstantinos and Wright Yuri M. "Modeling Split Injections of ECN Spray A Using a Conditional Moment Closure Combustion Model with RANS and LES". *SAE International Journal of Engines*, Vol. 9 n^o 4, pp. 2107–2119, 2016.

[147] Cung Khanh, Moiz Abdul, Johnson Jaclyn, Lee Seong Young, Kweon Chol Bum and Montanaro Alessandro. "Spray-combustion interaction mechanism of multiple-injection under diesel engine conditions". *Proceedings of the Combustion Institute*, Vol. 35 n^o 3, pp. 3061–3068, 2014.

[148] Moiz Ahmed Abdul, Cung Khanh D. and Lee Seong-Young. "Simultaneous Schlieren-PLIF Studies for Ignition and Soot Luminosity Visualization With Close-Coupled High-Pressure Double Injections of n-Dodecane". *Journal of Energy Resources Technology*, Vol. 139 n^o 1, pp. 012207, 2017.

[149] Maes Noud, Bakker P.C., Dam Nico and Somers Bart. "Transient Flame Development in a Constant-Volume Vessel Using a Split-Scheme Injection Strategy". *SAE Int. J. Fuels Lubr.*, Vol. 10, 03 2017.

[150] Moiz Ahmed Abdul, Ameen Muhsin M., Lee Seong Young and Som Sibendu. "Study of soot production for double injections of n-dodecane in CI engine-like conditions". *Combustion and Flame*, Vol. 173, pp. 123–131, 2016.

Chapter 3

Tools and Methodology

Contents

3.1 Introduction

The aim of this chapter is to give an detailed description of the experimental and theoretical tools, presenting some important parameters of the hardware, the principles of optical techniques and the processing methodologies employed to obtain the final data.

This chapter begins with a description of the experimental facilities including a high-pressure high-temperature constant pressure vessel and a two-stroke direct injection optical engine. After that, the next section details the fundamental knowledge of these optical diagnostics, followed the image processing methods employed. Furthermore, the Diffuse Back-Illumination (DBI) extinction imaging technique for soot quantification is described in detail. It is validated by Laser extinction method (LEM) and compared with two-color method. It needs to be pointed out, the DBI technique is the first time developed and applied in CMT. In addition, a new methodology by combing the soot extinction and radiation is presented. At last, an 1D spray model for validating the experimental data and backing up the analysis is elaborated.

3.2 Experimental facilities

3.2.1 High-pressure High-temperature vessel

The study of effects of combustion on spray dynamics of single injection under quiescent conditions were performed in a high pressure and high temperature test chamber, in which the thermodynamic conditions similar to a diesel engine at the instant of injection can be obtained. These experiments were conducted by previous PhD students Bardi [1] and Vera-Tudela [2]. On the other hand, the instantaneous soot production under quiescent conditions was measured in another similar vessel. The structure, heating system, control system are pretty similar. The only important difference is that it has two bigger optical accesses with 181 *mm* of diameter. Hence, only the smaller one is taken for example to be described here in detail. The vessel is classified as a constant-pressure flow (CPF) facility, as the conditions are reached by a continuous flow of high-pressure high temperature gas through the chamber (Figure 3.1(a)). The vessel is equipped with three large optical accesses (128 *mm* of diameter) arranged in an orthogonal manner so that there is a full vision of the injection event (Figure 3.1(b)).

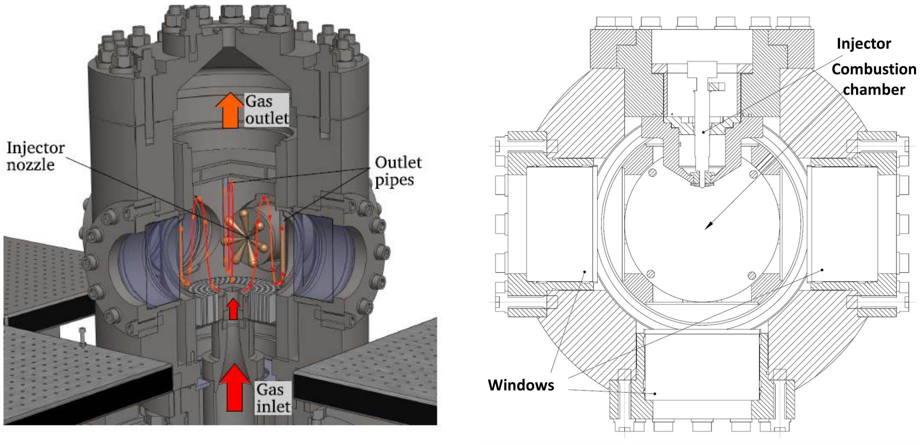

(a) Side section view

(b) Top section view

Figure 3.1. *High-pressure high-temperature vessel.*

The limits of the vessel are 15 MPa of air pressure and 1000 K of air temperature, and it is possible to obtain nearly quiescent and steady thermodynamic conditions in the test chamber [1, 3, 4]. A summary of the detailed parameters of the vessel is shown in Table 3.1. This equipment is also comprised of an injection system that allows to change the fuel injection pressure and duration of injection. Furthermore, the facility is prepared for single-hole and multi-hole injector; however, for the tests presented here a single-hole nozzle has been used, injecting the fuel horizontally (Figure 3.1(b))

The pressurized gas is supplied to the vessel by two volumetric compressors working in parallel, providing a continuous feed of 70 Nm^3/h. Additionally, in order to allow temporary variations of the gas flow without acting on the compressors, two high pressure tanks of a total volume of 0.1 m^3 have been placed in-between the test vessel and the compressors. Due to the configuration of the layout, it is possible to work in open or closed circuits in order to simulate EGR and testing under inert conditions. On one hand, under open circuit operation, the intake gas to the compressors is ambient air, which has an oxygen concentration of 21%, and the outlet gases of the vessel are discharged to the atmosphere. On the other hand, under closed circuit operation, the intake to the compressors is a mixture of atmospheric air and pure nitrogen, allowing the oxygen concentration to be varied from 0% to 21%. In this case, the outlet gases from the vessel are recirculated instead of being discharged to the atmosphere, and the gas oxygen content is measured

Table 3.1. *Characteristics of the High-pressure high-temperature vessel.*

Facility type	CPF
Chamber diameter	200 mm
Chamber height	250 mm
Window diameter	128 mm
Max. pressure	150 MPa
Max. temperature	1000 K
Max. density (@ 900 K)	53 kg/m^3
Main heater power	30 kW
Gas velocity	< 0.3 m/s

with a lambda sensor. The content of oxygen in the combustion chamber is then adjusted by either adding air or nitrogen by a reintegration system. It is important to note that even though the injected fuel and combustion products remain in the system when working under closed circuit operation, they do not affect the subsequent tests for two reasons. The first one is that there is an air-liquid separator that removes the injected fuel from the circulating air mixture. The second is that the combustion products are of no significance on the composition and density of the chamber air, as those few milligrams of burnt gases are negligible when compared to the kilograms of pressurised air that are being circulated for all the tests.

In order to heat the owing air, two electrical heaters of 15 kW each are placed upstream the chamber, allowing a maximum outlet temperature of 1173 K. Also, a secondary heater of 2.5 kW is placed at the bottom of the chamber to help maintain the temperature. Additionally, a 3 kW heating liner is placed in the periphery of the chamber to minimize the heat losses from the in-chamber air to the outside of the vessel. Finally, the conditions inside the combustion chamber are controlled by a closed loop PID system that adjusts the pressure and the power of the heaters to obtained the temperature required for the experiments. A more detailed description of the gas circuit, heating system, test chamber, temperature control and nozzle temperature control of the facility can be found in [1].

3.2.2 Two-stroke optical engine

An optically accessible single cylinder two-stroke engine with three-liter displacement, 15.6:1 compression ratio and low rotational speed of 500 *rpm* has been used for these experiments, which is described in detail in [5]. A cylindrical combustion chamber is designed with a diameter of 45 *mm*. This chamber has one upper access for the fuel injector, and four lateral orthogonal accesses. One of them is used for the pressure transducer whereas the other three are equipped with optical windows with geometrical dimensions of 88 x 37 *mm* and 28 *mm* thick. The Cross-sectional view of cylinder head is shown in Figure 3.2. During engine operation, the block temperature is controlled by an external heating-cooling system. The intake air temperature and pressure are controlled by electrical resistors and an air compressor respectively.

According to the needs of this study, the facility can be operated in two different working modes to achieve both inert and reacting operating conditions:

- **Reacting conditions:** A roots compressor takes atmospheric air and sends it into the cylinder, where the thermodynamic cycle takes place. The air goes through two conditioning units, which heat it and remove any liquid or particle before reaching the intake port. After combustion, the exhaust gases are expelled to the atmosphere again.
- **Inert conditions:** The working fluid is nitrogen, to avoid any combustion reaction while keeping similar physical properties as the atmospheric air. For this purpose, the facility works under a closed loop scheme. When the exhaust gases (nitrogen + fuel) leave the cylinder, they flow through an inter cooler and a cyclonic filter, to remove rests of fuel and oil out of the recirculated gas stream. This ensures proper operating conditions for a roots compressor, which is used to assist the air management of the engine. Then, nitrogen is impulsed into the cylinder, through the same conditioning units as the ones used for the reacting configuration. The circuit is refilled through an electronic valve to achieve the desired intake pressure and compensate blow-by and leakages.

An injection takes place every 30 cycles, which guarantees that there is no remaining residual gas from previous combustion cycles and the ambient conditions in the chamber are kept constant between consecutive repetitions.

Thanks to the high-speed pressure transducers equipped on the combustion chamber, the apparent heat release rate (AHRR) is able to be derived from

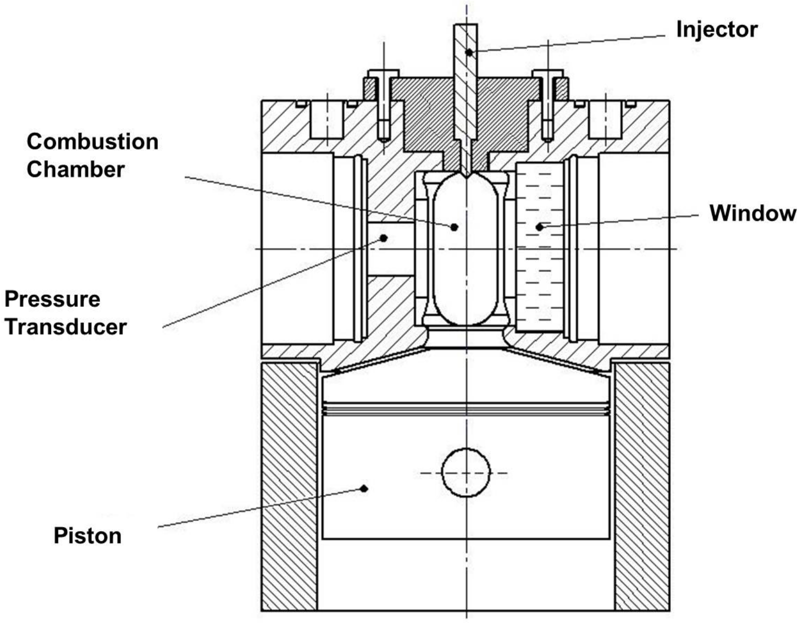

Figure 3.2. *Cross-section of the two-stroke engine with optical head.*

measured cylinder pressure trace according to the first law of thermodynamics [6].

$$\frac{dQ}{dt} = P\frac{dv}{dt} + mc_v\frac{dT}{dt} \tag{3.1}$$

where P is the cylinder pressure, v is the volume of combustion chamber, m is the fuel mass, T is the cylinder temperature, c_v is the specific heat at constant volume.

3.3 Optical techniques applied for spray combustion analysis

For this study, two different high-speed imaging techniques, Schlieren and UV-Light Absorption, were applied to quantify vapor penetration for non-reacting spray. On the other hand, for the experiments under reacting conditions, Schlieren was used again to quantify the spray penetration, spray boundary, ignition delay and LOL. Besides Schlieren, OH^* radical chemiluminescence was also applied to obtain the LOL.

3.3.1 High-speed Schlieren imaging

Schlieren imaging is a valuable technique for identifying density gradients, from which the spray area can be derived because of the density difference between vaporized fuel and ambient gases. The technique is based on the deviation suffered by a light beam, due to its refraction when crossing from one media to another, with different refractive index. This effect is known as beam steering. If a continuous non-homogeneous media is considered, the variation of the refractive index is represented by its gradient. Thus, it can be demonstrated that the deviation suffered by a light beam when traversing this media is proportional to the refractive index gradients within it [7]. Thanks to this phenomenon, the diesel spray has usually been able to be distinguished easily against the background light.

The images captured in the tests were processed following an intensity-based criterion and applying a dynamic background subtraction: the methodology, described in details in the work by Benajes et al. [8], proved to be a robust methodology and provides binarized images of the spray region. After that, an average spray boundary for a given time step, which is obtained by calculation of spray probability maps from the corresponding sample of binarized images (Figure 3.3). Such maps indicate the probability of finding a spray at one position. The average spray boundary is defined as the border of the region where the probability is equal to or higher than 50%. Moreover,by assuming an axysimmetric spray, the contour was summarized in only two variables: axial position, and spray width. Besides spray boundary, ignition delay was also obtained from Schlieren images based on the analysis on the total intensity increment within the spray between each two following images. The detail of this processing methodology can be found in [8], where the corresponding time of the peak of the total intensity increment was defined as ignition delay and it was also validated by broadband chemiluminescence technique.

In addition, the temporal averaged flame lift-off lengths was also able to be obtained from Schlieren images based on the analysis on the spray radial increment between each two positions away from the nozzle tip with 5 pixel interval. The corresponding position where the peak of the radial increment takes place was defined as LOL. Schlieren technique has been validated as a good tool for detecting LOL with OH^* chemiluminescence when the ambient temperature is higher than 800 K and at a density 22.8 kg/m^3 [9]. One example of the LOL from schlieren imaging is shown in Figure 3.4.

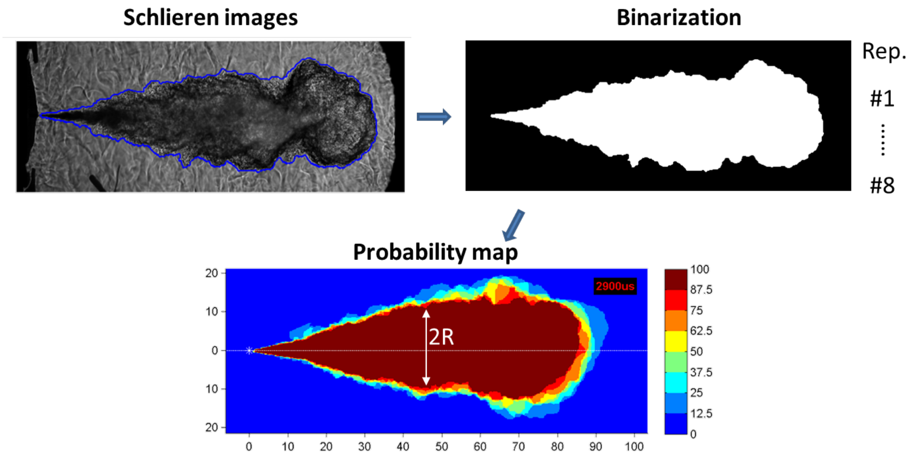

Figure 3.3. *The image processing workflow for Schlieren-derived spray width.*

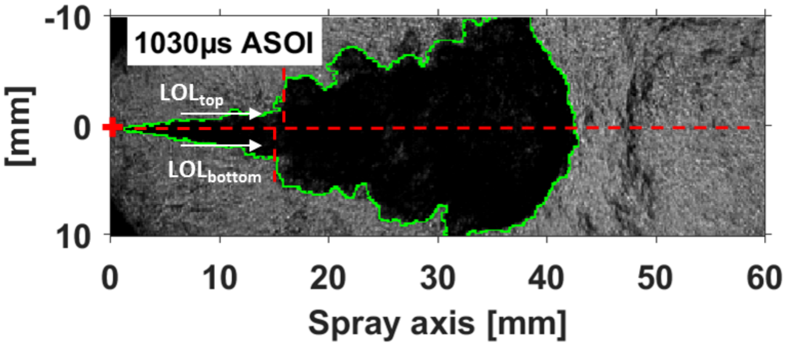

Figure 3.4. *Schematic of LOL from Schlieren imaging.*

3.3.2 Ultraviolet light absorption (UV-LA)

Under non-quiescent conditions, Schlieren imaging was not able to identify spray tip very well because of the interference from airflow. As a consequence, the vapor penetration of non-reacting spray in the two-stroke engine was also measured by a developed UV-LA technique which is based on the ultraviolet (UV) light attenuation by the vapor phase [10, 11]. Because of this absorption for UV light, the intensity within the spray is much lower than that of the background gas area. As a consequence, the spray boundary was identified easily. The vapor optical thickness, KL, can be obtained according to the well-known Beer-Lambert law.

$$\log(\frac{I_0}{I_t}) = KL \tag{3.2}$$

where I_0 is the incident radiation, as obtained from images before start of injection, and I_t is the intensity of transmitted light. K is the dimensional extinction coefficient and L is the path length of the light beam through the vapor phase. A fixed threshold of 20% the maximum KL value from KL images at each time position was applied here to distinguish the spray vapor phase and the background air. One example of the processed UV-LA images is shown in Figure 3.5.

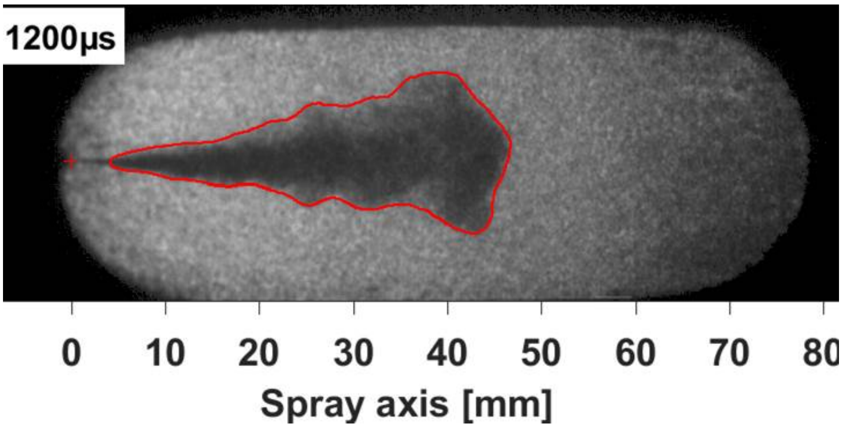

Figure 3.5. *Example of processed UV-LA images.*

3.3.3 OH^* Chemiluminescence

The energetic reactions and high temperatures that occur during stoichiometric combustion of typical hydrocarbon fuels form excited state species that include excited state OH (OH^*) [12]. Once formed, OH^* returns rapidly to its ground state, a portion through chemilumines-cent emission and a portion through collisional quenching. The OH^* chemiluminescence occurs at stoichiometric conditions and high temperatures, therefore being a good marker of the lift-off length [13]. Additionally, the wavelength band of 310 nm that corresponds to the chemiluminescence of the OH^* radical is the strongest one and therefore best for determining the lift-off length [12, 13]. Although soot radiation could also be contributing to the recorded signal in the images, previous studies in the literature also indicate that there should exist a spatial separation in both contributions. Therefore, while the downstream radiation will most probably be dominated by soot, the most upstream one is assumed to be essentially related to OH^* chemiluminescence [2, 13].

An intensified CCD camera equipped with a 310 ± 5 nm interferometric filter was used with a constant intensifier gating time widow to record the signal of OH^* chemiluminescence. In this way the steady part of the combustion process was averaged along the injection event and the shot-to-shot deviation was reduced. After filtering the image, two intensity profiles are obtained calculating the maximum intensity for each axial position in the upper and lower half of the image (Figure 3.6). The lift-off length was determined by finding the distances between the injector tip and the first axial locations above and below the spray centerline with intensity greater than 50% of the intensity peak. The average of these two axial distances is defined as the lift-off length. The detailed information about the processing methodology can be found from reference [13, 14].

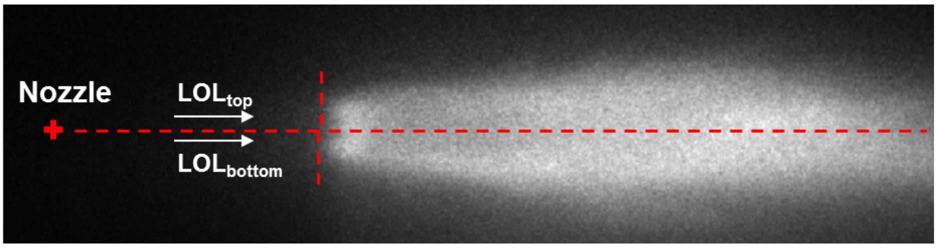

Figure 3.6. *Definition of Lift-off length.*

3.4 Diffuse Back-Illumination (DBI) extinction imaging technique for flame soot quantification

As described in Section 2.3.4, soot distribution diagnostic techniques can be divided into two groups based on soot thermal radiation and light extinction, respectively. As two typical techniques in this two groups, both Two-color method (based on radiation) and Diffused background-illumination extinction imaging (based on extinction) can obtain high-speed line-of-sight 2D spatial evolution of the soot. The objective of this section is to compare DBI and 2C performance when measuring soot amount both on temporal and spatial evolution under different operating conditions and find the advantages and limitations of each of them. Furthermore, in order to obtain a more reliable soot volume fraction and temperature by considering the soot self-absorption problems, a new diagnostic by combing the soot extinction and radiation is proposed in the end, which was further applied for soot analysis in later chapter.

3.4.1 Fundamentals

Two-color method

The Two-color method (2C) is an optical thermometry technique that makes use of the presence of soot within a flame. It is particularly useful for diesel combustion studies due to the fact that soot incandescence dominates the flame radiation emission during most of the heat release period [15]. In this sense, flame images recorded by means of conventional visualization techniques in the visible spectrum are basically soot radiation images. The measured soot temperature should provide a very close estimate of the true flame (gas phase) temperature, since differences between gas and soot temperature are expected to be less than 1 K [16, 17].

The starting point of the Two-color method is the assumption that radiation from a sooting flame with uniform spatial temperature and soot distributions depends on the wavelength, the temperature and the amount of soot within the flame. This statement can be translated into the following mathematical equation:

$$I_{soot} = \varepsilon \cdot I_b \tag{3.3}$$

where the black-body radiance I_b can be written from Planck's law:

$$I_b(\lambda, T) = \frac{1}{\lambda^5} \cdot \frac{c_1}{[exp(\frac{c_2}{\lambda T}) - 1]} \tag{3.4}$$

and the emissivity ε can be obtained using the empirical correlation developed by Hottel and Broughton

$$\varepsilon(KL, \lambda) = 1 - exp(\frac{-KL}{\lambda^{\alpha}}) \tag{3.5}$$

where c_1,c_2 and α are constants the KL is the soot optical thickness. $c_1 = 1.1910439 \cdot 10^{-16}\ WM^2sr^{-1}$, $c_2 = 1.4388 \cdot 10^{-2}\ mK$. Zhao et al. [18] reported that α values are less dependent to the wavelength in the visible range than in the infrared. In this regard, 550 and 650 nm were chosen for this work, so that $\alpha = 1.39$ for most of the fuels [19]. In order to transform grey levels into radiance values, calibration curves have been obtained by means of a tungsten-ribbon calibration lamp (Osram Wi17G), which was located at the same distance from the Two-Color cameras as the distance between the cameras and flame in the combustion chamber.

Diffused backgound-illumination extinction imaging

In this study, besides Two-color method, soot concentration in flames were also measured with diffused backgound-illumination extinction imaging(DBI). As an extinction-based diagnostic, the soot volume fraction is related to the amount of light that has been absorbed or scattered by the soot cloud [20]. The two-dimensional extinction measurements in this work were converted to optical thickness, KL, using the well-known Beer-Lambert law as presented

$$\log(\frac{I_0}{I_t}) = KL \tag{3.6}$$

where I_0 is the illuminated background intensity, as obtained from images before start of injection, and I_t is the transmitted intensity after passing through soot cloud. K is the dimensional extinction coefficient and L is the path length through the soot cloud.

According to the widely known small particle Mie theory [21], KL is an integral value of soot volume fraction (f_v) along the line-of-sight of the extinction pass. The relationship between KL and f_v is shown as follows:

$$KL = \int \frac{k_e}{\lambda} f_v dl \tag{3.7}$$

and

$$k_e = (1 + \alpha_{sa}) \cdot 6\pi \cdot E(m) \tag{3.8}$$

where λ is the wavelength of the incident illumination, k_e is the dimensionless extinction coefficient, α_{sa} is the scattering-to-absorption ratio, m is the refractive index of soot. k_e can be obtained from the Rayleigh-Debye-Gans (RDG) theory as $k_e = 7.61$. The details of the RDG theory and all the parameters used for calculating the k_e are referenced from [20, 22]. As a consequence, the sum of soot mass (m_{soot}) along the line-of-sight at each pixel was derived from Eq.3.7 using an assumed density of 1.8 g/cm^3 for soot (ρ_{soot}) [23].

$$m_{soot} = \frac{\rho_{soot} \cdot KL \cdot \lambda}{k_e} \cdot pixel\ area \tag{3.9}$$

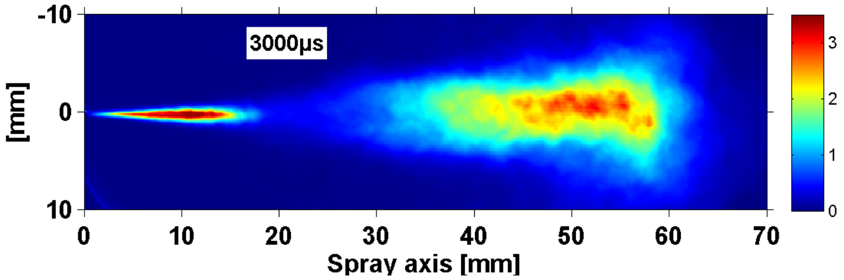

Figure 3.7. *Example of KL map processed from DBI.*

Figure 3.7 shows one example of the soot optical extinction (KL) distribution calculated from Eq.3.6. The spray enters the visualization window from the left side and penetrates from left to the right. Results show two extinction areas. The highest KL values close to the nozzle are due to liquid spray scattering. As a consequence, the liquid length was also quantified from DBI images following the approach recommended from Engine Combustion Network (ECN). The only difference is that the temporal liquid length evolution was obtained here from images averaged from all repetitions at each time position rather than just one time-averaged value. The detail of this processing methodology can be found from [24]. On the other hand, as for the soot analysis, in order to remove the liquid part and minimize the beam steering interference on soot quantification caused by ambient gas and spray vapor phase , the KL maps from the averaged images of Two-color method are used to mark the soot area and set it as the mask on DBI images.

3.4.2 Test matrix

All the measurements in this section were conducted in the optically accessible single cylinder two-stroke engine described in detail in section 3.2.2. The fuel used in these tests is a two component blend of 30% Decane and 70% Hexadecane (percentages in mass). Considering that the object of this paper is to compare the two different optical diagnostic techniques, the test matrix includes 3 operating conditions that have been selected from a wider previous study [25] and have been denoted as High Soot (HS), Middle Soot (MS) and Low Soot (LS) conditions. Injection pressure and chamber temperature at the top dead center (TDC) have been modified while keeping constant in-cylinder pressure at TDC and oxygen concentration. It is well known from previous research [20, 21, 26] that soot formation will decrease with higher injection pressure and lower ambient temperature. The energizing time was set as 2 *ms*, and the actual injection duration was approximately $4ms$. For each operating condition, 20 injections have been recorded to reduce measurement uncertainties due to engine operating variability.

Table 3.2. *Experimental conditions.*

Operating conditions	P_{inj} $[bar]$	P_{TDC} $[bar]$	T_{TDC} $[K]$	Oxygen [%]
HS	500	53	870	21
MS	1500	53	870	21
LS	1500	53	782	21

3.4.3 Optical setup

The optical system has been designed so that simultaneous high speed 2C and DBI measurements can be realized. The arrangement of the optical setup is shown in Figure 3.8.

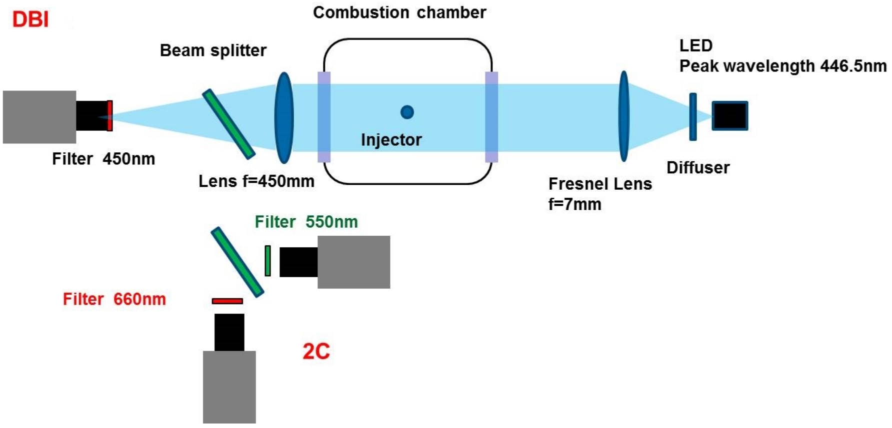

Figure 3.8. *Schematic of the optical setup.*

- **2C method:** The 2C was realized using two high-speed CMOS cameras and two bandpass filters (centered at 550 *nm* and 660 *nm*, both with 10 *nm* FWHM). After passing through a collecting spherical lens (f = 450 *mm*), the light emitted by the soot cloud crossed the first beam splitter, which transmits 50% of the intensity to the LEI camera, while the other 50% is reflected into the 2C system. Then, another beam splitter (50%/50%) is applied to distribute the remaining soot radiation equally into the two CMOS cameras. In order to make a comparison between DBI and 2C results at the same time during the same injection, all three cameras need to be synchronized. To ensure a better synchronization, all cameras employed here are identical (Photron SA-5), running with the same frequency at 20 *kHz*. One of the 2C cameras was set as the master camera while the other one and the DBI camera were set as slave cameras. In order to transform grey levels into radiance values, calibration curves have been obtained by means of a tungsten-ribbon calibration lamp (Osram Wi17G), which was located at the same distance from the 2C cameras as the distance between the cameras and flame in the combustion chamber.

- **DBI:** The DBI optical setup can be divided in two different sections, which are referred to as the illumination and collection sides. On the illumination side, a high-output blue LED with a Peak wavelength 450 *nm* was applied here as the light source. A LED pulse duration of 0.9 μs was used here to “freez” the soot fields within high velocity fuel jet. The light passed through a diffuser to create a diffused Lambertian intensity profiles. Behind the diffuser, a Fresnel lens (f = 7 *mm*) was mounted to magnify the visualization area so that it can cover the whole optical access window.

  On the collection side, the transmitted light of the LED and the thermal radiation from the combustion are collected by means of a spherical lens (f = 450 *mm*) to make sure the size of the images focused on the lens of the camera is smaller than the lens. What’s more, it also can reduce the effects of beam steering. After going through the beam splitter as mentioned above, the light was finally collected by a high-speed CMOS camera (Photron SA-5, recording at 20 *khz*) equipped with a bandpass filter (450 *nm*, 10 FWHM). The exposure time of the camera was set to 6.96 μs with 416 ×896 pixels image resolution and the *pixel/mm* ratio is 10.

  The light intensity detected by the camera includes two parts: the transmitted LED light intensity and the flame intensity. Due to the use of an interference filter, the crosstalk of flame radiation into the DBI camera is minimized in the visible wavelength range. However, the flashing frequency of the LED was set as half of the camera frame rate to capture an image between every two successive LED pulses, so that flame luminosity can be quantified and this information used to get the correct transmitted LED light. The schematic of LED synchronization is shown in Figure 3.9.

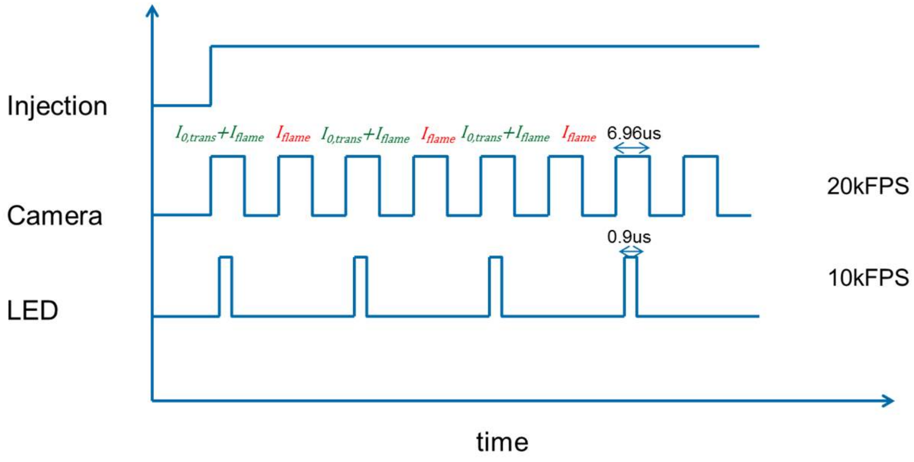

Figure 3.9. *Schematic of LED synchronization.*

According to the Beer-Lambert law, the soot optical thickness (KL) was obtained after the correction.

$$\log(\frac{I_0}{I - I_f}) = KL \tag{3.10}$$

I is the sum of the transmitted LED intensity and the flame luminosity as recorded by the DBI camera for a LED-on image, I_f is the intensity of the flame acquired for a LED-off image, K is the dimensional extinction coefficient and L is the path length of the light beam through the soot cloud. I_0 is the incident radiation, as obtained from images before start of injection.

Figure 3.10 shows one example of the soot optical extinction (KL) distribution and the corresponding values on the spray axis calculated from Eq.3.10. Where, I_f and I_0 are obtained from an ensemble average of 20 individual injections, at 3000 μs after start of energizing (ASOE) under HS operating condition. As shown at the bottom image of Figure 3.10, the spray enters the visualization window from the left side and penetrates from left to the right. Results show two extinction areas. The highest KL values close to the nozzle are due to liquid spray extinction, which is not the focus of the present investigation. The highest KL values close to the nozzle are due to liquid spray extinction, which is not the focus of the present investigation. Experimental liquid length has been measured for such condition (22.2 mm, according to additional tests in [27]). This means that no fuel exists downstream of this axial location, and therefore any attenuation should be due to the presence of soot. As mentioned in the above section, one injection takes place out of 30 cycles, which keeps the access window from fouling and make KL value equal to 0 before the start of injection. The red line in the top image of Figure 3.10 represents a theoretically maximum KL value (KL_{sat}) which was obtained from Eq.3.11, where I_{min} represents the minimum transmitted intensity. When KL value reaches the saturated value, it means that there is no transmitted light. Considering the camera shading uncertainty, I_{min} was set to 30 counts here, and the theoretically maximum KL value was calculated as:

$$\log(\frac{I_0}{I_{min}}) = KL_{sat} \tag{3.11}$$

Due to the non-uniformity in the diffuser, the saturated KL is not constant, but looking into the time evolution of the KL under all three conditions, it was found that all measured KL values are far below KL_{sat}.

In these tests, beam steering exists because of the imperfect Lambertian light source, which determines the lower KL detection limit. The incident intensity from LED, transmitted intensity and soot optical thickness along the spray axis at 6000 μs ASOE is shown in Figure 3.11, long after end of injection. No soot is expected at this time, and the light will only find hot gases. A difference can be found between incident and transmitted intensity which can be considered as a consequence of beam steering and the KL value is on average lower than 0.05.

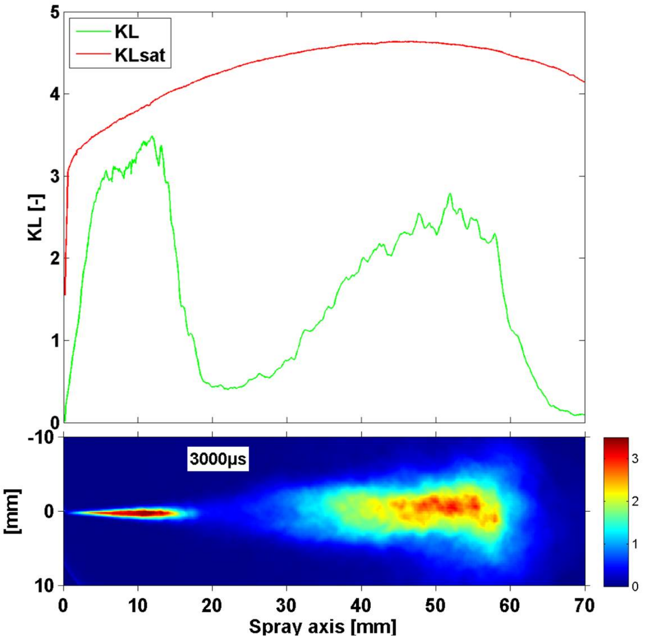

Figure 3.10. *Soot optical extinction (KL) of 2D distribution (top) and at spray axis (bottom) under HS operating condition.*

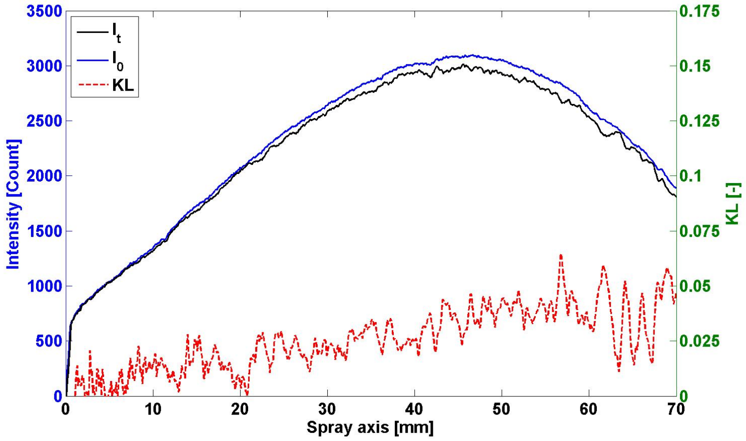

Figure 3.11. *Incident intensity (blue line), transmitted intensity (black line) and optical thickness KL (red dashed line) along the spray axis at 6000 μs ASOE under HS condition.*

3.4.4 Validation of DBI with LEM

Previous work by the authors has reported experimental data from LEM tests at the same operating conditions in the same test rig with the same fuel as here. The details of LEM setup can be found in [25]. Because of the same test conditions, the soot volume fraction (f_v) and the path length (L) detected from the two optical techniques are considered the same. According to the Mie theory for light interaction with small particles:

$$f_v = \frac{K_{DBI} \cdot \lambda_{DBI}}{k_{eDBI}} = \frac{K_{LEM} \cdot \lambda_{LEM}}{k_{eLEM}} \tag{3.12}$$

where λ is the wavelength of the incident illumination, k_e is the dimensionless extinction coefficient, which can be obtained from the Rayleigh-Debye-Gans (RDG) theory as $k_{eDBI} = 7.61$ and $k_{eLEM} = 7.46$. The details of the RDG theory and all the parameters used for calculating the k_e are referenced from [20, 22]. Hence, considering that the wavelength used for DBI and LEM are 450 nm and 514.5 nm and the Eq.3.12, the following expression can be derived to normalized the KL derived from different wavelengths:

$$KL_{DBI} = \frac{k_{eDBI} \cdot \lambda_{LEM}}{k_{eLEM} \cdot \lambda_{DBI}} \cdot KL_{LEM} = 1.167 \cdot KL_{LEM} \tag{3.13}$$

Figure 3.12 shows the comparison of the KL extinction between DBI and LEM of the three different operating conditions at the spray axis when the time is at 3000 μs ASOE, where $KL_{LEM\star}$ is converted according to Eq.3.13. It can be found that both techniques show a good sensitivity to the parametric variation and there is a good agreement between the two techniques at all tested conditions. The KL value of LEM is slightly higher than that of DBI, particularly at high soot area of HS condition, which may be caused by a couple of reasons: a) The spatial distribution of LEM measurements is limited, so only two locations can be compared. b) the two techniques were not applied simultaneously which may bring some measurement uncertainties due to injection-to-injection variability. c) RDG theory is based on some assumptions which could create a uncertainty on calculating the dimensionless extinction coefficient k_e.

3.4.5 Comparison between DBI and 2-color method

As for DBI technique, the extinction of light is caused both by scattering and absorption from particles. However, scattering has only limited impact on

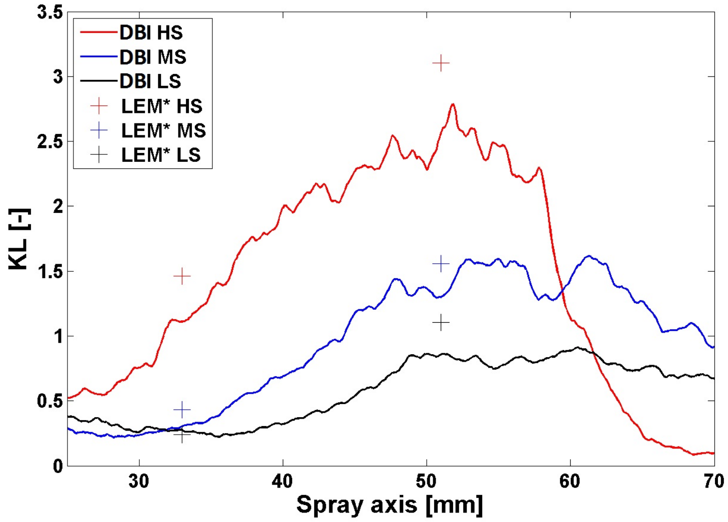

Figure 3.12. Comparison of KL between DBI and LEM techniques at 3000 μsASOE.

the total extinction (the scattering-to-absorption ratio is 0.083 obtained from RDG method), so it can be neglected in the comparison. Thus the absorptivity α_{λ_I} under wavelength λ_{DBI} can be obtained from the Eq.3.14 as follows:

$$\alpha_{\lambda_I} = 1 - \tau = 1 - exp(-KL_{DBI}) \tag{3.14}$$

where τ is transmissivity.

According to Kirchhoff law, under thermal equilibrium the absorptivity equals emissivity, and therefore:

$$1 - exp(-KL_{DBI}) = 1 - exp(\frac{-KL_{2C}}{\lambda_I^{\alpha}}) \tag{3.15}$$

Considering that the light wavelength used here is 450 nm and $\alpha = 1.39$, the relationship of the optical thickness between DBI and 2C can be expressed:

$$KL_{DBI} = 3.034 \cdot KL_{2C} \tag{3.16}$$

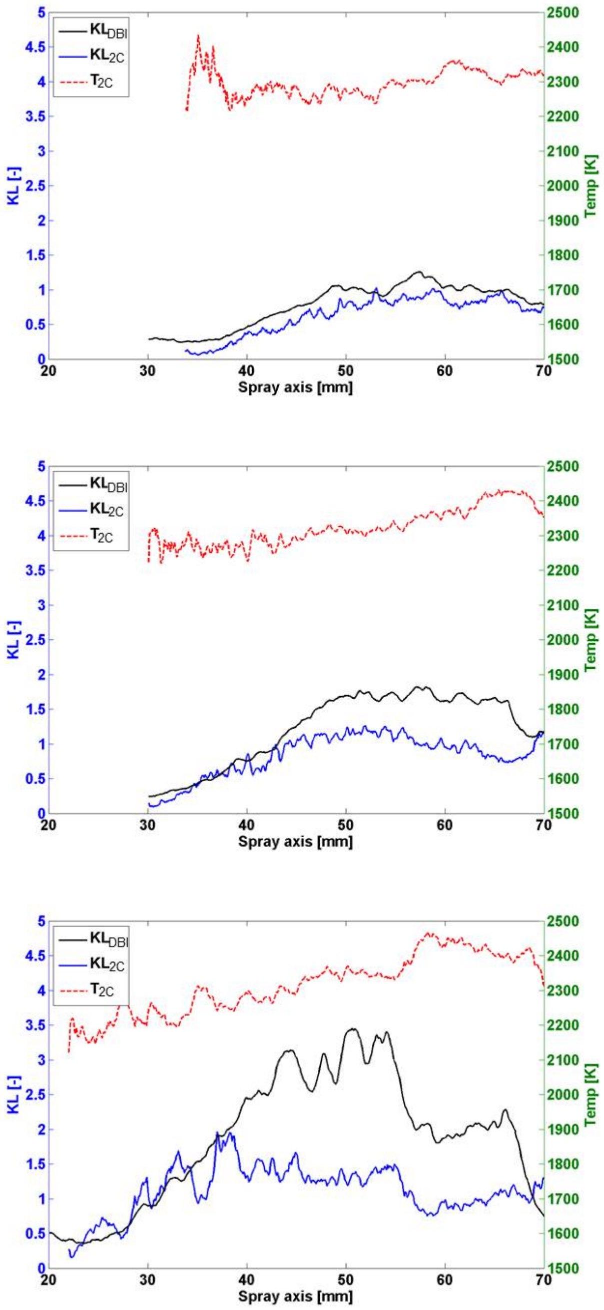

Figure 3.13. *KL value and soot temperature on the spray axis at 4000μs ASOE. Top LS, Medium MS, Bottom HS.*

Figure 3.13 shows the KL value as obtained from the two techniques and the soot temperature from 2C on the spray axis at 4000 μs ASOE for the three different soot conditions. Again, it shows that the DBI technique has more sensitivity with different soot amount than 2C. It can be seen that the KL from 2C has a good agreement with DBI at the upstream region and at the head of the soot cloud where the soot concentration is lower. However, there is a big difference in the middle high soot area. Differences in KL peak values increase with higher soot condition.

It is well-known that the 2C only renders true temperature and soot quantities for uniform temperature and soot spatial distributions. Temperature non-uniformities result in differences of both quantities to the real ones. And emission-absorption processes within the flame (i.e. signal trapping) may remove information from the soot layers farthest from the sensor, and therefore the 2C does not measure the true flame soot. In [17], authors made some simulations on the propagation of light showing that with higher soot within the flame, the 2C predicts lower soot than the real one. This agrees with the present experimental results. Consequently, to the authors' opinion, DBI can be considered the really quantitative technique, which should be considered as a reference. However, 2C results are based on radiation emission and absorption throughout the flame, which makes it a more qualitative technique.

3.4.6 A combined extinction-radiation soot diagnostic

Two-color method results have strong uncertainties because of the self-absorption issue while the extinction information is more reliable from DBI. As a consequence, a combined extinction-radiation soot diagnostic (CER) was applied in later chapter for soot analysis. This diagnostic was originally applied on a steady laminar axis-symmetric non-premixed ethylene flame by Legro et al and the detailed description of the methodology has been documented in [28]. Only some differences and main steps are briefly stated.

Both extinction and radiation measurements are based on integrated information along the line-of-sight optical path (projected data). This methodology divides quasi-steady soot cloud into two parts along spray axis and assumes each half part is an axis-symmetric configuration, as shown in Figure 3.14. Then, each part is processed following the same procedures.

According to Radiative transfer equation (RTE) [29], the transfer of radiative intensity $I(y, u)$ in a direction u at wavelength along an optical pathway y can be expressed:

$$\frac{dI(y,u)}{dy} = k(y)[I_b(y) - I(y,u)] \tag{3.17}$$

I_b is the blackbody radiation intensity which is a function of local temperature T, as shown in Eq.3.5.

At a given wavelength λ, the overall radiation intensity (I_r) obtained from projected line S (as shown in Figure 3.14) is a result of integrated positive contribution between radiation rate($k \cdot I_b$) and self-absorption. As known from Beer-Lambert law (Eq3.6), the transmitted blackbody radiation intensity at one position y after self-absorption along the remaining pathway can be expressed as follows:

$$I_r(y) = k(y)I_b(y)e^{-\int_y^{y_{max}} k_\lambda(y')dy'} \tag{3.18}$$

Thus, the overall projected radiation intensity, as shown in Figure 3.14(bottom), at each pixel position is obtained as follows:

$$I_r = \int_{y_{min}}^{y_{max}} I_r(y)dy \tag{3.19}$$

The local extinction coefficient field (k) can be calculated from the overall optical thickness (KL) obtained from extinction images, as shown in Figure 3.14 (top). The detailed methodology to this KL value can be found in section. However, considering different wavelength used for extinction and radiation tests, KL has to be converted according to:

$$m_{soot} = \rho_{soot} KL_1 \frac{\lambda_1}{k_{e1}} \cdot area = \rho_{soot} KL_2 \frac{\lambda_2}{k_{e2}} \cdot area \tag{3.20}$$

Thus,

$$KL_2 = KL_1 \cdot \frac{\lambda_1 \cdot k_{e2}}{\lambda_2 \cdot k_{e1}} \tag{3.21}$$

Finally, the local spectral emission rate($I_b K$) and temperature(T) can be reconstructed, as shown in 3.14 (bottom). In addition, the soot volume fraction(f_v) can be obtained from small particle Mie theory [21]:

$$f_v = \frac{k \cdot \lambda}{k_e} \tag{3.22}$$

where k_e is dimensionless extinction coefficient which can be derived from RDG theory, as presented in Eq3.8.

An onion-peeling method is employed here as the deconvolution method to calculate the local fields. Figure 3.14 shows the meshing of a half soot cloud cross section at a given distance away from injector tip for both extinction and radiation measurements. Detailed information about this onion-peeling method and mathematical formulation can be found from [28].

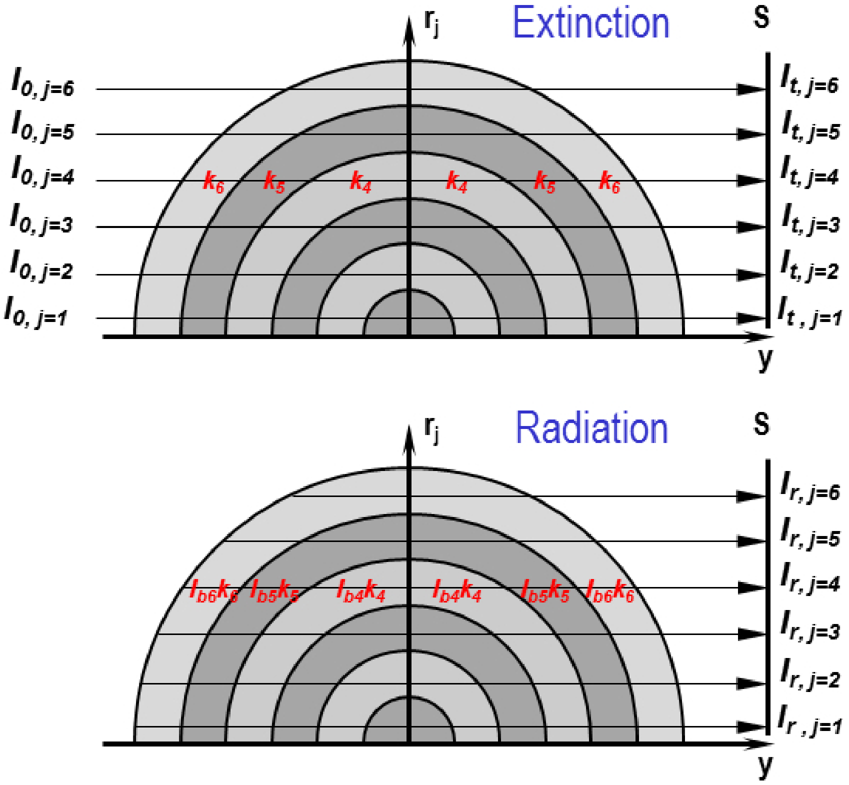

Figure 3.14. *Schematic of extinction and radiation optical path of a half soot cloud cross section at a given distance away from injector tip. I_0 represents the background illumination intensity , k represents local spectral absorption coefficient, It is the transmitted background intensity, I_b is the blackbody radiation intensity, I_r is the projected radiation intensity, S represents projected line provided by same pixel with soot cloud radius(N) from spray axis to soot boundary,(N is exampled as 6 here).*

3.5 1D spray model

A previously existing 1D spray model [30–32] has been used to substantiate the analysis of experimental results. The model solves 1D conservation equations of axial momentum and mixture fraction in terms of the axial distance to the nozzle. Radial evolution is considered by means of radial integral terms in the model by assuming a Gaussian self-similar profile. The model has been successfully used to predict inert spray penetration and liquid length [31, 32]. Compared to similar models in the literature, where local density is assumed to be radially homogeneous [33, 34] and is not always coupled into the momentum equations [34], the present approach feeds local density from state relationships into conservation equations from the radial distribution of mixture fraction. This makes it possible to include the effects of heat release by modifying the distribution of local density as a consequence of heat release, which will result in a modified velocity distribution. Under inert conditions, inputs for the model are

- Nozzle mass and momentum fluxes
- Fuel composition, temperature and density
- Ambient gas composition, pressure, temperature and density
- Spray cone angle

When dealing with reacting conditions, a simplified Burke-Schuman approach is followed, with a single-step reaction assumed for chemistry. Due to the absence of chemical kinetic effects, which would enable the prediction of ignition delay and lift-off length, two additional inputs for the model are

- Ignition delay t_{SOC} to identify when combustion will start. The 1D model assumes that a step transition from inert to reacting conditions occurs at ignition delay ($t = t_{SOC}$).
- On-axis mixture fraction at the lift-off length ($f_{cl,LOL}$), which will enable the model to spatially separate the location where the spray transitions from inert to reacting conditions. This is usually derived from the experimental lift-off length distance, and a model calculation under inert condition, and can be converted later to equivalence ratio at the lift-off length.

In addition to the previous parameters, information on the radial expansion process as a consequence of the transition from inert to reacting states has to be included. Initially, this effect was accounted for by means of a so-called "reacting spray cone angle" [32]. However, the analysis of more recent experimental information [35] has shown that the macroscopic geometry of a reacting spray is rather keeping a cone angle similar to the inert one, but with an increased width. Therefore, the present approach will consider that the radial expansion of the reacting spray is defined in terms of a single parameter, namely a predicted radius increase ΔR, which is calculated on the basis of the following additional hypotheses (Figure 3.15):

- Radial expansion process only happens at the time of start of combustion ($t = t_{SOC}$), which is an input parameter for the model. This is consistent with the simplified combustion description, which considers that the spray transitions from inert to fully reacting conditions at a given ignition delay timing, within a zero duration interval.
- At start of combustion the spray is only allowed to expand from the lift-off length location LOL till the spray tip S_{SOC}. Besides, expansion only happens radially, and is defined by a single ΔR value, which is constant along the reacting part of the spray.
- Neither the distribution of the mixture fraction on the axis nor the self-similar radial profile is modified in the inert-to-reacting transition process occurring at start of combustion. However, subsequent evolution of the reacting spray will obviously be affected by drop in density due to heat release.

Figure 3.15. *Schematic showing the simplified inert (left, $t = t_{SOC}-$) to reacting (right, $t = t_{SOC}+$) transition as described by the model.*

The equation to calculate the radial expansion states that the mixture undergoes a transition from inert to reacting conditions keeping a constant mass. This can be expressed in a formal way by the integral of the total mass between both $x = LOL$ and the spray tip at start of combustion $x = S_{SOC}$ as Eq. 3.23, which is evaluated at $t = t_{SOC}$.

$$\int_{LOL}^{S_{SOC}} \int_{0}^{R} \rho_{inert} \cdot 2\pi r \cdot dr \cdot dx = \int_{LOL}^{S_{SOC}} \int_{0}^{R+\Delta R} \rho_{react} \cdot 2\pi r \cdot dr \cdot dx \tag{3.23}$$

The same integral function appears on both sides of the equation, with the left hand side term being integrated under inert conditions and the right hand side one under reacting ones, just after start of combustion. Because the mixture state (mixture fraction distribution) is known just at start of combustion, one can apply the previous equation to solve ΔR and fully accounting for non-homogeneous density distribution.

A simplified analysis based upon the same equation is presented in Appendix 3.A, which shows that for a uniform density situation, ΔR depends explicitly on two parameters:

- Inert-to-reacting density drop $\rho_{inert}/\rho_{react}$
- Location with respect to the nozzle of the ready-to-burn mixture, i.e. the geometry and location of the reacting mass in terms of LOL and S_{SOC}. The further downstream the ready-to-burn mixture is located, the larger the induced radial expansion is, mainly due to a larger mass (radius) within each spray cross-section. The 1D model solves exactly the same problem, but within a non-uniform density distribution, meaning a space-dependent inert to reacting density drop, which is closer to reality. For a given spray case, such density drop depends on pure fuel and air thermal state and composition. This enables the consideration of cases where , for example, if ready-to-burn mixture is located further downstream, radial expansion will change not only because of the larger initial radius, but also because of the modification of the local density drop due to a non-uniform mixture.

3.A Appendix A: Simplified expansion for a uniform density spray

This section calculates the radial expansion induced by the inert-to-reacting transition for a spray flow under a simplified condition where the density throughout the spray is spatially uniform under both inert and also reacting conditions. Using Figure 3.15 as a reference, the model calculates the radial increase ΔR experience by a spray transiting in a zero time-step between the inert and reacting states at $t = t_{SOC}$. This means that density in Eq. 3.23 can be moved out of the integrals,

$$\rho_{inert} \int_{LOL}^{S_{SOC}} \int_{0}^{R} \cdot 2\pi r \cdot dr \cdot dx = \rho_{react} \int_{LOL}^{S_{SOC}} \int_{0}^{R+\Delta R} \cdot 2\pi r \cdot dr \cdot dx \tag{3.24}$$

And now the integrals just represent the volume that the ready-to-burn mixture occupies. Assuming that the inert spray is a cone, the volume integral reduces to:

$$\int_{LOL}^{S_{SOC}} \int_{0}^{R} \cdot 2\pi r \cdot dr \cdot dx = \frac{\pi}{3} \tan^2(\theta/2)[S^3 - LOL^3] \tag{3.25}$$

And applying a similar procedure for the reacting spray, with a wider cross-section downstream of LOL the following result is obtained:

$$\int_{LOL}^{S_{SOC}} \int_{0}^{R} \cdot 2\pi r \cdot dr \cdot dx = \frac{\pi}{3} \tan^2(\theta/2)[(S_{SOC} + \frac{\Delta R}{\tan(\frac{\theta}{2})})^3 - (LOL + \frac{\Delta R}{\tan(\frac{\theta}{2})})^3] \tag{3.26}$$

By substituting into the original equation, the following analytical result for the radial expansion can be obtained:

$$\Delta R = \tan(\frac{\theta}{2}) \cdot \frac{S_{SOC} + LOL}{2} \cdot [\sqrt{1 - (1 - \frac{\rho_{inert}}{\rho_{react}}) \cdot (\frac{2}{S_{SOC} + LOL}) \cdot \frac{2}{3} \cdot \frac{S_{SOC}^3 - LOL^3}{S_{SOC}^2 - LOL^2}} - 1] \tag{3.27}$$

The previous equation summarizes the main effects that govern the radial expansion:

- The density drop, as defined by $\frac{\rho_{inert}}{\rho_{react}}$

- The reacting volume geometry, as defined by the part of the cone from $x = LOL$ to $x = S_{SOC}$. This geometry appears in the previous equation in terms of two terms,
  - $\tan(\frac{\theta}{2}) \cdot \frac{S_{SOC}+LOL}{2}$ corresponds to a radius at an average distance from the $x = LOL$ to $x = S_{SOC}$.
  - The term $\frac{4}{3}\frac{S_{SOC}^3+LOL^3}{(S_{SOC}^2-LOL^2)(S_{SOC}+LOL)}$ which takes into account that the volume has a certain width in the axial direction. That means, the term tends to unity if $S_{SOC} - LOL$ tends to zero, and increases with the distance between LOL and S_{SOC}.

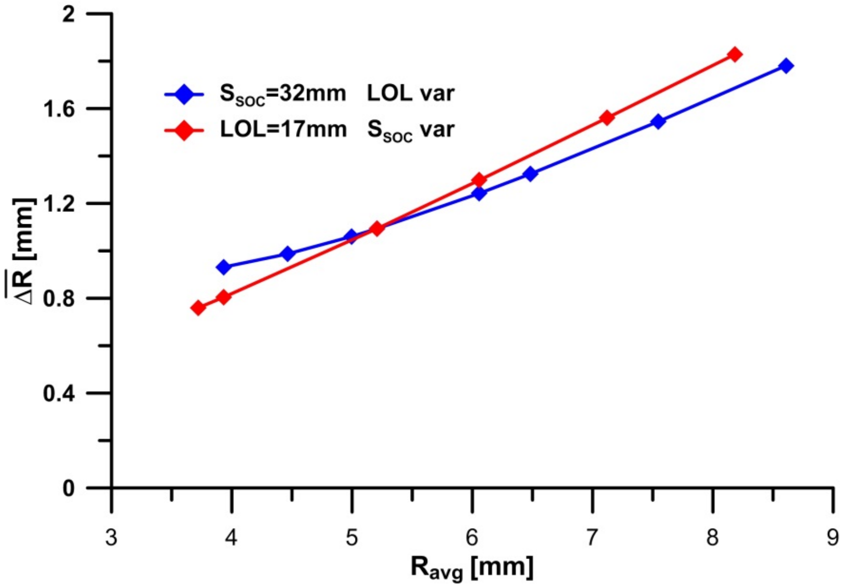

Figure 3.16. *Results of simplified radial expansion description for* $\rho_{inert}/\rho_{react} = 1.45$ *and* $\Theta = 24°$ *. Starting from a reference* $LOL = 17$ *mm and* $S_{SOC} = 32$ *mm, an independent variation of both parameters is shown.*

Figure 3.16 shows results of the simplified model for a given density drop and inert spray cone angle for two independent variations of s and LOL. Radial expansion is seen to depend on the geometry of the ready to burn mixture in terms of the average radius, i.e. in terms of S_{SOC} and LOL. Increasing any of them means moving the ready-to-burn mixture farther away from the nozzle, which always results in an increased radial expansion. The previous conclusions can be extended to non-uniform density distributions if the previously defined density values are assumed to be volume-averaged density values, i.e. increasing density drop or moving the ready-to-burn mixture away from the nozzle will increase radial expansion.

Bibliography

[1] Bardi Michele. *Partial Needle Lift and Injection Rate Shape Effect on the Formation and Combustion of the Diesel Spray.* Doctoral Thesis, Universitat Politecnica de Valencia, 2014.

[2] Fajardo Walter Martin Vera-Tudela. *An experimental study of the effects of fuel properties on diesel spray processes using blends of single-component fuels.* Doctoral Thesis, Universitat Politecnica de Valencia, 2015.

[3] Payri Raul, García-Oliver Jose M., Bardi Michele and Manin Julien. "Fuel temperature influence on diesel sprays in inert and reacting conditions". *Applied Thermal Engineering*, Vol. 35 n^o 1, pp. 185–195, 2012.

[4] Bardi Michele, Payri Raul, Malbec Louis-Marie, Bruneaux Gilles, Pickett Lyle M, Manin Julien, Bazyn Tim and Genzale Caroline L. "Engine Combustion Network: Comparison of Spray Development, Vaporization, and Combustion in Different Combustion Vessels". *Atomization and Sprays*, Vol. 22 n^o 10, pp. 807–842, 2012.

[5] Bermúdez, V. García J. Juliá E. and Martínez S. "Engine with Optically Accessible Cylinder Head: A Research Tool for Injection and Combustion Processes". *SAE Technical Paper*, 2003.

[6] Heywood J. B. *Internal combustion engine fundamentals.* McGraw-Hill Publishing, 1988.

[7] S Settles G. *Schlieren and sadowgraph techniques: visualizing phenomena in transparent media (Experimental Fluid Mechanic).* Springer Verlag, 2001.

[8] Benajes Jesús, Payri Raúl, Bardi Michele and Martí-Aldaraví Pedro. "Experimental characterization of diesel ignition and lift-off length using a single-hole ECN injector". *Applied Thermal Engineering*, Vol. 58 n^o 1-2, pp. 554–563, 2013.

[9] Pastor Jose V., Payri Raul, Garcia-Oliver Jose M and Briceño Francisco J. "Schlieren Methodology for the Analysis of Transient Diesel Flame Evolution". *SAE International Journal of Engines*, Vol. 6 n^o 3, pp. 1661–1676, 2013.

[10] Pastor José V, Garcia-oliver José M, Bermudez Vicente and Micó Carlos. "Spray Characterization for Pure Fuel and Binary Blends under Non-Reacting Conditions". *SAE Technical Paper*, 2014.

[11] Yamakawa, M. Takaki D. Li T. Zhang Y. "Quantitative Measurement of Liquid and Vapor Phase Concentration Distributions in a D.I. Gasoline Spray by the Laser Absorption Scattering (LAS) Technique". *SAE Technical Paper*, 2002.

[12] A. G. Gaydon D.Sc. F.R.S. *The Spectroscopy of Flames.* Springer Netherlands, 1974.

[13] Higgins Brian and Siebers Dennis. "Measurement of the Flame Lift-Off Location on Dl Diesel Sprays Using OH Chemiluminescence". *Sae 2001-01-0918*, n^o 724, 2001.

[14] Payri Raul, Gimeno Jaime, Bardi Michele and Plazas Alejandro H. "Study liquid length penetration results obtained with a direct acting piezo electric injector". *Applied Energy*, Vol. 106, pp. 152–162, 2013.

[15] Dec John E. “A conceptual model of DI diesel combustion based on laser-sheet imaging”. *Sae*, n^o 412, pp. 970873, 1997.

[16] Matsui Y Kamimoto T and S Matsuoka. “A study on the time and space resolved measurement of flame temperature and soot concentration in a DI diesel engine by the two-color method”. *SAE Technical Paper*, 1979.

[17] Payri F, Pastor J V, García J M and Pastor J M. “Contribution to the application of two-colour imaging to diesel combustion”. *Measurement Science and Technology*, Vol. 18 n^o 8, pp. 2579–2598, 2007.

[18] Zhao Hua and Ladommatos N. “Optical Diagnostics for soot and temperature measurement in diesel engines”. *Progress in energy and combustion science*, Vol. 24, pp. 221–255, 1998.

[19] H.C. Hottel and F.P. Broughton. “Determination of true temperature and total radiation from luminous gas flameames: Use of special two-color optical pyrometer”. *Industrial and Engineering Chemistry*, Vol. 4 n^o 2, pp. 166–175, 1932.

[20] Manin Julien, Pickett Lyle M. and Skeen Scott A. “Two-Color Diffused Back-Illumination Imaging as a Diagnostic for Time-Resolved Soot Measurements in Reacting Sprays”. *SAE International Journal of Engines*, Vol. 6 n^o 4, pp. 2013–01–2548, 2013.

[21] Pickett Lyle M. and Siebers Dennis L. “Soot in diesel fuel jets: Effects of ambient temperature, ambient density, and injection pressure”. *Combustion and Flame*, Vol. 138 n^o 1-2, pp. 114–135, 2004.

[22] O. Koylu U. and M. Faeth G. “Optical properties of overfire soot in buoyant turbulent diffusion flames at long residence times”. *Journal of heat transfer*, Vol. 116 n^o 1, pp. 152–159, 1994.

[23] Skeen Scott a, Manin Julien, Dalen Kristine and Pickett Lyle M. “Extinction-based Imaging of Soot Processes over a Range of Diesel Operating Conditions”. *Internal combustion and gas turbine engines*, pp. 1–13, 2013.

[24] Manin, J. Bardi M. and Pickett L.M. “Evaluation of the liquid length via diffused back-illumination imaging in vaporizing diesel sprays”. *International Symposium COMODIA 2012 SP2-4*, 2012.

[25] Pastor José V., García-Oliver José M., García Antonio, Micó Carlos and Möller Sebastian. “Application of optical diagnostics to the quantification of soot in n-alkane flames under diesel conditions”. *Combustion and Flame*, Vol. 164, pp. 212–223, 2016.

[26] Zheng Liang, Ma Xiao, Wang Zhi and Wang Jianxin. “An optical study on liquid-phase penetration, flame lift-off location and soot volume fraction distribution of gasoline-diesel blends in a constant volume vessel”. *Fuel*, Vol. 139, pp. 365–373, 2015.

[27] Pastor Jose V., Garcia-Oliver Jose M., Pastor Jose M. and Vera-Tudela W. “One-dimensional Diesel spray modeling of mulitcomponent fuels”. *Atomization and Sprays*, Vol. 25 n^o 6, pp. 485–517, 2015.

[28] Legros Guillaume, Wang Qianlong, Bonnety Jérôme, Kashif Muhammad, Morin Céline, Consalvi Jean-Louis and Liu Fengshan. “Simultaneous soot temperature and volume fraction measurements in axis-symmetric flames by a two-dimensional modulated absorption/emission technique”. *Combustion and Flame*, Vol. 162 n^o 6, pp. 2705 – 2719, 2015.

[29] Modest M.F. *Radiative Heat Transfer (second ed.).* Academic Press, 2003.

[30] Pastor J.V., García-Oliver J.M., López J.J. and Vera-Tudela W. "An experimental study of the effects of fuel properties on reactive spray evolution using Primary Reference Fuels". *Fuel*, Vol. 163, pp. 260 – 270, 2016.

[31] Pastor José V., Javier López J., García José M. and Pastor José M. "A 1D model for the description of mixing-controlled inert diesel sprays". *Fuel*, Vol. 87 n^o 13-14, pp. 2871–2885, 2008.

[32] Desantes J. M., Pastor J. V., García-Oliver J. M. and Pastor J. M. "A 1D model for the description of mixing-controlled reacting diesel sprays". *Combustion and Flame*, Vol. 156 n^o 1, pp. 234–249, 2009.

[33] X. Tauzia A. Maiboom and Ma G. "A 1D Model for Diesel Sprays under Reacting Conditions". *SAE Technical Paper*, 2015.

[34] Knox Benjamin W and Genzale Caroline L. "Reduced-order numerical model for transient reacting diesel sprays with detailed kinetics". *International Journal of Engine Research*, Vol. 17 n^o 3, pp. 261–279, 2016.

[35] Payri Raúl, Viera Juan Pablo, Pei Yuanjiang and Som Sibendu. "Experimental and numerical study of lift-off length and ignition delay of a two-component diesel surrogate". *Fuel*, Vol. 158, pp. 957–967, 2015.

Chapter 4

Spray Dynamics and Soot Production under Quiescent Conditions

Contents

4.1 Introduction

This chapter will focus on the study of reacting Diesel spray under quiescent conditions. As described in chapter 1, most of the studies investigating the air entrainment and mixing process of the spray are performed at non-reacting quiescent conditions. Few works address the effects that combustion has on the spray dynamics. For this reason, the studies on combustion-induced radial and axial expansion, the fuel effects on reacting spray dynamics are presented first. Next, soot production of quasi-steady flame will be studied with same injector and under same operating conditions.

The reacting diesel spray expansion was investigated using n-dodecane, n-heptane and one binary blend of Primary Reference Fuels (80% n-heptane and 20% iso-octane in mass) based on the existing database from previous experimental results from Schlieren imaging technique in the constant pressure flow(CPF) vessel. Here, we acknowledge previous PhD students Bardi [1] and Vera-Tudela [2] for their contributions on the database of n-dodecane and Primary Reference Fuels, respectively. The soot measurement was carried out by means of a combined extinction- radiation technique in the bigger CPF vessel. In order to check the repeatability and aid soot analysis, the Lift-off length was identified measuring OH^* chemiluminescence. The operating conditions and the injector used were chosen following the guidelines of the Engine Combustion Network.

4.2 Optical setup

Schlieren and OH^* chemiluminescence

A sketch of the experimental layout is presented in Figure 4.1. The Schlieren setup employed includes different components: Xe-Arc lamp and a 1 *mm* diameter pin-hole constituting the point light source of the system; a parabolic mirror used to collimate the light from the pin-hole in a parallel beam; a collecting lens to focus the parallel beam in a single point and a high-speed camera (50 *kfps*) with a spatial resolution 5.26 $pixel/mm$ and a shutter time 4 μs. A diaphragm (4 *mm* aperture) was used as a cut-off device to enhance the sensitivity of the setup while a shortpass filter (< 600 *nm*) was filtering the light beam to reject part of the soot incandescence light emissions.The OH^* chemiluminescence images were employed for the calculation of the Lift-off length. An ICCD camera (Andor I-star) fitted with a 100 $mmf/2.8$ UV lens and a 310 ± 5 *nm* interferometric filter was used with a constant intensifier gating time widow synchronized with the injection between 2.0 and 5.0 *ms* after the start of the injections (ASOI): in this way the steady part of the combustion process was averaged along the injection event and the shot-to-shot deviation was reduced.

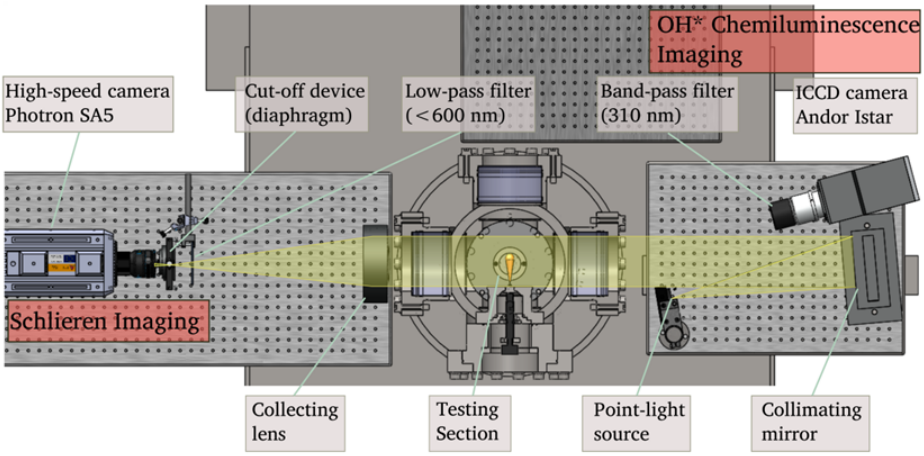

Figure 4.1. Experimental layout for tests in CPF.

Soot measurement

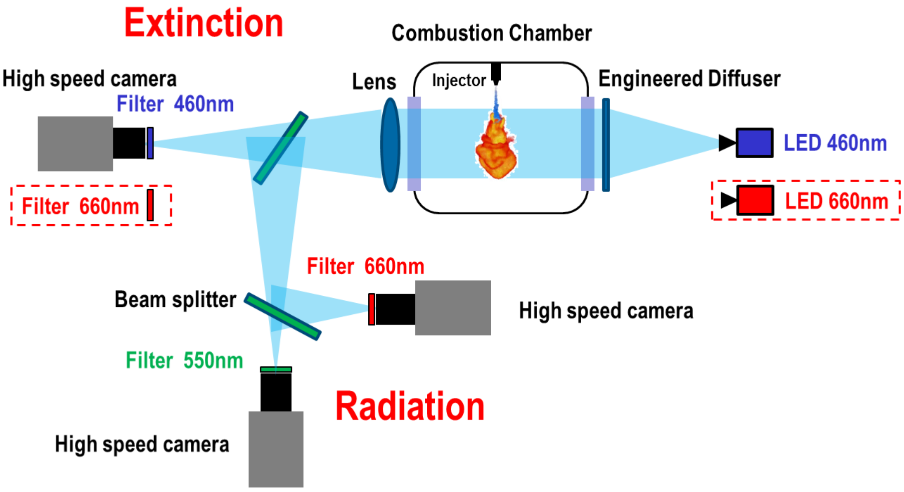

Figure 4.2. Experimental layout for soot measurement(top view).

Soot measurements were carried out by means of a combined extinction-radiation technique (CER) in the other CPF with bigger optical windows. A top view of the experimental arrangement is shown in Figure 4.2. It is quite similar with the optical setup as shown in Figure 3.8. First of all, soot extinction and radiation were measured simultaneously under a variety of operating conditions. For soot extinction measurement, a high-output blue LED with a Peak wavelength 460 nm and 2 μs pulse duration was applied here as the light source. An engineered diffuser close to the optical window was used to create a diffused Lambertian intensity profiles. The transmitted light of the LED and the thermal radiation from the combustion are collected by means of a spherical lens (f = 800 mm) to reduce the effects of beam steering. After going through the beam splitter (50%/50%) the transmitted LED light was collected by a high-speed CMOS camera (Photron SA-5, recording at 25 khz) equipped with a bandpass filter (460 nm, 10 FWHM). The exposure time of the camera was set to 1.91 μs with 704×384 pixels image resolution and the pixel/mm ratio is 6.48. After passing through a spherical lens and two beam splitters(50%/50%), the soot radiation were measured using two high-speed CMOS cameras (Photron SA-5, recording at 25 khz) and two bandpass filters (centered at 550 nm and 660 nm, both with 10 nm FWHM). The exposure time of two cameras was set to 6.64 μs with 704×384 pixels image resolution and the $pixel/mm$ ratio is 6.54. In order to transform grey levels into radiance values, calibration curves have been obtained by means of a tungsten-ribbon calibration lamp (Osram Wi17G), which was located at the same position of spray.

In order to check the extinction sensitivity with spectral wavelength of illumination light, another LED with a Peak wavelength 660 nm coupled with a corresponding filter(660 nm, 10 FWHM) was also applied to do the DBI tests as a reference.

Additionally, OH^* chemiluminescence was also measured here with the same optical setup as Figure 4.1 to check the repeatability of the measurements and back up soot analysis. The flame lift-off length(LOL) was derived according to standard ECN processing method [1, 3]. Besides that, OH^* contour on the flame-axis plane was also obtained through tomographic reconstruction.

4.3 Test Matrix

The standard ECN fuel, n-dodecane, was used for both spray dynamics and soot measurements. Another objective of this chapter is to study the effects of fuel properties on the transient reacting spray evolution. Thus, besides n-dodecane, n-heptane (PRF0) and one binary blend of Primary Reference Fuels (PRF20, made up of 80% n-heptane and 20% iso-octane in mass) have been investigated. Some general chemical and physical properties of the three pure components are shown in Table 4.1. In practical terms, thermochemistry properties of all three fuels are highly similar. In fact, 1D model calculations of local conditions in terms of state relationships (Figure 4.3) show that the mixture state under both inert and reacting conditions (temperature, density) is quite similar for all three fuels, which means that the expected differences in flow development among fuels are mainly related to chemical kinetics, which will set the pace for the transition from inert to reacting conditions.

Table 4.1. *Fuel properties for the pure components investigated in the present contribution.*

Fuel	ρ_f $[kg/m^3]$	LHV $[MJ/kg]$	T_{boil} $[K]$	CN [-]
n-dodecane (C12H26)	752	44.2	489	87
n-heptane (PRF0)	684	44.6	371.5	53
iso-octane (PRF100)	690	44.3	372.4	14

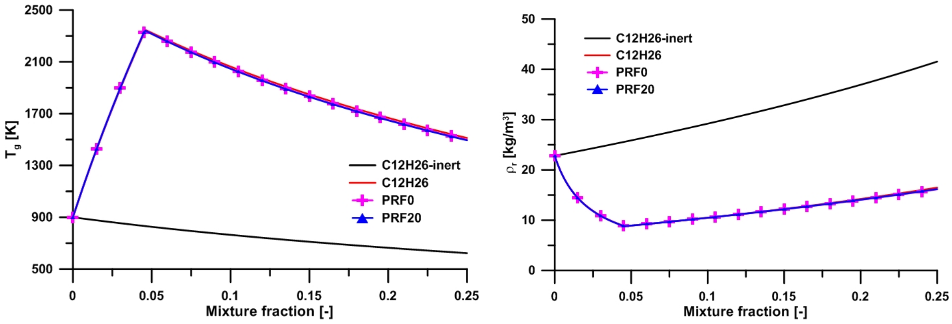

Figure 4.3. *State relationships for the three considered fuels. Temperature (left) and density (right) versus mixture fraction for C12H26 inert, and C12H26, PRF0 and PRF20 reacting. Nominal Spray A conditions.*

The standard Spray A injector within ECN group has been used which has a single-hole nozzle with a nominal diameter of 90 μm (Serial No. 210675). The parametric variation in the injection parameters (injection pressure), thermodynamic conditions within the chamber (ambient temperature and ambient density) and oxygen concentration sweep are shown in Table 4.2. A long injection energizing time was set as 3.5 ms at every operating point, which results in an injection duration of 5 ms (15°), approximately, in order to achieve a quasi-steady state flame. For each operating condition, during schlieren tests, 8 injection cycles were recorded for n-dodecane and 15 for PRF0 and PRF20 in CPF, while considering more scattering on soot production, 40 injection cycles were recorded for soot CER measurements.

Table 4.2. *Test conditions.*

Fuel	T_g [K]	P_{inj} [bar]	ρ_g $[kg/m^3]$	O_2 [%(vol)]	Tech.
C12H26	800,850,900	500,1000,1500	22.8	0,15,21	Sch.
PRF0	900,1000	500,1000,1500	22.8	0,15,18,21	
PRF20	900,950	500,1000,1500	22.8	15,18,21	
PRF100	900	500,1000,1500	22.8	0	
C12H26	800,900,1000	1000,1500	22.8	15,21	CER

4.4 A study on reacting spray dynamics

The analysis of this section focuses on the understanding of the impact that the combustion has on the modification of the spray boundaries. Based on the High-speed schlieren images and the processing methodology mentioned in section 3.3.1, new methods to quantify the axial and radial expansion of the direct-injection Diesel spray were developed. Further more, the effects of different parametric variations as well as fuel properties on this spray expansion were analyzed.

4.4.1 Analysis under baseline Spray A conditions

Taking into account the limitations of the optical access of the CPF chamber and the frequency of the cases used for comparison in later sections, the baseline *Spray A* ($P_{inj} = 1500$ *bar*, $T_g = 900$ *K*, $\rho_g = 22.8$ kg/m^3) condition was selected for the reference analysis in this section. Because of the early ignition caused by high ambient temperature and high density and fast spray development created by high injection velocity, the full development period of the spray can be recorded by the camera before the end of injection.

Tip penetration velocity

Figure 4.4 (top) shows the temporal evolution of the tip penetration of inert and reacting sprays under *Spray A* condition. In this figure as well as in the subsequent ones presented in this paper, the time is referred to the start of the injection with the acronym ASOI (After Start Of Injection). As shown in top plot of Figure 4.4, the red (in web version) and the blue solid line represent the average spray penetration from the eight repetitions under reacting and inert conditions, respectively. Due to the very small difference in molecular weight between oxygen and nitrogen, ambient pressure is essentially the same for the nominal ambient density and temperature values. The vertical red dashed line in Figure 4.4 (middle) represents the start of combustion obtained from Schlieren images following the methodology in Ref [4]. Both inert and reacting spray tip penetrations increase steadily with time, but the reacting case shows an apparent acceleration after the start of combustion. To further analyze this behavior, the bottom plot shows the penetration ratio (i.e. reacting divided by inert penetration at each time step), consistently with the analysis carried out in a previous work from Desantes et al. [5] for n-heptane sprays under similar operating conditions. As described in that paper, the temporal evolution of the reacting spray can be divided into five stages:

- **I Non-reacting phase:** from the start of injection to the start of combustion, where the penetration ratio should be essentially one. Results in Figure 4.4(middle) shows values lower than one. This is due to the small penetration values, so that scattering between inert and reacting tests may result in a relatively important deviations of the ratio from one.

- **II Autoignition expansion phase:** It is a relatively short phase marked by a first short-lived peak in penetration ratio. It spans from the start of combustion (SOC) to the time when the penetration between inert and reacting condition become the same again.

- **III Stabilization phase:** from the end of the previous stage to the time when the tip penetration starts to separate, as shown in [5] the duration of this phase depends a lot on the operating condition, under less reacting conditions this phase becomes longer. Under Spray A conditions this phase is almost non-existent.

- **IV Acceleration phase:** where the penetration ratio starts increasing with time.

- **V Quasi-steady flame phase:** where the tip penetration ratio reaches a steady value.

There is a decrease of the penetration ratio after the time exceeds 4 *ms* because the reacting case reaches the limit of the optical access, as shown in the top plot in Figure 4.4.

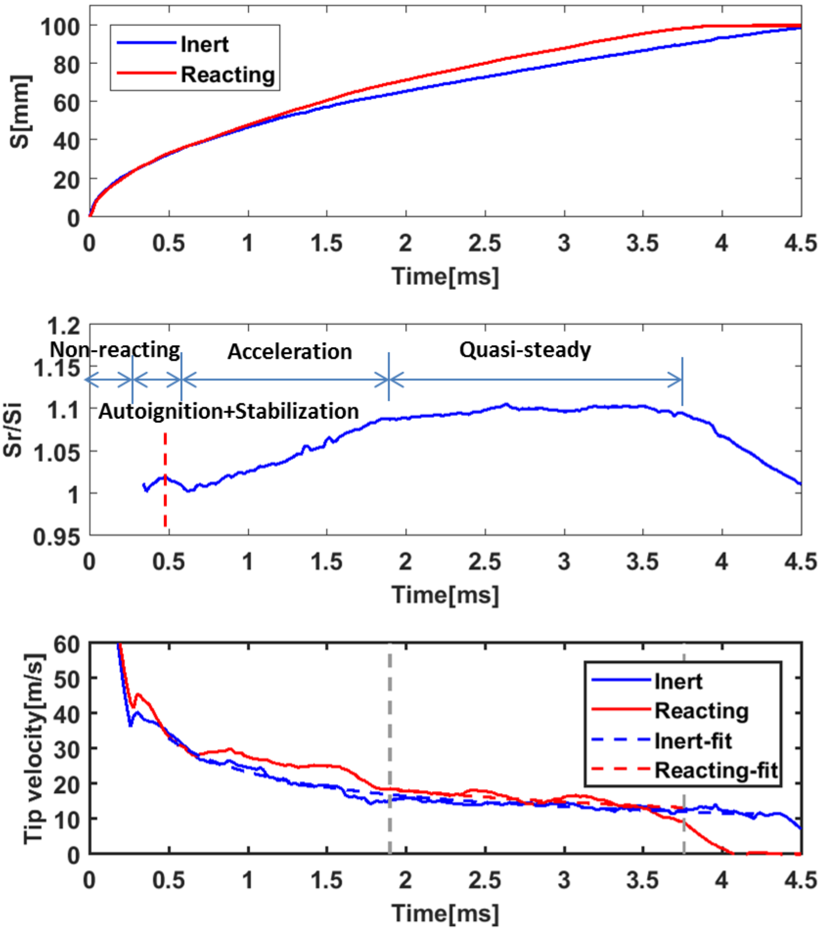

Figure 4.4. *Temporal evolution of the penetration and ignition delay (vertical dashed line) from Schlieren image processing for both inert and reacting conditions (top), penetration ratio(middle) and penetration velocity(bottom). (Spray A condition).*

As discussed above, reacting tip penetration undergoes several stages highly influenced by the strong coupling between chemistry and fluid dynamics, eventually leading to the quasi-steady penetration phase. To avoid the cumulative effect of the different stages on the analysis of this last phase, the later analysis will be performed in terms of the spray tip penetration velocity, i.e. the time-derivative of the tip penetration. This should help better characterize the instantaneous evolution of spray tip during this quasi-steady phase. Figure 4.4 (bottom) shows the time evolution of this characteristic velocity as calculated from tip penetration (Figure 4.4 (top)) for both the inert and reacting cases of the nominal Spray A condition with n-dodecane. A clearly decreasing trend with time is observed in both cases, with a more oscillating evolution in the reacting case due to the different stages mentioned in the Figure 4.4.

As shown in the literature [6–9], spray tip velocity for an inert spray is inversely proportional to square root of time. Following this idea, the experimental tip penetration velocity has been fitted to Eq.4.1 for both inert and reacting conditions:

$$\frac{ds}{dt} = \frac{k}{\sqrt{t}} \tag{4.1}$$

While the fit is performed from 0.5 ms ASOI to 4.2 ms ASOI for the inert cases, it is only applied during the quasi-steady penetration period for the reacting ones, as defined in Figure 4.4 (middle), i.e. during the period where the reacting to inert penetration ratio (s_r/s_i) is constant. The dashed trend lines in Figure 4.4 (bottom) show that for both cases Eq.4.1 describes adequately the tip penetration evolution. The k value for inert conditions can be derived from the consideration of a quasi-steady constant density mixing controlled spray, [9] leading to the theoretical constant k_{th} according to Eq. 4.2.

$$k_{th} = \sqrt[4]{\frac{Log(100)}{8\pi}} \cdot \sqrt[4]{\frac{\dot{M}_0}{\rho_a}} \cdot \frac{1}{\sqrt{\tan(\theta/2)}} \tag{4.2}$$

This means that, for an inert spray, tip velocity only depends on momentum flux $\dot{M}_0$, air density ρ_a and spreading angle θ. Figure 4.5 shows that for the investigated conditions under the present study, the inert tip penetration follows quite accurately the description in Eq.4.2, where experimental momentum flux and density values have been used, together with a constant angle $\theta = 24°$ Note that three pure fuels are considered under inert conditions, namely n-dodecane (C12H26), n-heptane (PRF0) and iso-octane (PRF100), so that any tested blend in-between should also produce the same results.

The fitted line under reacting condition in Figure 4.4 (bottom) indicates that a similar behavior of the reacting spray to the inert one can also be expected along the quasi-steady period. If this behavior is quantified in simple terms by means of Eq. 4.2, momentum flux influence should be the same under

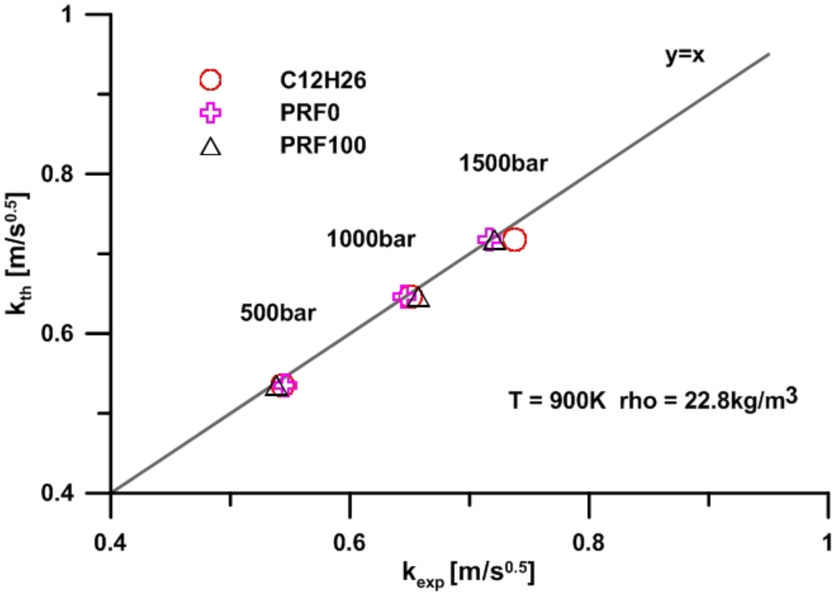

Figure 4.5. *Comparison of theoretical tip penetration velocity k constant according to Eq.4.2 with experimental values for the investigated inert conditions. A constant angle* $\theta = 24^\circ$ *has been used in Eq.4.2.*

both inert and reacting conditions, while for the latter case a density drop and increase spreading will be the main factors creating a tip velocity departure from the inert one. The extension to reacting conditions could be made by assuming a modified density and radial width parameter. However, no simple a priori solution exists due to the wide range of densities existing within the reacting spray. This is why the use of the 1D model is pertinent, especially if the focus on the quasi-steady phase is made, which removes the necessity of a detailed chemistry analysis.

Radial expansion

Figure 4.6 shows the temporal evolution of radial width of inert and reating sprays under Spray A condition. The image sequence on the left hand side of Figure 4.6 presents the temporal evolution of half images of a single injection for the reacting nominal Spray A condition. As mentioned above, the optical access was limited to 100 *mm* and the black area on the right top of these images is the window limit. As for the right image sequence of Figure 4.6, the temporal evolution of the spray half-width (i.e. the spray radius) as derived from the probability images under reacting and inert conditions are shown here for the indicated timings. Differences between left and right image sequences of Figure 4.6, are due to the comparison of average contours to instantaneous realizations of the experiment. The vertical red dashed line represents the average lift-off length as obtained from OH^* chemiluminescence images.

At 320 μs ASOI, the spray behaves as an inert spray which corresponds to the non-reacting phase of the penetration mentioned above and there is no expansion neither in axial nor in radial direction. The contours of inert and reacting conditions still keep similar at 400 μs ASOI, even though some part of the spray tip starts getting transparent as a consequence of the onset of cool flames. At about 450 μs ASOI, the ignition takes place which directly leads to a separation of the penetration and radial expansion in the front part of the spray. This agrees with the autoignition expansion phase observed in the penetration plot. At 660 μs ASOI, there is an obvious radial expansion for the reacting spray, and the tip penetration of both conditions become similar again. According to momentum conservation, the strong increase in radial width leads to a slower penetration. This image corresponds to the stabilization phase of penetration. The following images (1600 μs ASOI) correspond to the acceleration phase of the penetration evolution. It can be seen that the initial radial expansion part downstream of the lift-off length is stabilized compared with the same part of the next plot (2900 μs ASOI), with a spray slightly wider than under inert conditions. At 1600 μs ASOI a "waist" part was found at around 60 mm from the nozzle where the reacting spray contour trends to be almost flat and overlaps with the inert spray contour. The last images (2900 μs ASOI) correspond to the quasi-steady phase of the penetration. It was found that the stabilized part spans from the nozzle up to around 50 mm. An apparent vortex came up after the jet head (left image), which can also be seen one the contour derived from the probability, which means that the "waist" is statistically significative. This confirms that the transient tip of the spray is governed by a vortex with a very repetitive pattern. This phenomenon could also be found over a wide range of operating conditions which should be attributed to rapid gas entrainment [10].

Different approaches can be found in the literature to assess the radial dispersion of inert and reacting spray and many definitions for the spray spreading angle are given [5, 6, 11]. However, it was found that, especially at reacting conditions, the geometry of diesel spray is much more complicated than a cone shape and it was not well represented by a single parameter. In order to better understand the radial dispersion of the reacting spray, the radial widths for both inert and reacting spray under *Spray A* condition were compared. As shown in Figure 4.7, the red (in web version) and blue solid

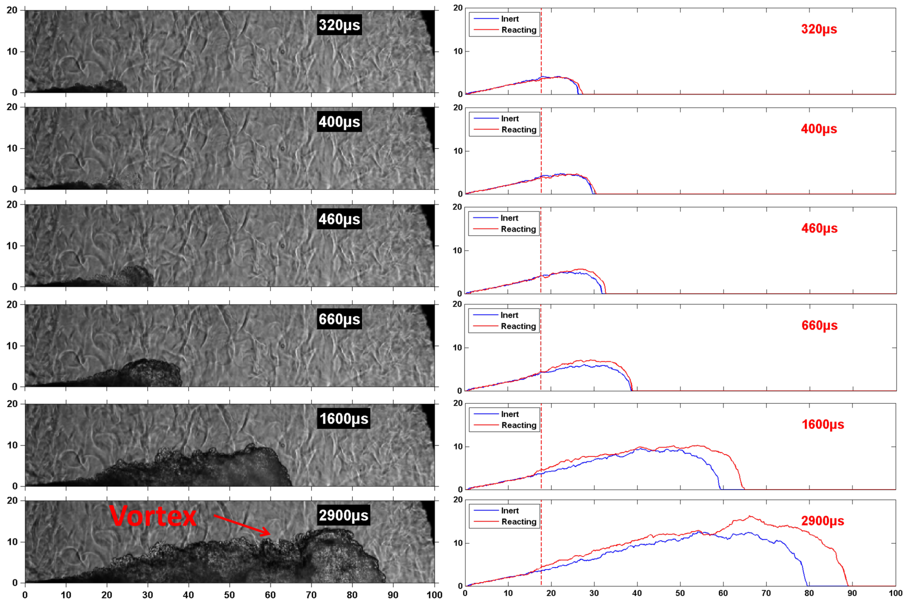

Figure 4.6. *Temporal evolution of the reacting spray contour obtained with Schlieren (left) and radial width both under inert and reacting condition (right) (spray A condition).*

lines represent the radius width of the reacting and inert spray separately. The red vertical dashed line represents the lift-off length as derived from OH^* chemiluminiscence images. It must be noted that the comparison of contours is performed at iso-spray tip penetration, not at the same timing. This means that while the time of inert spray is at 4380 μs ASOI and the time of reacting spray is at 3620 μs ASOI. According to several experimental evidences, the structure of the reacting spray can be divided into 3 parts as shown in Figure 4.7:

- **I Quasi-steady Inert part,** which is defined from the nozzle tip to the Lift-off length. Because of the absence of heat release, in this zone the spray behaves as an inert flow.

- **II Quasi-steady reacting part,** which is defined from lift-off length to the position where the contour stops increasing radially. In this part, the heat released by the oxidation reactions cause an increase in the radial width at every position of the spray axis. After a first transient where the radial width increases with the axial position, the difference remains almost constant throughout the region.
- **III Transient part:** which is defined from the end of the quasi-steady part to the spray tip. This part is much more complex than other two ones, due to its transient nature. In the same way as for an inert spray, a reacting one is made up of a quasi-steady part (I and II) led by a transient tip. As sketched in Figure 4.7, for a developed spray the extent of the steady part (I and II) is roughly 50% of the total spray tip penetration, compared to around 60% which is a reference value for the inert case.

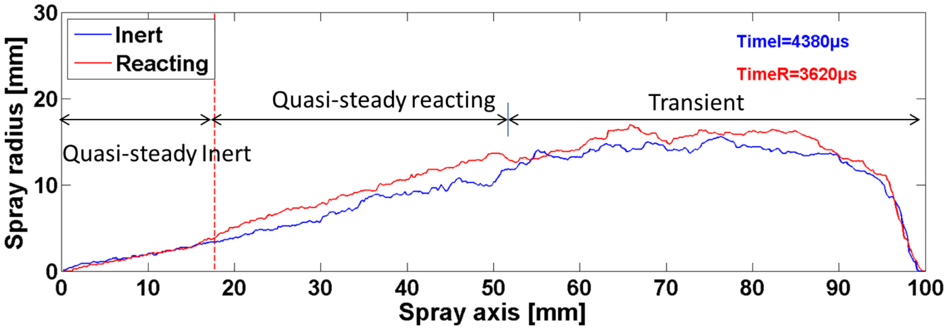

Figure 4.7. *Radial width for both inert and reacting spray under Spray A condition ($S_r = 97$ mm, $S_i = 97$ mm).*

One of the aims of this section is to gain understanding on the radial expansion characterizing the quasi-steady reacting region. To this end, it is necessary to define the position of the transition point from quasi-steady reacting part to the transient part. Two fitting lines to the inert and reacting spray contours were done by means of a least-squares algorithm from a distance to the nozzle 10% longer than the lift-off length to three different percentages (40%, 50%, 60%) of the tip penetration. shows the fitting lines with the contours of the three percentages at the same time. It is quite apparent that the 40% limit can be further extended downstream while still being valid, whereas the 60% case already runs into the transient tip. Accordingly, the lower limit of the transient tip will be defined hereafter as 50% of the tip penetration.

From the derived contours, both inert and reacting spray cone angles were calculated according to the slope of the fitting line.

$$\tan(\theta_r/2) = k_r \tag{4.3}$$

where θ_r is the spreading angle of the spray, k_r is the slope of the fitting line.

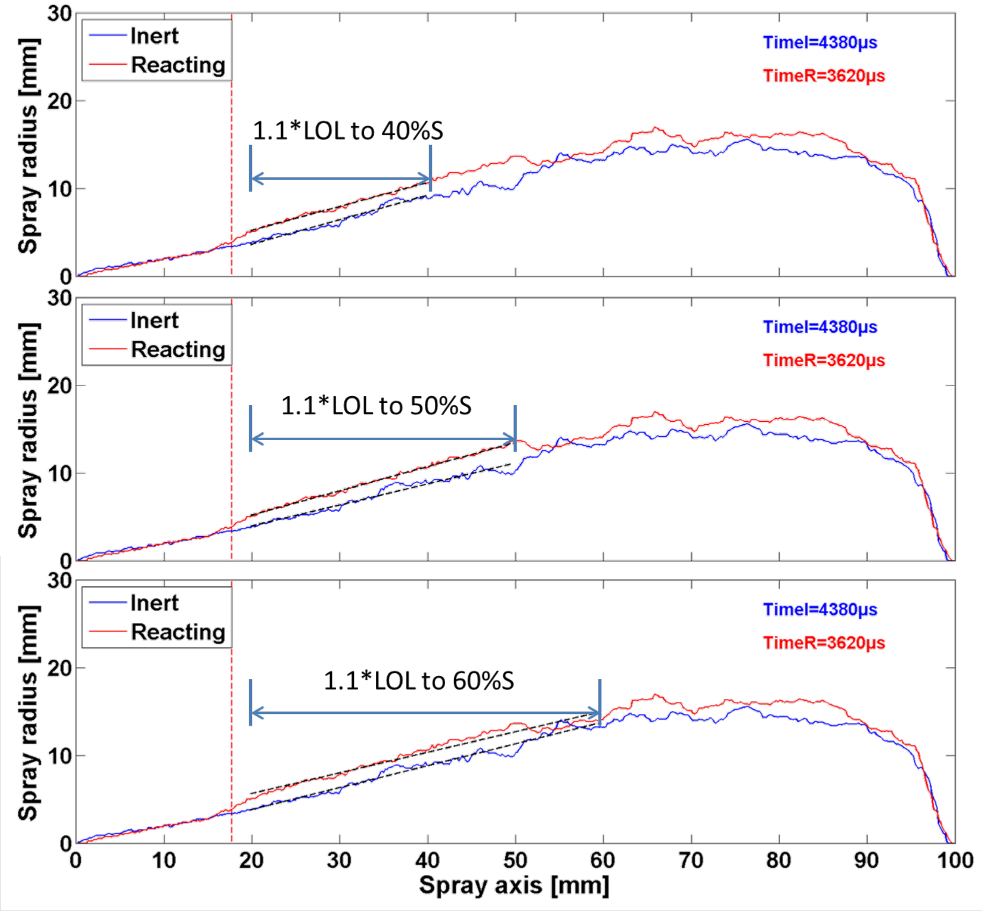

Figure 4.8. The fitting line of the inert and reacting spray at Spray A condition..

The plots in Figure 4.8 correspond to a single time instant. The corresponding time-resolved evolution of the spray angle under inert and reacting conditions is presented in Figure 4.9.

Results show that both inert and reacting angles trend to be the same value after some time interval, i.e. the two fitting lines become parallel. This means that the radial expansion at different axis position of the quasi-steady reacting part is similar, in other words, the radial contour of the reacting spray is simply the result of shifting the inert one by an approximately constant value.

Based on the previous analysis, the radial increase should adequately describe the combustion-induced radial expansion along the whole spray axis. In order to find a single parameter to evaluate the radial expansion of the quasi-steady reacting part, the average value of the radial difference between inert and reacting conditions at every time instant from a distance 10% longer than LOL to 50% of the spray tip has been calculated. After that, this spatially-averaged value was also time-averaged into the parameter $\overline{\Delta R}$. Because the reacting spray has not reached a stable states at the onset ignition period and the strong tip vortex has some influence on definition of this part, the time window for calculating the $\overline{\Delta R}$ was chosen from 1 ms to 2 ms after ignition delay. It has been observed that the defined parameter is stable in this time window for all cases except the low density case. One possibility for such a behavior is that the flame under low density condition is not as stable as that under high density. This quantitative indicator $\overline{\Delta R}$ will be used in the following section to evaluate the expansion of the spray under parametric studies.

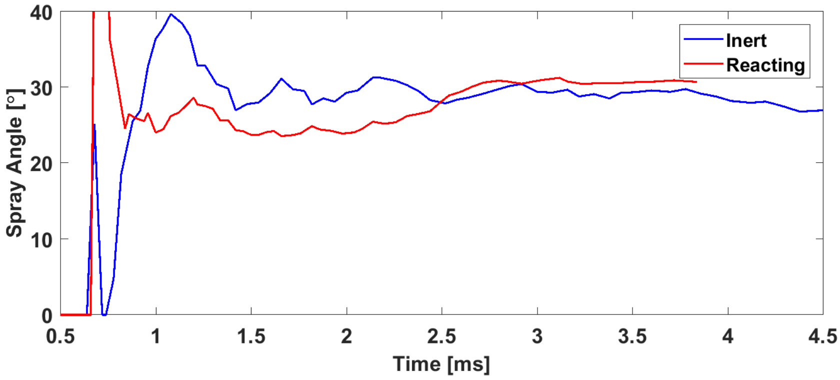

Figure 4.9. *The spread angle of the inert and reacting spray at Spray A condition.*

4.4.2 Parametric analysis

Tip penetration velocity

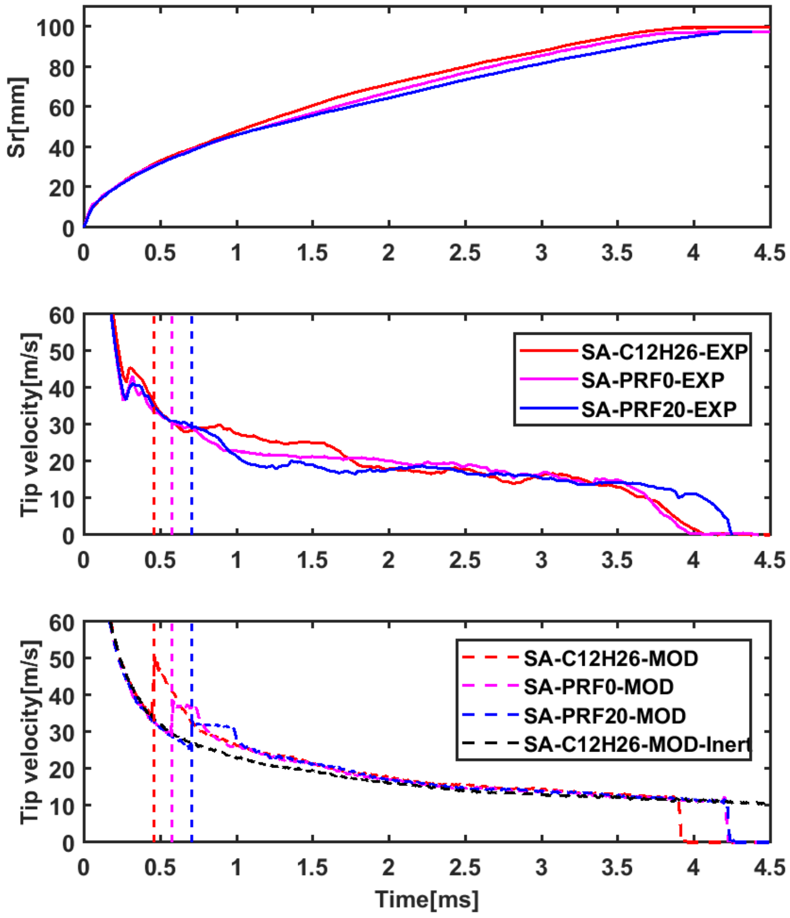

Figure 4.10. *Effect of fuel type on penetration-derived information for nominal Spray A conditions (900 K,* 15/0% *O_2, 1500 bar). Top plot: experimental penetration. Middle: experimental tip velocity Bottom: model tip velocity. Vertical dashed lines indicate auto-ignition time.*

Starting from the baseline condition, namely nominal *Spray A* with n-dodecane, the first parametric variable to be analyzed will be fuel type. Figure 4.10 shows a comparison of spray tip velocity for three fuels under the same operating conditions. The ignition delay has also been shown in terms of vertical lines. The sequence C12H26 > PRF0 > PRF20 (in decreasing cetane number) shows a later timing for inert-to-reacting transition. If analyzed in terms of spray tip penetration (top plot) one can observe that the lower the fuel reactivity the slower the reacting tip penetration is. However, if analyzed in terms of tip velocity (middle plot), the conclusions are not the same. In this case, main differences among fuels occur during the autoignition and acceleration phase. Keeping again the same sequence in decreasing cetane number, one can observe that the acceleration phase is shifted later in time, starting from 0.6 to 1.6 ms for C12H26, 0.9 to 2 ms for PRF0 and finally 1.5 to 2.5 ms for PRF20. The interesting feature, however, is that the later time development of spray tip velocity is the same regardless of fuel, i.e. the quasi-steady phase shows identical tip velocity for all three fuels. This means that the observed slower tip penetration (top plot) of the lower cetane number is mainly due to differences in the early stages of the penetration, which cannot be compensated later due to a similar penetration velocity. A similar trend is obtained from the modelling results (bottom plot). Because transition in chemistry in modelling is much faster than in experiments, one can observe an earlier collapse of the three cases, but behavior is also independent of fuel type.

Accordingly, for the investigated conditions, fuel cetane number has an effect on when the inert to reacting transition occurs (ignition delay), as well as how fast this transition is. A quasi-steady penetration period has been confirmed, in which spray tip velocity is the same for the investigated fuels, mainly due to the fact that they have very similar thermochemistry properties.

The effects of fuel properties observed for the nominal conditions can be extended to the whole set of operating conditions considered, as summarized in Figure 4.11. Here only the quasi-steady phase tip velocity constant k is analyzed. Again, fuel cetane numbers seam to have negligible effects on k value. In other words, tip velocity of the three fuels is the same during quasi-steady phase.

Figure 4.12 presents the effects of ambient gas temperature (top row), oxygen (middle row) and injection pressure (bottom row) on spray tip velocity temporal evolution (left column) and k value for all fuels (right column). In the latter case, solid symbols represent experimental results, while hollow ones correspond to 1D modelling results. k_{th} values from Eq.4.2 are also included

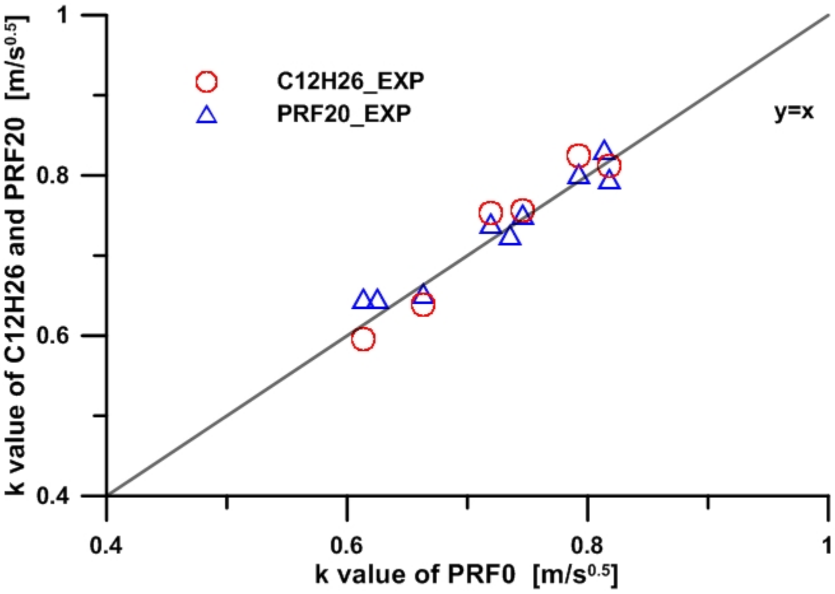

Figure 4.11. Analysis of fuel effects on tip penetration experimental k constant.

as a reference to represent the inert spray case. This parameter does not change with different fuels and ambient temperature when keeping a constant injection pressure (i.e. momentum flux), air density and spreading angle [6, 9]. A trend line has been included to qualitatively show the effect of a parametric variable on the experimental tip velocity. Due to the previously discussed negligible influence of fuel properties within the present study, a single trend line has been irrespective of fuel type.

k values of reacting cases are found to be always larger than k_{th}, which means reacting spray tip velocity during the quasi-steady phase is always faster than the inert one because of the combustion-induced density drop. On average, increases in tip velocity are around 15% compared to the inert case, which is linked to a combustion-induced decrease in entrainment. This is consistent with recent local velocity measurements [12] for n-dodecane under the same boundary conditions as in the present experiment, which showed an increase of around 50% in spray axis velocity in the reacting case compared to the inert one.

When considering the time development of tip velocity for n-dodecane, different evolutions are observed depending on the ambient temperature and oxygen concentration, due to strong differences in ignition delay and

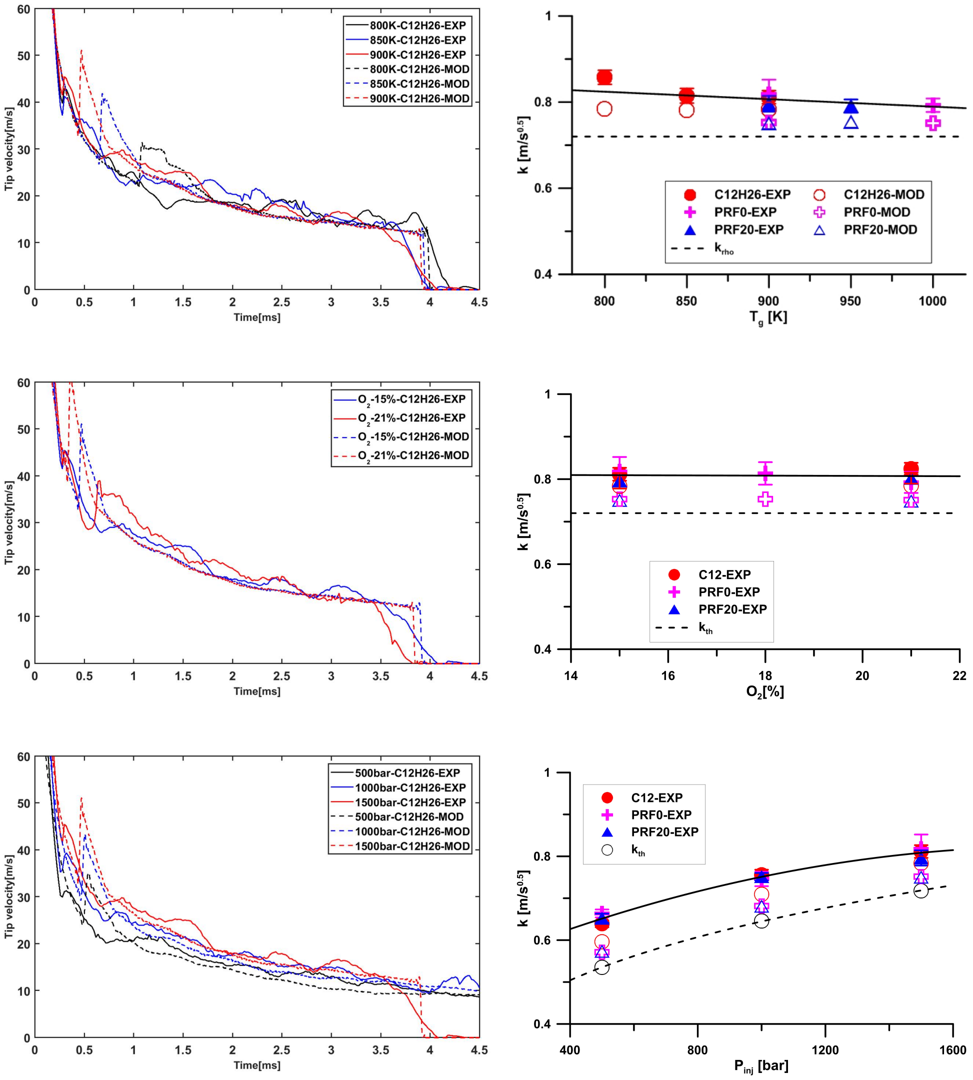

Figure 4.12. *Effect of air temperature (top row), oxygen (middle row) and injection pressure (bottom row) on tip velocity penetration. Left, time-resolved tip velocity versus penetration for n-dodecane. Solid lines correspond to experimental values, while dashed ones correspond to 1D modelling results. Right, normalized penetration vs ambient conditions for all investigated fuels. Solid symbols represent experimental results, while the hollow symbols represent 1D modelling results.*

acceleration phases. However, this parameter tends to a very similar value during quasi-steady phase for all three ambient temperature and oxygen values, i.e. none of these operating variables has a strong effect on the quasi-steady tip velocity (Figure 4.12, left) and therefore on k value (Figure 4.12, right). While velocity constant still shows a slight sensitivity to ambient temperature, the evolution with oxygen is clearly flat.

Figure 4.13 shows the local reacting to inert density ratio (ρ_r/ρ_i) from the 1D model state relationships as a function of mixture fraction. For all conditions, this parameter reaches a minimum at stoichiometric conditions, with increasing values towards both rich and lean sides. When considering the ambient temperature variation, such density ratio slightly increases with higher temperature all over the mixture fraction range, i.e. local flame density increases with higher ambient temperature. This can help explain the slightly decreasing trend in k value with higher temperature in Figure 4.12, i.e. flow progresses within a slightly higher density field, which will result in lower velocity due to momentum conservation (Eq.4.2). In the case of ambient oxygen, local density drop is noticeably different at stoichiometric conditions, but falls upon a single trend in the lean range. Taking into account that the quasi-steady tip penetration phase occurs late in time, when a relatively small proportion of the spray is at rich conditions, the local density drop in most of the spray will not change depending on the ambient oxygen content, which is consistent with the insensitivity of tip velocity constant to oxygen.

Finally, when changing injection pressure (Figure 4.12 bottom), tip velocity happens at different momentum flux values, so the different time evolutions do not overlap with each other, not even during the quasi-steady phase. Higher injection pressure values result in a faster tip velocity due to the higher momentum flux, consistently with inert conditions (Eq.4.2). Furthermore, sensitivity of k values to injection pressure is similar for both reacting and inert configurations. Just as an example, when moving from $P_{inj} = 500\ bar$ to $1500 bar$ the reduction in velocity constant is $\Delta k = 0.16\ m/s^{0.5}$ for the reacting and $\Delta k = 0.18\ m/s^{0.5}$ for the inert case. No influences of injection pressure on local density can be expected, and therefore this confirms a similar influence of injection pressure for both inert and reacting conditions. It could be argued that scalar dissipation rate effects might be important on local temperature and therefore density values, but the small size of the nozzle results in a fast mixing and therefore low gradients can be expected in the burning zone with consequently similar reacting density values.

Figure 4.14 shows an overall comparison of the k values as derived from both 1D model and experiments for all conditions in the present study. Again,

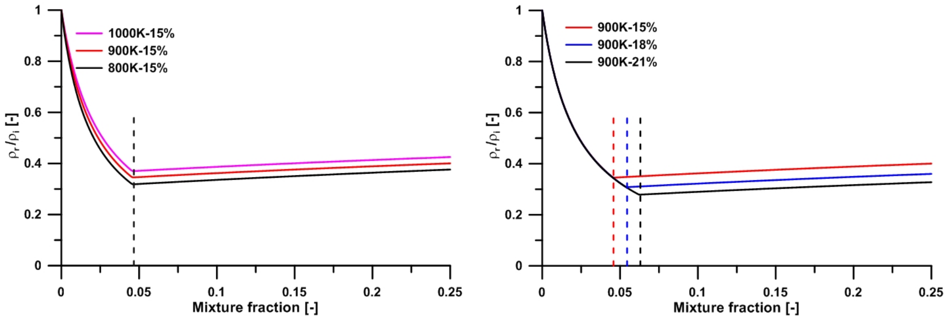

Figure 4.13. *Local reacting to inert density ratio as a function of mixture fraction for ambient gas temperature (left) and oxygen (rigth) sweep. Fuel is PRF0,* $\rho_g = 22.8$ kg/m^3, $O_2 = 15\%$. *Vertical dashed lines indicate stoichiometric mixture fraction.*

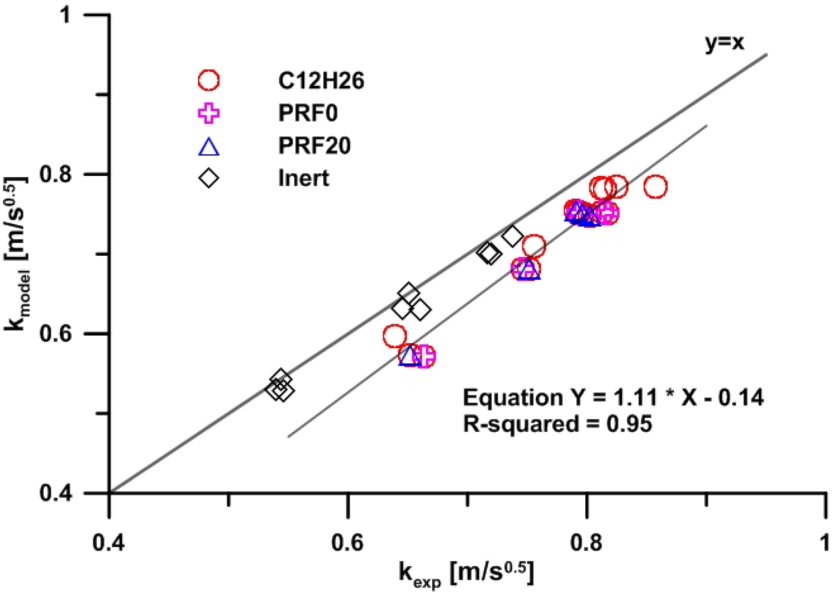

Figure 4.14. *Comparison of tip penetration velocity k constant from 1D model vs experimental values for the investigated conditions.*

predictions for the inert case are also good for the 1D model, which could be expected due to the fact that the derivation of Eq.4.2 is based upon similar hypotheses as the 1D model. As for reacting spray, they follow an adequate trend, but model results are slightly below the experimental ones. Using Eq.4.2 as a basis, one could argue that the reasons for underestimation could be in a non-adequate consideration of momentum flux, local density or radial spread. None of these gives a satisfactory explanation based upon the following: First, momentum flux just depends on the injection pressure and chamber pressure, with 1.3 *bar* difference between inert and reacting conditions, therefore this parameter is essentially constant. Second, local density has an inverse relationship to tip velocity. Therefore, the observed trend should mean that the model overestimates local density, delivering a reduced penetration. However, because of the very fast transition to reaction in the model, local densities should be rather underestimated compared to reality. Finally, next section will show that radial expansion in the model is lower than in experiments, which again should lead to a faster penetration rate. All in all, none of the three main parameters governing tip penetration seem to give a satisfactory explanation for the observed deviation. The divergence of the model compared to experiment may probably result from the description of the transient vortex area at the tip of the spray. It will be shown in later Figure 4.6, the transient head occupies around 30% of the total spray length under inert conditions, while it reaches around 50% under reacting ones. Probably this highly simplified description cannot consider the full phenomena happening during a highly transient reacting spray evolution. However, the model can still be valid for analysis purposes, as it shows a good sensitivity towards experiments.

Radial expansion

A detailed analysis of the radial expansion ($\overline{\Delta R}$) is presented in here for all three fuels. In addition, the 1D model expansion is also given here to provide a justification of the observed experimental trends.

Figure 4.15 (top) presents the effects of ambient gas temperature on $\overline{\Delta R}$. For all three fuels, $\overline{\Delta R}$ decreases with higher ambient temperature. In general, the scattering of measured values decreases with increasing ambient gas temperature, which means the flame structure is more repeatable within a higher temperature environment. In terms of modelling, one can observe a similar trend, with smaller radial dilation as temperature increases. Following the discussion in section 3.5 and Appendix A, there are two factors influencing the radial expansion when temperature is decreased:

- The higher the ambient temperature, the closer to the nozzle the burning mixture is located (shorter tsoc and LOL), which should decrease the ready-to-burn mixture radius and consequently $\overline{\Delta R}$, as from Eq.3.27.

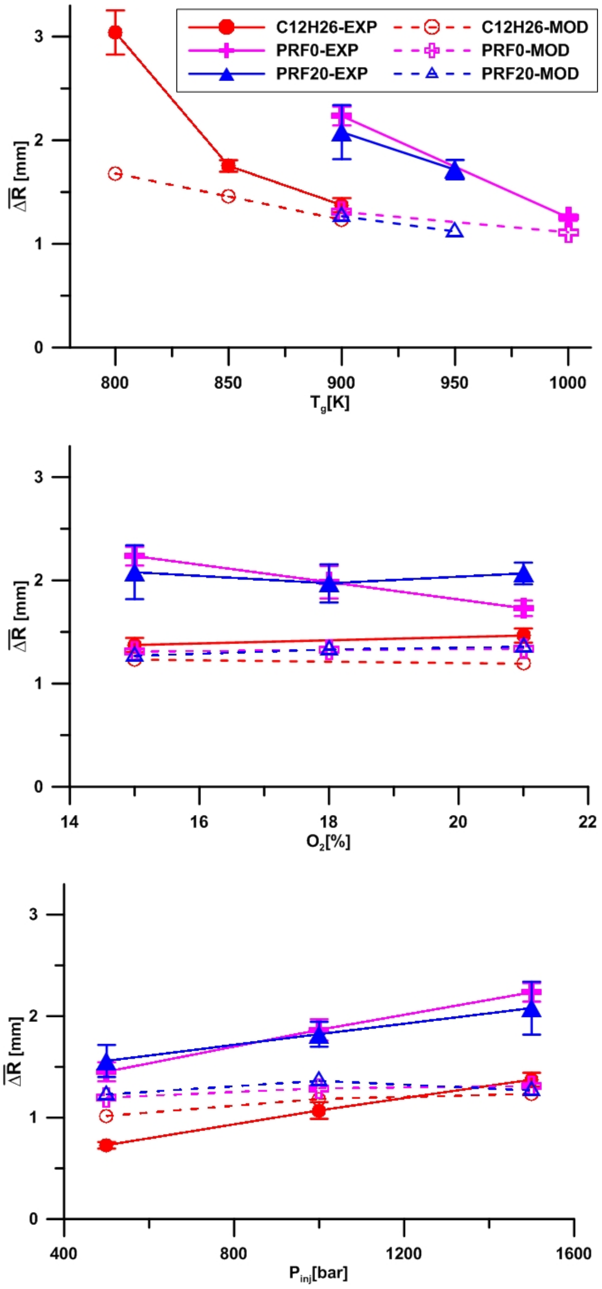

Figure 4.15. *$\overline{\Delta R}$ variation with ambient gas temperature (top), oxygen concentration (middle) and injection pressure (bottom). All variations are made based upon a nominal Spray A case, $T_g = 900K$, $O_2\% = 15\%$, $P_{inj} = 1500bar$. Solid lines represent experimental results, while the dashed lines represent modelling results.*

- Figure 4.13 has shown the local inert to reacting density ratio as a function of mixture fraction for three different temperature values and PRF0. This parameter is seen to decrease with higher temperature, which would justify a reduced lateral expansion when moving from inert to reacting conditions.

Both effects would result in the same trend, namely an increase in radial expansion, which agrees with both experimental and numerical results in Figure 4.15.

The effect of ambient oxygen concentration on $\overline{\Delta R}$ is shown in Figure 4.15 (middle), with no meaningful influence observed in neither experiments nor modelling results. According to the description in section 3.5, the density drop and the location of the ready-to-burn mixture can explain $\overline{\Delta R}$ results. Figure 4.13 has shown the local reacting to inert density ratio as a function of mixture fraction for the three oxygen values within the study. In the lean range (from the local minimum in density towards lower mixture fraction values) the local density drop is independent of oxygen concentration, while differences in the rich side are not too large. This fact confirms that the density drop will not change much with oxygen concentration. On the other hand, an increase in the oxygen content from 15 to 21% reduces ignition delay in $100\mu s$, as well as lift-off length in 5 *mm*, which locates the ready-to-burn mixture on average around 4 *mm* closer to the nozzle. When considering both effects, it is the constant inert-to-reacting density drop which explains the similar radial expansion for all three oxygen cases.

The influence of injection pressure on $\overline{\Delta R}$ is shown in Figure 4.15 (bottom). It can be seen that $\overline{\Delta R}$ shows a slight increase with increasing injection pressure. All fuels show a similar sensitivity with injection pressure under such operating conditions, which is consistent with previous finding. Modelling results tend to increase from 500 to 1000 *bar*, becoming flat in the 1000 to 1500 *bar* range. In a first order of magnitude, injection pressure should have no effect on the local density. In global terms, the effect of injection pressure is just shifting the burning zone geometry by acting upon the lift-off length and the maximum extent of the spray. The higher the injection pressure, the further away from the nozzle combustion will occur, and according to the description in Section4.4 this should result in a larger radial expansion, as experiments suggest.

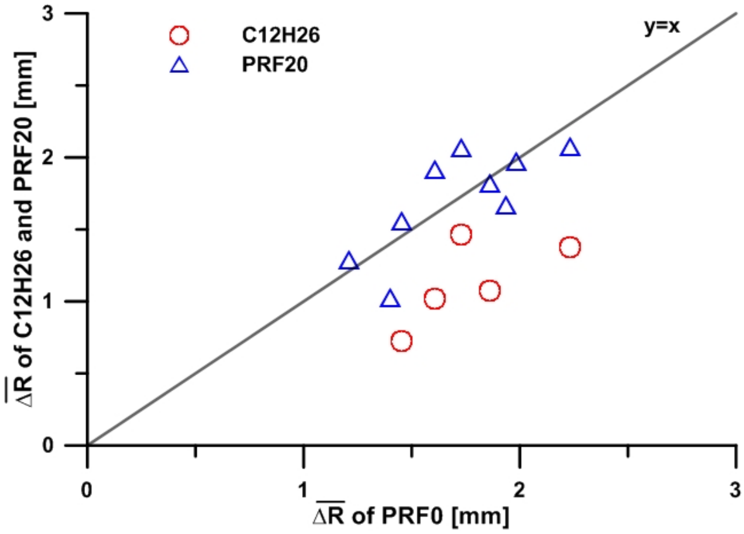

Figure 4.16. *Analysis of fuel effects on on average* $\overline{\Delta R}$.

Experimental values of $\overline{\Delta R}$ are shown in Figure 4.16 from the fuel perspective. Each point compares the radial expansion of two fuels at identical operating conditions. PRF0, which has an intermediate cetane number, has been used as a reference. In general terms, trends among fuels are proportional, i.e. conditions with large or small expansion values are the same for all three fuels. PRF0 and PRF20 are closer to each other, while $\overline{\Delta R}$ of n-dodecane shows smaller values than that of other two fuels, which can also be found from modelling results. It must be noted that the higher cetane number of n-dodecane will result in a shorter ignition delay and lift-off length for the same operating conditions. This will bring ready-to-burn mixture closer to the nozzle, which will result in lower radial expansion.

Finally, previous plots have shown that the radial expansion predicted by the 1D model is always smaller in magnitude than that observed in the experiments. However, there is a proportionality between the model results and experiments, meaning that the model seems to capture experimental trends although with a lower sensitivity. The differences can be explained on the base of two arguments:

- First, one has to consider that the definitions of radial increase are different. Experimental results are based upon a "median" location of the spray radial limit, while in case of modelling the radius corresponds to a more classical definition, namely the location where axial velocity is 1% of the on-axis velocity. Recent comparisons [12] between the present results and experimental local velocity results also indicate that the values of the second approach are smaller than those in the first one, in agreement with the modelling results shown here. In spite of that, model predictions of the velocity field within the spray for three investigated conditions are quite accurate compared to PIV experiments [12].

- Another point to consider is that, in the simplified description from the 1D model, the radial expansion is evaluated at start of combustion. Although this parameter does not change largely in time, temporal evolution shows that the initial values are below the quasi-steady ones. This might mean that in reality the radial expansion process extends towards later timings after combustion onset, which brings the mixture further away from the nozzle and should therefore result in larger expansion values compared to the model.

4.5 A study on soot production by combining extinction and radiation

Because of a higher soot radiation and extinction, as well as the signal-to-noise ratio, the $T_g = 1000\ K$ case ($P_{inj} = 1500\ bar$, $\rho_g = 22.8\ kg/m^3$, $O_2 = 15\%$) was chosen to study the diagnostic sensitivity and uncertainty first. After,the effects of parametric variation on soot production were analyzed in later section.

4.5.1 Analysis of diagnostic sensitivity and uncertainty

The parameters used to calculate k_e through the RDG theory are referenced from standard ECN parameters [13]. It has to be pointed all these parameters are kept same for three wavelength light applied for both extinction and radiation measurements. As a consequence, the k_e values are 7.59, 7.40 and 7.27 corresponding to blue (460 nm), green (550 nm) and red (660 nm) spectral light, respectively.

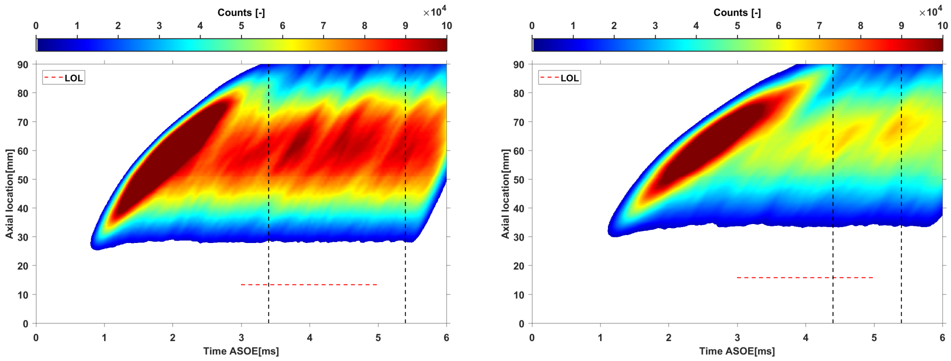

(a) $P_{inj} = 1500\ bar$, $\rho_g = 22.8\ kg/m^3$, $T_g = 1000\ K$, $O_2 = 15\%$

(b) $P_{inj} = 1000\ bar$, $\rho_g = 22.8\ kg/m^3$, $T_g = 900\ K$, $O_2 = 15\%$

Figure 4.17. *Examples of IXT plot. Vertical dashed lines represent the time-averaged zone for steady soot analysis.*

As mentioned in [13], quasi-steady period of the spray flames begins after a jet head separates from the rest of the flame and disappears from visualization window. Figure 4.17 shows a temporal and spatial flame luminosity map by integrating flame luminosity at each axial location for each frame of a natural luminosity with a 660 nm wavelength, namely IXT (Intensity-Axial-Time) plot [14] which was calculated as follows:

$$I(x,t) = \int_{r_1}^{r_2} I(x,r,t)dr \tag{4.4}$$

where x is the spray axial direction, r is the spray radial direction, r_1 and r_2 are the flame boundary positions. Even though this plot was obtained from averaged images from 40 repetitions, relatively high fluctuations can still be observed during this so-called quasi-steady period. As a consequence, in order to skip the effects of turbulence-induced fluctuations, the time-averaged images during this quasi-steady period was focused in this study. The time-averaged interval starts from the time when the flame tip disappears from optical window until the end of injection. It is $3.4 - 5.4\ ms$ and $4.4 - 5.4\ ms$ for $P_{inj} = 1500\ bar$ cases and $P_{inj} = 1000\ bar$ case respectively. The period for recording the OH^* chemiluminescence is $3 - 5\ ms$ ASOE. This time zone is presented as the vertical dashed lines in Figure 4.17.

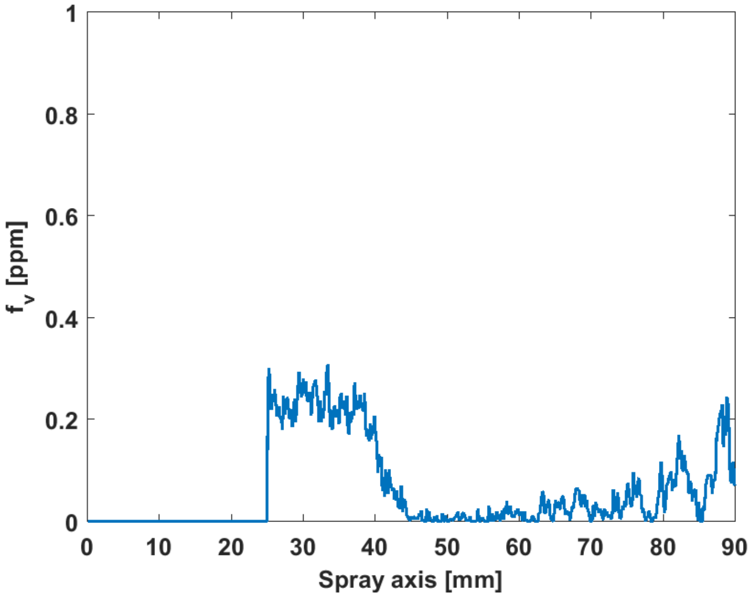

Figure 4.18. *Soot volume fraction along spray axis from time-averaged results* ($T_g = 800\ K$, $P_{inj} = 1500\ bar$, $\rho_g = 22.8\ kg/m^3$, $O_2 = 15\%$).

As mentioned by [13], beam steering defined lower extinction detection limit. When the ambient temperature is at 800 K (P_{inj} = 1500 bar, ρ_g = 22.8 kg/m^3, O_2 = 15%), no soot was observed from radiation images. Thus, it was used here to check this lower extinction limit. Figure 4.18 presents soot volume fraction along spray axis under such condition derived from time-averaged KL map(liquid part was removed). It can be seen that the lower detection limit is smaller than 0.3 ppm in general and it is reduced even less than 0.1 mm after 45 mm. Thus, the extinction caused by beam steering is negligible compared with a magnitude 10 ppm caused by soot extinction as shown in later section.

Extinction and Soot volume fraction Sensitivity

It is still a big challenge to get accurate quantitative soot extinction measurements as multiple parameters are not well known and are characterized by large uncertainties [13]. One source of the dominated uncertainties is the dimensionless extinction coefficient k_e (Eq.3.8) from RGD theory which depends on particle diameter, aggregate size and complex refractive index. According to the analysis in [13], the authors concluded that complex refractive index dominates the overall uncertainty. Figure 4.19 shows a comparison of time-averaged KL map between blue and red LED measurements during this quasi-steady period. The blue one(KL^*) was converted from Eq.3.21. It shows a pretty good agreement with [13] that the extinction signal from shorter wavelength light is stronger and the ratio is much higher in the upstream of soot cloud where nascent soot with higher hydrogen-to-carbon (H/C) ratios is expected. It can be concluded that the k_e value has a strong uncertainty and complex refractive index should be different with soot maturity rather than just one uniform value.

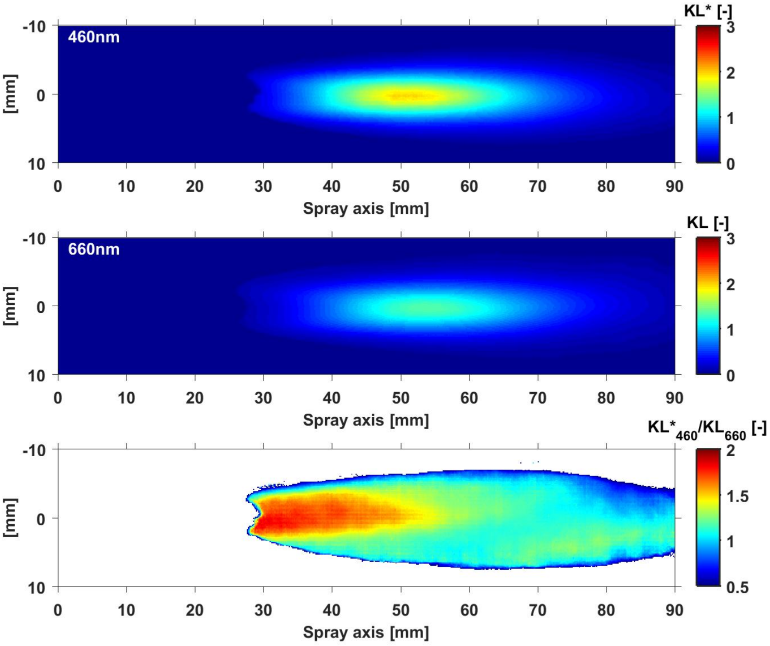

Figure 4.19. *Comparison of time-averaged KL map and KL ratio*($KL^{\star}_{460}/KL_{660}$) *derived from blue (460 nm) and red (660 nm) LED extinction measurements. The blue one was converted based on Eq.3.21.* ($P_{inj} = 1500$ *bar*, $T_g = 1000$ *K*, $\rho_g = 22.8$ kg/m^3, $O_2 = 15\%$).

Figure 4.20 presents a comparison of KL value on the spray axis from both LED tests under two ambient temperatures. For both λ, the same trend is observed that KL increases with higher ambient temperature and both LEDs present a similar sensitivity with different operating conditions. As a consequence, the later parametric study follows the suggestion from [13] that shorter wavelength is applied for the soot volume fraction analysis, as soot-generated extinction signal-to-noise ratio is higher.

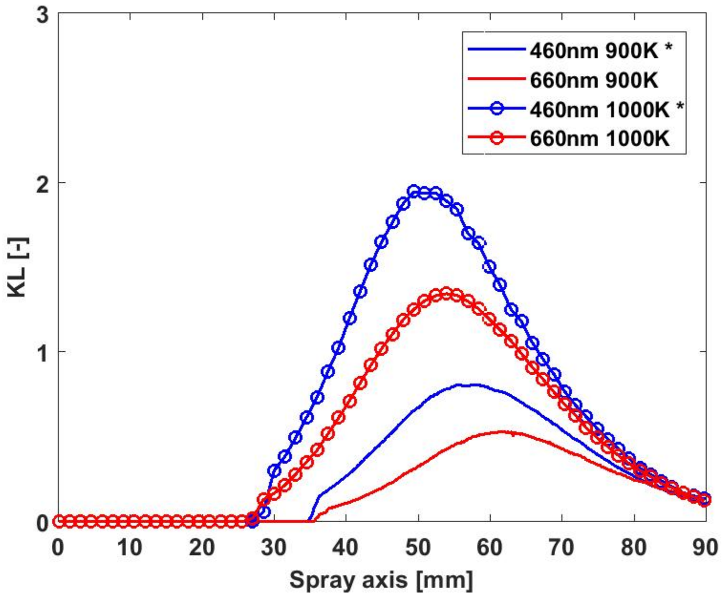

Figure 4.20. *Comparison of KL value on the spray axis derived from time-averaged KL map under two ambient temperatures. The blue one was converted based on Eq.3.21 (*$P_{inj} = 1500bar$*,*$\rho_g = 22.8kg/m^3$*,* $O_2 = 15\%$*)) .*

Besides onion-peeling method, the soot volume fraction is also reconstructed using an ECN recommended inverse Radon transformation as a reference. Figure 4.21 presents a comparison of soot volume fraction(f_v) obtained from these two method. It can be observed from f_v map and radial distribution, both methods show a good agreement on the magnitude all over the flame except the data on symmetric axis where onion-peeling method shows a higher noise level. Considering Inverse radon method is not able to be applied for local temperature reconstruction, onion-peeling method is used for later analysis.

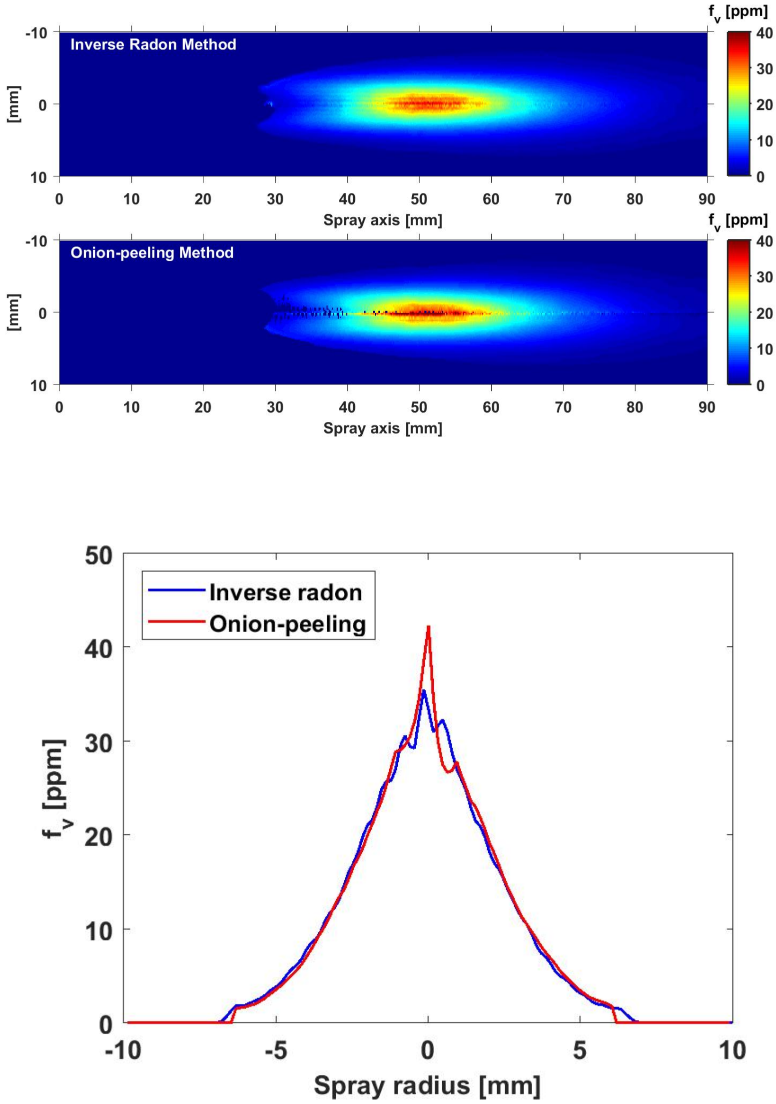

Figure 4.21. *Soot volume fraction on symmetric plane(top)and a radial distribution at* $x = 50mm$*(bottom) of the flame after reconstruction from Blue(460 nm) LED KL maps with inverse radon method and onion-peeling method respectively(*$P_{inj} = 1500$ *bar,* $T_g = 1000$ *K,* $\rho_g = 22.8$ kg/m^3*,* $O_2 = 15\%$*).*

Soot temperature sensitivity

Figure 4.22 presents a comparison of soot temperature on spray axis obtained from red LED (660 nm) KL map and blue LED (460 nm) KL map respectively, while the radiation images used here are red ones(660 nm). One thing needs to be kept in mind that the the temperature distribution on the axis presented here and in later analysis is averaged from both half flame part at 1 mm away from symmetry axis (horizontal dashed red lines in Figure 4.23), in order to skip the noise along symmetry axis brought by deconvolution. As we know from Figure 4.19 and Figure 4.20, the different wavelengths of extinction light result in an apparent difference on KL value. However, it can be seen from Figure 4.22 this KL difference doesn't bring a significant uncertainties on soot temperature, except the soot initial location where the KL ratio is much bigger(as show in Figure 4.19).

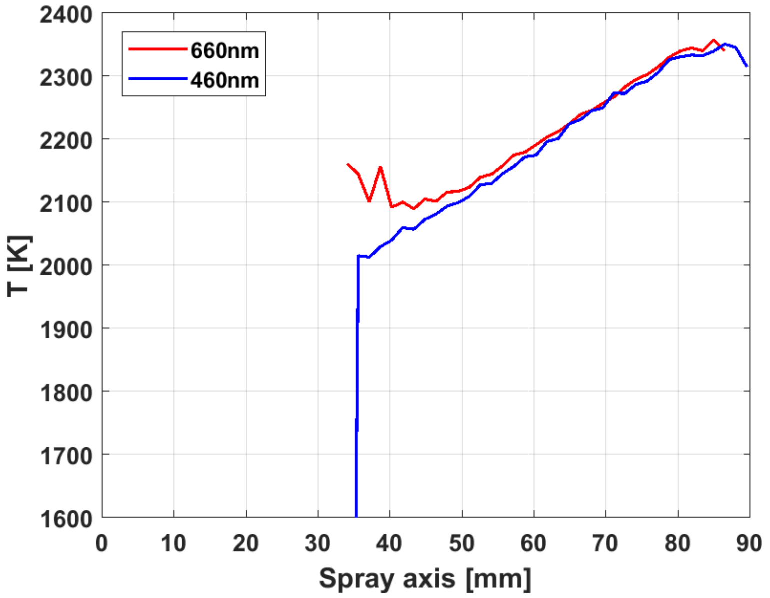

Figure 4.22. *Sensitivity of soot temperature on spray axis with wavelength of extinction light(*$P_{inj} = 1500\ bar$*,* $T_g = 1000\ K$*,* $\rho = 22.8\ kg/m^3$*,* $O_2 = 15\%$*).*

On the other hand, soot temperature sensitivity with radiation wavelength is also presented in Figure 4.23, where the extinction coefficient (k) used for this reconstruction is obtained from blue LED KL map.

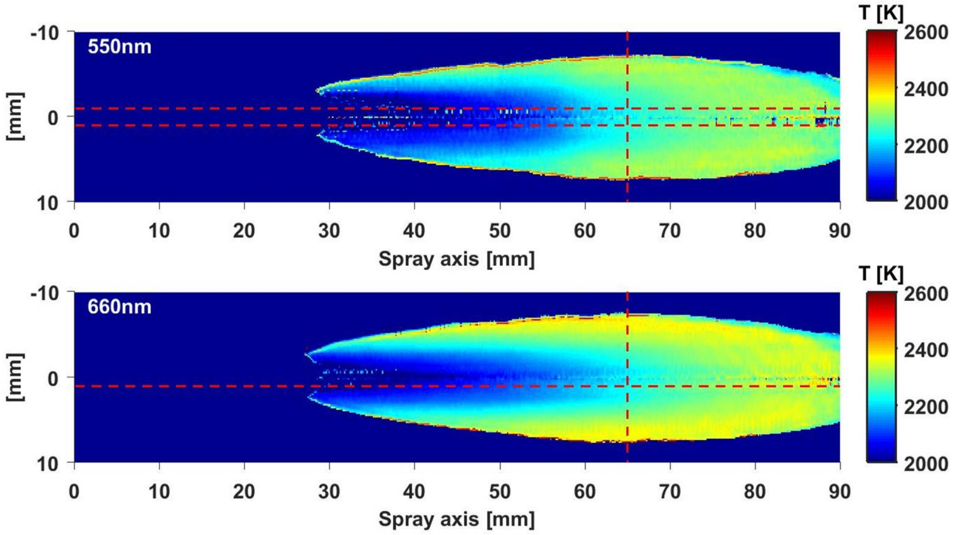

Figure 4.23. *Soot temperature on flame symmetric plane from reconstruction by green and red time-averaged radiation images. Blue LED KL map was applied for deconvolution(P_{inj} = 1500 bar, T_g = 1000 K, ρ = 22.8 kg/m^3, O_2 = 15%).*

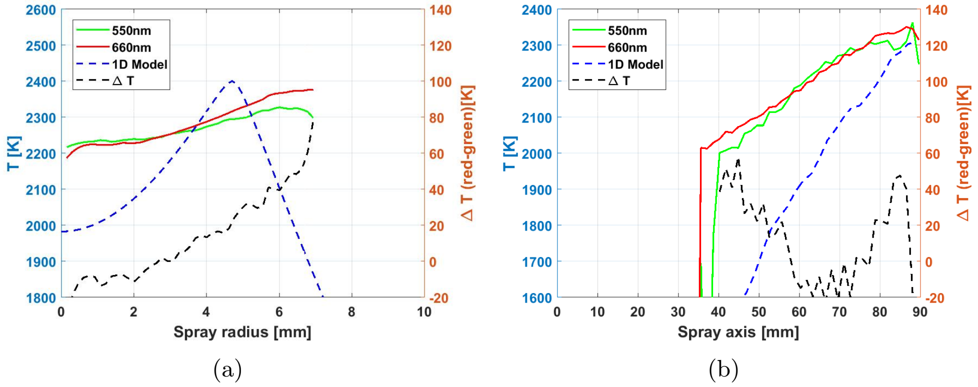

(a) (b)

Figure 4.24. *Radial temperature distribution at 65mm(a) and axial temperature distribution at 1mm away from spray axis(b). δT represent the temperature difference from red (660 nm) and green (550 nm) radiation wavelength(P_{inj} = 1500 bar, T_g = 1000 K, ρ = 22.8 kg/m^3, O_2 = 15%).*

Radial and axial temperature distribution, derived from Figure 4.23, are also shown in Figure 4.24. In addition, the temperature distribution from 1D spray model is also shown here as a reference. As shown from Figure 4.23 and Figure 4.24, the temperatures of both wavelength follow the same trend that temperature increases with spray radius and spray axis. However, experimental data presents a much less sensitivity with spatial evolution compared with the model ones. The peak of 1D spray model temperature curve in Figure 4.24 represents the stoichiometric adiabatic temperature (T_{ad}). Both green (550 nm) and red (660 nm) radiation-derived temperatures are lower than T_{ad} which indicates they are realistic. However, the temperature divergence between both wavelength is much higher at upstream and periphery of soot cloud, where the soot concentration as well as radiation intensity are much lower and so does the signal-noise ratio. The red radiation images are chosen for further analysis considering its higher intensity.

4.5.2 Parametric analysis

The Soot volume fraction(f_v) and Temperature (T) distribution on flame-axis plane under four different operating conditions reconstructed from blue (460 nm) LED KL map and red (660 nm) radiation images are provided in Figure 4.25. Meanwhile, OH^* contour derived from deconvolution of OH^* images as well as LOL are also presented here to check the relative location between soot cloud and OH radical. It has to be noted the OH^* chemiluminescence visualization window is $5mm$ shorter than soot tests. A cross-sectional average equivalence ratio at LOL($\bar{\phi}_H$) is also presented in Figure 4.25. Pickett and Siebers have proven $\bar{\phi}_H$ is a good indicator for soot formation. In addition, a flame coordinate ($1/\phi_{cl}(x)$) is applied in later parametric discussion to represent the effects solely due to the oxygen-fuel ratio in the combusting mixture. $\phi_{cl}(x)$ is equivalence ratio along spray axis at any axial location(x), which was calculated using following relationship:

$$\phi_{cl}(x) = \frac{Z_{cl}(x)}{1 - Z_{cl}(x)} \cdot \frac{1 - Z_{st}}{Z_{st}} \tag{4.5}$$

where $Z_{cl}(x)$ is the fuel mixture fraction along spray axis which is obtained from 1D spray model. Z_{st} is the stoichiometric mixture fraction.

It can be seen from Figure 4.25 that the high soot concentration region locates at the centre of flame for all cases, where the local temperature is lower than around $2200K$ and no OH radical is observed. When it comes to the downstream, soot amount decrease dramatically because of lower formation rate and faster oxidation rate caused by fuel-lean mixture and appearance of OH radical respectively. This trend is consistent with previous research

[13, 15, 16]. On the other hand, the high temperature soot location shows a consistency with OH radical area. The temperature gradient is quite big at upstream, where the temperature increases from spray axis to the flame periphery, while the temperature distribution at downstream is more uniform. It is consistent with Aizawa et al's research [17], where they measured the in-flame temperature at different location by means of a thermocouple.

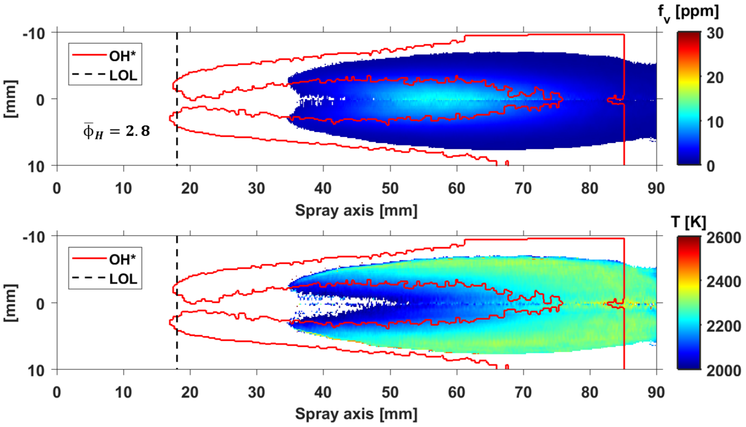

(a) (P_{inj} = 1500 bar, ρ_g = 22.8 kg/m^3, T_g = 900 K, O_2 = 15%)

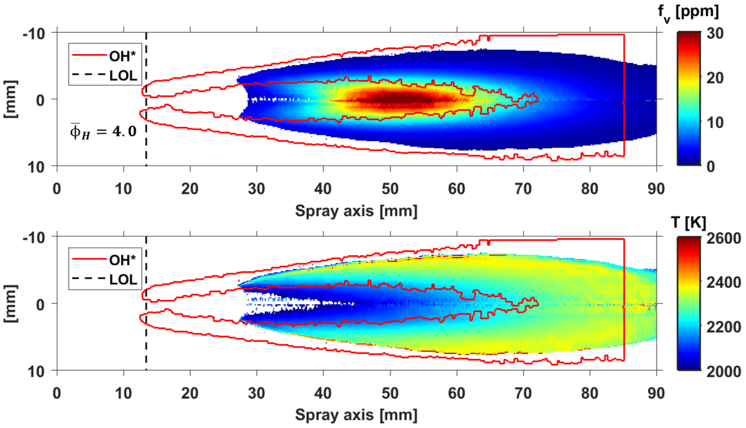

(b) (P_{inj} = 1500 bar, ρ_g = 22.8 kg/m^3, T_g = 1000 K, O_2 = 15%)

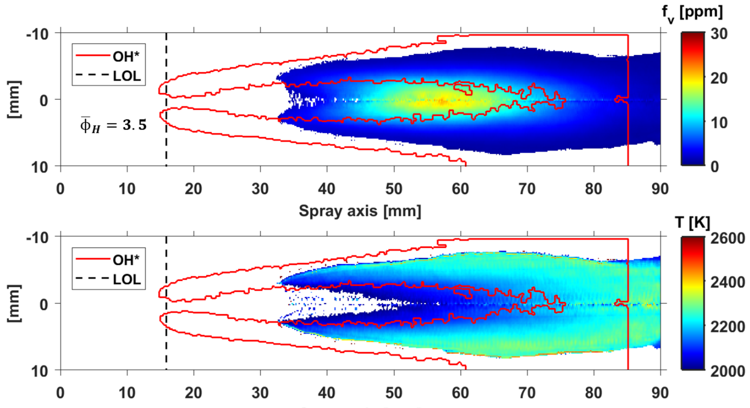

(c) (P_{inj} = 1000 bar, ρ_g = 22.8 kg/m^3, T_g = 900 K, O_2 = 15%)

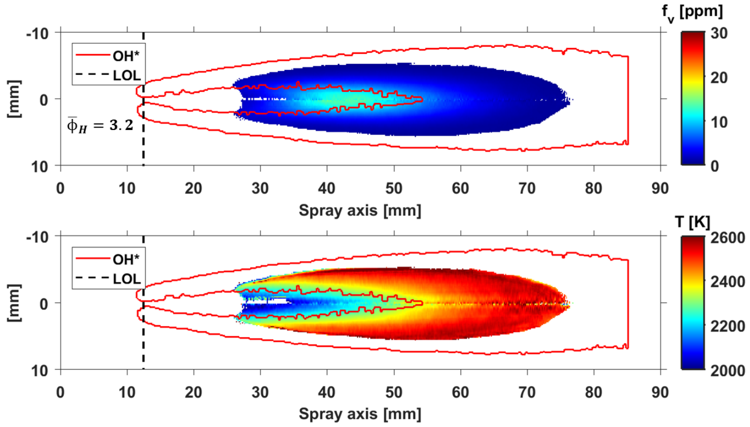

(d) (P_{inj} = 1500 bar, ρ_g = 22.8 kg/m^3, T_g = 900 K, O_2 = 21%)

Figure 4.25. *Soot volume fraction and Temperature distribution on flame symmetric plane reconstructed from blue (460 mm) LED KL map and red (660 mm) radiation images. Vertical dashed lines represent flame LOL. Red curves represent OH* contour.*

Ambient temperature

Soot volume fraction (f_v) and soot temperature (T) distribution with ambient temperature variation can be seen from Figure 4.25 (a) and Figure 4.25 (b). As expected, an increase in ambient temperature results in a shorter LOL, an higher $\bar{\phi}_H$, higher soot temperature and higher soot production. However the soot temperature doesn't show big sensitivity with ambient temperature, compared with that with oxygen concentration as shown in later section. The soot volume fraction and temperature along spray axis and flame coordinate under both temperatures are shown in Figure 4.26. It is well known net soot production is the balance between soot formation and soot oxidation. Soot formation rate is higher than oxidation rate from the initial soot location to the f_v peak location, while oxidation rate is more dominated from f_v peak location to flame tip. As shown in Figure 4.26, the f_v peak locations of two cases become closer for flame coordinate. It is a result of slightly higher the air entrainment with a higher ambient temperature at any axial location [12]. It can be seen from Figure 4.26 (b) that the soot level of 1000 K ambient temperature case is much greater than that of 900K from the start of soot to the peak, around three times. After the peak, the difference is becoming smaller and collapses to a single curve. However, the axial soot temperature difference between two cases is quite small and pretty uniform along the whole flame coordinate. The average temperature difference is just 48 K (from 0.4 to 0.6 flame coordinate). It indicates the higher flame temperature of 1000 K ambient temperature cases is not the dominated factor for the higher soot production. On the other side, the higher $\bar{\phi}_H$ value due to shorter LOL and higher ambient temperature contributes to more soot precursors (formaldehyde and PAH) , which makes the soot formation rate much faster for higher ambient temperature case. The axial soot temperature increase toward the downstream indicates the progress of fuel-air mixing. As obtained from 1D spray model, the stoichiometric surface at spray axis locates at around 100 mm.

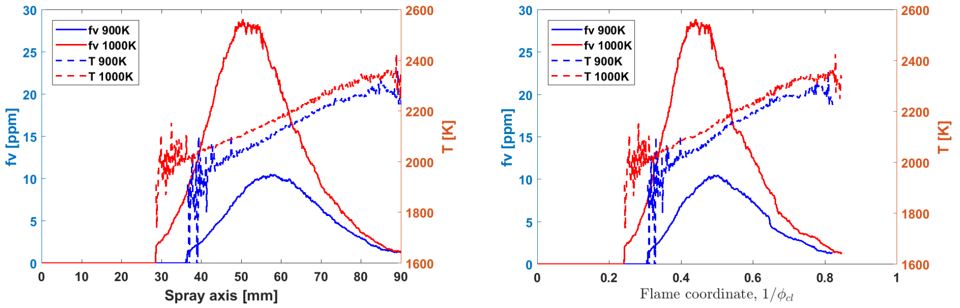

(a) (b)

Figure 4.26. *Soot volume fraction and soot temperature along spray axis(a) and flame coordinate(b) with ambient temperature variation (P_{inj} = 1500 bar, ρ_g = 22.8 kg/m^3,O_2 = 15%) .*

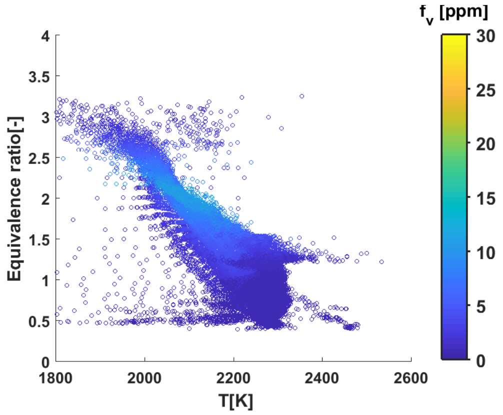

(a) $T = 900\ K$

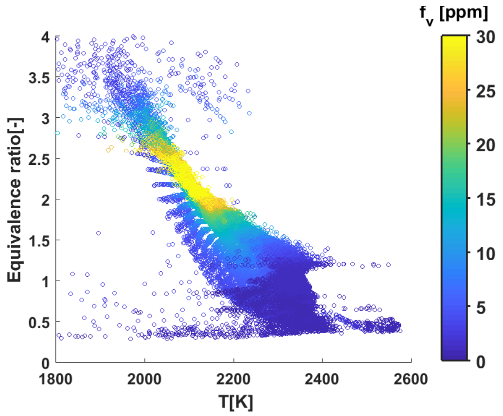

(b) $T = 1000\ K$

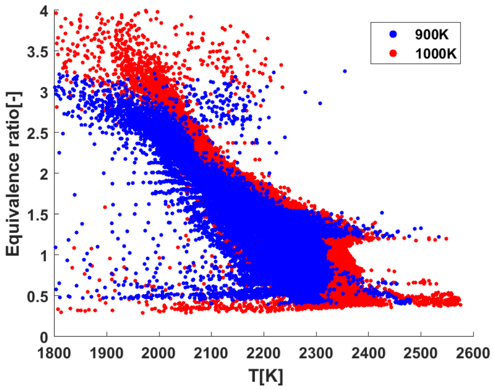

(c) Soot relative distribution

Figure 4.27. *$\phi - T$ with soot f_v plot of two ambient temperature cases and their relative distribution($P_{inj} = 1500\ bar$, $\rho_g = 22.8\ kg/m^3$, $O_2 = 15\%$).*

The $\phi - T$ plots and relative soot distribution of two temperature cases are shown in Figure 4.27, where T and f_v are derived from Figure 4.25, ϕ is obtained from 1D model. Keep in mind, the $\phi - T$ plots presented here are the competition results between soot formation and soot oxidation which are different with $\phi - T$ plots in [18, 19] where only the soot formation were considered. We already know from Figure 4.25 that the lower temperature($<$ 2200 K) region locates at the center of soot upstream with high equivalence which corresponds to the top parts in Figure 4.27, while the relatively higher temperature($>$ 2200 K) region locates at the downstream and periphery of soot cloud which corresponds to the bottom parts in Figure 4.27. In general, the $\phi - T$ plot of 1000 K case is shifted a little right compared with that of 900 K case, as shown in Figure 4.27(c). The f_v values of both cases decrease dramatically when the ϕ value is smaller than 1 where the spray is out of stoichiometric surface. Furthermore, it can be seen from Figure 4.27(c), the soot of 1000K case appears at higher ϕ region. As mentioned above, it is caused by higher the much more formaldehyde and PAH formation brought by the shorter LOL. One interesting thing observed is the difference of maximum soot temperature is quite close to the adiabatic temperature difference ($\Delta T_{ad} = 78$ K).

Injection pressure

Soot volume fraction and soot temperature along flame coordinate with injection pressure variation are shown in Figure 4.28. The air entrainment is same for both cases at any axial location because spray spreading angle and T_{ad} don't change with injection pressure. Thus, flame coordinate is same with spray axis for both cases and spray axis is not shown here. As expected, lower injection pressure leads to a lower soot production and the location of f_v peak is quite similar, as shown in Figure 4.28. The axial soot temperature shows slightly higher with higher injection pressure. However, difference between two cases is quite small, almost negligible compared with uncertainty. The average temperature difference is just 35 K (from 0.4 to 0.6 flame coordinate). Thus, it shouldn't be the dominated reason to bring the difference on soot production. As presented in Figure 4.25 (a) and Figure 4.25 (c), $\bar{\phi}_H$ increases slightly with lower injection pressure because of the shorter LOL, which contributes on soot formation. Another main contribution factor on this higher soot production for lower injection pressure is the longer residence time caused by the lower penetrating velocity and longer moving path from LOL to the f_v peak location. It provides a longer residence time for soot growth and agglomeration. On the other hand, if we assume the oxidation rate at each location is similar for both cases considering similar mixture and temperature distribution, more soot will be consumed at the same location because of the longer residence time.

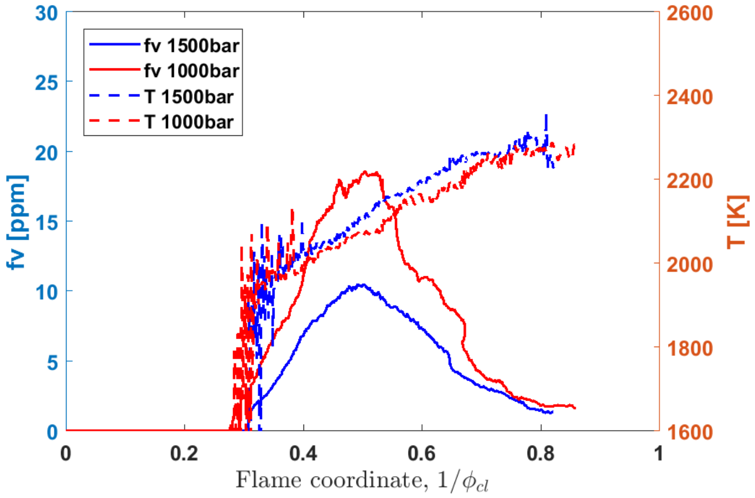

Figure 4.28. *Soot volume fraction and soot temperature along flame coordinate of two injection pressure cases*($T_g = 900\ K$, $\rho_g = 22.8\ kg/m^3$, $O_2 = 15\%$).

These findings can also be observed by the $\phi - T$ plot, as shown in Figure 4.29. Soot production of lower injection pressure case starts from a slightly higher equivalence ratio region because of the shorter LOL. It can be observed Figure 4.29 (c) that soot distribution shapes of two cases are pretty similar and the high soot locations are also pretty similar($T \approx 2050\ K$, $\phi \approx 2$). It indicates the injection pressure doesn't make significant difference on equivalence ratio and flame temperature and confirms the higher net soot production of of 1000 *bar* injection pressure case is mainly caused by the longer residence time. Once again, it is consistent with adiabatic temperature that maximum soot temperature doesn't change with injection pressure.

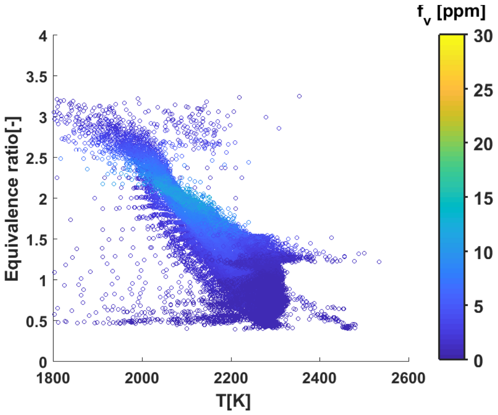

(a) $P_{inj} = 1500\ bar$

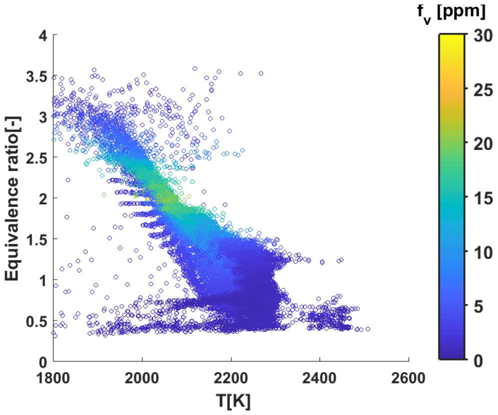

(b) $P_{inj} = 1000\ bar$

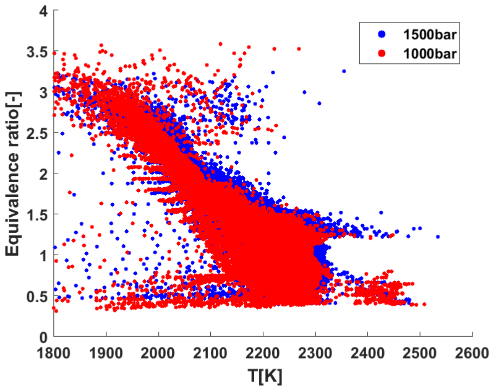

(c) Soot relative distribution

Figure 4.29. *$\phi - T$ with soot f_v plot of two injection pressure cases and their relative distribution($T = 900\ K$, $\rho_g = 22.8\ kg/m^3$, $O_2 = 15\%$).*

Oxygen concentration

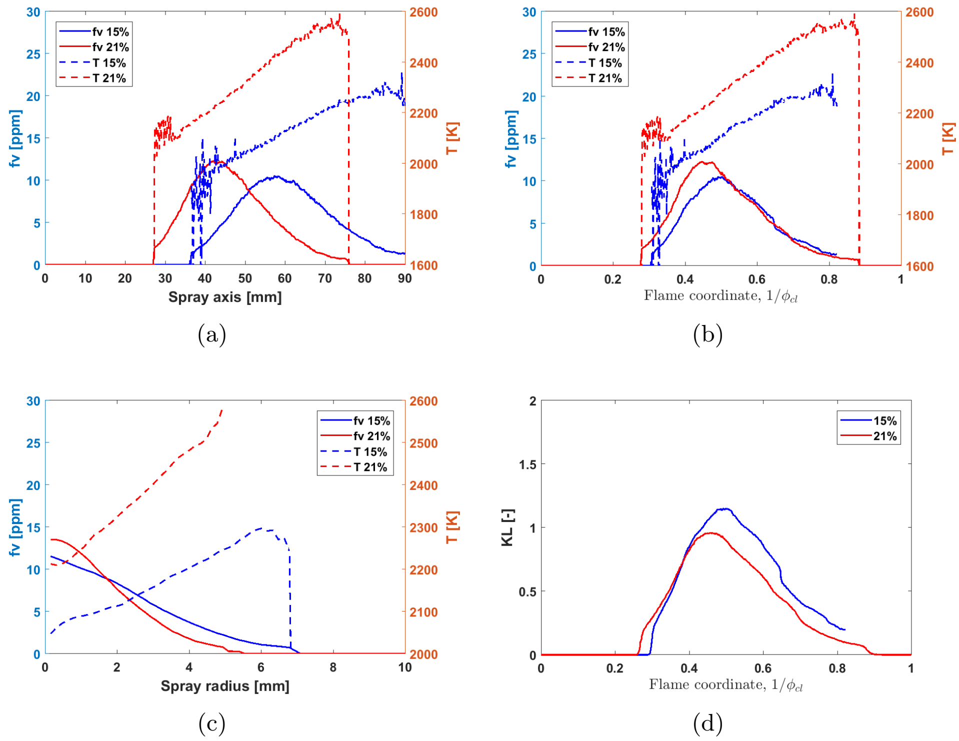

(a) (b)

(c) (d)

Figure 4.30. *Soot volume fraction and soot temperature along axial location (a) , flame coordinate (b) and spray radius at 0.9 flame coordinate (c) and KL along flame coordinate(d) with oxygen concentration variation(P_{inj} = 1500 bar,T_g = 900 K, $\rho_g = 22.8$ kg/m^3).*

Soot volume fraction and soot temperature along spray axis and flame coordinate with oxygen concentration variation are presented in Figure 4.30 (a) and Figure 4.30 (b) respectively. It can be found that the peak f_v location moves much farther away from injector nozzle with lower oxygen concentration. However, they become much closer with air entrainment conversion(flame coordinate). Apparently, the effects of oxygen on soot temperature is much greater compared with that of ambient temperature and injection pressure. The axial average temperature difference is 168 K (from 0.4 to 0.6 flame coordinate). However, the effects of oxygen on soot volume fraction is not as strong as ambient temperature and injection pressure.

Because of the slightly higher $\bar{\phi}_H$ and higher local flame temperature, soot production increases a little with increasing oxygen concentration before peak f_v location, while the two f_v curves collapse to a single one after the peak value.

Figure 4.30 (c) presents soot volume fraction and soot temperature along spray radial direction at same flame coordinate (0.9). It can be seen the soot cloud radius is narrower and f_v gradient is greater under 21% oxygen concentration than that under 15% oxygen concentration. In addition, the soot temperature difference increases with flame radius. They are caused by the sharper equivalence ratio gradient under higher oxygen concentration. The axial optical thickness (KL) along flame coordinate is shown in Figure 4.30 (d). KL is an integrated parameter and it is proportional with the integrated total soot mass along the line-of-sight optical path. It is interesting to see the trend of KL with oxygen is opposite with the f_v one, which increases with lower oxygen concentration. That can be explained from Figure 4.30 (c), the optical path under 15% oxygen concentration is longer and the f_v value is higher than 21% case after around 2 mm. As a conclusion, the overall soot production of 15% case is higher than that of 21% case.

The $\phi - T$ plots derived from Figure 4.25 and 1D model are shown in Figure 4.31. Because of the flame temperature of 21% oxygen case is higher overall spray, its $\phi - T$ plot is shifted to the higher temperature direction. However, the difference of maximum soot temperature(around 270 K) is much smaller than that of adiabatic temperature difference(ΔT_{ad} = 442 K). That can be explained by reference from Musculus [20] . He mentioned heat transfer from hot soot radiation can reduce the gas temperatures in the sooting zone. Hence, reduced gas temperatures cause reduced peak soot temperatures.

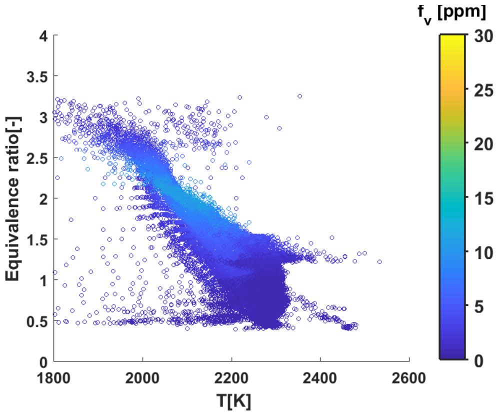

(a) $P_{inj} = 1500\ bar$

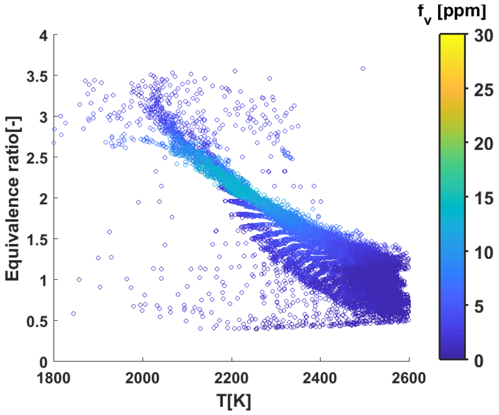

(b) $P_{inj} = 1000\ bar$

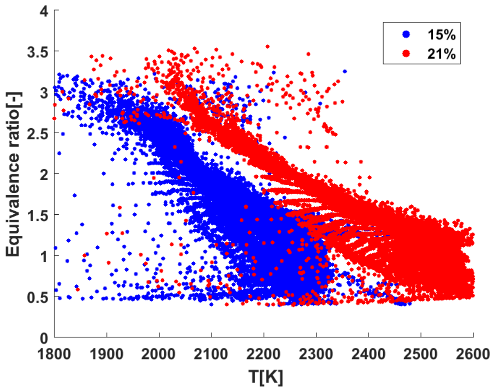

(c) Soot relative distribution

Figure 4.31. *$\phi - T$ with soot f_v plot of two injection pressure cases and their relative distribution($T = 900\ K$, $\rho_g = 22.8\ kg/m^3$, $O_2 = 15\%$).*

4.6 Summary and conclusions

Spray dynamics and soot production of single-hole reacting Diesel spray were studied under quiescent conditions(CPF). As the main tools, high-speed schlieren imaging technique was applied to measure the spray contours and quantify spray tip penetration and radial expansion, while a developed combined extinction-radiation technique was applied to quantify the soot volume fraction and temperature simultaneously. N-dodecane was used here as the main fuel in this study. Besides that, other two kinds of fuels were also measured to investigate the effects of fuel properties on radial expansion and penetration velocity. This study revealed the following conclusions:

- The radial width was calculated from the probability contours. From the analysis of the results it emerged that the shape of the reacting spray can be divided into three regions:

  I. Quasi-steady inert: from nozzle tip to the Lift-off length.

  II. Quasi-steady reacting: from lift-off length to the position where the contour stops increasing radially.

  III. Transient: from the end of the previous zone to the spray tip.

- After comparing of the radial width of reacting and inert spray at the same tip penetration, it was found that the contour at the quasi-steady reacting part is almost parallel to the corresponding part in the inert case. In other words, the radial contour of the reacting spray is simply the result of shifting the inert one by an approximately constant value.
- A scaling factor (k) on derivative of penetration was defined here to quantify the combustion-induced effect on spray tip velocity in the quasi-steady phase. Inert spray follows quite accurate definition of this value which is only depending on momentum flux $\dot{M}_0$, air density ρ_g and spreading angle.
- $\overline{\Delta R}$ of different fuels shows consistent trend with parametric variations. It increases with lower ambient temperature and higher injection pressure, while it is insensitive to oxygen content. A simplified description indicates that this parameter is governed by density drop due to combustion, as well as location of the ready-to-burn mixture to the nozzle at combustion onset.
- k values of reacting cases are always bigger than those from inert ones for both experimental and theoretical results. Based upon this parameter,

quasi-steady tip penetration under the investigated conditions seems not to be affected by ambient temperature, oxygen content or fuel cetane number. This has been explained in terms of the similar density drop due to similar fuel thermochemistry properties. Injection pressure scales k, but with a similar trend as under inert conditions.

- 1D model results indicate an underestimation of both tip velocity and radial expansion, mainly due to limitations in the simplified approach. Trends are similar to experiments with a reduced sensitivity. Still, the model provides a good background for the explanation of experimental results and for a first order of magnitude analysis of combustion effects upon spray development.

- A combined extinction-radiation technique was developed and applied to obtain soot volume fraction and temperature simultaneously. The optical thickness (KL) is higher with a shorter wavelength, especially at the soot onset position where the hydrogen-to-carbon (H/C) ratios is higher. Compared with the effects of extinction wavelength on KL value, the effects of radiation wavelength on soot temperature is much smaller. In general, the soot temperature obtained from higher wavelength light is higher and the temperature difference increases towards to low radiation intensity part where the single-to-noise is lower.

- High soot concentration region locates at the centre of flame for all cases, where the local temperature is relatively low and no OH radical is observed. When it comes to the downstream, soot amount decreases dramatically because of lower formation rate and faster oxidation rate caused by fuel-lean mixture and appearance of OH radical respectively.

- As for ambient temperature variation, the flame temperature does not present a significant difference. The higher $\bar{\phi}_H$ value of higher ambient temperature case due to shorter LOL could play a key role on higher soot production. The difference of maximum soot temperature is quite close to the adiabatic temperature difference. The longer residence time caused by the lower penetrating velocity is the main factor to bring higher soot production of lower injection pressure case. Injection pressure doesn't bring significant effects on soot temperature distribution and it is consistent with adiabatic temperature that maximum soot temperature doesn't change with injection pressure neither. Different oxygen concentration brings a big difference on soot temperature,but not on soot production. The soot volume fraction in the center line of flame symmetric plane is higher with higher oxygen concentration which is opposite with the trend of KL value integrated along extinction optical path. It is because the optical path under 15% oxygen concentration is longer and the f_v value is higher than 21% case after around 2 mm toward to flame periphery.

Bibliography

[1] Benajes Jesús, Payri Raúl, Bardi Michele and Martí-Aldaraví Pedro. "Experimental characterization of diesel ignition and lift-off length using a single-hole ECN injector". *Applied Thermal Engineering*, Vol. 58 n^o 1-2, pp. 554–563, 2013.

[2] Fajardo Walter Martin Vera-Tudela. *An experimental study of the effects of fuel properties on diesel spray processes using blends of single-component fuels*. Doctoral Thesis, Universitat Politecnica de Valencia, 2015.

[3] Siebers D.L. and Higgins Brian. "Flame lift-off on direct-injection diesel sprays under quiescent conditions". *Sae Transactions*, Vol. 110 n^o 3, pp. 400–421, 2001.

[4] S Settles G. *Schlieren and sadowgraph techniques: visualizing phenomena in transparent media (Experimental Fluid Mechanic)*. Springer Verlag, 2001.

[5] Desantes José M., Pastor José V., García-Oliver José M. and Briceño Francisco J. "An experimental analysis on the evolution of the transient tip penetration in reacting Diesel sprays". *Combustion and Flame*, Vol. 161 n^o 8, pp. 2137–2150, 2014.

[6] Naber Jeffrey D and Siebers Dennis L. "Effects of Gas Density and Vaporization on Penetration and Dispersion of Diesel Sprays". *SAE Paper 960034*, Vol. 105 n^o 412, pp. 82—-111, 1996.

[7] Hiroyasu Hiro and Arai Masataka. "Structures of Fuel Sprays in Diesel Engines". In *SAE Technical Paper*. SAE International, 02 1990.

[8] Payri F., BermÃºdez V., Payri R. and Salvador F.J. "The influence of cavitation on the internal flow and the spray characteristics in diesel injection nozzles". *Fuel*, Vol. 83, pp. 419 – 431, 2004.

[9] Desantes J. M., Payri R., Salvador F. J. and Gil A. "Development and validation of a theoretical model for diesel spray penetration". *Fuel*, Vol. 85 n^o 7-8, pp. 910–917, 2006.

[10] Kosaka H, Aizawa T and Kamimoto T. "Two-dimensional imaging of ignition and soot formation processes in a diesel flame". *International Journal of Engine Research*, Vol. 6 n^o 1, pp. 21–42, 2005.

[11] Pickett Lyle M, Manin Julien, Genzale Caroline L, Siebers Dennis L, Musculus Mark P B and Idicheria Cherian A. "Relationship Between Diesel Fuel Spray Vapor Penetration/Dispersion and Local Fuel Mixture Fraction". *SAE Int. J. Engines*, Vol. 4 n^o 1, pp. 764–799, 2011.

[12] García-Oliver José M., Malbec Louis-Marie, Toda Hubert Baya and Bruneaux Gilles. "A study on the interaction between local flow and flame structure for mixing-controlled Diesel sprays". *Combustion and Flame*, Vol. 179, pp. 157 – 171, 2017.

[13] Manin Julien, Pickett Lyle M. and Skeen Scott A. "Two-Color Diffused Back-Illumination Imaging as a Diagnostic for Time-Resolved Soot Measurements in Reacting Sprays". *SAE International Journal of Engines*, Vol. 6 n^o 4, pp. 2013–01–2548, 2013.

[14] Moiz Ahmed Abdul, Ameen Muhsin M., Lee Seong Young and Som Sibendu. “Study of soot production for double injections of n-dodecane in CI engine-like conditions”. *Combustion and Flame*, Vol. 173, pp. 123–131, 2016.

[15] Skeen Scott a, Manin Julien, Dalen Kristine and Pickett Lyle M. “Extinction-based Imaging of Soot Processes over a Range of Diesel Operating Conditions”. *Internal combustion and gas turbine engines*, pp. 1–13, 2013.

[16] Bardi Michele, Bruneaux Gilles, Nicolle André and Colin Olivier. “Experimental Methodology for the Understanding of Soot-Fuel Relationship in Diesel Combustion: Fuel Characterization and Surrogate Validation”. *SAE Technical Paper*, mar 2017.

[17] Aizawa Tetsuya, Harada Tsuyoshi, Kondo Katsufumi, Adachi Takayuki, Zhou Beini and Kusaka Jin. “Thermocouple temperature measurements in diesel spray flame for validation of in-flame soot formation dynamics”. *International Journal of Engine Research*, Vol. 18 n^o 5-6, pp. 453–466, 2017.

[18] Kamimoto T. and Bae M. “High Combustion Temperature for the Reduction of Particulate in Diesel Engines”. *SAE Paper 880423*, 1988.

[19] Pickett Lyle M., Caton J A, Musculus Mark P. B. and Lutz Andrew E. “Evaluation of the equivalence ratio-temperature region of diesel soot precursor formation using a two-stage Lagrangian model”. *International Journal of Engine Research*, Vol. 7 n^o 5, pp. 349–370, 2006.

[20] Musculus Mark P. B. “Measurements of the Influence of Soot Radiation on In-Cylinder Temperatures and Exhaust NOx in a Heavy-Duty DI Diesel Engine”. *SAE Technical Paper*, apr 2005.

Chapter 5

Spray Characteristics under Non-quiescent Conditions

Contents

5.1 Introduction

Visualization of single-hole nozzles into quiescent ambient has been used in chapter 4 to characterize reacting spray dynamics and soot formation. However, in-cylinder flow may have some meaningful impact on the spray evolution. On the other hand, effects of different split-injection strategies on the mixing and combustion processes are still not well understood.

In the present work, visualization of direct diesel injection spray for single-injection and different split-injection strategies under both non-reacting and reacting operating conditions was conducted in an optically accessible two-stroke engine equipped with a single-hole injector. Schlieren and OH^* chemiluminescence were simultaneously applied to obtain the spray tip penetration and flame lift-off length, while the Diffuse Back Illumination (DBI) was applied to quantify the instantaneous soot formation under the same TDC density and temperature. Results of single-injection were compared with those from the Engine Combustion Network database obtained under quiescent ambient conditions, as presented in chapter 4.

5.2 Optical setup

Schlieren and UV-LA

Both Schlieren and UV-Light Absorption(UVLA) were applied here to quantify vapor penetration for single-injection non-reacting spray. A schematic of the optical setup is shown in Figure 5.1. The actual Schlieren optical setup is quite similar with the one for CPF tests(Figure 4.1). The diameter of the Schlieren stop is 6 *mm*. The high speed camera (Vision Research Phatron SA-5) run at 30 *kfps* with a spatial resolution 6.8 *pixel/mm*. As for the reacting spray measurement, in order to eliminate soot radiation effect, a bandpass filter (310-440 *nm*) was placed in front of the Schlieren stop and the shutter time is reduced to 0.37 μs compared with 9.85 μs for non-reacting spray, while the other settings were kept the same with non-reacting one. As for UVLA, the optical setup is pretty similar with Schlieren. A continuous broadband 1000 W Xenon Arc lamp was used here as the light source to create the desired UV light. On the collection side, an intensified high speed camera Photron I2 coupled to an interference filter (centered at 280 *nm*, with 10 *nm* FWHM) was applied,as shown in the red dashed rectangle in Figure 5.1. Other settings were kept same as that of Schlieren. It must be noted that the UV light was also collimated by the parabolic mirror. The images were recorded at a speed of 8 *kfps* and a spatial resolution 8 *pixel/mm*. An Andor Solis iStar ICCD intensified camera equipped with a 100 *mm* focal length $f/2$ UV objective and a 310 *nm* interference filter (FWHM = 10 *nm*) was used to measure the OH^*

chemiluminescence. Only one image per injection event was recorded from 4 *ms* to 5 *ms* after start of energizing (ASOE) with a *pixel/mm* ratio of 10.9.

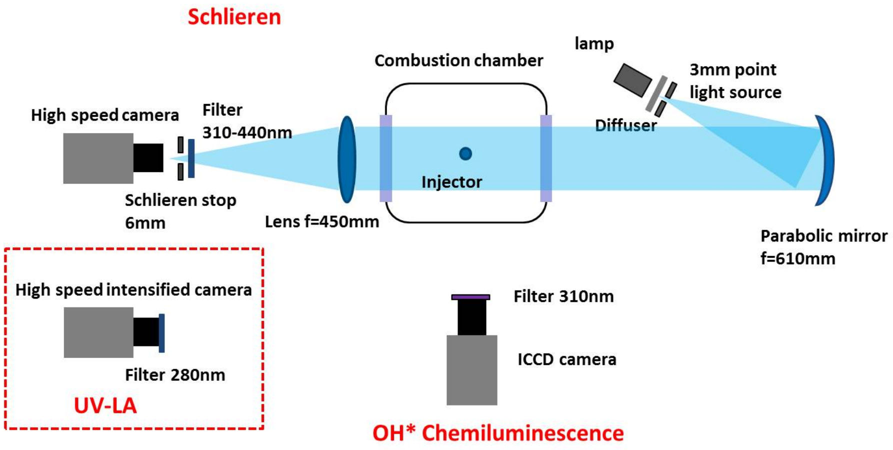

Figure 5.1. *Optical setup of Schlieren and UV-LA.*

Diffused backgound-illumination

The schematic of DBI setup is pretty similar with Figure 3.8. The only differences are the relative distance among the optical tools and the camera settings. Light source is a blue LED with a Peak wavelength 450 *nm*. Pulse duration of LED is 0.9 μs. The light passed through a diffuser to create a diffused Lambertian intensity profiles. Behind the diffuser, a Fresnel lens ($f = 7\ mm$) was mounted to magnify the visualization area. On the collection side, the transmitted light of the LED and the thermal radiation from the combustion are collected by a spherical lens $f = 450\ mm$. A high-speed CMOS camera (Photron SA-5, recording at 35 *khz*) equipped with a bandpass filter (450*nm*, 10 *FWHM*) was used to collect the light. The exposure time of the camera was set to 6.62 μs with $264 * 640$ pixels image resolution. The *pixel/mm* ratio is 7.71.

Based on the line-of-sight integrated soot mass map obtained from Eq.3.9, the soot mass $m_{soot}(x,r,t)$ can be integrated along the radial direction of spray to do a one-dimensional time-dependent analysis according to

$$m_{soot}(x,t) = \int_{-r_1}^{r_2} m_{soot}(x,r,t)dr \tag{5.1}$$

where x is the spray axial direction, y is the spray radial direction, r_1 and r_2 are the spray boundary positions. One example of a $m_{soot}(x,r,t)$ map at 1.6 *ms* is shown in Figure 5.2, together with a derived $m_{soot}(x,t)$ map for a Single-injection case with an injection duration 1.5 *ms*. The AHRR and corresponding ID are also presented in these plots with black line and vertical blue line respectively. The injection duration is also shown with the grey line. It can be seen from Figure 5.2 that soot takes place after a short dwell time from ignition delay and the soot onset length stabilized around 28 *mm* which is much farther downstream than that of flame lift-off length (near 15 *mm* as shown in later section). The boundary of this soot cloud represents the place where the soot is oxidized completely within the limitation this optical technique. No clear soot recession was found after end of injection.

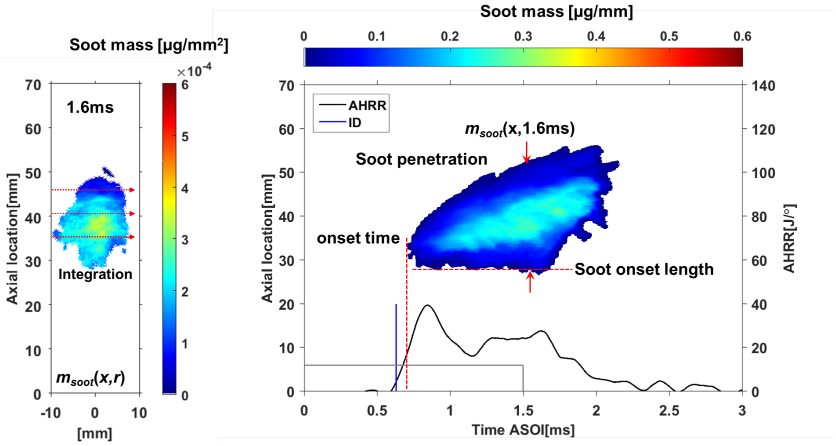

Figure 5.2. $m_{soot}(x,r,t)$, $m_{soot}(x,t)$ *plot, AHRR and ignition delay of a Single injection case(*$P_{inj} = 1500$ *bar*, $T_g = 870$ *K*, $\rho_g = 22.8$ kg/m^3, $O_2 = 15\%$*).*

Due to the spatial separation between the liquid part of the spray and the flame under the investigated conditions, DBI could also be used to quantity the liquid length. Both Schlieren and DBI were measured in independent runs because of limitations in the optical accesses.

5.3 Test matrix and experimental methodology

The operating conditions of single-injection cases forming the test matrix are summarized in Table 5.1, while the operating points of split-injection cases are summarized in Table 5.2. In-cylinder conditions are parametrized in terms of TDC temperature T_g and density ρ_g.

As for single-injection tests, the operating point *NO* (nominal condition, $T_g = 870\ K$, $\rho_g = 22.8\ kg/m^3$) was chosen as the baseline condition. Parametric variations in injection parameters (injection pressure) and thermodynamic conditions within the chamber at TDC (ambient temperature and ambient density) were performed both under non-reacting (in-cylinder mixture contained pure nitrogen) and reacting conditions (injection into ambient air, with 21% oxygen (vol.)). The test matrix also includes a condition denoted as *SA* that reproduces TDC conditions similar to the so-called Spray-A condition from ECN, at 15%, 21% oxygen volume fraction. This makes it possible to compare the evolution of sprays in the present combustion chamber with ECN data measured in a constant pressure chamber, where thermodynamic and flow conditions are nearly quiescent and steady.

Table 5.1. *Test matrix of single-injection cases.*

Case	T_g [K]	P_{inj} [bar]	ρ_g $[kg/m^3]$	$O_2\%$ [%(vol)]	Comments
NO	870	1500	22.8	0,21	Baseline
SA	900	500,1000,1500	22.8	0,15,21	ECN-Spray A
MT	830	1500	22.8	21	Medium T
LT	780	1500	22.8	21	Low T
LD	900	1500	15.2	0	Low density

Table 5.2. *Test matrix of split-injection cases.*

Case	O_2 [%(vol)]	Inj. 1^{st} $[\mu s]$	m_f 1^{st} $[mg]$	Dwell $[\mu s]$	Inj. 2^{nd} $[\mu s]$	m_f 2^{nd} $[mg]$
Single_500	0,21	500	0.8	–	–	–
Single_1500	0,21	1500	0.8	–	–	–
D250	0,21	500	0.8	250	500	0.8
D750	0,21	500	0.8	750	500	0.8
F500	21	500	0.8	500	1000	1.4
F750	21	750	1.1	500	1000	1.4

As for Split-injection tests, in-cylinder conditions and injection pressure were the same for all operating conditions, namely those corresponding to a TDC density of 22.8 kg/m^3, a temperature of 870 K and a injection pressure 1500 *bar*. Two single injection cases, with 500 μs and 1500 μs injection duration separately, were also measured and analyzed in this study as a reference. As for dwell variation, two points (D250 and D750) were conducted with same injected quantities for both injections (500μs) but changing the dwell from 250 μs to 750 μs. As for the first injection quantity variation, the injection duration could not be set shorter than 500 μs because of the limitation of the electronic control. The first injection duration changes from 500 μs (F500) to 750 μs (F750), meanwhile, the dwell time and the second injection duration were fixed at 500 μs and 1000 μs, respectively. The first 4 points in Table 1 were measured under both non-reacting (in-cylinder mixture contained pure nitrogen) and reacting conditions (injection into ambient air, with 21% oxygen (vol.)), while the last two points were only measured under reacting conditions.

A common rail single-hole injector fitted with a 82 μm nozzle has been used in the experiments. The fuel used throughout these tests in optical engine was n-Dodecane for all techniques except for the UV-LA imaging technique, where 80% of dodecane (in mass) was blended with a blend of additional components with high absorptivity for UV light. UV-LA was only appied here for single-injection cases. More information about this blend can be found in reference [1]. For all experiments performed within the present study, 30 injections have been recorded for Schlieren and UV-LA tests and 40 injections have been recorded for soot tests at each operating point to reduce measurement uncertainties due to engine operating variability.

To determine the intake pressure and temperature values required to achieve the target TDC conditions, an accurate characterization of the engine has been performed. Thermodynamic conditions inside the cylinder have been calculated from measured pressure, using a first-law thermodynamic analysis. An example of the in-cylinder pressure and density temporal evolution during the injection event (at $T_g = 870\ K$, $\rho_g = 22.8\ kg/m^3$) is plotted in Figure 5.3. The injector was energized starting at $-6.35°$ ATDC, while the actual injection starts at around $-5.35°$ ATDC, to minimize piston-induced volume variations conditions during the injection event.

The mass flow rate of injection was measured using commercial long-tube equipment. The measuring principle used is the Bosch method [2, 3], which consists of a injector that injects the fuel into a fuel filled measuring tube. A total of 50 repetitive measurements were carried out for each operating point.

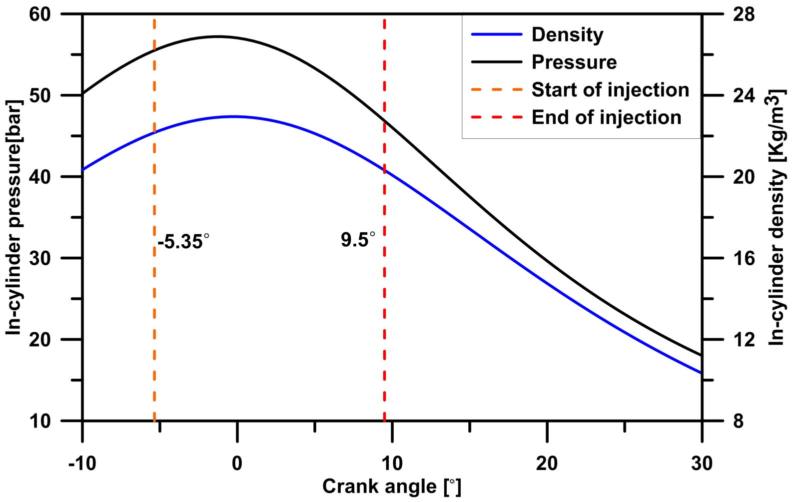

Figure 5.3. *Thermodynamic in-cylinder conditions along engine cycle at* $T_g = 870$ K,$\rho_g = 22.8$ kg/m^3.

In order to avoid artifacts from real experimental data and reduce its effect on the 1D modeling, the mass flow rate was standardized with a model provided in [4]. One example of both experimental and modeled mass flow rate curves for the single long injection case is shown in Figure 5.4. The spray momentum flux as an input in the 1D modeling was calculated from modeled mass flow rate, already known area coefficient and velocity coefficient of this injector from previous research [5].

5.4 Study on single-injection under non-quiescent conditions

This section focuses on the study of the interference of airflow induced by piston movement in the two-stroke engine (subsection 3.2.2) on spray visualization and spray development. Results were compared with those from the Engine Combustion Network database as analyzed in chapter 4. Additionally, a PIV measurement from previous work [1] for characterizing in-cylinder flow motion of this engine was also used here to back up the analysis.

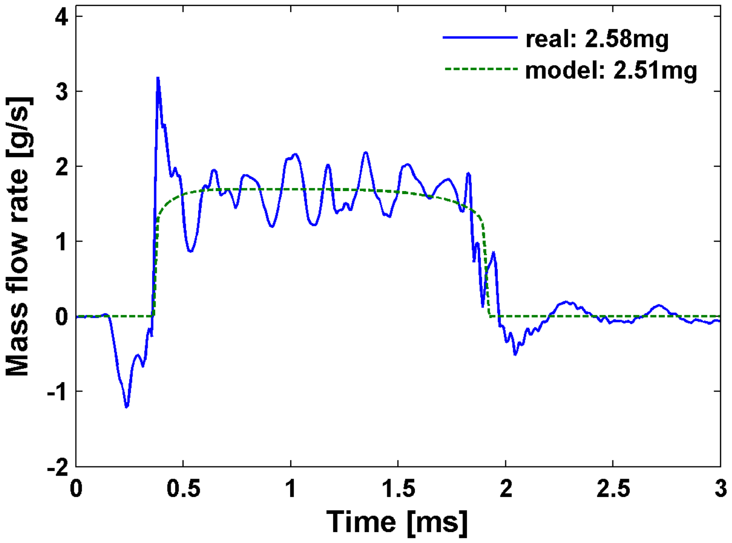

Figure 5.4. *Experimental and modeled mass flow rate for Single_1500 operating point.*

5.4.1 Non-Reacting Spray Analysis

Velocity of the airflow in the combusiton chamber of this engine was studied by previous PhD student [1]. Velocity fields corresponding to the plane on the spray cross section is shown in Figure 5.5(T_g = 760 K, ρ_g = 19.27 kg/m^3). They have been obtained by averaging the velocity magnitude from 75 repetitions. The color map corresponds to the velocity magnitude (i.e. the modulus of the 2D projection of the velocity vector on the measurement plane), while the black lines represent the flow stream lines. At $-5°$ ATDC the airflow is entering into the combustion chamber at more than 20 m/s, while at the upper part of the combustion chamber the speed is reduced to 5 m/s approximately. As piston approaches TDC position, velocity values decrease, but the high velocity region is observed to move closer to the nozzle and towards the left part of the combustion chamber. Near TDC this high velocity region vanishes drastically, as expected. However, a clockwise vortex appears on the right part of the combustion chamber. This flow structure seems to move towards the left of the combustion chamber and disappears as the piston moves down and the outlet flow speed increases.

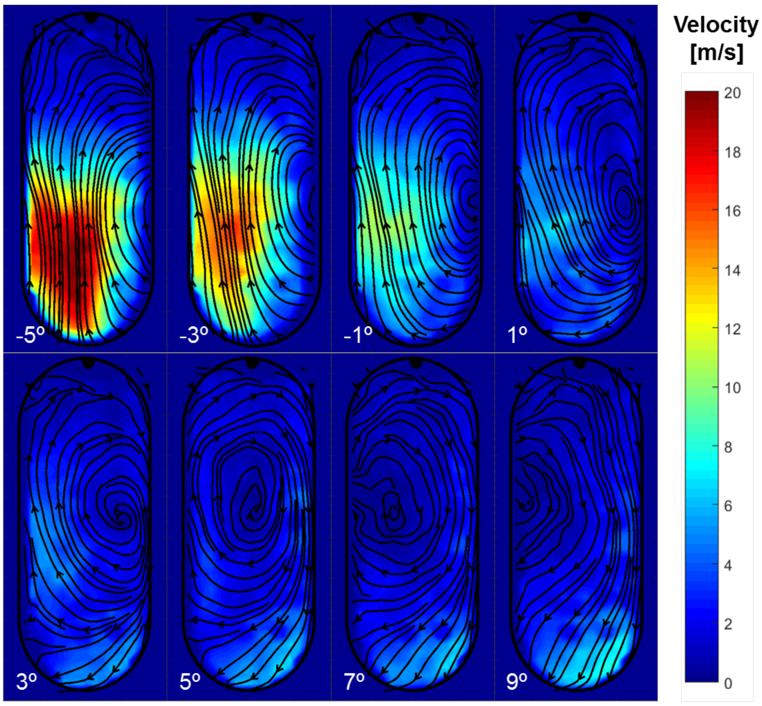

Figure 5.5. *Evolution of the average air flow velocity on plane of spray cross section [1].*

After the analysis of in-cylinder flow, Schlieren results are analyzed to describe non-reacting spray behaviour. The tip penetration of n-Dodecane at two different ambient densities are shown in Figure 5.6. In this figure as well as in the subsequent ones presented in this paper, the time is referred to the start of injection with the acronym ASOI (After Start of Injection) and all the plots represent the average value from 30 repetitions. The corresponding standard error (SE) with 95% confidence level is also included. From Figure 5.6, the spray vapor under low ambient density is seen penetrating faster than that of high density condition due to lower air entrainment, which is consistent with previous research [6]. However, these penetration curves tend to level-off after around 50 *mm*, while the optical limitation is around 80 *mm*. It looks as if these sprays "stop" in the middle of combustion chamber. This phenomenon is considered as Schlieren limitation which is marked with the gray region.

Two examples of processed Schlieren images at two different time position are shown at the top of Figure 5.7. At start of injection (1200 μs), fuel mass fraction within vapor phase is high, and accordingly density gradients are also

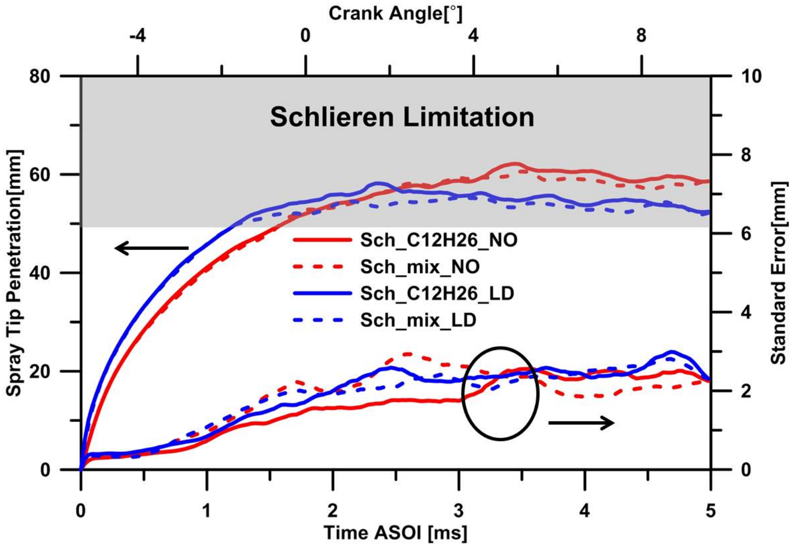

Figure 5.6. *Spray tip penetration of n-Dodecane and mixture at NO and LD conditions as derived from high-speed Schlieren.*($T_g = 870K$, $O_2\% = 0\%$, $P_{inj} = 1500bar$).

important, which makes it possible for the processing routine to capture the spray boundary precisely, which is done based on a fixed threshold. However, with the increase of air entrainment further away from the nozzle, fuel mass fraction at spray tip decreases, and so do spray-induced density gradients. On the other hand, the velocity of the air at the other end of the chamber is much higher than that of upstream spray, as shown in previous PIV maps, which can also increase the air entrainment. In addition, the high flow velocity on that end of the chamber also creates a deflection of light rays, which produces a non-uniform time-variable background. As a result, the detection of the spray is not accurate enough, as it gets diluted into the noisy background. This can be seen in the Schlieren image at 3200 μs in Figure 5.7, for which a spray almost as long as the previous image at 1200 μs is detected. This explains the levelling-off effect shown on Schlieren penetration plots (Figure 5.6).

To avoid the previous shortcomings from the Schlieren technique, UV-LA visualization was carried out, where the only absorbing media should be the fuel. As mentioned above, in order to get high absorptivity for UV light when doing UV-LA tests, 80% (in mass) n-Dodecane was blended with a highly-absorbing surrogate, detailed in [1]. The resulting fuel was investigated with Schlieren and UV-LA techniques and compared against pure n-Dodecane.

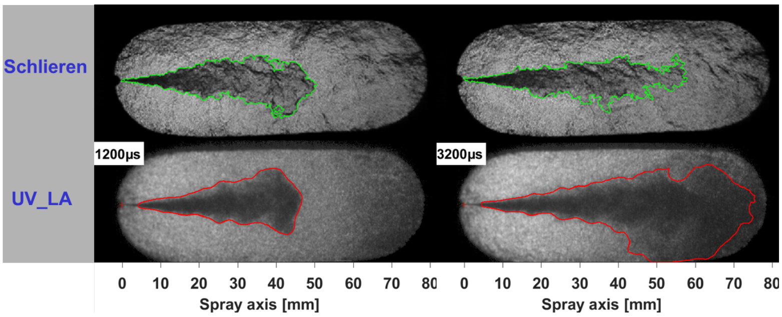

Figure 5.7. *Comparison between Schlieren and UV-LA images at UV and LD conditions ($T_g = 870$ K, $O_2\% = 0\%$, $P_{inj} = 1500$ bar).*

Apparently, as shown in Figure 5.6, fuel effects on vapor penetration are negligible, because momentum flux, which is the main driver for penetration, does not depend on fuel properties when operating at constant injection pressure, which is coherent with previous research [7]. As a consequence, it can be concluded that vapor penetration of this mixture fuel can be applied to represent that of n-Dodecane.

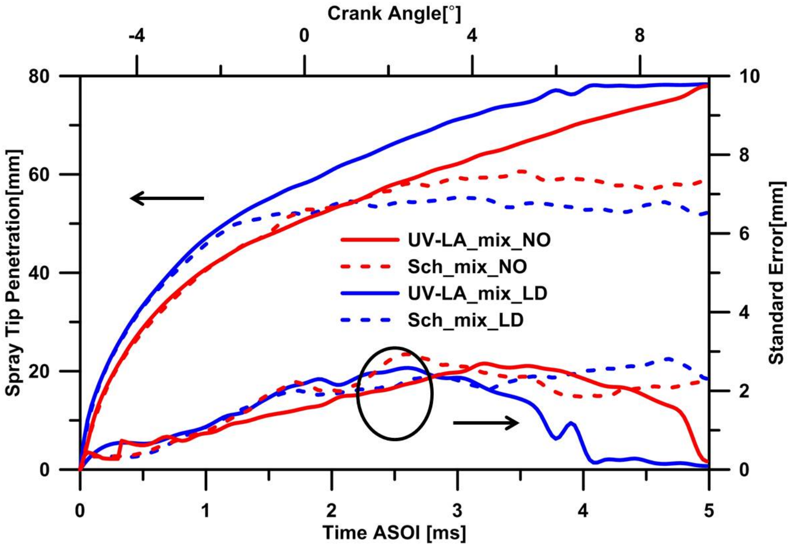

Figure 5.8. *Schlieren and UV-LA comparison at NO condition($T_g = 870$ K, $O_2\% = 0\%$, $P_{inj} = 1500$ bar,$\rho_g = 22.8$ kg/m^3).*

Finally, Figure 5.8 shows tip penetration temporal evolution of mixture obtained both from Schlieren and UV-LA techniques at the same conditions as Figure 5.6. It can be seen that the results from both techniques are consistent when the penetration is shorter than 50 *mm*. After that, UV-LA is still able to capture the spray tip very well until the optical limit, which is also confirmed by the UV-LA image at 3500 μs in Figure 5.7. That is because ambient gas shows a quite low absorptivity for UV light compared with that of the vapor phase of the mixture spray and it is easy for the processing routine to identify the dark spray against the bright background. As a conclusion of this section, UV-LA performs better than Schlieren on capturing tip penetration for the non-reacting spray under non-quiescent conditions and the penetration value of n-Dodecane will be replaced with that of this mixture fuel for further analysis because of the negligible fuel effects.

As a reference experiment under quiescent chamber conditions, the Spray A condition defined by ECN [8] has been chosen to make a comparison with these engine tests points which have the same density and temperature as defined at TDC. The ECN database used here was obtained under quiescent conditions with n-Dodecane in the constant pressure vessel, as presented in chapter 4. In addition, the standard Spray A injector was equipped with a single-hole nozzle with a diameter 90 μm.

On the other hand, for a mixing-controlled spray injected into a quiescent ambient, vapor tip penetration under constant injection and ambient boundary conditions can be described by the following equation:

$$S = k\sqrt{u_0 \cdot d\sqrt{\frac{\rho_g}{\rho_f}} \cdot t} \tag{5.2}$$

where d is the orifice diameter, u_0 is injection velocity, ρ_g is ambient gas density, ρ_f is fuel density, t is time after start of injection and k is a proportionality constant that can be related to the air entrainment rate [9]. The penetration velocity studied in chapter 4 is derived from this equation. Compared to ECN data, the same fuel and injection pressure are used, and hence a similar injection velocity can be expected. Average chamber density in the engine for Spray A condition should also be similar to the nominal ECN one. Therefore, to enable a comparison between both sets of data, ECN results were scaled by orifice diameter as shown in the following equation:

$$S_{scale} = S \cdot \sqrt{\frac{d_{ENG}}{d_{ECN}}} \tag{5.3}$$

where S_{scale} is the scaled penetration which will be used in the following comparison, d_{ENG} and d_{ECN} are the nozzle orifice diameter used in the optical engine and ECN tests, respectively.

Figure 5.9 shows the temporal evolution of tip penetration under *SA* non-reacting conditions for three injection pressures from both facilities. It has to be reminded that ECN vapor penetration was processed from Schlieren images, while engine data was obtained from UV-LA tests. It can be seen that, at start of injection, the vapor penetration from the engine is consistent with that from ECN. However, after around 40 *mm*, divergence between both sets of data appears, and becomes larger with time. Although, the density drop due to piston motion might contribute to an increase on penetration velocity, the density difference from TDC to the end of injection is just around 2.5 kg/m^3, thus, its influence would be considered negligible. On the contrary, the gas flow was considered to play the main role.

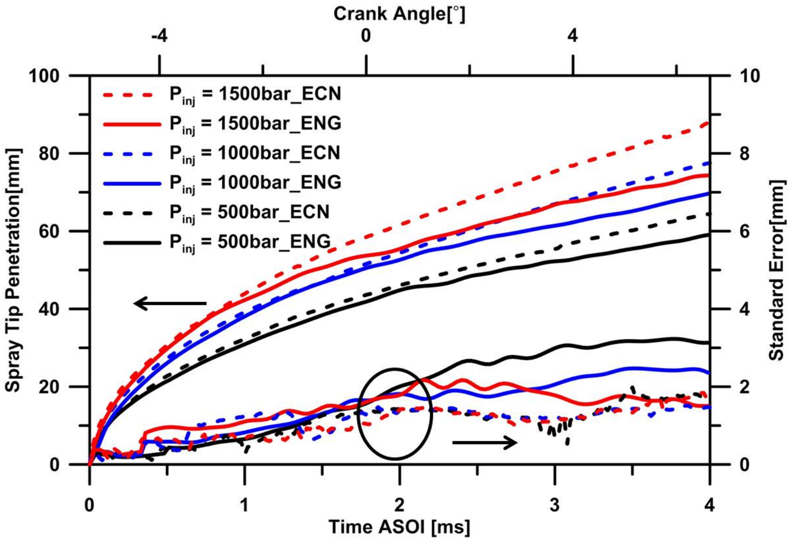

Figure 5.9. *Comparison of vapor penetration with ECN data section 4.4 and corresponding standard error of the mean at SA conditions* ($T_g = 900\ K$, $O_2\% = 0\%$, $\rho_g = 22.8\ kg/m^3$).

One example of the temporal evolution of spray shape obtained from UV-LA at $SA(P_{inj} = 1500\ bar)$ condition is shown in Figure 5.10. The injection time and corresponding crank angle are marked on the top left and top right of this figure respectively. It can be seen, at early stage of injection (−3.25° ATDC), the spray shape is cone-like, which is same as that under quiescent condition. This is because the spray is still far away from the window bottom and the velocity of ambient gas in that zone is quite low compared with the spray velocity, as shown in above PIV images. However, from 2° ATDC to 5° ATDC, the spray geometry is much more complicated than a cone shape. First, the spray tip part becomes flat and then, some part at spray side is moving back. The PIV-derived flow streamlines are overlaid onto the UV-LAS images. It must be noted that PIV results were obtained under different in-cylinder conditions, to avoid evaporation of seeding test fluid. However, in a first approximation, the flow can be assumed to be the same due to the operation of the engine at the same rotational speed. A strong airflow was found at the bottom side moving in opposite direction towards the spray, with a clockwise vortex. The spray can be seen to follow such a flow pattern, which results in a much wider non-symmetrical spray tip.

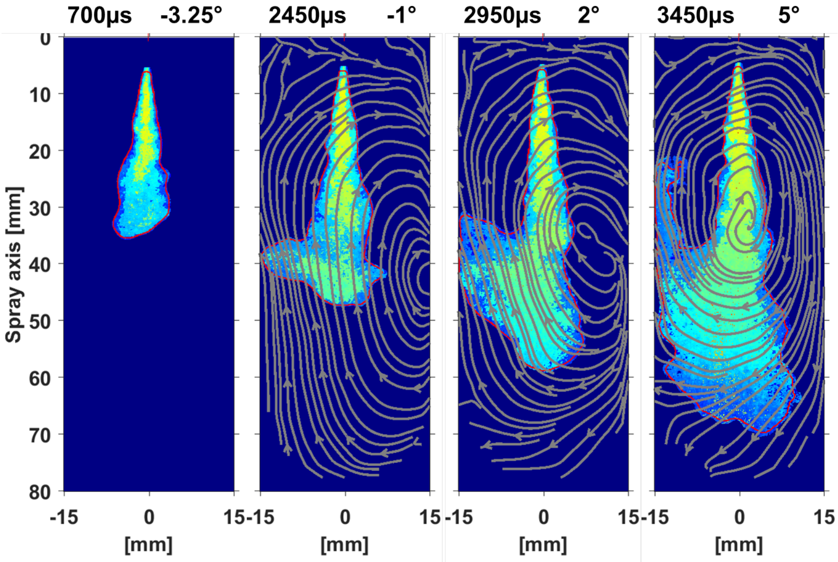

Figure 5.10. *Superposition of PIV-derived streamlines and spray evolution from UV-LA processed images at SA non-reacting condition. Top labels indicate time ASOI (left) and piston position in crankangle degrees (right) ($T_g = 900\ K$, $P_{inj} = 1500\ bar$, $O_2\% = 0\%$, $\rho_g = 22.8\ kg/m^3$).*

In addition, standard error of penetration is also detecting this airflow effect, as shown in Figure 5.9. Standard error of engine measurements shows a small value at start of injection, very similar to the ECN ones for a quiescent ambient. By 1.5 *ms* SE in the engine rises clearly above ECN results, which approximately coincides in time with the departure of the average penetration plots. Note that engine measurements are carried out with a much larger sample size (30 injections) than ECN ones. Therefore, air flow effects are observed in terms of both a slow-down of the average spray penetration, and also of an increase of shot-to-shot scattering. On the other hand, the lower injection pressure case also included in the plot shows a higher SE during the later phase of injection, which may be caused by the lower momentum within the spray at this lower injection pressure, which makes it more prone to disturbances from the air flow.

5.4.2 Reacting Spray Analysis

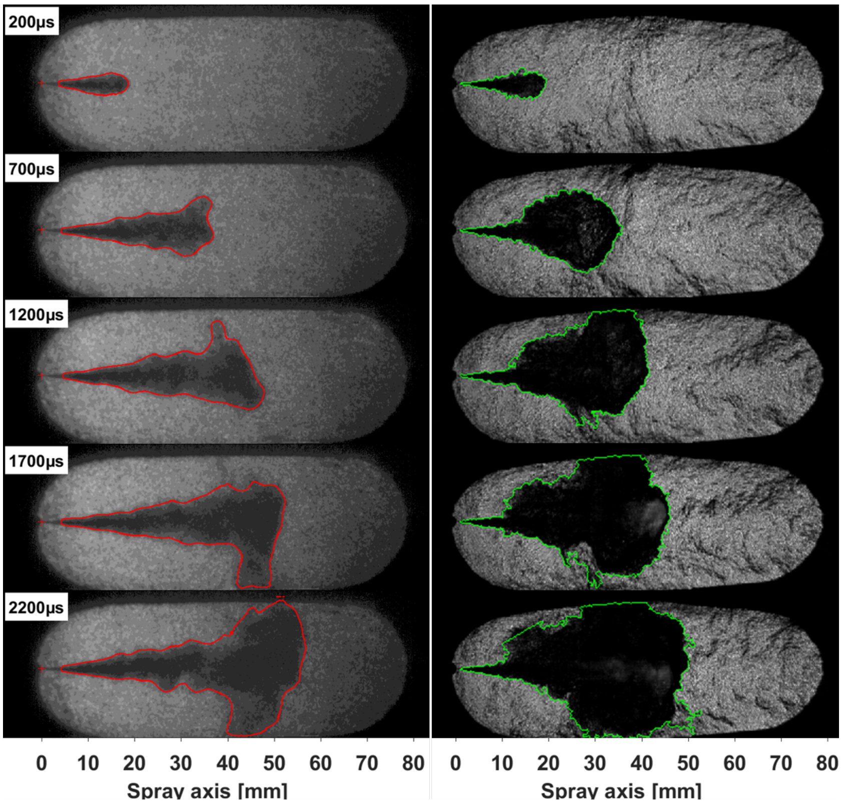

Figure 5.11. *Non-reacting (left) and reacting (right) spray temporal evolution at SA condition ($T_g = 900\ K$, $P_{inj} = 1500\ bar$, $\rho_g = 22.8\ kg/m^3$, $O_2 = 21\%$).*

Spray tip penetration was measured with high-speed Schlieren under reacting conditions, where the high refractive density gradient created by combustion gives a very intense Schlieren signal, without the shortcomings of the non-reacting cases. A sequence of images of reacting spray temporal evolution at *SA* condition($P_{inj} = 1500\ bar$, $O_2 = 21\%$) were shown on the right of Figure 5.11, meanwhile, the non-reacting ones from UV-LA at corresponding time were shown on the left as reference. At start of injection (200 μs), there is still no combustion happening, thus, the spray behaves as under non-reacting conditions, and there is no expansion neither in axial nor in radial direction. At that time, airflow influence is still non-significant as spray is far away from the high velocity zone. Around the ignition timing (700 μs), combustion leads to a fast radial expansion on the spray, which produces such a slowdown of the spray tip penetration that it is even shorter than the non-reacting one. From 1200 μs to 2200 μs (around -2 to 1° ATDC), spray tip is entering into the high velocity field zone. It can be seen that the tip penetration of reacting spray is being kept shorter than the non-reacting one. One speculation is that the airflow influence on reacting tip penetration might be stronger than the non-reacting one owning to the lower density caused by combustion within spray.

A comparison of reacting penetration with ECN data under *SA* condition($P_{inj} = 1500\ bar$, $O_2 = 21\%$) is shown in Figure 5.12, together with the non-reacting cases as a reference. Vertical solid and dashed lines represent ignition delay (ID) for engine and quiescent data, respectively. As shown in this figure, in both facilities reacting spray does not penetrate faster than the non-reacting one during the early stage of combustion. Based on momentum conservation, density drop due to combustion should result in a faster penetration of the spray, as shown in chapter 4. However, this is compensated by the strong initial increase in radial width. This stage is defined as "stabilization phase" in section 4.4. After that, penetration difference of reacting spray between two facilities is larger than that of non-reacting spray. As for ECN case, reacting spray tip starts accelerating and penetrates faster than the non-reacting one after the radial expansion becoming stable [5, 10]. One the other hand, a slower tip penetration in the reacting case compared to the non-reacting one is obtained in the present engine tests, as shown in Figure 5.12. This can be explained from different factors, such as vortex and more air entrainment, brought by the airflow might be able to lead to a wider radial expansion compared with the non-reacting one, because of lower density within reacting spray.

The sensitivities of tip penetration with oxygen concentration at *SA* reacting conditions under both engine non-quiescent and ECN quiescent

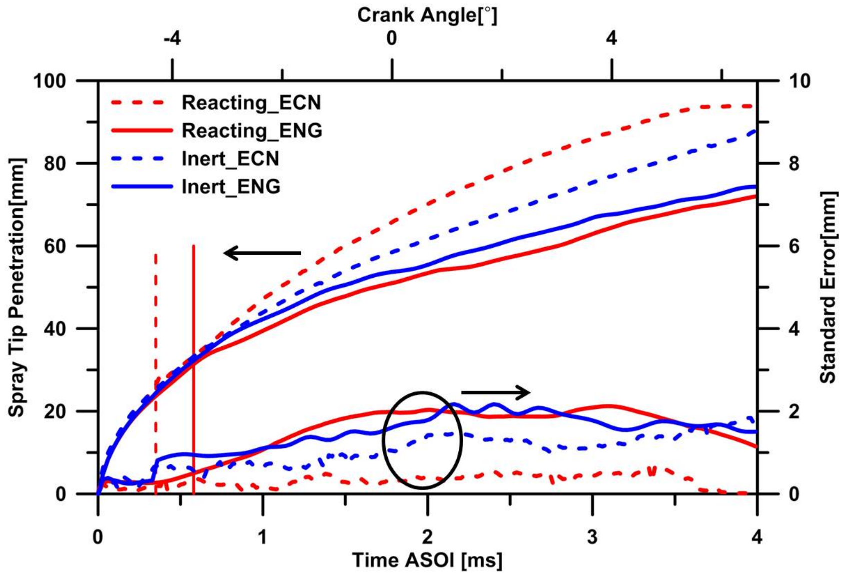

Figure 5.12. *Comparison of tip penetration with ECN data section 4.4 at SA reacting conditions*($T_g = 900\ K$, $P_{inj} = 1500\ bar$, $O_2\% = 21\%$, $\rho_g = 22.8\ kg/m^3$, $O_2 = 21\%$).

conditions are shown in Figure 5.13. It is consistent that the ECN sprays penetrate faster than that in the engine because of the airflow effects. As proved in *section* 4.4, oxygen concentration doesn't have a effect on penetration velocity during quasi-steady phase. However, the earlier auto-ignition of higher oxygen concentration case, as shown in Figure 5.14(a), make the spray tip accelerate earlier, which results in a farther penetration at the same time ASOI under quiescent conditions. On the other hand, the sensitivity of ignition delay with oxygen concentration is almost negligible under such engine condition, as shown in Figure 5.14(a). As a consequence, the spray penetration curves of two engine cases almost overlap each other.

The sensitivities of ID and LOL with oxygen concentration at *SA* reacting conditions under both engine non-quiescent and ECN quiescent conditions are shown in Figure 5.14. There may be a nozzle diameter effect on ID, but there is no simple re-scaling as in the case of penetration, so no correction has been performed. As for LOL, ECN data have been scaled here and in later analysis according to the empirical result from Siebers [11, 12]

$$LOL_{scale} = LOL(\frac{d_{ENG}}{d_{ECN}})^{0.34} \tag{5.4}$$

As we can see, the ignition delay of engine cases are much longer than that of corresponding ECN cases under such conditions. However, it is different that LOL values of both facilities are more similar. Furthermore, it is clear to see the sensitivities of both ignition delay and LOL with oxygen centration of engine cases are much smaller compared with ECN cases. In addition, a much stronger scattering on LOL for engine cases can be observed, which is mainly caused by the cycle-to-cycle airflow variation.

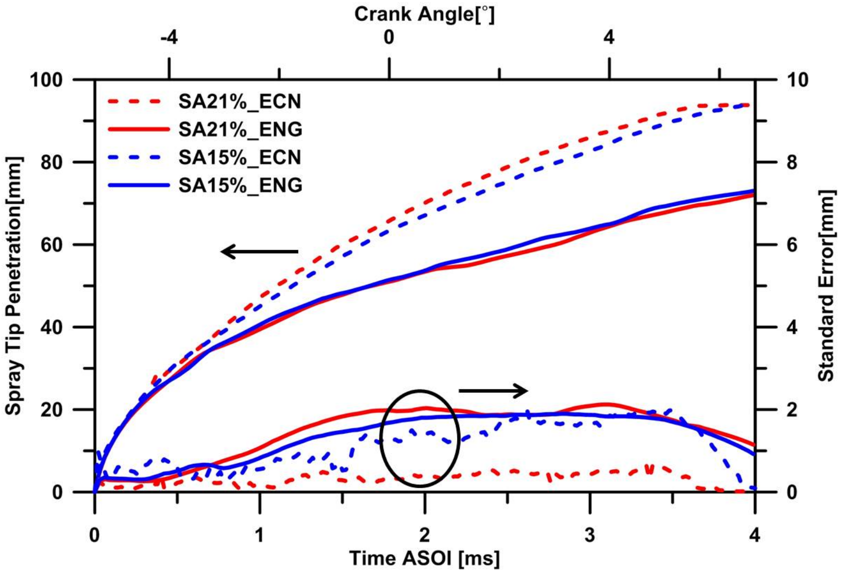

Figure 5.13. *Sensitivity of tip penetration with oxygen concentration at SA reacting conditions($T_g = 900\ K$, $P_{inj} = 1500\ bar$, $\rho_g = 22.8\ kg/m^3$).*

The effects of TDC temperature on ignition delay and lift-off length were presented in Figure 5.15. Note that the temperature sweep was carried out at constant TDC density, oxygen content and injection pressure. ECN data under the same ambient density, oxygen concentration and injection pressure was also shown here as a reference. Both ID and LOL exhibit a much lower sensitivity to in-cylinder temperature compared to results under quiescent conditions. It is remarkable that above 850 K of both parameters are almost constant. Fuyuto et al. [13, 14] have studied the LOL for multi-hole nozzle spray in engine combustion chamber and compared it with that of single free spray calculated based on Pickett et al. empirical equation which is obtained under quiescent conditions. They also observed a much smaller sensitivity of LOL with ambient conditions. They contributed it to the backward flow of hot burned gas caused by the much higher backward flow velocity compared

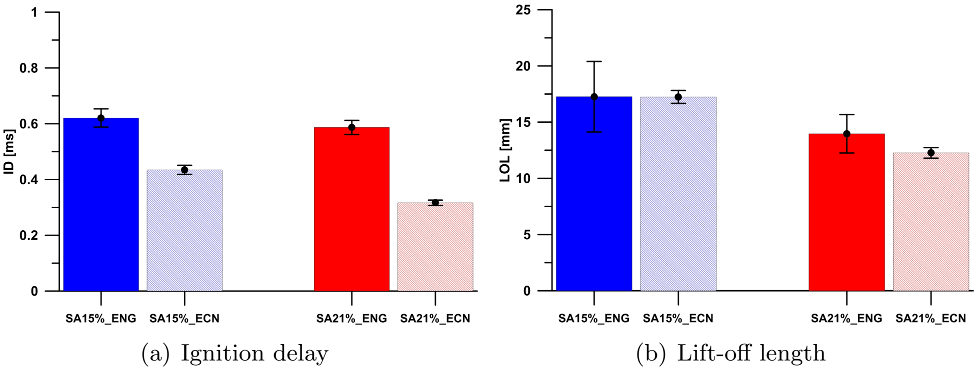

(a) Ignition delay (b) Lift-off length

Figure 5.14. *Ignition delay and Lift-off length with oxygen sweep at SA reacting conditions((*$T_g = 900\ K$*,* $P_{inj} = 1500\ bar$*,* $\rho_g = 22.8\ kg/m^3$*).*

with single free spray. Even though the spray conducted in the engine is also a single-hole spray, the strong airflow caused by piston movement could also play similar role as the multi-hole nozzle. It is just a primary speculation. These results are difficult to explain in detail with the present data. CFD analysis is needed to clarify if flow interaction could also have an influence on this result. On the other hand, while standard deviation of ID is pretty similar in both facilities, for LOL the standard deviation of the engine is much larger than that of quiescent data, which is consistent with previous work [8] and could stem from flow interaction.

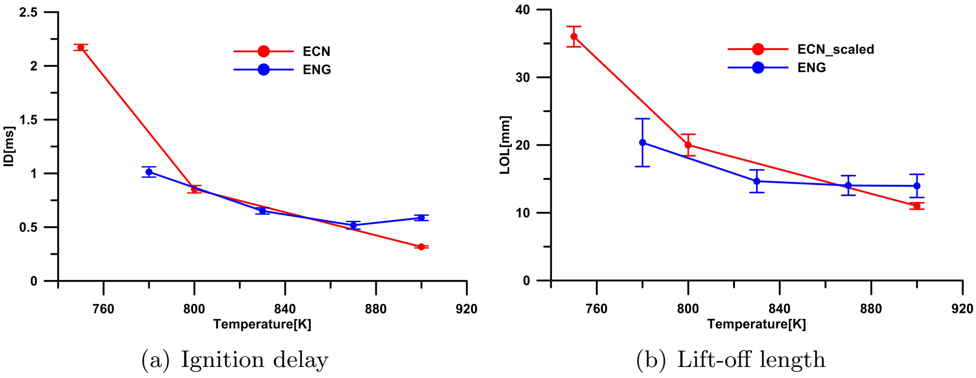

(a) Ignition delay (b) Lift-off length

Figure 5.15. *Ignition delay and Lift-off length with ambient temperature sweep(*$P_{inj} = 1500\ bar$*,* $\rho_g = 22.8\ kg/m^3$*,* $O_2 = 21\%$*).*

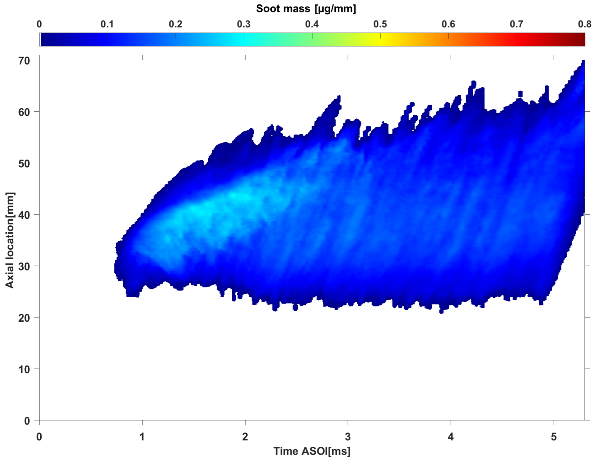

(a) Engine

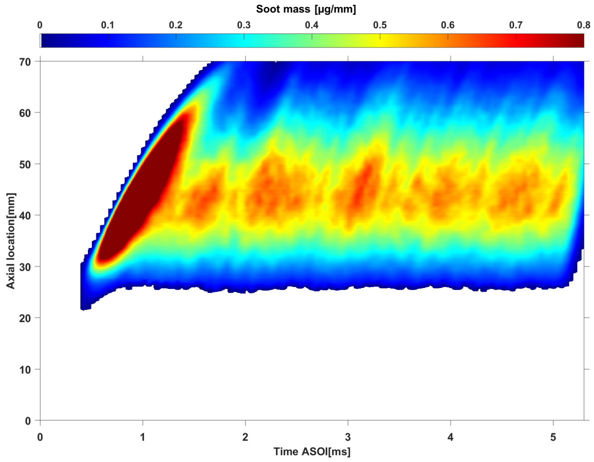

(b) ECN

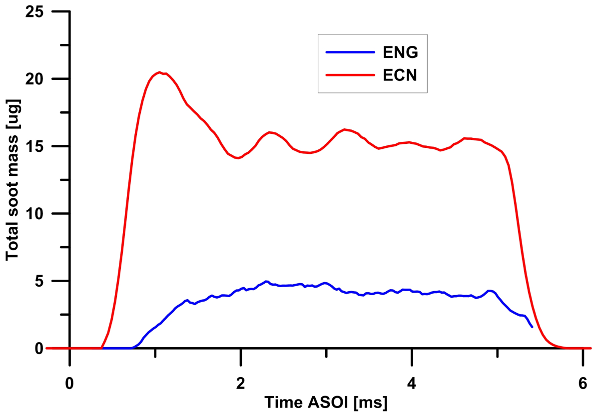

(c) Total soot mass

Figure 5.16. *Comparison of $m_{soot}(x,t)$ map and total soot mass with ECN data section 4.4 at SA reacting conditions($P_{inj} = 1500$ bar, $T_g = 900$ K, $\rho_g = 22.8$ kg/m^3, $O_2 = 21\%$).*

Figure 5.16 presents a comparison of $m_{soot}(x,t)$ map (derived from Eq.5.1) and temporal soot mass evolution with ECN data at *SA* conditions. The total soot mass is integrated within the same optical window(70 *mm* along spray axis). Apparently, soot onset time of ECN data is earlier, which is consistent with ignition delay trend at *SA* condition, as shown in Figure 5.15(a). It is interesting to see the initial soot location in the engine starts from a farther distance away from the nozzle tip than the stabilized soot onset length, which is opposite with the observation from ECN data. It should be caused by the airflow movement which pushes the burning mixture towards to the backward direction. What's more, it can be seen the flame length in the engine(below 60 *mm*) is also much shorter than ECN result(longer than 70 *mm*), which also confirms the effects of the airflow. As shown in Figure 5.16(c), the total soot mass of ECN case is much higher than that of engine. There are a couple of reasons. One reason is that the ECN injector orifice diameter is little bigger, which makes the fuel mass flow rate as well as the fuel mixture fraction of ECN spray are higher. Furthermore, the ECN LOL is shorter than that of engine(Figure 5.15(b)) at *SA* condition, which results in a richer fuel combustion and more soot formation. In addition, more air entrainment brought by the airflow as mentioned above can accelerate soot oxidation rate and contributes to a less net soot production.

5.5 Study on Split-injection under non-quiescent conditions

5.5.1 Non-reacting spray analysis

A time sequence of processed Schlieren images from one individual cycle and its corresponding simulated equivalence ratio contours for Single_1500 and D250 cases under non-reacting condition are provided in Figure 5.17. Additionally, in Figure 5.18 the measured penetration, as well as the modelled one have been plotted against time. The images layout is typical in this sort of experiments, with the dark cone-shaped spray penetrating into the combustion chamber. The detected contours are overlaid on the images to highlight the measured penetration. From the processed contours of Single_1500 (top) one can observe that when the spray tip reaches around 40 *mm* away from the nozzle, the detection of the spray is not accurate enough, as it gets diluted into the noisy background caused by the high velocity motion of airflow from the piston movement. The detailed analysis of this airflow influence on spray development has already been included in section 5.4, where the spray evolution is shown to be slowed down due to the interaction with a high-velocity area on the region located around 40 *mm* from the nozzle.

Figure 5.18 shows that the 1D model can predict the spray tip quite accurately before it reaches 40 *mm* because of the negligible airflow effect during this period. However, the model starts over predicting the spray tip penetration after 40 *mm*. This is consistent with the fact that the model simulates a spray being injected into a quiescent chamber, and therefore any deviation from this situation results in the model not being able to predict the spray event. According to the mentioned deviation of penetration by the model, the effect of the flow hints at a slower spray evolution compared to a quiescent environment, which is consistent with previous results in section 5.4 . Therefore, 1D model predictions of the spray until 40 *mm* should be considered as reliable. As for the D250 case (Figure 5.17, bottom), the second injection appears at 797 μs after start of injection (ASOI) from Schlieren images. During the first instants, the remaining density gradients of spray head from first injection makes the processing routine still capture the first injection tip rather than the second spray. When such density gradients disappear, the second injection spray is properly detected (e.g. 997 μs ASOI). After the end of each injection (797 μs, 1597 μs ASOI), the entrainment wave phenomenon [15] leads to a fast leaning out of the spray. Figure 5.17 also

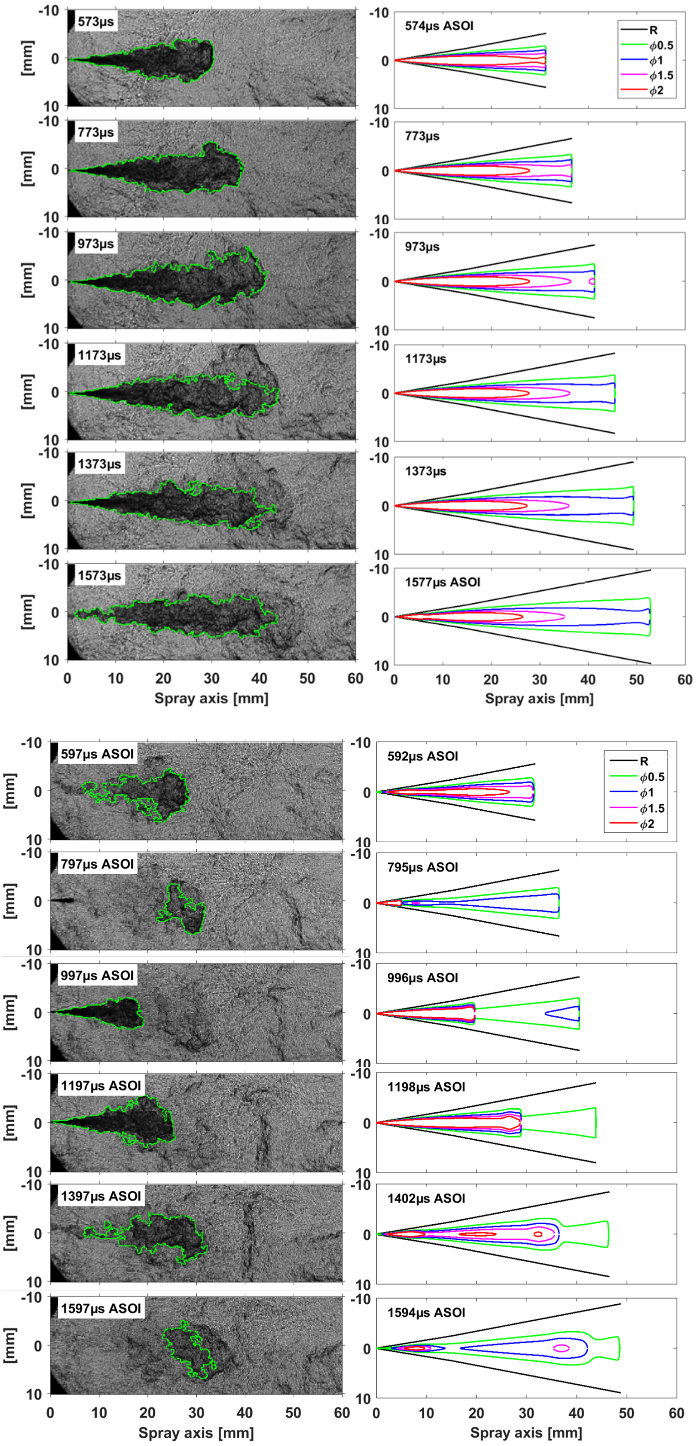

Figure 5.17. *Time sequence of Schlieren images and corresponding equivalence ratio contours derived from the model for Single_1500 (top) and D250 (bottom) cases. R represents the spray boundary.*

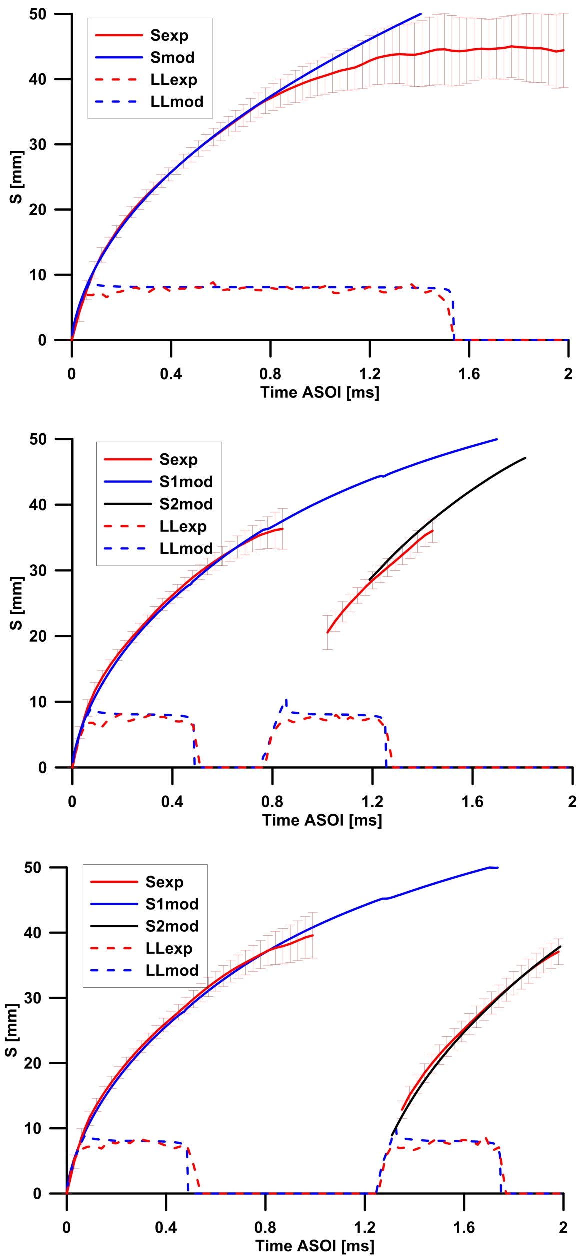

Figure 5.18. *Vapor (solid line) and liquid (dashed line) penetration of Single_1500 (top), D250 (middle) and D750 (bottom) cases from both experiment and model. Vapor penetration corresponds to inert cases, while liquid one has been derived from reacting cases. However, no effect can be observed in the latter cases due to combustion. The corresponding standard deviation is included as vertical bars.*

shows the equivalence ratio contours as derived from the 1D model. For single injection case, equivalence ratio at spray tip drops with time gradually after EOI. But for D250 case, the second injection can be easily identified by the rich mixture pulse evolving within the lean mixture field created by the first pulse. As a consequence, the $\phi = 1$ contour was applied for quantifying tip penetration of second injection and it can only be obtained when the equivalence ratio of first injection becomes smaller than 1. In addition, it is interesting to observe that the stagnant mixture remaining near the injector caused by the entrainment wave from both injections was also captured by this model (795 μs ASOI, 1594 μs ASOI), which might contribute to a combustion recession, UHC or more soot formation for the second injection. This will be discussed in detail in the reacting spray section.

The comparison for vapor and liquid penetration between experimental and modeling results are shown in Figure 5.18. It has to be noted that the experimental liquid length in these plots is from DBI tests under reacting conditions. However, for all three cases no difference can be observed in the liquid length (LL) behavior before and after start of combustion, as liquid fully vaporizes before the lift-off length. Hence this information is also used here for non-reacting spray model validation. Figure 5.18 shows a very good agreement between modeling and experimental results on both vapor penetration (below 40 mm) and liquid length.

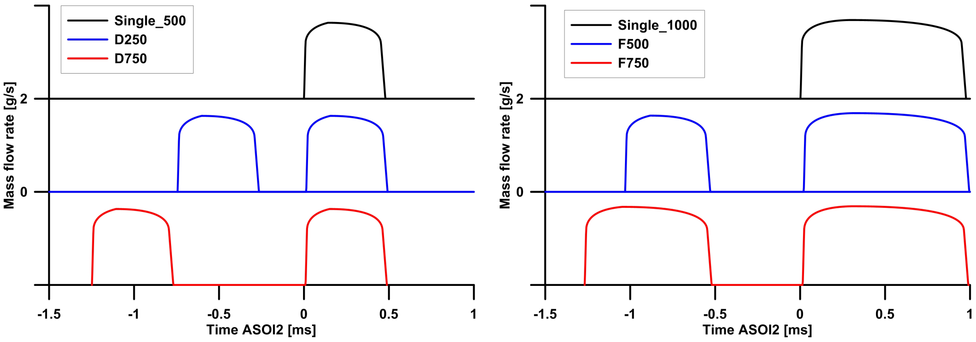

Figure 5.19. *Injection rate plot with a shifted time base to show the definition of the timing "after start of second injection" (ASOI2). Dwell (left) and first injection duration (right) variations are shown.*

To study how the first injection affects the second one, the time base was shifted, so that the origin was set at the start of second injection, and the new time base is expressed in time units after start of second injection (ASOI2). The mass flow rates are shown in Figure 5.19 to help explain the time shift and the definition of ASOI2. Two single injection cases of Single_500 and Single_1000 are also used as references for further analysis. The Single_1000 is a case of single injection with 1000 μs injection duration, which mimics the second pulse of the F500/F750 cases. This condition was not measured experimentally, but modelling is used here for the analysis.

Figure 5.20 shows the vapor penetration of the second injection for dwell variation cases from both experiments (left) and modeling (right). Vapor penetration of Single_500 is also shown here as a reference which presents the same penetration evolution as the first injection of both dwell variation cases. Vapor penetrations of first injection for cases D250, D750 and Single_500 overlap with each other until the corresponding end of injection, because their injection rates are identical. Both experiments and modelling show a consistent trend in terms of the second injections penetrating faster than single one after some axial distance because of the "slipstream" effects [16, 17]. As for parametric trends, the second injection penetrates faster with a shorter dwell time, even though the experimental difference at around 40 mm between D250 and D750 is not as obvious as the modeling ones, which could be caused by the above mentioned airflow interference (section 5.4).

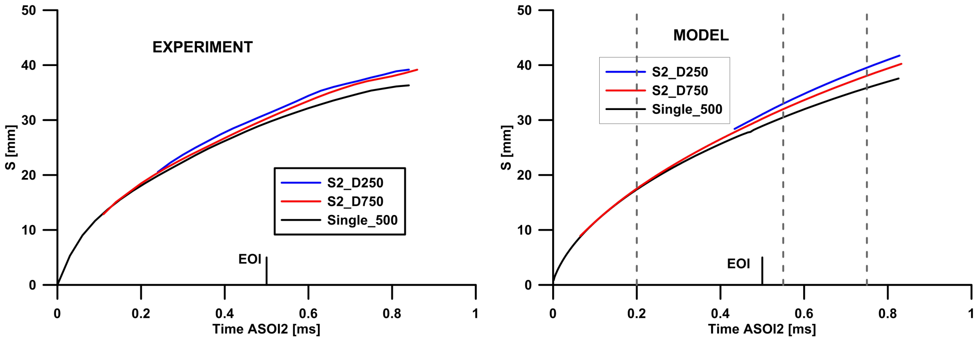

Figure 5.20. *Vapor penetration of the second injection pulse as a function of time ASOSI from both experiment (left) and model (right) for dwell variation cases under non-reacting conditions. Vertical dashed lines correspond the time positions at which modelling results are analyzed as shown in Figure 5.21. For the reference single injection case Single_500, time base is expressed after start of first injection (ASOI1).*

In order to explain the penetration difference brought about by different dwell, a time sequence of the on-axis mixture fraction and the momentum flux along the spray axis corresponding to three time instants are shown in Figure 5.21 (actual timings are also presented on the penetration plot in Figure 5.20 as vertical dashed lines). Momentum flux is the main driver behind spray velocity field, while on-axis mixture fraction will provide information on the local mixture composition. For a top-hat injection profile, momentum flux is almost constant along the spray during the injection, while mixture fraction drops with a well know $1/x$ trend. This can be observed clearly for the single injection pulse at 200 μs ASOI2. At the same timing but for a second injection pulse, the spray is injected into the remaining mixture from the first pulse. The boundary between first injection and second injection pulses can be identified easily from the step drop at around 18 mm in both on-axis mixture fraction and momentum flux curves. Because of the longer time after end of first injection and the corresponding larger entrained mass, the first injection pulse of the D750 case is leaner and with a lower momentum flux at the same timing ASOI2, as shown in Figure 5.21 from around 17 mm to spray tip. For both D250 and D750 cases, the momentum left from the first injection pulse in the near nozzle region is quite small, which does not bring a significant impact on the momentum exchange between the head of second injection and the tail of first injection. As a consequence, the difference of the second pulse penetration of D250 and D750 cases at this time is not so obvious, as shown in Figure 5.20. In fact, the second pulse overlaps with the penetration of a single pulse with the same duration (Single_500) at the same time ASOI2. At 550 μs ASOI2, second injection has just finished. The mass conservation requires a fast gas entrainment to compensate the decreasing fuel mass flux, which makes the mixture fraction and axis momentum near the nozzle decrease dramatically [18]. The entrainment wave starts propagating downstream with a much faster speed than the tip penetration rate [15]. Simultaneously, the tip of the second pulse approaches the zone where momentum left from the first injection is still present with non-negligible values. This results in the second pulse of the split injection cases penetrating faster than a single one (D250 and D750 vs Single_500), as the time to reach the quasi-steady momentum flux is reduced. This effect is more noticeable the shorter the dwell time, because of the higher momentum flux left by the first injection at the same timing ASOI. At 750 μs ASOI2, the second pulse has almost reached the tip of the first one, with similar differences to the ones observed at 500 μs ASOI2.

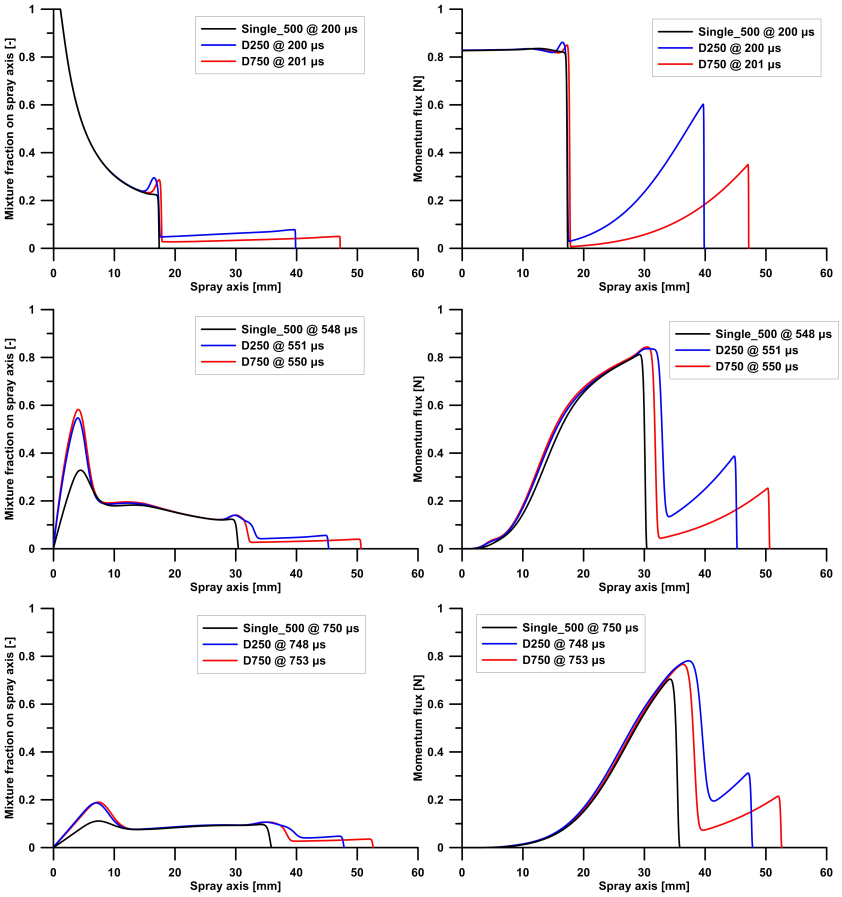

Figure 5.21. *On-axis mixture fraction (left column) and momentum flux (right column) of dwell time variation cases at time position 200 µs ASOI2 (top), 550 µs ASOI2 (middle) and 750 µs ASOI2 (bottom). For Single_500 case, timing values are expressed after start of first injection (ASOI1).*

Although experiments of F500 and F750 under non-reacting conditions have not been done, the 1D model is used here to analyze the effects of first injection on vapor penetration. Time evolution of vapor penetration of the second injection for F500 and F750 cases under non-reacting condition is shown in Figure 5.22. The Single_1000 case is also presented here as a reference. Consistently with the dwell variation cases analyzed before, the second pulse penetrates faster than the single injection one after some axial distance away from the nozzle. However, compared to dwell variations Figure 5.22 shows that the change on first injection duration does not seem to have an influence on the second injection penetration when the dwell time is kept constant.

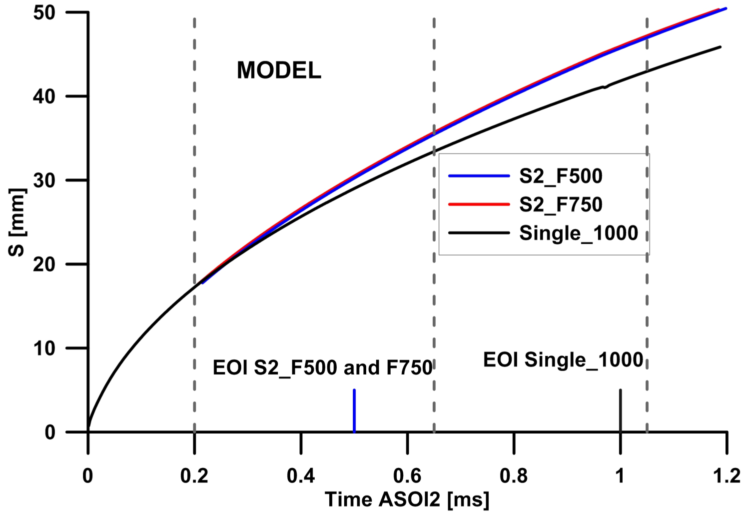

Figure 5.22. *Vapor penetration of the second injection pulse as a function of time ASOSI from model (right) for first injection duration variation cases under non-reacting conditions. Vertical dashed lines correspond the time positions at which modelling results are analyzed in Figure 5.23.For the reference single injection case Single_500, time base is expressed after start of first injection (ASOI1).*

To analyze the previous result, a time sequence of on-axis mixture fraction and momentum flux along the spay axis of F500, F750 and the referenced Single_1000 are presented in Figure 5.23. After the end of the first injection, the behaviour of the F500 and F750 is pretty similar, with the flow slowing down and leaning out from the nozzle downstream. Because of the quasi-steady structure of the preceding flow induced by a spray penetrating with a constant injection rate, differences caused by injection duration between F500 and F750 are only observed in the tip region of both cases, while in the near-nozzle region no differences exist among injeciton patterns. This structure is maintained at 200 μs ASOI2, where the second injection is already proceeding, i.e. momentum and fuel mass distribution left from the previous injection are only different between 45 and 50 *mm*. The second injection pulse eventually reaches locations where significant momentum values from first injection are present (650 μs ASOI2, 1050 μs ASOI2). This will result in faster evolution of the second injection pulse. As a consequence, the difference of vapor tip penetration between single and double injection cases increases with time, as shown in Figure 5.22.

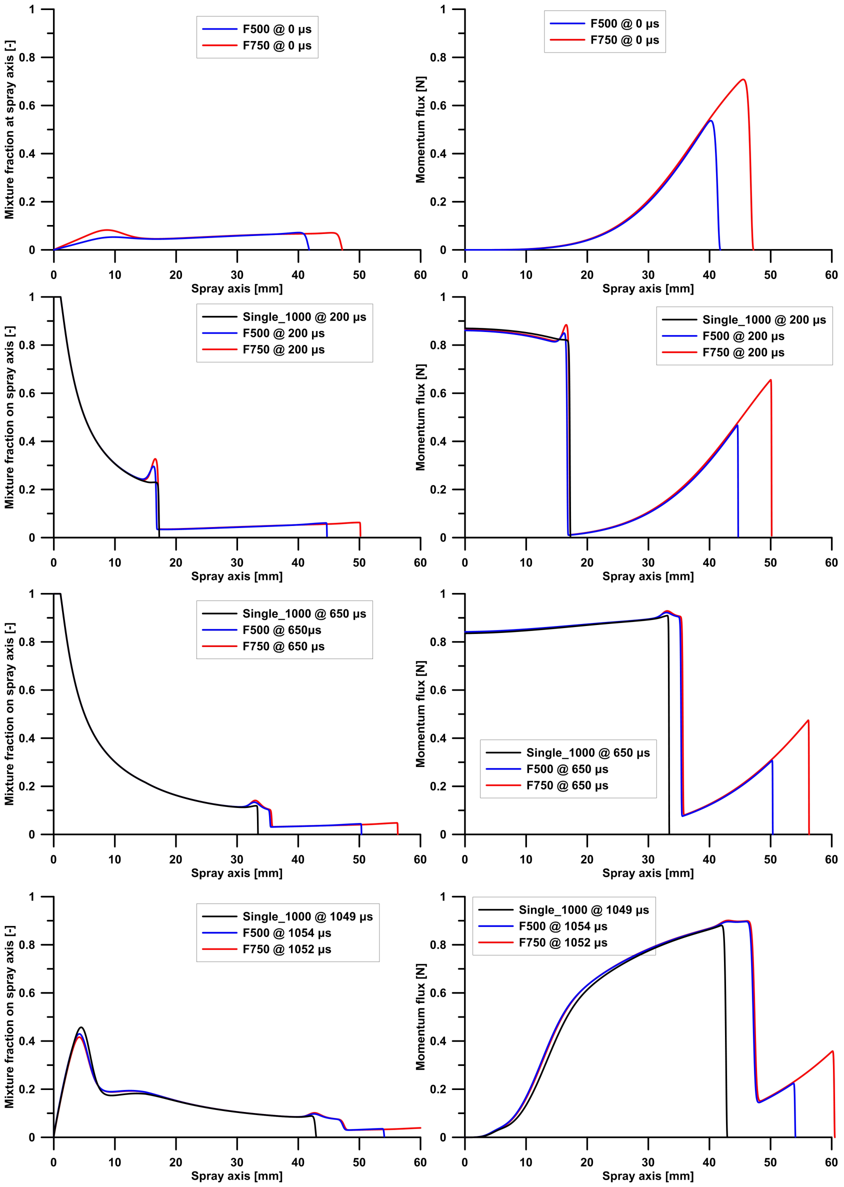

Figure 5.23. *On-axis mixture fraction (left column) and momentum flux (right column) of first injection duration variation cases at time position 0 µs ASOI2 ,200 µs ASOI2 , 650 µs ASOI2 and 1050 µs ASOI2. For Single_1000 case, timing values are expressed after start of first injection (ASOI1).*

5.5.2 Reacting spray analysis

Combustion development

A time sequence of processed Schlieren images for Single_1500 (left), D250 (middle) and D750 (right) cases under reacting conditions are shown in Figure 5.24. For the single injection case, measured ignition delay is $ID = 630$ μs. Therefore, combustion start occurs between the first two frames. For this single injection case, the quasi-steady LOL is stabilized near 15 mm. As for split-injection cases, the spray of first injection still behaves as an inert spray at 563 μs ASOI, where injection has already come to the end, while the combustion starts before the second image at 763 μs ASOI. It is interesting to note that, independently of the dwell between injection pulses, the most upstream location of the combustion products from the first injection remains around the LOL position during the dwell period. This effect could be caused by the "entrainment wave" after the end of first injection, which slows down momentum flux, and hence local velocities. But it can also be amplified because of the radial expansion induced by combustion onset [19].

As discussed in the inert spray analysis, for the investigated condition the second injection pulse is penetrating into a flow field with very little momentum close to the nozzle, reaching the hot combustion products from the first injection combustion, which causes a much faster ignition delay compared to the first pulse [17, 20], where fuel only mixes with ambient air. Consistently with [17] [20], LOL of the second injection pulse is also closer to the nozzle exit than that of first injection, as well as that of a single injection (Single_1500 case). A similar result has been recently observed by Maes [20], which has been explained in terms of the ignition location happening closer to the nozzle than for the first pulse.

The summary of effects of both dwell time and first injection duration on ignition delay and LOL are shown in Figure 5.25. Considering the fact that the first injection duration of F500 is the same as D250 and D750 cases, as well as that the dwell time of F500 is 500 μs, F500 is included in the dwell variation as a reference. The Single_1500 case is also presented on the right plot as a reference for the variation of the first injection. As expected, the ID1 (ignition delay for the first injection) for all cases is pretty similar. Under such thermal condition (870 K, 22.8 kg/m^3), end of injection of the first injection pulse occurs before (D250, D750 and F500 cases) or after (F750 and Single_1500 cases) ignition delay. Therefore, injection duration does not seem to have an impact on ignition delay of the first injection, ID1, consistently

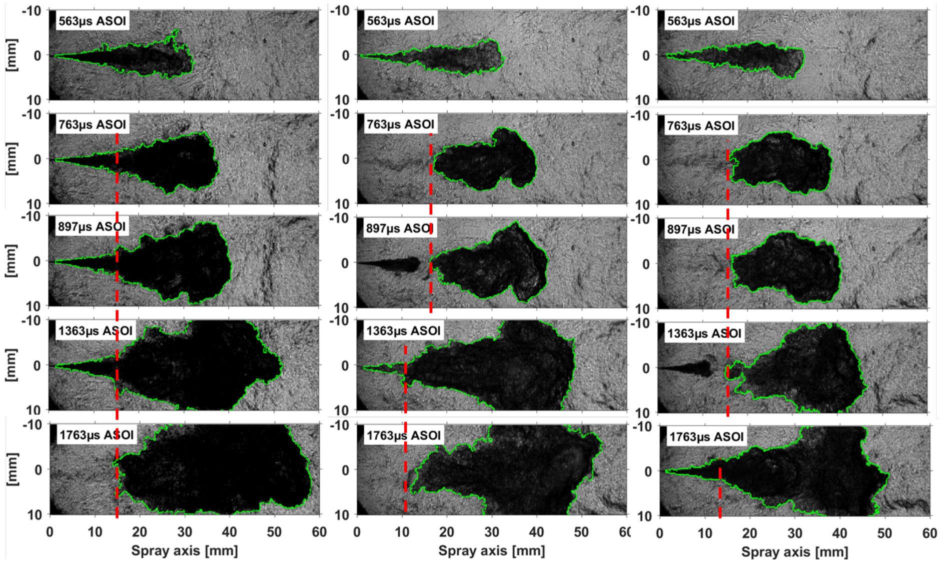

Figure 5.24. *Time sequence of Schlieren images for Single_1500 (left column) and D250 (middle column) and D750 (right column) cases under reacting conditions. Red vertical dashed lines represent LOLs..*

with previous work [21] which shows that this parameter was not influenced by EOI at temperatures of 850 K and 900K. Ignition delay of the second pulse (ID2) seems to be relatively insensitive to dwell time variation, with roughly 250 μs shorter values compared to ID1. As shown in the images, the upstream location of the combustion products for D250 and D750 is pretty similar (as shown in Figure 5.24), and it does not shift downstream significantly with time probably because of the contrary airflow effect. A similar conclusion can be drawn from the images for the first injection duration variation (F500 vs F750, not shown here). Additionally, inert spray analysis has shown that the second injection of D250 penetrates faster than that of D750 only after 20 mm (Figure 5.20), which is farther downstream than the combustion products location. As for the first injection mass variation, differences are even less important. As a result, the second injection of all split injection cases reaches the hot combustion products at a similar time. Assuming that the reduced ignition delay of the second injection is due to the injection into this hot products cloud, where a the higher temperature exist, the previous arguments indicate that ID2 should not be affected largely by neither dwell time, nor first pulse duration. A similar behavior is observed for LOL2 compared to that of the first injection, i.e. this parameter is not largely affected by dwell or first injection duration. Only a slight reduction of LOL2 (smaller than 2 mm) is observed with shorter dwell time. The mechanism by which LOL2 is sensitive to dwell, while ID2 is not, is still an open point, which needs more input from detailed modelling.

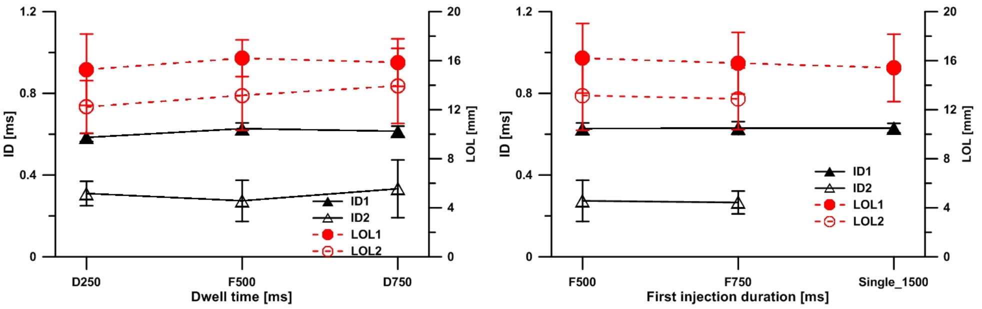

Figure 5.25. *Ignition delay and LOL of double injections for dwell time variation (left) and first injection duration variation (right). Symbols show average values, and error bars indicate standard deviation. (ID1, LOL1) and (ID2, LOL2) correspond to the first and second injection pulses, respectively..*

Instantaneous soot production

Figure 5.26 presents the $m_{soot}(x, t)$ plots and corresponding temporal evolution of total soot mass ($m_{soot}(t)$ plot) of D250 and D750 cases. No soot formation can be observed for the first injection of either case, which can be explained by the fact that injection finishes before start of combustion. As previously discussed, the rapid air entrainment after EOI leans out the mixture before ignition to values too low to produce soot, which makes the equivalence ratio is not rich enough for soot formation. The modelled equivalence ratio of D250, D750 and F500 cases at the start of first-stage combustion is same, as presented in Figure 5.28(Left). Only a quite small part has an equivalence ratio higher than 2. According to the classic $\phi - T$ map [22], equivalence ratio values higher than 2 are very favorable for soot formation. However, the soot can be observed immediately after ID2 (vertical dashed line) which takes place before EOI2. It must be noted that while ignition delay is an averaged value from the sample of the cycle-resolved ignition delay, soot mass was calculated based on the averaged images. This can create some scattering between ID2 and soot onset time, as shown in Figure 5.26 for D250 case.

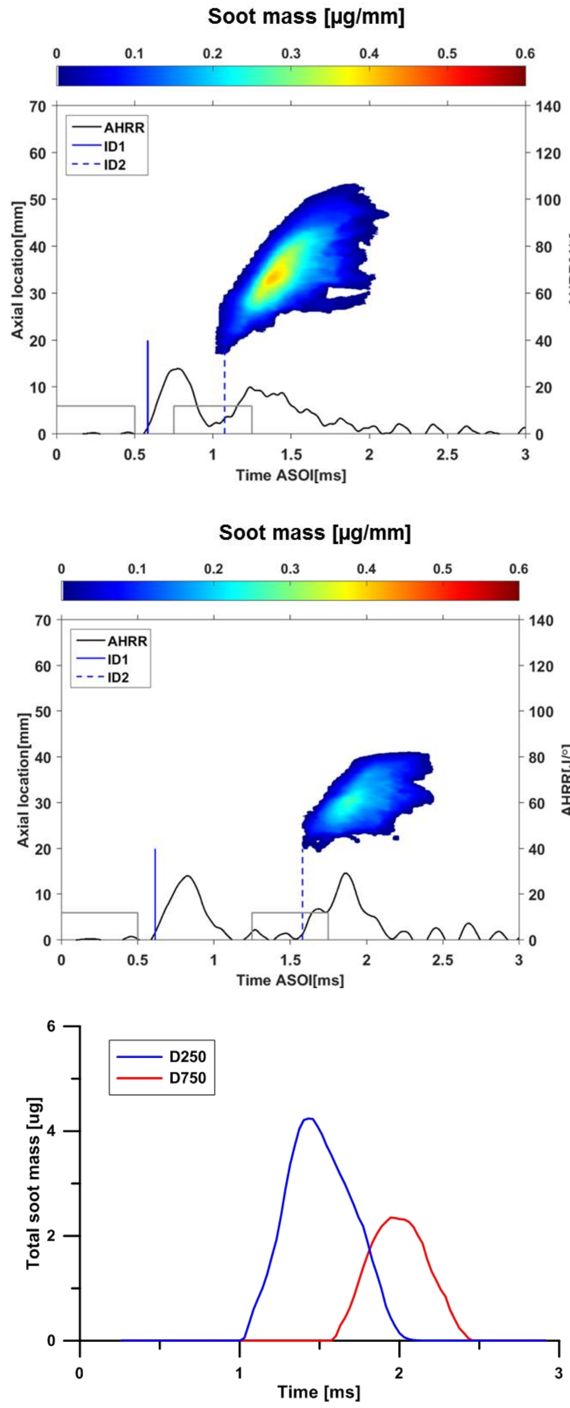

Figure 5.26. *$m_{soot}(x,t)$ plot , AHRR, ID1 , ID2 of D250 (up) and D750 (middle) cases and corresponding temporal evolution of total soot mass (bottom).*

From Figure 5.26 one can conclude that the soot mass formed by the second injection pulser is larter with a shorter dwell time, which is consistent with the CFD results from [23]. As shown in the inert spray analysis, the equivalence ratio and momentum flux distribution of the spray during the initial stages of the second injection is not dependent on dwell. Under reacting conditions, combustion-induced radial expansion and slower mixing [19] will create differences compared to the inert case, but this effect is essentially the same for both dwell cases, as demonstrated by the same ignition delay for both injection pulses. However, initial rise in heat release indicates faster chemical activity once combustion starts for the shorter dwell case, which may contribute to higher local temperatures and hence more soot production. Another possible contribution comes from the small reduction in LOL2 with shorter dwell, which will increase equivalence ratio at the flame base.

Figure 5.27 presents the $m_{soot}(x,t)$ plots and $m_{soot}(t)$ plot of F500 and F750 cases. Consistently with D250 and D750 cases, no soot is formed during the first injection for F500 case. However, soot is present for the F750 case after a short dwell time from ID1. Firstly, more fuel is injected and therefore more heat is released during the first-stage combustion for F750 case compared with F500, which will result in a more beneficial thermal condition for soot formation. Secondly, it can be seen from Figure 5.27 clearly that the first ignition occurs after EOI for F500, while it occurs before EOI for F750. As mentioned above, the end of injection transient contributes to the reduction in local equivalence ratio a lot within a quite short time. The modelled equivalence ratio radius of both cases at SOC1 is presented in Figure 5.28. Note that the spray model results have been obtained before start of combustion, which is applicable until this particular timing. Apparently, the fuel-rich mixture of F750 where the ϕ is greater than 2 in the core spray area is much higher than that of F500. Therefore, the soot was detected during the first injection for F750 case.

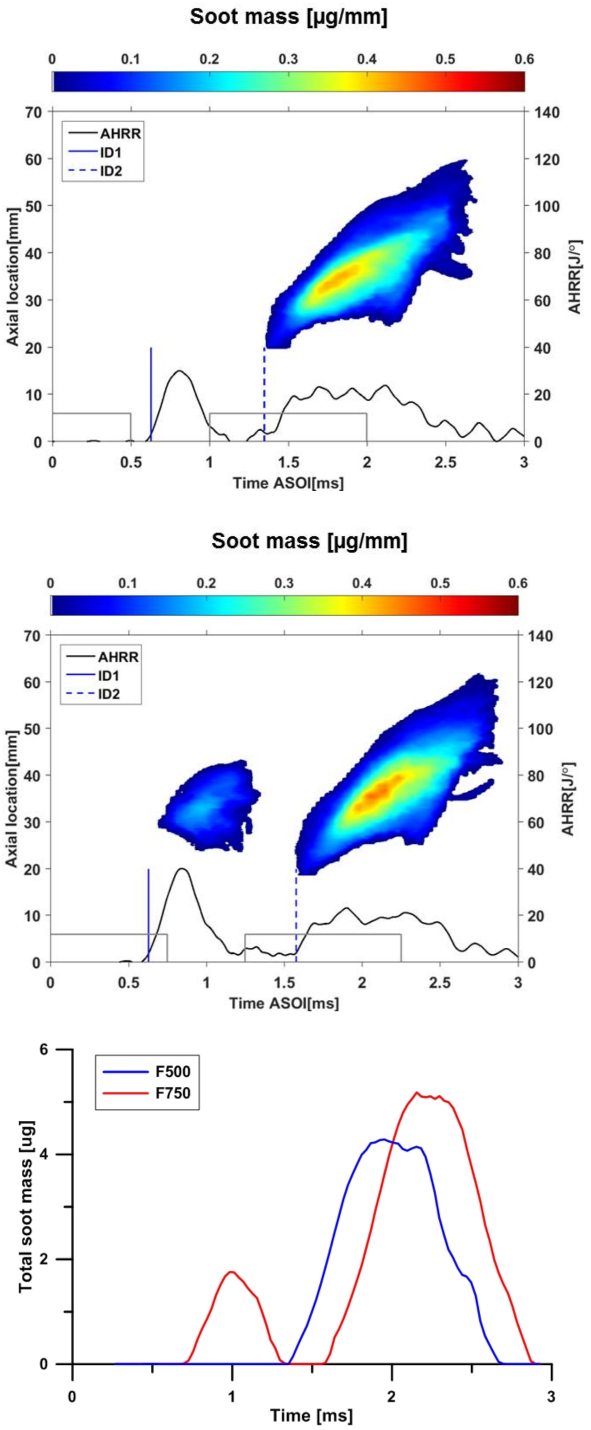

Figure 5.27. $m_{soot}(x,t)$ *plot , AHRR, ID1 , ID2 of F500 (up) and F750 (middle) cases and corresponding temporal evolution of total soot mass (bottom).*

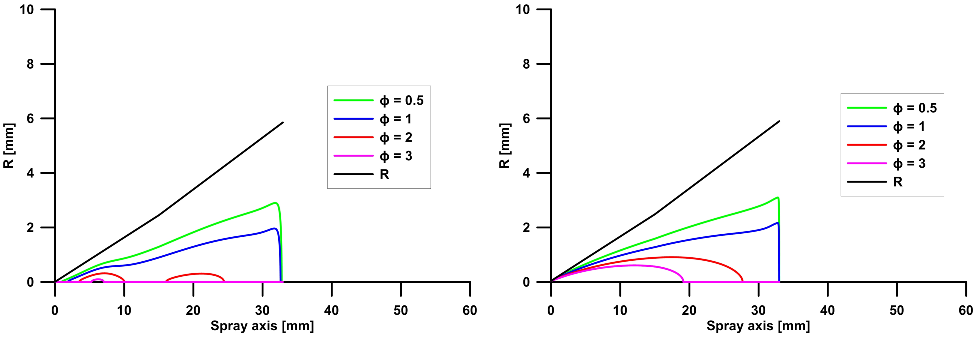

Figure 5.28. *Equivalence ratio radius of D250/D750/F500 (left) and F750 (right) cases at SOC1 from modeling. R represents the spray boundary..*

As for the second injection pulse, results show that soot is formed immediately after ID2 for both F500 and F750 cases. Figure 5.27 indicates that the soot cloud shapes of the second injection are quite similar for these two cases, which indicates they have similar temporal evolution of soot onset length and penetration. Furthermore, initial rise in the total soot mass plot is very similar for both cases, confirming an almost identical soot development in the second injection pulse, in agreement with the combustion development that has been previously analyzed. The main observed different is the fact that the maximum soot amount within the soot cloud for the F750 case is higher than in the F500, as confirmed by both the soot mass map as well as the integrated soot mass plot. Evolution around ignition location and during the early flame development is identical for F500/F750, pointing at similar equivalence ratio and temperature values. However, as the second pulse further progresses into the hot combustion products of the first one, it reaches locations where the larger injected mass of the first injection for F750 enables higher temperature levels compared to F250, and therefore more soot is formed. Due to the longer injection in the first one, spray penetration as well as high temperature combustion products region is wider in axial direction, which may contribute to the enhanced soot formation in the second pulse.

Figure 5.29 presents an overlap of the soot cloud contours derived from $m_{soot}(x,t)$ plots for all split-injection cases, together with a reference single case. For all split-injection cases, the soot penetration of second injection penetrates faster than that of the single case, in agreement with the faster spray penetration shown from the inert tests. It can also be found that the soot onset position for the second injection is always closer to the injector than that of Single case. Furthermore, the trend of onset position between D250 and D750, and between F500 and F750 are consistent with LOL ($LOL_{D250} \leqslant LOL_{D750}$, $LOL_{F500} \approx LOL_{F750}$). In addition, soot onset position are shifted downstream which is consistent with the observation with chemiluminescence from [17].

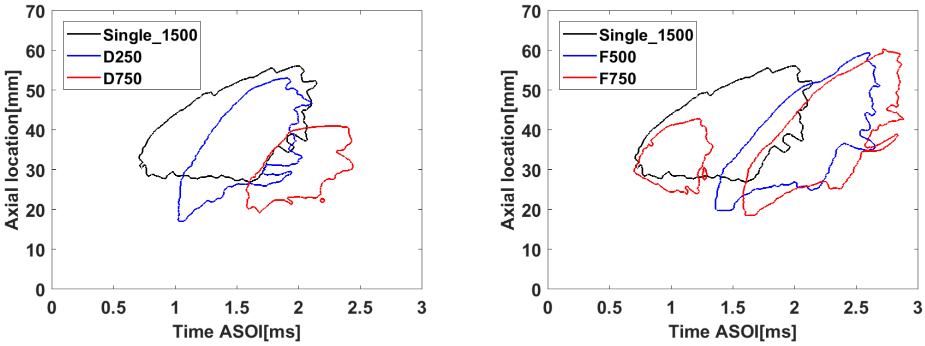

Figure 5.29. *Soot cloud contours derived from $m_{soot}(x,t)$ plots of Figure 5.2, Figure 5.26 and Figure 5.27.*

5.6 Summary and conclusions

The characteristics of both single-injection and split-injection spray dynamics and soot formation under non-quiescent conditions have been investigated in a single-cylinder two stroke optical engine. High-speed Schlieren imaging was applied to visualize the spray geometry development, while the Diffuse Back Illumination (DBI) was applied to quantify the instantaneous soot formation. The results of single-injection cases were compared to ECN data from quiescent chambers, which have been analyzed in Chapter 4, in order to study the effects of in-cylinder flow on spray geometry and soot formation. Furthermore, a detailed analysis of the effects of dwell time and first injection quantity sweep on the characteristic of second injection for split-injection cases under both non-reacting and reacting conditions was provided. Some important conclusions are summarized as follows:

- Under non-reacting conditions, Schlieren technique was not able to identify spray tip very well when it penetrated more than 50 *mm* because of the interference from airflow. A UV-LA technique was developed and it works better on capturing spray penetration under such non-quiescent condition when the spray becomes diluted and the Schlieren effect from the spray is not strong enough compared to the background.

- As for the non-reacting spray, the tip penetration from the engine was kept almost consistent with ECN data at the start of injection. When the spray reached the high velocity region of airflow (around 40 mm), it was slowed down owning to the from airflow.

- As for the reacting spray, the divergence of tip penetration with the ECN data appears earlier than that of non-reacting spray. Both ignition delay and flame lift-off length from the engine show much less sensitivity with ambient temperature sweep. Under ECN Spray A operating condition($O_2 = 21\%$), instantaneous soot formation under such non-quiescent condition is much less than that in the quiescent chamber. Besides the leaner mixture caused by smaller nozzle orifice, the airflow induced by piston movement can also accelerate soot oxidation.

- Under inert conditions the spray evolution has been investigated by means of both experiments and 1D spray model, to evaluate the evolution of the mixing process.

  Dwell time variation: The second injection penetrates faster with a shorter dwell time when the injection durations were kept same. Although the initial evolution close to the nozzle is almost independent of dwell, the spray eventually reaches a zone where flow from the first injection is still present, resulting in a faster penetration than for a single injection case. When decreasing dwell time, a higher momentum remains from first injection, which creates a faster accommodation of the flow to the second injection, and therefore a faster penetration.

  First injection duration variation: There is no difference on the remaining momentum from first injection in the vicinity of the nozzle, with differences being found at the spray tip. Due to the fact that for the investigated conditions the second pulse never reaches the tip within the observation window, the penetration of second injection has been found to be the same when changing the first injection duration.

- The ignition delay of the second injection (ID2) decreases slightly compared with the first one. Neither ignition delay nor lift-off length for the second injection seem to be affected by the duration of the first injection.

- In terms of soot, no soot has been observed for a first injection duration of 500μs (D250, D750 and F500), because of the fuel-lean mixture caused by the fast air entrainment after the end of injection. One the other hand, the soot formation was able to be detected for F750 case because of the much higher equivalence ratio at start of ignition compared with other cases. With a shorter dwell time, the faster heat release induces higher temperature of combustion products, which contributes to a higher soot production in the second injection pulse. At the beginning-stage of soot formation of second injection, F500 and F750 cases keep a similar soot production rate, which is caused by the similar equivalence ratio, temperature and similar LOL2. However,as the second pulse further progresses into the hot combustion products of the first one, it reaches locations where the larger injected mass of the first injection for F750 enables higher temperature levels compared to F250, and therefore more soot is formed.

Bibliography

[1] Reche Carlos Mico. *Development of measurement and visualization techniques for characterization of mixing and combustion processes with surrogate fuel.* Doctoral Thesis, Universitat Politecnica de Valencia, 2015.

[2] W Bosch. "The fuel rate indicator: a new instrument for of the characteristic of individual injection". *SAE Technical Paper*, 1966.

[3] Payri R., Salvador F.J., Gimeno J. and Bracho G. "A new methodology for correcting the signal cumulative phenomenon on injection rate measurements". *Experimental Techniques*, Vol. 32 n^o 1, pp. 46–49, 2008.

[4] Payri Raul, Gimeno Jaime, Novella Ricardo and Bracho Gabriela. "On the rate of injection modeling applied to direct injection compression ignition engines". *International Journal of Engine Research*, Vol. 17 n^o 10, pp. 1015–1030, 2016.

[5] Nerva Jean-Guillaume. *An assessment of fuel physical and chemical properties in the combustion of a Diesel spray.* Doctoral Thesis, Universitat Politecnica de Valencia, 2013.

[6] Naber Jeffrey D and Siebers Dennis L. "Effects of Gas Density and Vaporization on Penetration and Dispersion of Diesel Sprays". *SAE Paper 960034*, Vol. 105 n^o 412, pp. 82—-111, 1996.

[7] Kook Sanghoon and Pickett Lyle M. "Liquid length and vapor penetration of conventional, Fischer-Tropsch, coal-derived, and surrogate fuel sprays at high-temperature and high-pressure ambient conditions". *Fuel*, Vol. 93, pp. 539–548, 2012.

[8] Payri Francisco, Pastor Jose V, Nerva Jean-Guillaume and Garcia-Oliver Jose M. "Lift-Off Length and KL Extinction Measurements of Biodiesel and Fischer-Tropsch Fuels under Quasi-Steady Diesel Engine Conditions". *SAE International Journal of Engines*, Vol. 4 n^o 2, pp. 2278–2297, 2011.

[9] John Abraham. "Entrainment characteristics of transient gas jets". *Numerical Heat Transfer, Part A: Applications*, Vol. 30 n^o 4, 1996.

[10] Pastor Jose V., Payri Raul, Garcia-Oliver Jose M and Briceño Francisco J. “Schlieren Methodology for the Analysis of Transient Diesel Flame Evolution”. *SAE International Journal of Engines*, Vol. 6 n^o 3, pp. 1661–1676, 2013.

[11] Siebers D.L. and Higgins Brian. “Flame lift-off on direct-injection diesel sprays under quiescent conditions”. *Sae Transactions*, Vol. 110 n^o 3, pp. 400–421, 2001.

[12] Siebers Dennis, Higgins Brian and Pickett Lyle. “ Flame Lift-Off on Direct-Injection Diesel Fuel Jets : Oxygen Concentration Effects In-Cylinder Diesel Particulates and NOx Control”. *SAE paper*, n^o 724, 2002.

[13] Fuyuto Takayuki and Hattori Yoshiaki. “Backward Flow of Hot Burned Gas Surrounding High- Pressure Diesel Spray Flame from Multi-hole Nozzle”. *SAE International Journal of Engines*, 2015.

[14] Fuyuto Takayuki, Hattori Yoshiaki, Yamashita Hayato, Toda Naoki and Mashida Makoto. “Set-off length reduction by backward flow of hot burned gas surrounding high-pressure diesel spray flame from multi-hole nozzle”. *International Journal of Engine Research*, Vol. 18 n^o 3, pp. 173–194, 2017.

[15] Musculus Mark P. B. “Entrainment waves in decelerating transient turbulent jets”. *Journal of Fluid Mechanics*, Vol. 638 n^o 1, pp. 117, 2009.

[16] Bruneaux Gilles and Maligne David. “Study of the Mixing and Combustion Processes of Consecutive Short Double Diesel Injections”. *SAE International Journal of Engines*, Vol. 2 n^o 1, pp. 1151, 2009.

[17] Skeen Scott, Manin Julien and Pickett Lyle M. “Visualization of Ignition Processes in High-Pressure Sprays with Multiple Injections of n-Dodecane”. *SAE Int. J. Engines*, Vol. 8 n^o 2, pp. 696–715, 2015.

[18] Kook Sanghoon, Pickett Lyle M and Musculus Mark P B. “Influence of Diesel Injection Parameters on End-of-Injection Liquid Length Recession”. *SAE Int. J. Engines*, Vol. 2 n^o 1, pp. 1194–1210, 2009.

[19] García-Oliver José M., Malbec Louis-Marie, Toda Hubert Baya and Bruneaux Gilles. “A study on the interaction between local flow and flame structure for mixing-controlled Diesel sprays”. *Combustion and Flame*, Vol. 179, pp. 157 – 171, 2017.

[20] Maes Noud, Bakker P.C., Dam Nico and Somers Bart. “Transient Flame Development in a Constant-Volume Vessel Using a Split-Scheme Injection Strategy”. *SAE Int. J. Fuels Lubr.*, Vol. 10, 03 2017.

[21] Malbec Louis-Marie Malbec, Eagle W. Ethan, Musculus Mark P. B. and Schihl Peter. “Influence of Injection Duration and Ambient Temperature on the Ignition Delay in a 2.34L Optical Diesel Engine”. *SAE Int. J. Engines*, Vol. 9 n^o 1, 2016.

[22] Kamimoto T. and Bae M. “High Combustion Temperature for the Reduction of Particulate in Diesel Engines”. *SAE Paper 880423*, 1988.

[23] Moiz Ahmed Abdul, Ameen Muhsin M., Lee Seong Young and Som Sibendu. “Study of soot production for double injections of n-dodecane in CI engine-like conditions”. *Combustion and Flame*, Vol. 173, pp. 123–131, 2016.

Chapter 6

Conclusions and Future Work

Contents

6.1 Conclusions

As mentioned in the *Introduction* chapter, the main goal of this thesis is to improve the understanding of spray dynamics and soot formation during combustion process for direct injection Diesel spray by means of different kinds of optical techniques. In order to do so, two main steps were conducted based on the ambient conditions.

As an intermediate step to study Diesel spray in a real combustion engine, the study was firstly carried out under nearly quiescent conditions in a specific constant pressure flow vessel (CPF). This part work has been developed within the framework of the Engine Combustion Network (ECN) activities with the single-hole Spray A injector. The combustion-induced spray expansion was firstly investigated under a wide range of operating conditions with the fuel of n-dodecane. Besides that, the effects of fuel properties on this reacting spray expansion was also studied with another two additional fuels(n-heptane and one binary blend of primary reference fuels (80% n-heptane and 20% isooctane in mass)). The soot formation of quasi-steady Diesel flame was studied by means of a combined extinction-radiation technique. Thanks to that, the soot volume fraction and temperature was able to be obtained simultaneously. The uncertainties of this technique and parametric variations were evaluated.

The second step of this work is to study the spray dynamics and soot formation under non-quiescent conditions by means of a two stroke single-cylinder optical engine equipped with a single-hole injector. The fuel used here is also n-dodecane. Firstly, the visualization of single-injection cases was conducted and the results were also compared with above mentioned ECN data obtained under the same operating conditions. The effects of in-cylinder air flow on spray geometry development and soot formation were analyzed. Furthermore, the effects of dwell time and first injection quantity variation on the the mixing and combustion processes of second injection for split-injection cases were investigated. Some important findings and conclusions are summarized in upcoming sections.

6.1.1 Spray Dynamics and Soot production under Quiescent Conditions

First of all, spray penetration and radial width of the spray were investigated with particular focus to the axial and radial expansion of the spray occurring during the combustion with ECN recommended fuel of n-dodecane. A scaling factor (k) on derivative of penetration was defined to quantify the combustion-induced effect on spray tip velocity in the quasi-steady phase. Inert spray follows quite accurate definition of this value which is only depending on momentum flux, air density and spreading angle, while the reacting k values are always bigger than those from inert ones. Based on the analysis of this k value, ambient temperature, oxygen content or fuel cetane number doesn't affect quasi-steady tip penetration under the investigated conditions . However, injection pressure scales k, but with a similar trend as under inert conditions. As for the radial expansion, the radial width was calculated from the probability contours. From the analysis of the results it emerged that the shape of the reacting spray can be divided into three regions: **I.** Quasi-steady inert, from nozzle tip to the Lift-off length. **II.** Quasi-steady reacting,from lift-off length to the position where the contour stops increasing radially. **III.** Transient part, from the end of the previous zone to the spray tip. It was found the contour at the quasi-steady reacting part is almost parallel to the corresponding part in the inert case. Based on the analysis of axial and radial expansions with different parametric variations, results show that the radial expansion increases with increasing injection pressure and decreasing ambient temperature and ambient density, while oxygen concentration has no obvious effect on the radial expansion.

A combined extinction-radiation technique was successfully applied to obtain soot volume fraction and temperature simultaneously. By means of the evaluation on the uncertainties of this technique, it was found a shorter wavelength of the background light will results in a higher optical thickness which is mainly caused by the strong uncertainty of extinction coefficient(k_e), while effects of radiation wavelength on soot temperature is much smaller. As for the parametric variation analysis, it seems the soot temperature is not a dominated factor for soot production under the investigated conditions. The difference of maximum soot temperature is similar with adiabatic temperature difference for relatively lower soot temperature cases. However, it is much smaller than that of adiabatic temperature difference when it comes to the ambient oxygen variation. That is mainly caused by heat transfer from hot soot radiation, which can reduce the gas temperatures in the sooting zone.

6.1.2 Spray Dynamics and Soot production under Non-Quiescent Conditions

Because of the shortage of Schlieren technique on detecting non-reacting spray vapor penetration with the interference from airflow, a UV-LA technique was developed and it works better under such non-quiescent conditions. After comparison with ECN data, the tip penetration from the engine was kept almost consistent with ECN data at the start of injection. But a divergence appears when the engine spray is penetrating some distance away from the injector because of high-velocity airflow. The divergence appears earlier for reacting spray compared with that of non-reacting spray. Both ignition delay and flame lift-off length from the engine show much less sensitivity with ambient temperature sweep. Under ECN Spray A operating condition($O_2 =$ 21%), instantaneous soot formation under such non-quiescent condition is much less than that in the quiescent chamber. Besides the thinner mixture caused by smaller nozzle orifice, the air flow induced by piston movement can also accelerate soot oxidation.

Based on the investigation of split-injection Diesel sprays with different injection strategies, it was found the second injection penetrates faster with a shorter dwell time because of a higher momentum remains from first injection, while the penetration of second injection doesn't change when changing the first injection duration because of same remaining momentum from first injection. Bringing the fuel to the location of the first injection combustion products seems to be the main mechanism for the second injection to ignite. As a consequence, both ignition delay and lift-off length of second injection present very little sensitivity to dwell time and the duration of the first injection. In terms of soot, no soot has been observed for a first injection duration of $500\mu s$ (D250, D750 and F500), because of the fuel-lean mixture caused by the fast air entrainment after the end of injection. One the other hand, the soot formation was able to be detected for F750 case because of the much higher equivalence ratio at start of ignition compared with other cases. Soot production in the second injection pulse increases with shorter dwell time and longer first injection duration.

6.2 Future Work

The present thesis represents the optical investigation focused on the spray dynamics and soot formation of direct injection Diesel spray under both quiescent and non-quiescent conditions. Even though the spray behavior has been understood well in many aspects with the help this work, certain features should be further improved and investigated. Some suggested future works are provided as follows:

- Even though the 1D spray model can capture the experimental trends on axial and radial expansion, the predicted ones are always smaller in magnitude than that observed in the experiments. The assumed simplified one-step ignition process could be one of main reasons. Detailed chemical reaction mechanism should be implemented in this 1D model to improve the simulation accuracy. Furthermore, more work is needed with detailed CFD simulations that can confirm these findings.

- The large amount of assumption on these parameters used in Rayleigh-Debye-Gans (RDG) theory results in a strong uncertainty on the extinction coefficient(k_e) value. Further deep analysis needs to be done on this uncertainty, especially for the soot complex refractive index. The soot density is assumed uniform through the whole soot formation process in this thesis, the uncertainty of that is also needed to be further checked. The processing methodology applied in this combined extinction-radiation technique in this thesis brings a big noise in the flame symmetrical axis, more advanced processing methodology needs to be developed.

- With the help of developed extinction-radiation technique, only the study on soot formation during the quasi-steady flame was focused here. The instantaneous soot formation process can be further analyzed. In addition, these soot precursors, like formaldehyde and PAH, can also be measured to acid the soot analysis. Finally, more detailed CFD simulations work is also needed with advanced soot formation mechanisms.

- Only preliminary work on the effects of airflow on spray development is studied here. Even though some trends in this non-quiescent engine combustion chamber is found similar with the that from the observations under quiescent conditions, there are also some disagreement and they are still now well understood. Further microscopic work still needs to be carried out by means of CFD simulations.

- This thesis presents a study on different split-injection strategies which includes two injection pulses. More complicated multiple-injection strategies with three injection pluses(pilot injection, main injection, post injection) could also be investigated.

Bibliography

A. G. Gaydon D.Sc. F.R.S.
The Spectroscopy of Flames.
Springer Netherlands, 1974. (cited on p. 56)

Aggarwal S.K.
A review of spray ignition phenomena: Present status and future research.
Progress in Energy and Combustion Science, Vol. 24 n^o 6, pp. 565–600, 1998.
(cited on p. 25)

Aizawa Tetsuya, Harada Tsuyoshi, Kondo Katsufumi, Adachi Takayuki, Zhou Beini and Kusaka Jin.
Thermocouple temperature measurements in diesel spray flame for validation of in-flame soot formation dynamics.
International Journal of Engine Research, Vol. 18 n^o 5-6, pp. 453–466, 2017.
(cited on p. 114)

Bardi Michele.
Partial Needle Lift and Injection Rate Shape Effect on the Formation and Combustion of the Diesel Spray.
Doctoral Thesis, Universitat Politecnica de Valencia, 2014.
(cited on pp. iv, 2, 17, 25, 49, 50, 51)

Bardi Michele, Bruneaux Gilles and Malbec Louis-marie.
Study of ECN Injectors ' Behavior Repeatability with Focus on Aging Effect and Soot Fluctuations.
SAE Technical Paper, Vol. 01 n^o 0845, 2016. (cited on p. 16)

Bardi Michele, Bruneaux Gilles, Nicolle André and Colin Olivier.
Experimental Methodology for the Understanding of Soot-Fuel Relationship in Diesel Combustion: Fuel Characterization and Surrogate Validation.
SAE Technical Paper, mar 2017. (cited on p. 113)

Bardi Michele, Payri Raul, Malbec Louis-Marie, Bruneaux Gilles, Pickett Lyle M, Manin Julien, Bazyn Tim and Genzale Caroline L.
Engine Combustion Network: Comparison of Spray Development, Vaporization, and Combustion in Different Combustion Vessels.
Atomization and Sprays, Vol. 22 n^o 10, pp. 807–842, 2012. (cited on pp. iv, 3, 16, 50)

Baumgarten C, Stegemann J and Merker G.
A new model for cavitation induced primary break-up of diesel sprays.
Zaragoza, Vol. 9 n^o 11, 2002. (cited on p. 14)

Benajes Jesús, Payri Raúl, Bardi Michele and Martí-Aldaraví Pedro.
Experimental characterization of diesel ignition and lift-off length using a single-hole ECN injector.
Applied Thermal Engineering, Vol. 58 n^o 1-2, pp. 554–563, 2013.
(cited on pp. 22, 28, 54, 81, 83)

Bermúdez, V. García J. Juliá E. and Martínez S.
Engine with Optically Accessible Cylinder Head: A Research Tool for Injection and Combustion Processes.
SAE Technical Paper, 2003. (cited on p. 52)

Bhattacharjee Subhasish and Haworth Daniel C.
Simulations of transient n-heptane and n-dodecane spray flames under engine-relevant conditions using a transported PDF method.
Combustion and Flame, Vol. 160 n^o 10, pp. 2083–2102, 2013. (cited on p. 3)

Blomberg Christopher Kim, Zeugin Lucas, Pandurangi Sushant S., Bolla Michele, Boulouchos Konstantinos and Wright Yuri M.
Modeling Split Injections of ECN Spray A Using a Conditional Moment Closure Combustion Model with RANS and LES.
SAE International Journal of Engines, Vol. 9 n^o 4, pp. 2107–2119, 2016. (cited on p. 36)

Bohren C. F. and Huffman D. R.
Absorption and scattering of light by small particles.
1983. (cited on p. 16)

Bolla Michele, Chishty Muhammad Aqib, Hawkes Evatt R and Kook Sanghoon.
Modeling combustion under engine combustion network Spray A conditions with multiple injections using the transported probability density function method.
International Journal of Engine Research, Vol. 18 n^o 1-2, pp. 6–14, 2017.
(cited on p. 36)

Bower Glenn R and Foster David E.
The Effect of Split Injection on Fuel Distribution in an Engine-Fed Combustion Chamber.
Papers\SAE Papers\Diesel 1990-2002, n^o 412, 1993. (cited on p. 35)

Bravo Luis and Kweon Chol-bum.
A Review on Liquid Spray Models for Diesel Engine Computational Analysis.
Army Research Laboratory, n^o May, 2014. (cited on pp. iv, 13)

Briceno F J, Garcia-Oliver J M, Pastor J V and Payri R.
Analysis of Transient Liquid and Vapor Phase Penetration for Diesel Sprays Under Variable Injection Conditions.
Atomization and Sprays, Vol. 21 n^o 6, pp. 503–520, 2011. (cited on p. 19)

Bruneaux G.
Liquid and Vapor Spray Structure in High Pressure common rail Diesel Injection.
Atomization and Sprays, Vol. 11, pp. 533–556, 2001. (cited on pp. 19, 21)

Bruneaux G.
Combustion structure of free and wall-impinging diesel jets by simultaneous laser-induced fluorescence of formaldehyde, poly-aromatic hydrocarbons, and hydroxides.
International Journal of Engine Research, Vol. 9 n^o 3, pp. 249–265, 2008.
(cited on pp. v, 11, 23, 25, 26, 29, 31)

Bruneaux Gilles.
Mixing Process in High Pressure Diesel Jets by Normalized Laser Induced Exciplex Fluorescence Part I: Free Jet.
SAE Technical Paper, 05 2005. (cited on p. 21)

Bruneaux Gilles and Maligne David.
Study of the Mixing and Combustion Processes of Consecutive Short Double Diesel Injections.
SAE International Journal of Engines, Vol. 2 n^o 1, pp. 1151, 2009.
(cited on pp. 4, 36, 153)

Cenker E., Bruneaux G., Pickett L.M. and Schulz C.
Study of soot formation and oxidation in the engine combustion network (ECN), Spray A: Effects of ambient temperature and oxygen concentration.
SAE Int. J. Engines, Vol. 6, pp. 352–365, 2013. (cited on p. 32)

Coghe A. and Cossali G. E.
Quantitative optical techniques for dense sprays investigation: A survey.
Optics and Lasers in Engineering, Vol. 50 n^o 1, pp. 46–56, 2012. (cited on p. 14)

Cung Khanh, Moiz Abdul, Johnson Jaclyn, Lee Seong Young, Kweon Chol Bum and Montanaro Alessandro.
Spray-combustion interaction mechanism of multiple-injection under diesel engine conditions.
Proceedings of the Combustion Institute, Vol. 35 n^o 3, pp. 3061–3068, 2014.
(cited on p. 36)

Dahms Rainer N., Manin Julien, Pickett Lyle M. and Oefelein Joseph C.
Understanding high-pressure gas-liquid interface phenomena in Diesel engines.
Proceedings of the Combustion Institute, Vol. 34 n^o 1, pp. 1667–1675, 2013.
(cited on p. 14)

Dec John E.
A conceptual model of DI diesel combustion based on laser-sheet imaging.
Sae, n^o 412, pp. 970873, 1997. (cited on pp. iv, 2, 3, 11, 26, 58)

Dec John E.
Advanced compression-ignition engines - Understanding the in-cylinder processes.
Proceedings of the Combustion Institute, Vol. 32 II n^o 2, pp. 2727–2742, 2009.
(cited on p. 25)

Dec John E. and Canaan Robert E.
PLIF imaging of NO formation in a DI diesel engine.
Proceedings of the 1998 SAE International Congress & Exposition, n^o 724, pp. 79–105, 1998.
(cited on p. 27)

Dec John E and Coy Edward B.
OH Radical Imaging in a DI Diesel Engine and the Structure of the Early Diffusion Flame.
SAE Technical Paper, n^o 412, 1996. (cited on p. 27)

Dec John E. and Espey Christoph.
Ignition and early soot formation in a DI diesel engine using multiple 2-D imaging diagnostics.
SAE Transactions, Vol. 104 n^o 3, pp. 853–875, 1995. (cited on pp. 11, 21)

Dec John E and Espey Christoph.
Chemiluminescence Imaging of Autoignition in a DI Diesel Engine.
SAE Technical Paper 982685, n^o 724, 1998. (cited on pp. 11, 21, 23)

Delacourt E., Desmet B. and Besson B.
Characterisation of very high pressure diesel sprays using digital imaging techniques.
Fuel, Vol. 84 n^o 7-8, pp. 859–867, 2005. (cited on p. 20)

Dent J. C.
A Basis for the Comparison of Various Experimental Methods for Studying Spray Penetration.
In *SAE Technical Paper.* SAE International, 02 1971. (cited on p. 19)

Desantes J M, Lopez J J, Garcia J M and Pastor J M.
Evaporative diesel spray modeling.
Atomization and Sprays, Vol. 17 n^o 3, pp. 193–231, 2007. (cited on p. 18)

Desantes J. M., Pastor J. V., García-Oliver J. M. and Pastor J. M.
A 1D model for the description of mixing-controlled reacting diesel sprays.
Combustion and Flame, Vol. 156 n^o 1, pp. 234–249, 2009. (cited on pp. 72, 73)

Desantes J. M., Payri R., Salvador F. J. and Gil A.
Development and validation of a theoretical model for diesel spray penetration.
Fuel, Vol. 85 n^o 7-8, pp. 910–917, 2006. (cited on pp. 19, 88, 97)

Desantes Jose M., Pastor J. V., Payri Raul and Pastor Jose M.
Experimental characterization of internal nozzle flow and diesel spray behavior. Part II: evaporative conditions.
Atomization and Sprays, Vol. 15 n^o 5, pp. 517–544, 2005. (cited on p. 20)

Desantes José M., Pastor José V., García-Oliver José M. and Briceño Francisco J.
An experimental analysis on the evolution of the transient tip penetration in reacting Diesel sprays.
Combustion and Flame, Vol. 161 n^o 8, pp. 2137–2150, 2014. (cited on pp. 33, 86, 90)

Dinos Arcoumanis Take Kamimoto et al.
Flow and Combustion in Reciprocating Engines.
Springer Berlin Heidelberg, 2009. (cited on pp. 15, 16)

Egermann, J. Göttler A. and Leipertz A.
Application of Spontaneous Raman Scattering for Studying the Diesel Mixture Formation Process Under Near-Wall Conditions.
SAE Technical Paper, 2001. (cited on p. 21)

Espey Christoph, Dec John E., Litzinger Thomas A. and Santavicca Domenic A.
Planar laser rayleigh scattering for quantitative vapor-fuel imaging in a diesel jet.
Combustion and Flame, Vol. 109 n^o 1, pp. 65 – 86, 1997. (cited on p. 21)

Fajardo Walter Martin Vera-Tudela.
An experimental study of the effects of fuel properties on diesel spray processes using blends of single-component fuels.
Doctoral Thesis, Universitat Politecnica de Valencia, 2015. (cited on pp. 9, 49, 57, 81)

Flynn Patrick F., Durrett Russell P., Hunter Gary L., zur Loye Axel O., Akinyemi O. C., Dec John E. and Westbrook Charles K.
Diesel Combustion: An Integrated View Combining Laser Diagnostics, Chemical Kinetics, And Empirical Validation.
SAE Technical Paper, n^o 1999-01-0509, 1999. (cited on p. 26)

Fuyuto Takayuki and Hattori Yoshiaki.
Backward Flow of Hot Burned Gas Surrounding High- Pressure Diesel Spray Flame from Multi-hole Nozzle.
SAE International Journal of Engines, 2015. (cited on p. 146)

Fuyuto Takayuki, Hattori Yoshiaki, Yamashita Hayato, Toda Naoki and Mashida Makoto.
Set-off length reduction by backward flow of hot burned gas surrounding high-pressure diesel spray flame from multi-hole nozzle.
International Journal of Engine Research, Vol. 18 n^o 3, pp. 173–194, 2017.
(cited on p. 146)

García J. M.
Aportaciones al estudio del proceso de combustión turbulenta de chorros en motores Diesel de inyección directa.
Doctoral Thesis, 2004. (cited on p. 18)

García-Oliver José M., Malbec Louis-Marie, Toda Hubert Baya and Bruneaux Gilles.

A study on the interaction between local flow and flame structure for mixing-controlled Diesel sprays.
Combustion and Flame, Vol. 179, pp. 157 – 171, 2017.
(cited on pp. 97, 105, 116, 158, 162)

Gong Cheng, Jangi Mehdi, Lucchini Tommaso, D'Errico Gianluca and Bai Xue-Song.
Large Eddy Simulation of Air Entrainment and Mixing in Reacting and Non-Reacting Diesel Sprays.
Flow, Turbulence and Combustion, Vol. 93 n^o 3, pp. 385–404, 2014. (cited on p. 33)

Han Z, Uludogan a, G. Hampson and Reitz R.
Mechanism of Soot and NOx Emission Reduction Using Multiple-injection in a Diesel Engine.
SAE Technical Paper series, Vol. 960633 n^o 412, 1996. (cited on p. 35)

H.C. Hottel and F.P. Broughton.
Determination of true temperature and total radiation from luminous gas flameames: Use of special two-color optical pyrometer.
Industrial and Engineering Chemistry, Vol. 4 n^o 2, pp. 166–175, 1932. (cited on p. 59)

Heywood J. B.
Internal combustion engine fundamentals.
McGraw-Hill Publishing, 1988. (cited on pp. 9, 11, 25, 26, 53)

Higgins Brian and Siebers Dennis.
Measurement of the Flame Lift-Off Location on Dl Diesel Sprays Using OH Chemiluminescence.
Sae 2001-01-0918, n^o 724, 2001. (cited on pp. 12, 27, 56, 57)

Higgins Brian, Siebers Dennis L and Aradi Allen.
Diesel-Spray Ignition and Premixed-Burn Behavior.
SAE Technical Paper 2000-01-0940, n^o 724, 2000. (cited on pp. 21, 22, 23)

Higgins Brian S, Mueller Charles J and Siebers Dennis L.
Measurements of Fuel Effects on Liquid-Phase Penetration in DI Sprays.
SAE transactions, Vol. 108 n^o 724, pp. 630–643, 1999. (cited on p. 16)

Hiroyasu Hiro and Arai Masataka.
Structures of Fuel Sprays in Diesel Engines.
In *SAE Technical Paper.* SAE International, 02 1990. (cited on pp. 4, 19, 20, 33, 88)

Hoffmann T, Hottenbach P, Koss H, Pauls C and Grünefeld G.
Investigation of Mixture Formation in Diesel Sprays under Quiescent Conditions using Raman , Mie and LIF Diagnostics.
SAE Technical Paper, Vol. 2008 n^o 724, pp. 776–790, 2008. (cited on p. 21)

Hua Zhao N. Ladommatos.
Engine combustion instrumentation and diagnostics.
Warrrendale PA: Society of Automotive Engineers, 2001. (cited on p. 30)

Idicheria Cherian A. and Pickett Lyle M.
Soot Formation in Diesel Combustion under High-EGR Conditions.
SAE Technical Paper, n^o 724, pp. 2005–01–3834, 2005. (cited on pp. 29, 32)

Idicheria Cherian A. and Pickett Lyle M.
Formaldehyde Visualization Near Lift-off Location in a Diesel Jet.
SAE International, 2006. (cited on p. 25)

Idicheria Cherian A and Pickett Lyle M.
Quantitative Mixing Measurements in a Vaporizing Diesel Spray by Rayleigh Imaging.
SAE Technical Paper, Vol. 2007 n^o 724, pp. 776–790, 2007. (cited on p. 21)

Jansons Marcis, Brar Amandeep, Estefanous Fadi, Florea Radu, Taraza Dinu, Henein Naeim and Bryzik Walter.
Experimental Investigation of Single and Two-Stage Ignition in a Diesel Engine.
SAE Technical Paper 2008-01-1071, Vol. 2008 n^o 724, pp. 776–790, 2008.
(cited on p. 21)

Jarrahbashi Dorrin, Kim Sayop, Knox Benjamin W and Genzale Caroline L.
Computational analysis of end-of-injection transients and combustion recession.
International Journal of Engine Research, pág. 146808741770128, 2017. (cited on p. 34)

Jenny Patrick, Roekaerts Dirk and Beishuizen Nijso.
Modeling of turbulent dilute spray combustion.
Progress in Energy and Combustion Science, Vol. 38 n^o 6, pp. 846–887, 2012.
(cited on pp. iv, 14, 15)

Jing Wei, Roberts William L. and Fang Tiegang.
Spray combustion of Jet-A and diesel fuels in a constant volume combustion chamber.
Energy Conversion and Management, Vol. 89 n^o x, pp. 525–540, 2015. (cited on p. 26)

John Abraham.
Entrainment characteristics of transient gas jets.
Numerical Heat Transfer, Part A: Applications, Vol. 30 n^o 4, 1996. (cited on p. 139)

Jung Yongjin, Manin Julien, Skeen Scott and Pickett Lyle M.
Measurement of Liquid and Vapor Penetration of Diesel Sprays with a Variation in Spreading Angle.
SAE Technical Paper 2015-01-0946, 2015. (cited on p. 16)

Kamimoto T. and Bae M.
High Combustion Temperature for the Reduction of Particulate in Diesel Engines.
SAE Paper 880423, 1988. (cited on pp. 118, 160)

Kamimoto Takeyuki and Kobayashi Haruki.
Combustion processes in diesel engines.
Progress in Energy and Combustion Science, Vol. 17 n^o 2, pp. 163–189, jan 1991.
(cited on p. 9)

Knox Benjamin and Genzale Caroline.
Effects of End-of-Injection Transients on Combustion Recession in Diesel Sprays.
SAE International Journal of Engines, Vol. 9 n^o 2, pp. 2016–01–0745, 2016.
(cited on pp. 12, 34)

Knox Benjamin W and Genzale Caroline L.
Reduced-order numerical model for transient reacting diesel sprays with detailed kinetics.
International Journal of Engine Research, Vol. 17 n^o 3, pp. 261–279, 2016.
(cited on p. 72)

Knox Benjamin W. and Genzale Caroline L.
Scaling combustion recession after end of injection in diesel sprays.
Combustion and Flame, Vol. 177, pp. 24–36, 2017. (cited on pp. 12, 34)

Knox Benjamin W, Genzale Caroline L, Pickett Lyle M, Garcia-Oliver Jose M and Vera-Tudela Walter.
Combustion Recession after End of Injection in Diesel Sprays.
SAE Int. J. Engines, Vol. 8 n^o 2, pp. 679–695, 2015. (cited on pp. 12, 34)

Kook Sanghoon and Pickett Lyle M.
Liquid length and vapor penetration of conventional, Fischer-Tropsch, coal-derived, and surrogate fuel sprays at high-temperature and high-pressure ambient conditions.
Fuel, Vol. 93, pp. 539–548, 2012. (cited on pp. 16, 20, 137)

Kook Sanghoon and Pickett Lyle M.
Soot Volume Fraction and Morphology of Conventional, Fischer-Tropsch, Coal-Derived, and Surrogate Fuel at Diesel Conditions.
SAE Int. J. Fuels Lubr., Vol. 5 n^o 2, pp. 647–664, 2012. (cited on p. 32)

Kook Sanghoon, Pickett Lyle M and Musculus Mark P B.
Influence of Diesel Injection Parameters on End-of-Injection Liquid Length Recession.
SAE Int. J. Engines, Vol. 2 n^o 1, pp. 1194–1210, 2009. (cited on pp. 12, 35, 154)

Kosaka H, Aizawa T and Kamimoto T.
Two-dimensional imaging of ignition and soot formation processes in a diesel flame.
International Journal of Engine Research, Vol. 6 n^o 1, pp. 21–42, 2005.
(cited on pp. v, 23, 29, 31, 90)

Kosaka Hidenori, Drewes Volker H, Catalfamo Luca, Aradi Allen a, Iida Norimasa and Kamimoto Takeyuki.
Two-Dimensional Imaging of Formaldehyde Formed During the Ignition Process of a Diesel Fuel Spray.
SAE Technical Paper, n^o 724, 2000. (cited on pp. 21, 23)

Kosaka Hidenori and Kamimoto Takeyuki.
Quantitative Measurement of Fuel Vapor Concentration in an Unsteady Evaporating Spray via a 2-D Mie-Scattering Imaging Technique.
SAE Technical Paper, 10 1993. (cited on p. 21)

Krüger S and Grünefeld G.
Droplet velocity and acceleration measurements in dense sprays by laser flow tagging.
Applied Physics B, Vol. 615, pp. 611–615, 2000. (cited on p. 14)

Krüger S and Grünefeld G.
Gas-phase velocity field measurements in dense sprays by laser-based flow tagging.
Applied Physics B: Lasers and Optics, Vol. 70 n^o 3, pp. 463–466, 2000. (cited on p. 14)

Lachaux Thierry and Musculus Mark P B.
In-cylinder unburned hydrocarbon visualization during low-temperature compression-ignition engine combustion using formaldehyde PLIF.
Proceedings of the Combustion Institute, Vol. 31 II, pp. 2921–2929, 2007. (cited on p. 34)

Legros Guillaume, Wang Qianlong, Bonnety Jérôme, Kashif Muhammad, Morin Céline, Consalvi Jean-Louis and Liu Fengshan.
Simultaneous soot temperature and volume fraction measurements in axis-symmetric flames by a two-dimensional modulated absorption/emission technique.
Combustion and Flame, Vol. 162 n^o 6, pp. 2705 – 2719, 2015. (cited on pp. 69, 71)

Lillo Peter M, Pickett Lyle M, Persson Helena, Andersson Oivind and Kook Sanghoon.
Diesel Spray Ignition Detection and Spatial/Temporal Correction.
SAE Paper 2012-01-1239, pp. 1–21, 2012. (cited on p. 21)

Linne Mark.
Imaging in the optically dense regions of a spray: A review of developing techniques.
Progress in Energy and Combustion Science, Vol. 39 n^o 5, pp. 403–440, 2013. (cited on pp. iv, 14)

Linne Mark A., Paciaroni Megan, Berrocal Edouard and Sedarsky David.
Ballistic imaging of liquid breakup processes in dense sprays.
Proceedings of the Combustion Institute, Vol. 32 II n^o 2, pp. 2147–2161, 2009. (cited on p. 14)

Liu Zunping, Im Kyoung-Su, Xie Xing-bin, Wang Yujie, Zhang Xusheng, Moon Seoksu, Gao Jian, Fezzaa Kamel, Lai Ming-Chia, Harkay Kathy, Sajaev Vadim, Emery Louis and Wang Jin.
Ultra-Fast Phase-Contrast X-ray Imaging of Near-Nozzle Velocity Field of High-Speed Diesel Fuel Sprays.
Ilass, n^o May, 2010. (cited on p. 14)

MacIan V., Payri R., Garcia A. and Bardi M.
Experimental evaluation of the best approach for diesel spray images segmentation.
Experimental Techniques, Vol. 36 n^o 6, pp. 26–34, 2012. (cited on p. 20)

Maes Noud, Bakker P.C., Dam Nico and Somers Bart.
Transient Flame Development in a Constant-Volume Vessel Using a Split-Scheme Injection Strategy.
SAE Int. J. Fuels Lubr., Vol. 10, 03 2017. (cited on pp. 36, 158)

Maes Noud, Meijer Maarten, Dam Nico, Somers Bart, Baya Toda Hubert, Bruneaux Gilles, Skeen Scott A., Pickett Lyle M. and Manin Julien.
Characterization of Spray A flame structure for parametric variations in ECN constant-volume vessels using chemiluminescence and laser-induced fluorescence.
Combustion and Flame, Vol. 174, pp. 138–151, 2016. (cited on pp. v, 28, 29)

Malbec Louis-Marie Malbec, Eagle W. Ethan, Musculus Mark P. B. and Schihl Peter.
Influence of Injection Duration and Ambient Temperature on the Ignition Delay in a 2.34L Optical Diesel Engine.
SAE Int. J. Engines, Vol. 9 n^o 1, 2016. (cited on pp. 25, 159)

Manin, J. Bardi M. and Pickett L.M.
Evaluation of the liquid length via diffused back-illumination imaging in vaporizing diesel sprays.
International Symposium COMODIA 2012 SP2-4, 2012. (cited on p. 60)

Manin J., Bardi M., Pickett L. M., Dahms R. N. and Oefelein J. C.
Microscopic investigation of the atomization and mixing processes of diesel sprays injected into high pressure and temperature environments.
Fuel, Vol. 134, pp. 531–543, 2014. (cited on p. 14)

Manin Julien, Pickett Lyle M. and Skeen Scott A.
Two-Color Diffused Back-Illumination Imaging as a Diagnostic for Time-Resolved Soot Measurements in Reacting Sprays.
SAE International Journal of Engines, Vol. 6 n^o 4, pp. 2013–01–2548, 2013.
(cited on pp. 32, 59, 61, 66, 105, 106, 107, 108, 113)

Matsui Y Kamimoto T and S Matsuoka.
A study on the time and space resolved measurement of flame temperature and soot concentration in a DI diesel engine by the two-color method.
SAE Technical Paper, 1979. (cited on p. 58)

Meijer Maarten.
Direct Injection Fuel Spray Combustion Studied by Optical Diagnostics "A spray A".
Doctoral Thesis, Eindhoven University of Technology, 2014. (cited on p. 1)

Menkiel Barbara.
Investigation of soot process in an optical diesel engine.
Doctoral Thesis, Brunel University, January 2012. (cited on p. 28)

Miyamoto Noboru, Ogawa Hideyuki Shibuya Masahiko Arai Keiji and Olivier Esmilaire.
Influence of the Molecular Structure of Hydrocarbon Fuels on Diesel Exhaust Emissions.
SAE Technical Paper, n^o 412, 1994. (cited on p. 32)

Modest M.F.
Radiative Heat Transfer (second ed.).
Academic Press, 2003. (cited on p. 69)

Moiz Ahmed Abdul, Ameen Muhsin M., Lee Seong Young and Som Sibendu.
Study of soot production for double injections of n-dodecane in CI engine-like conditions.
Combustion and Flame, Vol. 173, pp. 123–131, 2016. (cited on pp. 4, 36, 106, 162)

Moiz Ahmed Abdul, Cung Khanh D. and Lee Seong-Young.
Simultaneous Schlieren-PLIF Studies for Ignition and Soot Luminosity Visualization With Close-Coupled High-Pressure Double Injections of n-Dodecane.
Journal of Energy Resources Technology, Vol. 139 n^o 1, pp. 012207, 2017.
(cited on pp. 4, 36)

Musculus Mark P B.
Effects of the in-cylinder environment on diffusion flame lift-off in a DI diesel engine.
SAE transactions, n^o 724, 2003. (cited on p. 28)

Musculus Mark P. B.
Measurements of the Influence of Soot Radiation on In-Cylinder Temperatures and Exhaust NOx in a Heavy-Duty DI Diesel Engine.
SAE Technical Paper, apr 2005. (cited on p. 122)

Musculus Mark P. B.
Entrainment waves in decelerating transient turbulent jets.
Journal of Fluid Mechanics, Vol. 638 n^o 1, pp. 117, 2009.
(cited on pp. 3, 4, 12, 18, 33, 35, 149, 154)

Musculus Mark P. B., Lachaux Thierry, Pickett Lyle M. and Idicheria Cherian A.

End-of-Injection Over-Mixing and Unburned Hydrocarbon Emissions in Low-Temperature-Combustion Diesel Engines.
Sae, Vol. 2007-01-09 n^o 724, pp. 776–0790, 2007. (cited on pp. 12, 34, 35)

Musculus Mark P B, Miles Paul C. and Pickett Lyle M.
Conceptual models for partially premixed low-temperature diesel combustion, volume 39.
Elsevier Ltd, 2013. (cited on pp. 3, 11, 18, 21, 26)

Musculus Mark P B and Pickett Lyle M.
Diagnostic considerations for optical laser-extinction measurements of soot in high-pressure transient combustion environments.
Combustion and Flame, Vol. 141 n^o 4, pp. 371–391, 2005. (cited on p. 32)

Musculus Mark P B, Singh Satbir and Reitz Rolf D.
Gradient effects on two-color soot optical pyrometry in a heavy-duty DI diesel engine.
Combustion and Flame, Vol. 153 n^o 1-2, pp. 216–227, 2008. (cited on p. 30)

Naber Jeffrey D and Siebers Dennis L.
Effects of Gas Density and Vaporization on Penetration and Dispersion of Diesel Sprays.
SAE Paper 960034, Vol. 105 n^o 412, pp. 82—-111, 1996.
(cited on pp. 3, 11, 19, 20, 33, 88, 90, 97, 136)

Nerva Jean-Guillaume.
An assessment of fuel physical and chemical properties in the combustion of a Diesel spray.
Doctoral Thesis, Universitat Politecnica de Valencia, 2013.
(cited on pp. 9, 23, 26, 134, 143)

O. Koylu U. and M. Faeth G.
Optical properties of overfire soot in buoyant turbulent diffusion flames at long residence times.
Journal of heat transfer, Vol. 116 n^o 1, pp. 152–159, 1994. (cited on pp. 59, 66)

O'Connor Jacqueline and Musculus Mark.
Optical Investigation of the Reduction of Unburned Hydrocarbons Using Close-Coupled Post Injections at LTC Conditions in a Heavy-Duty Diesel Engine.
SAE Int. J. Engines, Vol. 6 n^o 1, pp. 379–399, 2013. (cited on p. 36)

O'Connor Jacqueline and Musculus Mark P. B.
Post Injections for Soot Reduction in Diesel Engines: A Review of Current Understanding.
SAE Int. J. Engines, Vol. 6 n^o 1, pp. 400–421, 2013. (cited on p. 36)

O'Connor Jacqueline, Musculus Mark P B and Pickett Lyle M.
Effect of post injections on mixture preparation and unburned hydrocarbon emissions in a heavy-duty diesel engine.
Combustion and Flame, Vol. 170, pp. 111–123, 2016. (cited on p. 36)

Osta A R, Lee J and Sallam K A.
Investigating the Effect of the Injector Length/Diameter ratio on the Primary Breakup of Liquid Jets using X-ray Diagnostics.
Iclass, n^o July, 2009. (cited on p. 14)

Pastor J. V., García-Oliver J. M., Nerva J. G. and Giménez B.
Fuel effect on the liquid-phase penetration of an evaporating spray under transient diesel-like conditions.
Fuel, Vol. 90 n^o 11, pp. 3369–3381, 2011. (cited on p. 16)

Pastor José V, Garcia-oliver José M, Bermudez Vicente and Micó Carlos.
Spray Characterization for Pure Fuel and Binary Blends under Non-Reacting Conditions.
SAE Technical Paper, 2014. (cited on pp. 16, 55)

Pastor José V., García-Oliver José M., García Antonio, Micó Carlos and Möller Sebastian.
Application of optical diagnostics to the quantification of soot in n-alkane flames under diesel conditions.
Combustion and Flame, Vol. 164, pp. 212–223, 2016. (cited on pp. 30, 61, 66)

Pastor Jose V., Garcia-Oliver Jose M., Pastor Jose M. and Vera-Tudela W.
One-dimensional Diesel spray modeling of mulitcomponent fuels.
Atomization and Sprays, Vol. 25 n^o 6, pp. 485–517, 2015. (cited on p. 64)

Pastor José V., Javier López J., García José M. and Pastor José M.
A 1D model for the description of mixing-controlled inert diesel sprays.
Fuel, Vol. 87 n^o 13-14, pp. 2871–2885, 2008. (cited on pp. 18, 19, 33, 72)

Pastor Jose V., Payri Raul, Garcia-Oliver Jose M and Briceño Francisco J.
Schlieren Methodology for the Analysis of Transient Diesel Flame Evolution.
SAE International Journal of Engines, Vol. 6 n^o 3, pp. 1661–1676, 2013. (cited on pp. 54, 143)

Pastor Jose Vicente, Arrègle Jean and Palomares A.
Diesel spray images segmentation using a likelihood ratio test.
Applied Optics, Vol. 40 n^o 17, pp. 2876–2885, 2001. (cited on p. 20)

Pastor Jose Vicente, Payri Raul, Garcia-Oliver Jose Maria and Nerva Jean-guillaume.
Schlieren Measurements of the ECN-Spray A Penetration under Inert and Reacting Conditions.
SAE Technical Paper 2012-01-0456, 2012. (cited on pp. 19, 22)

Pastor J.V., García-Oliver J.M., López J.J. and Vera-Tudela W.
An experimental study of the effects of fuel properties on reactive spray evolution using Primary Reference Fuels.
Fuel, Vol. 163, pp. 260 – 270, 2016. (cited on p. 72)

Payri F., BermÃºdez V., Payri R. and Salvador F.J.
The influence of cavitation on the internal flow and the spray characteristics in diesel injection nozzles.
Fuel, Vol. 83, pp. 419 – 431, 2004. (cited on pp. 20, 88)

Payri F, Pastor J V, García J M and Pastor J M.
Contribution to the application of two-colour imaging to diesel combustion.
Measurement Science and Technology, Vol. 18 n^o 8, pp. 2579–2598, 2007. (cited on pp. 30, 58, 69)

Payri F, Pastor J V, Pastor J M and Julian J E.
Diesel Spray Analysis by Means of Planar Laser-Induced Exciplex Fluorescence.
International Journal of Engine Research, Vol. 7 n^o 1, pp. 77–89, 2006. (cited on p. 21)

Payri F., Payri R., Bardi M. and Carreres M.
Engine combustion network: Influence of the gas properties on the spray penetration and spreading angle.
Experimental Thermal and Fluid Science, Vol. 53, pp. 236–243, 2014. (cited on p. 19)

Payri Francisco, Pastor Jose V, Nerva Jean-Guillaume and Garcia-Oliver Jose M.

Lift-Off Length and KL Extinction Measurements of Biodiesel and Fischer-Tropsch Fuels under Quasi-Steady Diesel Engine Conditions.
SAE International Journal of Engines, Vol. 4 n^o 2, pp. 2278–2297, 2011. (cited on pp. 28, 139, 146)

Payri R., Salvador F.J., Gimeno J. and Bracho G.
A new methodology for correcting the signal cumulative phenomenon on injection rate measurements.
Experimental Techniques, Vol. 32 n^o 1, pp. 46–49, 2008. (cited on p. 133)

Payri Raul, Bracho Gabriela, Marti-Aldaravi Pedro and Viera Alberto.
Near field visualization of diesel spray for different nozzle inclination angles in non-vaporizing conditions.
Atomization and Sprays, Vol. 27 n^o 3, pp. 251–267, 2017. (cited on p. 14)

Payri Raul, García-Oliver Jose M., Bardi Michele and Manin Julien.
Fuel temperature influence on diesel sprays in inert and reacting conditions.
Applied Thermal Engineering, Vol. 35 n^o 1, pp. 185–195, 2012. (cited on p. 50)

Payri Raul, Gimeno Jaime, Bardi Michele and Plazas Alejandro H.
Study liquid length penetration results obtained with a direct acting piezo electric injector.
Applied Energy, Vol. 106, pp. 152–162, 2013. (cited on pp. 16, 57)

Payri Raul, Gimeno Jaime, Novella Ricardo and Bracho Gabriela.
On the rate of injection modeling applied to direct injection compression ignition engines.
International Journal of Engine Research, Vol. 17 n^o 10, pp. 1015–1030, 2016. (cited on p. 133)

Payri Raul, Viera Juan P., Gopalakrishnan Venkatesh and Szymkowicz Patrick G.
The effect of nozzle geometry over ignition delay and flame lift-off of reacting direct-injection sprays for three different fuels.
Fuel, Vol. 199, pp. 76 – 90, 2017. (cited on p. 28)

Payri Raúl, Viera Juan Pablo, Pei Yuanjiang and Som Sibendu.
Experimental and numerical study of lift-off length and ignition delay of a two-component diesel surrogate.
Fuel, Vol. 158, pp. 957–967, 2015. (cited on pp. 28, 73)

Pei Yuanjiang.
Transported PDF Modelling of Spray Combustion at Practical Diesel Engine Conditions.
Doctoral Thesis, University of New South Wales, 2013. (cited on p. 1)

Peters Norbert.
Turbulent Combustion.
Cambridge Monographs on Mechanics. Cambridge University Press, 2000.
(cited on p. 27)

Pickett Lyle M., Caton J A, Musculus Mark P. B. and Lutz Andrew E.
Evaluation of the equivalence ratio-temperature region of diesel soot precursor formation using a two-stage Lagrangian model.
International Journal of Engine Research, Vol. 7 n^o 5, pp. 349–370, 2006.
(cited on pp. 29, 118)

Pickett Lyle M, Kook Sanghoon and Williams Timothy C.
Transient Liquid Penetration of Early-Injection Diesel Sprays.
SAE Int. J. Engines, Vol. 2 n^o 1, pp. 785–804, 2009. (cited on pp. 4, 36)

Pickett Lyle M, Kook Sanghoon and Williams Timothy C.
Visualization of Diesel Spray Penetration, Cool-Flame, Ignition, High-Temperature Combustion, and Soot Formation Using High-Speed Imaging.
SAE Int. J. Engines, Vol. 2 n^o 1, pp. 439–459, 2009. (cited on pp. 11, 22, 33)

Pickett Lyle M, Manin Julien, Genzale Caroline L, Siebers Dennis L, Musculus Mark P B and Idicheria Cherian A.
Relationship Between Diesel Fuel Spray Vapor Penetration/Dispersion and Local Fuel Mixture Fraction.
SAE Int. J. Engines, Vol. 4 n^o 1, pp. 764–799, 2011. (cited on pp. 16, 19, 20, 90)

Pickett Lyle M and Siebers Dennis L.
Fuel Effects on Soot Processes of Fuel Jets at DI Diesel Conditions.
SAE Technical Paper, n^o 724, pp. –, 2003. (cited on p. 32)

Pickett Lyle M. and Siebers Dennis L.
Non-sooting, low flame temperature mixing controlled DI diesel combustion.
SAE transactions, n^o 724, 2004. (cited on p. 32)

Pickett Lyle M. and Siebers Dennis L.
Soot in diesel fuel jets: Effects of ambient temperature, ambient density, and injection pressure.
Combustion and Flame, Vol. 138 n^o 1-2, pp. 114–135, 2004. (cited on pp. 59, 61, 70)

Pickett Lyle M, Siebers Dennis L and Idicheria Cherian A.
Relationship Between Ignition Processes and the Lift-Off Length of Diesel Fuel Jets.
SAE Technical Paper, n^o 724, pp. –, 2005. (cited on pp. 25, 28)

Ranz William E.
Some experiments on orifice sprays.
The Canadian Journal of Chemical Engineering, Vol. 36 n^o 4, pp. 175–181, 1958.
(cited on p. 20)

Reche Carlos Mico.
Development of measurement and visualization techniques for characterization of mixing and combustion processes with surrogate fuel.
Doctoral Thesis, Universitat Politecnica de Valencia, 2015.
(cited on pp. iv, ix, 2, 21, 26, 30, 133, 134, 136, 137)

Reitz R. D.
Atomization and other breakup regimes of a liquid jet.
Doctoral Thesis, Princeton Univ., NJ., 1978. (cited on p. 14)

Reitz Rolf D. and Bracco F. B.
On the Dependence of Spray Angle and Other Spray Parameters on Nozzle Design and Operating Conditions.
In *SAE Technical Paper.* SAE International, 02 1979. (cited on pp. 4, 20)

Ricou F. P. and Spalding D. B.
Measurements of entrainment by axisymmetrical turbulent jets.
Journal of Fluid Mechanics, Vol. 11, pp. 21, 1961. (cited on p. 11)

S Settles G.
Schlieren and sadowgraph techniques: visualizing phenomena in transparent media (Experimental Fluid Mechanic).
Springer Verlag, 2001. (cited on pp. 54, 86)

Sanghoon Kook and Pickett Lyle M.
Effect of fuel volatility and ignition quality on combustion and soot formation at fixed premixing conditions.
SAE Int. J. Engines, Vol. 2 n^o 2, pp. 11–23, 2009. (cited on p. 32)

Sasaki, Satoru Akagawa Hisashi and Tsujimura Kinji.
A Study on Surrounding Air Flow Induced by Diesel Sprays.
SAE Technical Paper, n^o 724, 1998. (cited on p. 3)

Sedarsky David, Berrocal Edouard and Linne Mark.
Numerical Analysis of Ballistic Imaging for Revealing Liquid Breakup in Dense Sprays.
Atomization and Sprays, Vol. 20 n^o 5, pp. 407–413, 2010. (cited on p. 14)

Siebers Dennis, Higgins Brian and Pickett Lyle.
Flame Lift-Off on Direct-Injection Diesel Fuel Jets : Oxygen Concentration Effects In-Cylinder Diesel Particulates and NOx Control.
SAE paper, n^o 724, 2002. (cited on pp. 27, 28, 144)

Siebers Dennis L.
Liquid-Phase Fuel Penetration in Diesel Sprays.
In *SAE Technical Paper.* SAE International, 02 1998. (cited on pp. iv, 16, 17)

Siebers Dennis L.
Scaling liquid-phase fuel penetration in diesel sprays based on mixing-limited vaporization.
SAE Paper 1999-01-0528, Vol. 199-01-052 n^o 724, pp. 01–0528, 1999.
(cited on pp. 11, 18)

Siebers Dennis L. and Higgins Brian S.
Effects of Injector Conditions on the Flame Lift-Off Length of DI Diesel Sprays.
In *Thermalfluidynamic Processes in Diesel Engines*, pp. 253–277, 9 2000.
(cited on p. 28)

Siebers D.L. and Higgins Brian.
Flame lift-off on direct-injection diesel sprays under quiescent conditions.
Sae Transactions, Vol. 110 n^o 3, pp. 400–421, 2001. (cited on pp. 12, 27, 28, 83, 144)

Sjöholm Johan.
High Repetition Rate Laser Diagnostics for Combustion Applications.
Doctoral Thesis, Lund University, 2012. (cited on p. 30)

Skeen Scott, Manin Julien, Pickett Lyle, Dalen Kristine and Ivarsson Anders.
Quantitative Spatially Resolved Measurements of Total Radiation in High-Pressure Spray Flames.
SAE Technical Paper, 2014. (cited on p. 30)

Skeen Scott, Manin Julien and Pickett Lyle M.
Visualization of Ignition Processes in High-Pressure Sprays with Multiple Injections of n-Dodecane.
SAE Int. J. Engines, Vol. 8 n^o 2, pp. 696–715, 2015.
(cited on pp. v, 4, 11, 22, 34, 35, 36, 153, 158, 165)

Skeen Scott a, Manin Julien, Dalen Kristine and Pickett Lyle M.
Extinction-based Imaging of Soot Processes over a Range of Diesel Operating Conditions.
Internal combustion and gas turbine engines, pp. 1–13, 2013. (cited on pp. 32, 60, 113)

Skeen Scott A., Manin Julien and Pickett Lyle M.
Simultaneous formaldehyde PLIF and high-speed schlieren imaging for ignition visualization in high-pressure spray flames.
Proceedings of the Combustion Institute, Vol. 35 n^o 3, pp. 3167–3174, 2015.
(cited on pp. iv, 11, 21, 22, 23, 24)

Som S. and Aggarwal S. K.
Effects of primary breakup modeling on spray and combustion characteristics of compression ignition engines.
Combustion and Flame, Vol. 157 n^o 6, pp. 1179–1193, 2010. (cited on p. 14)

Svensson K I, Richards M J, Mackrory A J and Tree D R.
Fuel composition and molecular structure effects on soot formation in direct-injection flames under diesel engine conditions.
SAE Transactions, Vol. 114 n^o 3, pp. 594–604, 2005. (cited on p. 32)

Tow T. C., Pierpont D. A. and Reitz Rolf D.
Reducing Particulate and NOx Emissions by Using Multiple Injections in a Heavy Duty D.I. Diesel Engine.
In *SAE Technical Paper.* SAE International, 03 1994. (cited on p. 35)

Tree Dale R. and Svensson Kenth I.
Soot processes in compression ignition engines.
Progress in Energy and Combustion Science, Vol. 33 n^o 3, pp. 272–309, 2007.
(cited on pp. v, 28, 30)

Ullman, T., Spreen, K., and Mason R.
Effects of Cetane Number on Emissions From a Prototype 1998 Heavy-Duty Diesel Engine.
SAE Technical Paper 950251, n^o 412, 1995. (cited on p. 32)

van de Hulst H. C.
Light Scattering by Small Particles.
1957. (cited on p. 16)

Venugopal Rishikesh and Abraham John.
A Review of Fundamental Studies Relevant to Flame Lift-off in Diesel Jets.
SAE Transactions, n^o 724, pp. 776–0790, 2009. (cited on p. 27)

Viskup Richard, Stanger Thomas, del Re Luigi, Reinisch Tristan and Bergmann Alexander.
Development of In-Situ, Full Stream, Laser Induced Incandescence Technique for Measurement of Transient Soot Emissions.
SAE International, pág. 7, 2013. (cited on p. 30)

W Bosch.
The fuel rate indicator: a new instrument for of the characteristic of individual injection.
SAE Technical Paper, 1966. (cited on p. 133)

Wan Yuepeng and Peters Norbert.
Scaling of spray penetration with evaporation.
Atomization and Sprays, Vol. 9 n^o 2, pp. 111–132, 1999. (cited on p. 20)

Weber Constantin.
Zum Zerfall eines Flüssigkeitsstrahles.
ZAMM - Journal of Applied Mathematics and Mechanics / Zeitschrift für Angewandte Mathematik und Mechanik, Vol. 11 n^o 2, pp. 136–154, 1931. (cited on p. 14)

Westlye Fredrik R., Penney Keith, Ivarsson Anders, Pickett Lyle M., Manin Julien and Skeen Scott A.
Diffuse back-illumination setup for high temporally resolved extinction imaging.
Applied Optics, Vol. 56 n^o 17, pp. 5028, 2017. (cited on p. 32)

Wiltafsky Georg, Stolz Wolgang, Kohler Jurgen, Espey Christoph and 961200 S a E Technical Paper.
The Quantification of Laser-Induced Incandescence (LII) for Planar Time resolved Measurements of the Soot Volume Fraction in a Combusting Diesel Jet.
International Spring Fuels & Lubricants Meeting, n^o Lii, 1996. (cited on p. 30)

X. Tauzia A. Maiboom and Ma G.
A 1D Model for Diesel Sprays under Reacting Conditions.
SAE Technical Paper, 2015. (cited on p. 72)

Yamakawa, M. Takaki D. Li T. Zhang Y.
Quantitative Measurement of Liquid and Vapor Phase Concentration Distributions in a D.I. Gasoline Spray by the Laser Absorption Scattering (LAS) Technique.
SAE Technical Paper, 2002. (cited on p. 55)

Zeoli N. and Gu S.
Numerical modelling of droplet break-up for gas atomisation.
Computational Materials Science, Vol. 38 n^o 2, pp. 282–292, 2006. (cited on p. 15)

Zhang Ji, Jing Wei, Roberts William L. and Fang Tiegang.
Soot temperature and KL factor for biodiesel and diesel spray combustion in a constant volume combustion chamber.
Applied Energy, Vol. 107, pp. 52–65, 2013. (cited on p. 30)

Zhao Hua and Ladommatos N.
Optical Diagnostics for soot and temperature measurement in diesel engines.
Progress in energy and combustion science, Vol. 24, pp. 221–255, 1998.
(cited on pp. 30, 58)

Zheng Liang, Ma Xiao, Wang Zhi and Wang Jianxin.
An optical study on liquid-phase penetration, flame lift-off location and soot volume fraction distribution of gasoline-diesel blends in a constant volume vessel.
Fuel, Vol. 139, pp. 365–373, 2015. (cited on pp. 32, 61)